NTNU
Norwegian University of
Science and Technology

Master Thesis

Formation control of marine vessels

Author:
Christoffer Thorvaldsen

June 12, 2011

NTNU Trondheim
Norwegian University of Science and Technology
Department of Marine Technology

MASTER THESIS IN MARINE CONTROL ENGINEERING

Name of the candidate: Christoffer F. L. Thorvaldsen
Field of study: Marine control engineering
Thesis title (Norwegian): Formasjonsstyring av maritime fartøy
Thesis title (English): Formation control of marine vessels

Background
Research on formation control problems has through the latest years been extensive. Recent results opens, however, up for further extensions of the formation control methodology for marine vessels and other dynamical systems. A formation control problem involves the tasks of group coordination and a mission objective. While group coordination includes subproblems such as formation reconfigurations, intervessel communication, obstacle detection, and collision avoidance, the mission objective is often formulated as a tracking task, a path-following task, or more complex operations.

Work description
This master thesis project is concerned with group coordination and path-following for marine surface vessels, where path-following is typically solved as a maneuvering problem. The main objective is to separate the pursuit of group coordination from path-following by dividing an operation into a coordination phase and a mission phase. To the extent possible, efforts should be made into controlling the transient behavior of the vessels within the operational phases, and the behavior of the formation when failures occur.
A literature study and a study of relevant concepts and terms related to formation control shall be conducted and reported. The main task for the candidate is, however, to develop constructive methods for formation control solving the group coordination objective and the path-following objective according to the abovementioned aspects. Each proposed design shall be conceptually illustrated, analyzed, and demonstrated through computer simulations. The designs shall be concluded by proven theorems.

Guidelines
The scope of work may prove to be larger than initially anticipated. By the approval from the supervisor, described topics may be deleted or reduced in extent without consequences with regard to grading.
The candidate shall present his personal contribution to the resolution of problems within the scope of work. Theories and conclusions should be based on mathematical derivations and logic reasoning identifying the various steps in the deduction.

The report shall be organized in a rational manner to give a clear exposition of results, assessments, and conclusions. The text should be brief and to the point, with a clear language. The report shall be written in English (preferably US) and contain the following elements: Summary, table of contents, main body, conclusions with recommendations for further work, list of symbols and acronyms, references, and (optional) appendices. All figures, tables, and equations shall be numerated. The original contribution of the candidate and material taken from other sources shall be clearly identified. Work from other sources shall be properly acknowledged using a Harvard citation style (e.g. *natbib* Latex package). Any plagiarism is taken very seriously by the university, and any such practice will have consequences.
The thesis shall be submitted in 3 printed copies, each signed by the candidate. The final revised version of this project description must be included. The report must appear in a bound volume or a binder according to the NTNU standard template. Computer code and a PDF version of the report should be included electronically.
A 15 min. presentation (conference style) should be given on your main results around due date.

Start date: February 1, 2011 **Due date:** As specified by the administration.
Supervisor: Professor Roger Skjetne

Trondheim

_____
Roger Skjetne (supervisor)

Preface

This thesis concludes my five-year M.Sc. education at the Norwegian University of Science and Technology. Starting out in the program *Engineering and ICT*, I did certainly not foresee that I would be immersed in theoretical control design at the end of my studies. Looking back at the crossroads faced, I am truly happy with my choices, as designing control systems is a highly rewarding and exciting endeavor. I would like to thank my supervisor Professor Roger Skjetne for his encouragement and assistance throughout the project in general, and for his efforts in co-authoring the paper submitted to the *50th IEEE Conference on Decision and Control and European Control Conference, 2011*. I would also like to thank my family and friends for their continuous support.

Christoffer F.L. Thorvaldsen,
Trondheim, June 12, 2011

Summary

As an enabling technology of coordinated multi-vessel operations, formation control has received considerable attention in recent times, with specific applications ranging from satellites in space to wheeled robots on the ground. This thesis will serve as a continuation of previous efforts within the marine control community, focusing on formation control design for fully actuated marine surface vessels. The main objective for the designs is to enable a group of vessels to automatically position themselves in a specified formation structure, which in turn should propagate along a parameterized path at a desired speed. Although this problem statement forms the basis of many designs in the literature, a new approach is taken herein where the vessels establish the formation in their immediate vicinity prior to initiation of a collective movement towards the path. This separation between group coordination and path following has, at least to the authors knowledge, not been pursued in previous works.

In Chapter 1, terms relevant to formation control systems are explained, and a review of earlier work is conducted. Mathematical background is given in Chapter 2, after which the control designs take center stage in Chapter 3. Three different designs are presented. The first two combine a decentralized group coordination framework with maneuvering theory, utilizing the former to coordinate the vessels into a formation, and the latter to ensure subsequent path following. Generic maneuvering theory forms the basis of the third design, where an intuitive Line-of-sight steering algorithm is incorporated to ensure feasible and predictable motion towards the path for the formation. Strong, global stability results are achieved for all three designs, and computer simulations in Matlab/Simulink are used to illustrate their performance.

In Chapter 4, the proposed control designs are evaluated with respect to inter-vessel communication requirements, behavior during vessel failure scenarios, collision avoidance capabilities, and transient behavior during group coordination and path following. An ability to maintain formation structure during mild and severe single vessel failures is demonstrated, illustrating the intuitive notion that the separation and prioritization of group coordination and path following increases safety. However, a guarantee against collisions is not given, as none of the designs incorporate explicit collision avoidance capabilities. Moreover, the designs are shown to require considerable inter-vessel communication during operations in general, which could limit their applicability for large groups.

Abbreviations

CLF	Control Lyapunov function
FRF	Formation reference frame
FRP	Formation reference point
GNC	Guidance, navigation, and control
IMU	Inertial measurement unit
LOS	Line-of-sight
UGAS	Uniformly globally asymptotically stable
UGES	Uniformly globally exponentially stable
UGS	Uniformly globally stable

Contents

Preface ii

Summary iii

Abbreviations iv

1 Introduction 1
- 1.1 Motivation . . . 1
- 1.2 Explanation of terms . . . 4
- 1.3 Review of earlier work . . . 9
  - 1.3.1 The behavioral approach . . . 9
  - 1.3.2 The leader-follower approach . . . 10
  - 1.3.3 The virtual structure approach . . . 10
  - 1.3.4 The cooperative approach . . . 11
- 1.4 Main contributions . . . 14
- 1.5 Publications . . . 15

2 Preliminaries 16
- 2.1 Notation . . . 16
- 2.2 Stability properties . . . 17
  - 2.2.1 Stability of equilibrium points . . . 17
  - 2.2.2 Set-stability . . . 17
- 2.3 Reference frames . . . 17
- 2.4 Vessel models . . . 18
  - 2.4.1 Dynamical model without environmental disturbances . . . 18
  - 2.4.2 Dynamical model including a constant environmental disturbance . . . 19
- 2.5 Communication topology . . . 19
- 2.6 Kronecker products . . . 20

3 Formation Control Design 21
- 3.1 Introduction . . . 21
- 3.2 Design 1: Formation control using group agreement protocols . . . 23
  - 3.2.1 Setup . . . 23
  - 3.2.2 Problem statement . . . 24
  - 3.2.3 Control design . . . 24
  - 3.2.4 Stability analysis . . . 28
  - 3.2.5 Practical considerations . . . 34
  - 3.2.6 Simulations . . . 38
- 3.3 Design 2: Closed-loop guidance and control design . . . 45
  - 3.3.1 Guidance system design aspects and approach . . . 45

3.3.2 Setup and problem statement . . . 46
3.3.3 Preliminary tracking control design . . . 46
3.3.4 Preliminary guidance control design . . . 48
3.3.5 Final control design . . . 48
3.3.6 Stability analysis . . . 49
3.3.7 Notes on implementation . . . 55
3.3.8 Simulation . . . 56
3.4 Design 3: Generic maneuvering design using a LOS approach . . . 59
3.4.1 The LOS algorithm . . . 59
3.4.2 Setup and problem statement . . . 61
3.4.3 Control design . . . 62
3.4.4 Stability analysis . . . 67
3.4.5 Practical considerations . . . 70
3.4.6 Simulations . . . 73

4 Evaluation of control designs **78**
4.1 Evaluation criteria . . . 78
4.2 Evaluation . . . 78
4.2.1 Communication requirements . . . 78
4.2.2 Behavior during vessel failures . . . 79
4.2.3 Collision avoidance capabilities . . . 89
4.2.4 Transient behavior during group coordination and path following . . . 90
4.3 Comparison of designs . . . 90

5 Conclusion **92**
5.1 Recommendations for future work . . . 93

Bibliography **94**

Appendices **96**

A Stability theorems **97**
A.1 Nested Matrosov Theorem . . . 97
A.2 Partial set-stability for interconnected systems . . . 98

B Vessel Simulation Model **99**

C Calculations **101**
C.1 Proof of Lemma 1 . . . 101
C.2 Further details on proofs of theorems 1 and 2 . . . 101
C.3 Proof of Proposition 2 . . . 102
C.4 Proof of diffeomorphism property for the third design . . . 102
C.5 Further details on the proof of Theorem 3 . . . 103
C.6 Feedforward signals for the third design . . . 103

D Conference paper **107**

Chapter 1

Introduction

Formation control is concerned with simultaneous control of multiple dynamical systems, termed *agents*, where the core objective is to get the agents to obtain and maintain a specified relative spatial configuration in their output space. As an enabling technology of coordinated collective movement, fulfilling a desired behavior for the formation as a whole often forms a second objective for the control designer. Examples are setpoint regulation, trajectory tracking, and path following. In this thesis, the desired behavior for the formation will involve path following, and solutions to the formation control problem will be proposed for fully actuated marine surface vessels.

1.1 Motivation

Applications of formation control are diverse and can be found on land, at sea, in the air and in space, within both civil and military operations. The governing idea is to use formations to improve performance in operations traditionally executed by single agents, and to enable execution of operations that are infeasible for any single agent. Many applications have been envisioned in relation to the field of autonomous vessel technology, where unmanned, self-governing vessels are used to aid or replace humans in tedious, dangerous and hazardous missions. Applications of formation control can, however, also be found in operations involving groups of manned vessels to improve performance and reduce fatigue and difficulty for the people involved.

Applications of formation control involving unmanned vessels can be found at different levels of operational autonomy. Some operations are highly autonomous in the sense that unmanned vessels are used exclusively, while others have a lower level of autonomy through involvement of manned vessels. An example of the former is the massive, distributed sensing networks envisioned in Breivik (2010), where fleets of autonomous vessels cooperate in providing real-time data from areas that may be unaccessible or too large to cover for manned vessels. Some examples of applications where such networks could be useful are coastline surveillance, oil and gas exploration in arctic regions, and oceanographic sampling. By making sure that the groups of autonomous vessels travel in formation structures during such missions, the collective range of sensor equipment can be maximized, ensuring that larger areas can be covered in shorter time. Moreover, reliability is achieved through redundancy, as remaining vessels can reconfigure into new formation structures to minimize loss of collective sensing ability after individual vessel failures. In space, satellites would be important assets in distributed sensing networks, and formation control can also be utilized in this domain, as sensor arrays of multiple satellites can provide images of higher resolution than single satellites(Breivik 2010). Other examples of highly autonomous operations where the use of formations would be natural can be found in the military domain, including reconnaissance and coordinated mine clearing using robots, combat using autonomous aerial vehicles, search and rescue mis-

sions and security patrols. In the future, it is also envisioned formations of unmanned ships for efficient transport of cargo, and for towing of large structures (e.g. semi-submersibles, floating wind turbines).

Although fully autonomous, massive, distributed sensing networks are visions of the future, similar applications of formation control can be found in present time. An example is seabed mapping operations, where a vessel carrying sensor equipment propagates along the ocean surface in order to obtain information about the topology of the seabed underneath. The sensor equipment can only retrieve information within a certain area below the ship, so in order to map a large area, a single ship will have to track back and forth in straight lines offset by some distance for each pass. By including additional unmanned surface vessels in a formation with the manned survey ship, a larger area can be covered in each pass, thus reducing the time of operation to great extent.

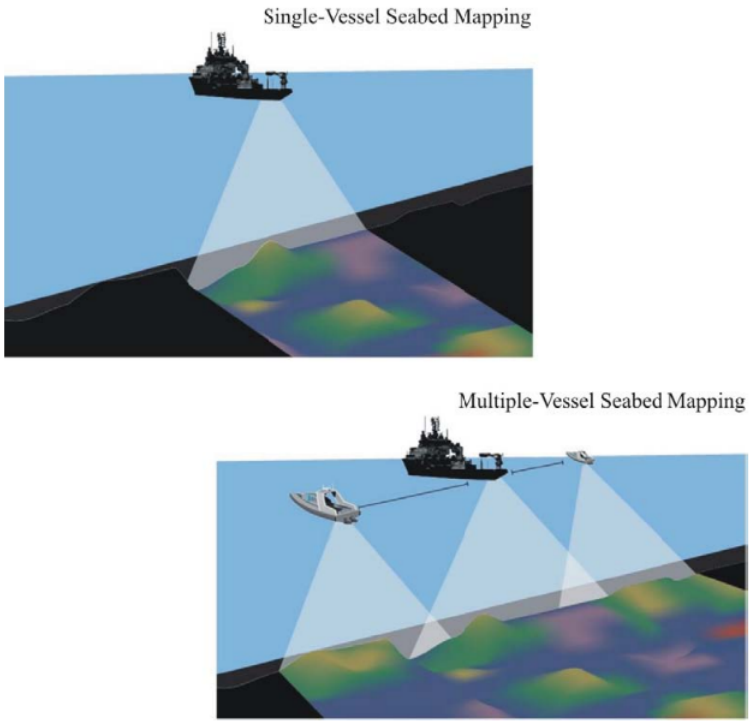

Figure 1.1: Single and multiple-vessel seabed mapping. Illustration courtesy of Breivik (2010).

In operations involving groups of manned vessels, applications of formation control can be found both in the air and at sea. Automated formation flight could reduce pilot fatigue during missions involving extensive transit by making the pilots take turns on being formation leaders, letting formation controllers ensure that the other aircraft stay in formation with respect to the assigned leader. Aerial refueling is another natural application, as tight formation flying is vital to such operations. The marine equivalence of aerial refueling - underway replenishment of ships - constitutes another application. Underway replenishment operations are motivated by the prohibitive costs of taking large ships to port whenever supplies and fuel need to be replenished, as well as by the desire to decrease the downtime of operations. They are typically performed by one or more supply ships lining up at the side of the receiving ship, after which all ships strive to maintain equal and constant forward speed and bearing while supplies are being transferred across messenger lines(Wikipedia 2010b).

Figure 1.2: USS Harry S. Truman CVN-75, USNS Arctic T-AOE-8 and USS Monterey CG-61 performing an underway replenishment in the Persian Gulf. Courtesy of MaritimeQuest (2010).

In replenishment operations requiring close proximity between the ships, hydrodynamic phenomena creating attraction and repulsion forces can arise(Skejic et al. 2009). Considering that small deviations in course and speed can lead to collisions, these hydrodynamic effects introduce notable risk. If the crucial role of the helmsmen could be replaced by formation controllers taking the hydrodynamic phenomena into consideration, the formation keeping capabilities of the ships would not be influenced by human errors, thereby increasing safety.

1.2 Explanation of terms

Important terms related to formation control will be addressed in the following.

- **Formation:** A formation is a specific physical arrangement of a group of entities. It is a geometrical concept where only the relative positioning of the entities is of relevance.
- **Agent:** Herein, an agent is defined as an entity (e.g. marine vessel, satellite, ground vehicle) that can be systematically controlled/manipulated.
- **Group coordination problem:** A group coordination problem is concerned with coordinating a group of agents to obtain a desired configuration for the group as a whole.
- **Group agreement problem:** A group agreement problem is a special case of the group coordination problem, where it is desired to steer variables of interest to common values across the group of agents(Arcak 2007).
- **Consensus problem:** Consensus problems are the same as group agreement problems (see e.g. Olfati-Saber and Murray (2003)).
- **Cooperative control:** Cooperative control deals with design of control protocols that will solve group coordination problems.
- **Formation control:** Formation control is concerned with design of control schemes that will enable a group of agents to obtain and maintain a specified formation structure in their output space. Typically, additional requirements to the collective behavior of the formation are also considered in the design procedure. This could for instance involve trajectory tracking, path following, or setpoint regulation.
- **Swarming:** Swarming is related to the movement of a formation. According to Wikipedia (2010a), swarming refers to the behavior of an aggregate of animals migrating in the same direction. Furthermore, it is stated that flocking refers to swarming of birds, while schooling refers to swarming of fish. The two latter terms are sometimes given different meanings in the formation control literature. The alternative definitions are stated below.
- **Flocking:** In Leonard and Fiorelli (2001), flocking is explained as a maneuver where the agents in a formation circles a stationary point so that the center of mass of the group is stationary.
- **Schooling:** In Leonard and Fiorelli (2001), schooling is explained as a maneuver corresponding to a pure, steady translation of a formation. This implies that the formation as a whole does not rotate, which makes it fundamentally different from a flocking maneuver.
- **Leader-Follower:** In the context of formation control, leader-follower refers to a design framework where a formation is split into leaders and followers. The role of the leaders is to dictate the motion of the formation as a whole, while the followers role is to move relative to the leaders so that they maintain the formation. The reader is referred to Section 1.3 for a more thorough explanation of the leader-follower approach and the other common design approaches within formation control.
- **Virtual structure:** The concept of a virtual structure is introduced in Lewis and Tan (1997), where it is given the following definition: "A virtual structure is a collection of elements, e.g. robots, which maintain a (semi-)rigid geometric relationship to each other and a frame of reference".

  In formation control, the virtual structure approach forms a framework for control design where the desired formation is treated as a rigid structure whose motions generate the desired trajectories for each agent. A more detailed description of the virtual structure approach and how it relates to other design approaches is given in Section 1.3.3.

- **Virtual leader:** A virtual leader is a virtual agent that can be used to define desired formation configurations for agents in the group (e.g. as a specified distance or position vector relative to the virtual leader), and to direct the motion of the formation as a whole within the virtual structure and leader-follower approaches of formation control.

- **Artificial potential functions:** As stated in Leonard and Fiorelli (2001), artificial potential functions are used to derive interaction forces between neighboring agents in a formation. The potentials are designed so that the corresponding forces acts as attractors or repulsers, depending on the distance between the agents relative to a set of desired distances.

- **Formation reference point, Formation reference frame:** Formation reference points (FRPs) and formation reference frames (FRFs), as illustrated in Skjetne (2005), constitute an approach to specification of a desired formation configuration. The configuration for n agents is specified as a set of vectors $\mathbf{l}_i$, $i = 1 \dots n$, in a local frame of reference termed the formation reference frame. The origin of the formation reference frame is termed the formation reference point. In this thesis, however, the formation reference point will be given a more general meaning by defining it as a vector containing the orientation and position of origin of the corresponding FRF relative to the global reference frame.

  To illustrate the approach, consider three marine surface vessels in an equilateral triangle formation, where vessels 3 and 2 have an orientation offset of $\pm\frac{\pi}{2}[rad]$ relative to vessel 1. Fix an FRF in the geometrical center of the triangle and align its orientation with vessel 1:

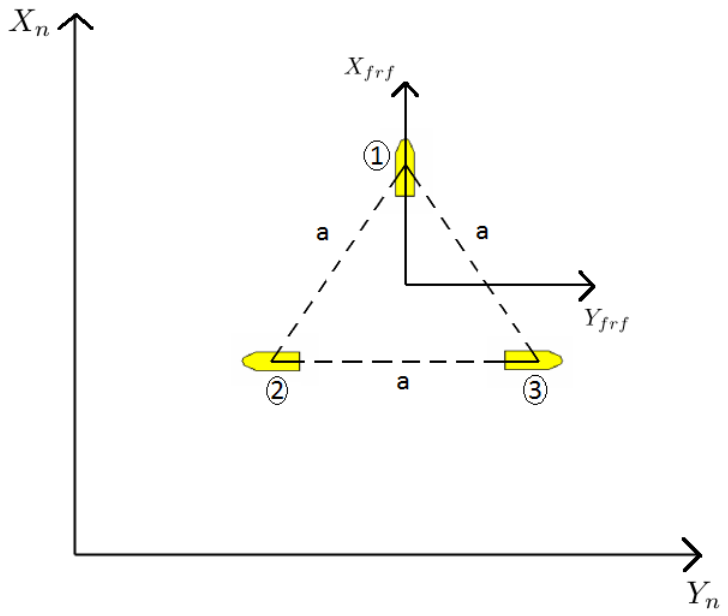

Figure 1.3: Illustration of an equilateral triangle formation using a formation reference frame

The generalized position vectors $\boldsymbol{\eta}_i = [x_i, y_i, \psi_i]^\top$ containing the positions and orientations of the three vessels relative to the global reference frame can now be expressed as

$$\boldsymbol{\eta}_i = \mathbf{x_0} + \mathbf{R}(\psi_f)\mathbf{l}_i \qquad i = 1, 2, 3, \tag{1.1}$$

where $\mathbf{x_0} = [x_f, y_f, \psi_f]^\top$ is the FRP containing the position and orientation of the FRF with respect the global frame, $\mathbf{R}(\cdot)$ is the rotation matrix in yaw (see Section 2.4.1) , and the vectors $\mathbf{l}_i$ are equal

to

$$\mathbf{l}_1 = [\frac{\sqrt{3}a}{4}, 0, 0]^\top$$
$$\mathbf{l}_2 = [-\frac{\sqrt{3}a}{4}, -\frac{a}{2}, -\frac{\pi}{2}]^\top$$
$$\mathbf{l}_3 = [-\frac{\sqrt{3}a}{4}, \frac{a}{2}, \frac{\pi}{2}]^\top$$

In a straight forward formation control design, the objective would now be to get the vessels to converge to desired generalized positions given by the right hand side of (1.1), where it is noted that the FRF may translate and rotate in time according to a desired motion for the formation.

- **Anti-collision:** Anti-collision is concerned with design of control protocols that enable vessels to automatically avoid collisions with objects in their surrounding environment during operations. As stated in Breivik (2010), such designs involve sense and avoid capabilities, where the former includes having access to global and local information about the environment, and the latter includes long-term proactive planning and short-term reactive planning.

- **Navigation, guidance, and control:** Navigation, guidance and control refers to the three building blocks that constitute a motion control system.

  The navigation block deals with processing of sensor signals and estimation of unmeasured states (e.g. velocity and acceleration) from measured states (e.g. position). The role of the navigation block can thus be summarized as determining "where we are".

  The guidance block deals with generation of reference signals that is fed to the control block. These signals contain the instantaneous desired states for the vessel. The role of the guidance block can thus be summarized as determining "where we want to go".

  The control block, typically consisting of high-level force and moment controllers in cascade with low-level actuator controllers, generates actuator commands to get the states of the vessel to converge to the reference signals received from the guidance block. Its role can thus be summarized as getting the vessel from "where we are", to "where we want to go".

- **Setpoint regulation, trajectory tracking, path following, maneuvering, generic maneuvering:** These expressions are related to different control objectives.

  Setpoint regulation refers to a control objective where the output of the system in question should be controlled to a fixed value. In marine operations, setpoint regulation is referred to as station-keeping, where the control system should make the vessel obtain and maintain a fixed position and orientation.

  Trajectory tracking involves getting the output of the system to follow a time-varying reference signal.

  Path following involves getting the output of the system to follow a parameterized path, without any constraint on the propagation along the path (i.e. path following only involves a spatial constraint. Including a temporal constraint would make it a trajectory tracking problem).

  Maneuvering, as treated in Skjetne (2005), refers to a control objective consisting of two subtasks.

The *geometric task* consists of getting the output of the system, $\mathbf{y}(t)$, to converge to a desired path parameterized by a path variable θ. Denoting the desired output states corresponding to the path as $\mathbf{y}_d(\theta)$, the first objective is thus given by

$$\lim_{t\to\infty} |\mathbf{y}(t) - \mathbf{y}_d(\theta(t))| = 0$$

The *dynamic task* consists of getting the path variable to satisfy either a time assignment, speed assignment or acceleration assignment in the limit. For a speed assignment with desired speed function $v_s(\theta, t)$, this task can be expressed as

$$\lim_{t\to\infty} |\dot{\theta}(t) - v_s(\theta(t), t)| = 0$$

By having separate geometric and dynamic tasks, it is possible to prioritize between the two so that one always has precedence over the other. When the geometric task is given highest priority, the transient dynamics of θ can be assigned to yield faster convergence of the system output to the path, and thus faster fulfillment of the geometric task (this is done with gradient optimization in Skjetne (2005)). The result is increased flexibility with respect to the trajectory tracking scenario, where the temporal and spatial tasks are entwined.

The **Generic maneuvering** problem, introduced in Skjetne (2005) and proposed thoroughly in Skjetne et al. (2011), is a generalization of the maneuvering problem. As in the maneuvering problem, two tasks are considered: the geometric task and the dynamic task. Rather than targeting convergence to a parameterized path, the geometric task involves convergence to a a manifold of dimension $q \geq 1$. For a system with state vector $\mathbf{x} \in \mathbb{R}^n$ and output $\mathbf{y} = \mathbf{h}(\mathbf{x})$, $h : \mathbb{R}^n \mapsto \mathbb{R}^m$, the desired manifold can be expressed by the set

$$\mathcal{Q} = \{\mathbf{x} \in \mathbb{R}^n : \exists \boldsymbol{\zeta} \in \mathbb{R}^q \quad s.t. \quad \mathbf{h}(\mathbf{x}) = \mathbf{h}_d(\boldsymbol{\zeta})\},$$

where $\mathbf{h}_d : \mathbb{R}^q \mapsto \mathbb{R}^m$. The geometric task then becomes

$$\lim_{t\to\infty} |\mathbf{y}(t) - \mathbf{h}_d(\boldsymbol{\zeta}(t)| = 0$$

The dynamic task involves satisfying a desired dynamical assignment $\mathbf{f}_d(\boldsymbol{\zeta}, \mathbf{y}, t)$ for $\dot{\boldsymbol{\zeta}}$ in the limit, typically corresponding to the desired dynamics when the geometric task is fulfilled:

$$\lim_{t\to\infty} |\dot{\boldsymbol{\zeta}}(t) - \mathbf{f}_d(\boldsymbol{\zeta}(t), \mathbf{y}(t), t)| = 0$$

- **Configuration Space, work Space:** The work space can be defined as the space in which a vessel moves(Fossen and Breivik). For a marine surface vessel, the work space can be regarded as two-dimensional (neglecting vertical motions on the ocean surface due to waves, etc.), while it is three dimensional for a submarine. The configuration space is constituted by a set of variables that are sufficient to specify all points of the vessel in the workspace(Fossen and Breivik). For the marine surface vessel, this space is three-dimensional (two position variables and one orientation variable), while it can be six or seven-dimensional for the submarine (three position variables, and three/four orientation variables for Euler angles/quaternions).

- **Centralized/Decentralized control:** The terms centralized and decentralized control are used to describe the amount of communication required in a multi-agent control scheme. In centralized schemes, the control law for each agent requires input signals that only can be obtained by gathering and processing information from all the agents in the group. Typically, the only feasible way this can be done for large groups is for each agent to send relevant data to a central location where all the data is gathered, processed, and redistributed back to the vessels.

In a decentralized scheme, efforts have been made to decrease the required inter-agent communication, so that the control law for each agent only requires input from a subset of the other agents. The lines of communication could be time-varying, e.g. where each agent requires input from other agents that are within some proximity threshold, or time-invariant, where they have been established prior to the operation.

1.3 Review of earlier work

Formation control has received a considerable amount of attention in the last two decades, resulting in control designs for a wide range of applications and dynamical systems. It is common to divide the research efforts into three main groups based on the approach used in the control designs; the behavioral approach, the virtual structure approach, and the leader-follower approach. Although there is a clear distinction between the behavioral approach and the other two approaches, the differences between the leader-follower and virtual structure approaches are more subtle and open to interpretation. Some of the papers that have been examined in relation to this thesis do not lend themselves well to the abovementioned categorization. Because of this, a fourth category consisting of the *cooperative approach* will be used. For clarity of presentation, work related to the different approaches will be treated separately.

1.3.1 The behavioral approach

In the behavioral approach, the controller of each agent enforces local motion primitives similar to those observed in migrating groups of animals in nature. The approach has its origin in the work of computer scientist Craig W. Reynolds in Reynolds (1987), where a new method for animation of flocks, herds and schools was proposed. Rather than scripting the individual paths of the animals explicitly, it was proposed that animations could be generated through computer simulation by representing each animal as a dynamical system, and assigning acceleration vectors in accordance with three fundamental local behaviors in order of decreasing precedence; collision avoidance, velocity matching, and flock centering. The former represents each animals desire to avoid collisions with nearby flock mates and external objects, the latter each animals desire to stay close to nearby flock mates, while velocity matching represents a desire to obtain a common velocity for the group. The proposed algorithm is that each fundamental behavior assigns its own desired acceleration vector, which then is processed through a weighting algorithm to provide the final acceleration vector of each animal.

Although the idea of letting the motion of each group member be influenced by a weighting of fundamental motion primitives has been passed on to the behavioral approach in formation control, the motion primitives have been modified. The reason should be quite apparent, as the motion primitives in Reynolds (1987) yields no possibilities to specify a certain formation structure, and no control of the collective motion of the group. In Balch and Arkin (1998), behavior-based control is applied to wheeled robots. The local motion primitives, termed *motor-schemas*, are given by collision avoidance with static objects and other robots, formation maintaining, and movement towards a target-position. The desired position of each robot with respect to formation maintaining can be calculated in three different ways, either relative to the centroid of the instantaneous position of the group, relative to an assigned formation leader, or relative to one of the other robots (termed the neighbor). The motion assignment of each robot is given by combining individual contributions from each motion primitive, where a simple weighted average is used.

In Arrichiello et al. (2006), the behavior-based method is used to control groups of underactuated marine vessels. The control system consists of local maneuvering controllers that receive reference values from a centralized guidance system based on the so-called null-space-based behavioral approach. The local motion primitives, termed *tasks*, are associated with analytical functions of the system configuration (the generalized position vectors of the vessels). Desired trajectories for the functions are specified, after which corresponding, desired velocities for the ships are generated through inverse kinematics. The total commanded velocity for each vessel is given by a null-space based weighting algorithm, where strict prioritization is achieved in the sense that velocity components of a task conflicting with the velocity corresponding to a task of higher priority are removed. Three tasks are considered; Obstacle avoidance

(with external objects and other ships), movement of the average position of the group, and keeping in formation with respect to the average position of the group.

1.3.2 The leader-follower approach

In the leader-follower approach, hierarchy is assigned within the group of agents that is to be controlled in formation. Followers strive to stay in formation with respect to their assigned leader(s), whose motions are unaffected by their followers[1]. The leaders do not necessarily have to be agents, as virtual leaders can be used effectively to control the movement of the group. By including multiple levels of leader-hierarchy (so that the group has one true leader while some agents are both leaders and followers at the same time), the leader-follower methodology allows for distributed control of large groups. This approach is taken in e.g. Desai et al. (2001), where graph-theory and combinations of so-called $l - \psi$ and $l - l$ control are used to control mobile robots into reconfigurable formations, and in Mesbahi and Hadaegh (1999), where graph-theory and hybrid control solutions are used on groups of flying spacecraft.

In Breivik et al. (2006), a guided formation control scheme is proposed to get a group of unicycle-type robots into formation with respect to a virtual leader propagating along a regularly parameterized path. The design consists of three modules in cascaded structure, where the first consists of local motion controllers for each robot controlling their forward and rotational speed as well as their orientation to reference values received from guidance systems. The guidance system of each robot, all of which are collected in the second module, utilizes look-ahead-based steering rules to drive the robot into formation with respect to a local point on the path, termed the collaborator. The guidance systems collect inputs from the third module, whose job is to ensure that all collaborator points are synchronized with the virtual leader in the limit. This is done solely by adjusting the velocity reference signals to the ships, not by manipulating the motion of the virtual leader. The design thus falls into the leader-follower category. In Breivik et al. (2008), the same guided formation control approach is applied to marine surface vessels subjected to an unknown, constant environmental disturbance.

Formation control design for underway replenishment operations is well suited to the leader-follower approach. By controlling the supply ship and letting the receiving ship be a passive leader, the demands placed on the technology of the receiving ship are reduced compared to a cooperative control design. This can in turn broaden the applicability of operations into the civil domain. In Kyrkjebø and Pettersen (2003), a leader-follower design is proposed. By using an observer-controller structure for the supply ship, the control system only requires that position and orientation measurements are available from the two ships. Furthermore, no demands are placed on the availability of a dynamical model for the receiving ship.

1.3.3 The virtual structure approach

The virtual structure approach of formation control has its origin in Lewis and Tan (1997). An iterative algorithm is proposed to make a collection of mobile robots comply with a virtual structure, specified as a set of desired position vectors in a local reference-frame. Each iteration in the proposed algorithm consists of four steps. The first step is to align the virtual structure to the instantaneous position of the robots. This involves an optimization problem where the local reference-frame is moved to minimize the positional errors between the robots and their designated positions in the virtual structure. The second step involves displacing the virtual structure in accordance with an underlying mission objective, e.g. moving to a target position. The third step involves computing trajectories for each robot to catch up

[1] The absence of mutual influence between leaders and followers is often not included in descriptions of the leader-follower approach in the literature. The description used herein, which is supported by e.g. Ren and Beard (2003) and Ghommem et al. (2007), enables a more clear-cut separation with the virtual structure approach, as explained in Section 1.3.3.

with the displaced virtual structure within an allotted time-window, while the final step involves following the calculated trajectories. A method for ensuring reasonable displacement of the virtual structure in the second step is also proposed by defining reachability regions for each robot (which are based on nonholonomic constraints and limitations in actuators) and using optimization techniques.

As the origin of the virtual structure approach is found within an algorithmic framework, a natural question to ask is how the approach translates to a general control design methodology. A common characterization of the approach in the literature is that it involves treating the formation as a rigid structure whose motion generates the desired trajectories for each agent. Although this general characterization certainly complies with Lewis and Tan (1997), it also yields a possible overlap with the leader-follower approach. After all, if the virtual structure moves without any consideration for the agents in the group, it can essentially be viewed as a virtual formation leader in accordance with the leader-follower methodology. Since we have emphasized that leaders should be unaffected by their followers in the leader-follower approach, a natural way to separate the two approaches is to require collaboration or mutual influence in the virtual structure approach. This characterization fits very well with Lewis and Tan (1997), as the first step in the proposed control algorithm effectively involves feedback from the robots to the motion of the virtual structure.

In Skjetne (2005; Chap. 6), the formation control problem is solved for fully actuated agents belonging to a general class of dynamical systems. The approach consists of defining an FRF that propagates along a parameterized path, specifying the formation as a set of vectors to be attained in the FRF, and restating the problem as a maneuvering problem. Two designs are presented, the first of which follows the virtual structure approach. In this design, the path variable in the path parameterization is assumed to be available for each vessel. The dynamic update law for the variable is chosen to consist of a nominal term corresponding to a desired speed profile along the path, and a perturbation term that tries to minimize the Lyapunov function used in the control design through gradient optimization. This perturbation term provides the feedback from the vessels to the motion of the FRF that makes the design comply with the virtual structure approach. The gradient optimization provides some very nice robustness properties, demonstrated through simulations for marine surface vessels where one of the vessels in the group saturates. The FRF slows down, adjusting to the weakest link in the group, ensuring that the formation travels at a speed that all the vessels can follow.

In Egerstedt and Hu (2001), a model-independent formation control scheme is introduced. Instead of designing control laws for the agents directly, it is assumed that tracking controllers already are implemented, so that the problem can be reduced to designing intelligent reference signal generators. The desired formation structure is specified relative to a virtual leader that moves along a parameterized path. The reference trajectory for each agent is chosen to propagate in a direction that minimizes a so-called *formation control function*, where the magnitude of the motion depends on the tracking error. Similarly, the velocity of the virtual leader along the path depends on the tracking errors of all the agents, slowing down when they are large and speeding up when they are small. The result is a robust scheme guaranteeing that the reference positions converge into formation as long as the tracking controllers of the agents can guarantee upper bounds on the tracking errors (obviously, the agents will only converge to the formation if the tracking controllers have asymptotical convergence properties).

1.3.4 The cooperative approach

A considerable amount of work on formation control does not seem to fit comfortably into the behavioral, leader-follower, or virtual structure veins. In these efforts, there is no explicitly stated virtual structure or leader dictating the desired positions for all the agents. The challenge of obtaining and maintaining a

desired formation structure is instead approached as a problem of mutual coordination and synchronization, where the agents are controlled relative to one another with little or no restrictions to their absolute positions (i.e. synchronization within some manifold, e.g. a parameterized path, with no restrictions on absolute position within the manifold).

The second formation control design in Skjetne (2005; Chap. 6) follows the cooperative approach. The assumption of a commonly known path variable from the first design is relaxed. Each agent is instead assigned a local path variable corresponding to a local FRF, and is controlled to its correct position with respect to this FRF. The update law for each local path variable consists of a nominal term chosen in accordance with a speed assignment, and a perturbation term that is designed to enable asymptotical agreement with the other local path variables. Calculation of the perturbation term for a given agent only requires communication with a limited number of other agents, resulting in a decentralized control scheme. Furthermore, the perturbation term incorporates gradient optimization of a local Lyapunov function, thus retaining some of the nice robustness properties of the first design.

We now move on to the work presented in Arcak (2007) and Bai et al. (2008). Although these papers contain specific applications to formation control, it is the general design frameworks that are interesting in relation to this thesis. In Arcak (2007), a passivity based framework for solving a class of group coordination problems is presented. In the class of group coordination problems that is considered, the control objective is to get coordination variables, taken as the difference between output variables for the agents and an optional virtual leader, to converge to prescribed compact sets, while simultaneously getting the time derivative of the output variables to converge to a function that is assumed to be known by the agents a priori (i.e. a common velocity input). Under certain passivity assumptions on the dynamics of the agents, the framework solves the control objectives in a decentralized manner by utilizing a communication topology. The resulting closed-loop system has a very nice property in that the trajectories of the coordination variables are restricted to propagate in prescribed open sets. To illustrate this property, the author solves the formation control problem for fully actuated point masses. The output variables to be coordinated are chosen as the positions of the point masses, while the compact sets that the coordination variables should converge to are chosen in accordance with the formation specification as a set of rigid body constraints. Finally, the open sets that the trajectories of the coordination variables are allowed to propagate in are chosen to exclude the origin. By doing this, local asymptotic stability is guaranteed with the addition of collision free operations.

A special case of the design framework in Arcak (2007) occurs when the prescribed compact sets for the coordination variables are chosen as the origin. This implies that the control objective consists of getting the output variables of the agents, and the optional virtual leader, to converge to a common value, thus forming a group agreement problem. The framework provides strong, global stability properties for this special case.

In Bai et al. (2008), the authors provide an extension to the framework presented in Arcak (2007). The assumption that the common velocity input is known by each agent a priori is relaxed. It is instead assumed that the velocity function can be parameterized by a set of base functions that are known by each agent. The weights in the parameterization are unknown for all but one agent (termed the leader), so that the other agents have to estimate these. The result is an adaptive scheme which guarantees that the coordination variables converge to their target compact sets under the same assumptions as in Arcak (2007). Parameter convergence is however not guaranteed in the general case, which implies that the agents not always will reach a common velocity in the limit.

In Ihle et al. (2007), the decentralized formation control scheme presented in Skjetne (2005; Chapter

6) is extended by incorporating the ideas of Arcak (2007). The control laws are chosen identical to those derived in Skjetne (2005). The only difference lays in the way the perturbation terms in the local path variable update laws are computed. Two main designs are presented. In both designs, the perturbation term for each agent is taken as the output of a prescribed static or dynamical system being passive. The input to the abovementioned system includes a synchronization term which is calculated in accordance with the group agreement framework in Arcak (2007). The resulting designs are shown to be robust and flexible, retaining integrity in the case of pointwise loss of connectivity in time, and enabling vessels to enter/leave the formation during operations.

In Olfati-Saber and Murray (2002), a cooperative formation control scheme utilizing a communication topology and the notions of rigid and unfoldable graphs is proposed. The control laws for the agents are taken as gradients of *structural potential functions* obtained from rigid body constraints representing the desired formation structure. By imposing certain restrictions on the interconnection between the vessels, convergence to a unique formation is guaranteed, with the addition of collision-free trajectories and bounded control inputs.

To conclude the review of earlier work within formation control, the author would like to emphasize that the number of published papers on the matter is vast, and that the work covered herein must be considered as "a tip of the iceberg". Furthermore, the categorization of efforts into behavioral, leader-follower, virtual structure, and cooperative approaches must be considered as quite rough, as research efforts often combine ideas from the different approaches. An example is the control scheme proposed in Leonard and Fiorelli (2001), where artificial potential functions are used to derive mutual interaction forces between agents, and one-way interaction forces between agents and virtual leaders. As pointed out in the paper, the interaction forces are designed to emulate the local behavior of individual animals migrating in groups in nature. The virtual leaders are included to manipulate group geometry and motion, and their trajectories are unaffected by the agents. It is clear that elements from both the leader-follower and behavioral approaches are incorporated in such a design.

1.4 Main contributions

This thesis is concerned with formation control within a path-based framework, where we ultimately want the formation to propagate along a parameterized path at a specified speed. In the marine control community, established designs within this framework (Skjetne (2005; Chap. 6), Ihle et al. (2007), Breivik et al. (2008)) solve the problem by controlling the individual vessels to their correct positions relative to a point on the path. When the formation is established, it is thus already located on the path, meaning that the task of coordinating the vessels is entwined with the path following operation. The main contribution of this thesis is to provide designs that enable separation and prioritization between the tasks of group coordination and path following. The idea is for the vessels to primarily establish a formation in the vicinity of their present location, and secondarily to initiate a collective motion towards the path when they are sufficiently coordinated. The main motivation behind this separation is safety, as the danger of collisions during the transient motion towards the path is alleviated by ensuring that the vessels travel in a formation structure. A related notion is system behavior during individual vessel failures such as saturations and blackouts. By making group coordination the sole focus of the control system whenever the vessels are out of formation, the probability of collisions during such events can be reduced.

Other contributions of this thesis can be found within the specificities of the proposed control designs. The first control design will demonstrate a new approach to formation control within the group coordination framework of Arcak (2007). By controlling points offset from the vessels and using a special case of the framework for group agreement problems, the design circumvents the problem with unstable equilibria that arise by following the proposed approach. Moreover, it will be shown how the common velocity input in the framework can be used to achieve path following. Another contribution of the thesis is related to the third control design, where it will be shown how the generic maneuvering methodology can be used to solve the formation control problem.

1.5 Publications

In relation to the work on this thesis, a paper presenting a variation of the first control design has been submitted to the *50th IEEE Conference on Decision and Control and European Control Conference, 2011*. The paper, entitled *Formation control of fully-actuated marine vessels using group agreement protocols*, is included in Appendix D.

Chapter 2

Preliminaries

2.1 Notation

- **Norms:** The p-norm of a vector $\mathbf{x} \in \mathbb{R}^n$ is given by $|\mathbf{x}|_p := \left(\sum_{i=1}^n |x_i|^p\right)^{\frac{1}{p}}$. For $p = \infty$, this reduces to $|\mathbf{x}|_\infty = \max_i\{|x_i|\}$. The induced p-norm of a matrix $\mathbf{A}$ is given by

$$||\mathbf{A}||_p := \max_{\mathbf{x}\neq\mathbf{0}} \frac{|\mathbf{A}\mathbf{x}|_p}{|\mathbf{x}|_p}$$

  For convenience, the subscript will be omitted for the 2-norm and the induced 2-norm: $|\mathbf{x}| := |\mathbf{x}|_2$, $||\mathbf{A}|| := ||\mathbf{A}||_2$.

- **Composite vectors and matrices:** For a collection of column vectors $\mathbf{x}_i \in \mathbb{R}^{n_i}$, $i = 1 \dots k$, the following convention is used:

$$col(\mathbf{x}_1, \mathbf{x}_2, \dots, \mathbf{x}_k) = [\mathbf{x}_1^\top, \mathbf{x}_2^\top, \dots, \mathbf{x}_k^\top]^\top \quad \in \mathbb{R}^{\sum_{i=1}^k n_i}$$
$$row(\mathbf{x}_1, \mathbf{x}_2, \dots, \mathbf{x}_k) = [\mathbf{x}_1^\top, \mathbf{x}_2^\top, \dots, \mathbf{x}_k^\top] \quad \in \mathbb{R}^{1\times(\sum_{i=1}^k n_i)}$$

  The "*col*" prefix will sometimes be omitted for convenience. Specifically, $\big|(\mathbf{x}, \mathbf{y})\big| = \big|col(\mathbf{x}, \mathbf{y})\big|$.

  For a collection of matrices $\mathbf{A}_i \in \mathbb{R}^{n\times n}$, $i = 1 \dots k$,

$$diag(\mathbf{A}_1, \mathbf{A}_2, \dots, \mathbf{A}_k) \quad \in \mathbb{R}^{kn\times kn}$$

  denotes a block diagonal matrix with the matrices $\mathbf{A}_i$ along the diagonal band.

- **Derivatives:** Total time derivatives of a function $\mathbf{h}(t)$ is denoted by $\dot{\mathbf{h}}, \ddot{\mathbf{h}}$, etc. Partial derivatives of functions $\mathbf{f} : \mathbb{R}^n \times \mathbb{R}^m \times \mathbb{R} \mapsto \mathbb{R}^q$, $g : \mathbb{R} \mapsto \mathbb{R}$ will, whenever convenient, be denoted by superscripts *prior* to the argument list. Other operations will be indicated after the argument list, with partial differentiation as the primary operation:

$$\mathbf{f}^{\mathbf{x}}(\mathbf{x}, \mathbf{y}, t) = \frac{\partial \mathbf{f}(\mathbf{x}, \mathbf{y}, t)}{\partial \mathbf{x}} = \begin{bmatrix} \frac{\partial f_1(\mathbf{x},\mathbf{y},t)}{\partial x_1} & \cdots & \frac{\partial f_1(\mathbf{x},\mathbf{y},t)}{\partial x_n} \\ \vdots & & \vdots \\ \frac{\partial f_q(\mathbf{x},\mathbf{y},t)}{\partial x_1} & \cdots & \frac{\partial f_q(\mathbf{x},\mathbf{y},t)}{\partial x_n} \end{bmatrix} \quad \in \mathbb{R}^{q\times n}$$
$$\mathbf{f}^{\mathbf{x}}(\mathbf{x}, \mathbf{y}, t)^\top = \left(\frac{\partial \mathbf{f}(\mathbf{x}, \mathbf{y}, t)}{\partial \mathbf{x}}\right)^\top \quad \in \mathbb{R}^{n\times q}$$
$$\mathbf{f}^{\mathbf{x},t}(\mathbf{x}, \mathbf{y}, t) = \frac{\partial \left(\mathbf{f}^{\mathbf{x}}(\mathbf{x}, \mathbf{y}, t)\right)}{\partial t} \quad \in \mathbb{R}^{q\times n}$$
$$\mathbf{f}^{t^n}(\mathbf{x}, \mathbf{y}, t) = \frac{\partial^n \mathbf{f}(\mathbf{x}, \mathbf{y}, t)}{\partial t^n} \quad \in \mathbb{R}^q$$
$$g^{\theta^2}(\theta)^3 = \left(\frac{\partial^2 g(\theta)}{\partial \theta^2}\right)^3 \quad \in \mathbb{R}$$

For single-variable scalar functions, the argument list will sometimes be omitted to save space. The following conventions will then be used: $g^{\theta^2} = g^{\theta^2}(\theta)$, $\left(g^{\theta}\right)^2 = g^{\theta}(\theta)^2$.

2.2 Stability properties

2.2.1 Stability of equilibrium points

Consider the system

$$\dot{\mathbf{x}} = \mathbf{F}(t, \mathbf{x}), \tag{2.1}$$

where $\mathbf{x} \in \mathbb{R}^n$ and $\mathbf{x} = \mathbf{0}$ is an equilibrium point for the system. We then have the following definitions:

Definition 1. *The origin of* (2.1) *is said to be uniformly globally stable (UGS) if there exists a function* $\gamma \in \mathcal{K}^\infty$ *such that for each* $(t_0, \mathbf{x}_0) \in \mathbb{R} \times \mathbb{R}^n$ *the solution* $\mathbf{x}(t, t_0, \mathbf{x}_0)$ *satisfies*

$$|\mathbf{x}(t, t_0, \mathbf{x}_0)| \leq \gamma(|\mathbf{x}_0|) \qquad \forall t \geq t_0 \tag{2.2}$$

Definition 2. *The origin of* (2.1) *is said to be uniformly globally asymptotically stable (UGAS) if there exists a Class-*$\mathcal{KL}$ *function* β *such that for each* $(t_0, \mathbf{x}_0) \in \mathbb{R} \times \mathbb{R}^n$ *the solution* $\mathbf{x}(t, t_0, \mathbf{x}_0)$ *satisfies*

$$|\mathbf{x}(t, t_0, \mathbf{x}_0)| \leq \beta(|\mathbf{x}_0|, t - t_0) \qquad \forall t \geq t_0 \tag{2.3}$$

2.2.2 Set-stability

Consider the autonomous system

$$\dot{\mathbf{x}} = \mathbf{F}(\mathbf{x}), \tag{2.4}$$

where $\mathbf{x} \in \mathbb{R}^n$. In some cases, it might be of interest to examine the stability properties of a general set $\mathcal{A} \subset \mathbb{R}^n$, rather than the typical compact equilibrium set $\mathcal{A}_e = \{\mathbf{x} \in \mathbb{R}^n : \quad \mathbf{x} = \mathbf{x}_e\}$. With respect to such general sets, stability is defined through bounds on the distance-to-set function

$$|\mathbf{x}|_{\mathcal{A}} = \inf_{\mathbf{y} \in \mathcal{A}} |\mathbf{x} - \mathbf{y}|$$

For non-compact sets, it is possible for the system (2.4) to escape to infinity in finite time even though $|\mathbf{x}|_{\mathcal{A}}$ remains bounded. In the analysis of such sets, it is therefore important to establish that the system is *forward complete*, i.e. that there are no finite escape-times.

Definition 3. *If the system* (2.4) *is forward complete, a set* $\mathcal{A} \subset \mathbb{R}^n$ *is UGAS if there exists a class-*$\mathcal{KL}$ *function* β *such that* $\forall \mathbf{x}_0 \in \mathbb{R}^n$*, the solution* $\mathbf{x}(t, \mathbf{x}_0)$ *satisfies*

$$|\mathbf{x}(t, \mathbf{x}_0)|_{\mathcal{A}} \leq \beta\left(|\mathbf{x}_0|_{\mathcal{A}}, t\right), \quad \forall t \geq 0$$

Remark 1. *Any nonautonomous system* $\dot{\mathbf{x}} = \mathbf{f}(t, \mathbf{x})$ *can be made autonomous by extending the state vector according to* $\mathbf{z} := col(\mathbf{x}, t)$*, yielding* $\dot{\mathbf{z}} = \mathbf{F}_z(\mathbf{z})$*, where* $\mathbf{F}_z(\mathbf{z}) := col(\mathbf{f}(t, \mathbf{x}), 1)$*. The corresponding initial conditions are given by* $\mathbf{z}(0) = col(\mathbf{x}_0, t_0)$*, where* t_0 *is the initial time of the original system.*

2.3 Reference frames

The reader is referred to Fossen (2010) for a thorough treatment of the reference frames that are applicable in marine operations. In this thesis, local operations on the sea surface are assumed. An earth-fixed tangent frame on the sea surface, with x-axis pointing towards north and y-axis pointing towards east, will therefore be used as a global reference frame throughout the thesis. This frame will be denoted as the $\mathcal{E}$-frame, and is assumed to be inertial.

In addition to the $\mathcal{E}$-frame, several local reference frames will be utilized in this thesis:

- **Vessel body frames:** Each vessel is assigned a body-fixed reference frame, termed the $\mathcal{B}$-frame, which moves and rotates with the vessel. As stated in Skjetne (2005), the origin of this frame is typically chosen in the principle plane of symmetry, with x-axis directed from aft to fore, y-axis directed from port to starboard, and z-axis directed from top to bottom.
- **Formation reference frames:** Formation reference frames will be denoted by $\mathcal{F}$, with subscripts added in the case of multiple frames. The position of origin and orientation of an FRF relative to the $\mathcal{E}$-frame will be collected in a vector referred to as the FRP. For convenience, the velocity vector of the origin of an FRF relative to $\mathcal{E}$, decomposed along the x and y-axes of the FRF, will be termed its surge and sway velocities, respectively. Similarly, rotational motion for the frame will be termed as yaw motion.

2.4 Vessel models

This thesis will deal with fully actuated marine surface vessels. As for any rigid body, complete dynamical models for this class of vessels require six degrees of freedom. However, by assuming that the heave, roll and pitch motion excited by the environment and the control action of the actuators are sufficiently small (These are valid assumptions for vessels with large longitudinal and transversal metacentric heights), the work space of the vessels can be limited to two-dimensional planar motion (herein, along the $\mathcal{E}$-frame), and the configuration space will be three dimensional, consisting of two position-variables (the north and east positions) and one orientation variable (the yaw angle). Dynamical models for marine surface vessels that are simplified according to the previous discussion are derived in Fossen (2010). Two of these models will now be introduced, one excluding all environmental disturbances, and one including a constant environmental disturbance in the $\mathcal{E}$-frame.

2.4.1 Dynamical model without environmental disturbances

The following three degree-of-freedom model is given in Fossen (2010):

$$\dot{\boldsymbol{\eta}}_i = \mathbf{R}(\psi_i)\boldsymbol{\nu}_i \tag{2.5a}$$

$$\mathbf{M}_i\dot{\boldsymbol{\nu}}_i + \mathbf{D}_i(\boldsymbol{\nu}_i)\boldsymbol{\nu}_i + \mathbf{C}_i(\boldsymbol{\nu}_i)\boldsymbol{\nu}_i = \boldsymbol{\tau}_i \tag{2.5b}$$

Here, $\boldsymbol{\eta}_i = col(x_i, y_i, \psi_i) \in \mathbb{R}^3$ contains the north position (x_i), east position (y_i), and yaw angle (ψ_i) of the i'th vessel in the $\mathcal{E}$-frame, $\boldsymbol{\nu}_i = col(u_i, v_i, r_i) \in \mathbb{R}^3$ is a generalized velocity vector, decomposed in the $\mathcal{B}$-frame, containing velocity components in surge, sway, and yaw, and $\boldsymbol{\tau}_i$ is a generalized commanded force vector decomposed in the $\mathcal{B}$-frame. Furthermore, the matrix

$$\mathbf{R}(\psi_i) = \begin{bmatrix} \cos(\psi) & -\sin(\psi) & 0 \\ \sin(\psi) & \cos(\psi) & 0 \\ 0 & 0 & 1 \end{bmatrix}$$

is the rotation matrix in yaw satisfying

$$\mathbf{R}(\psi_i)\mathbf{R}(\psi_i)^\top = \mathbf{R}(\psi_i)^\top\mathbf{R}(\psi_i) = \mathbf{I}_{3\times 3}$$

$$\dot{\mathbf{R}}(\psi_i) = \mathbf{R}(\psi_i)\mathbf{S}\dot{\psi}_i = \mathbf{R}(\psi_i)\mathbf{S}r_i$$

$$\mathbf{S} = \begin{bmatrix} 0 & -1 & 0 \\ 1 & 0 & 0 \\ 0 & 0 & 0 \end{bmatrix}$$

Finally, the matrices $\mathbf{M}_i$, $\mathbf{D}_i(\mathbf{v_i})$ and $\mathbf{C}_i(\mathbf{v_i})$, corresponding to total mass (i.e. including added mass), damping and centripetal/Coriolis forces respectively, are assumed to satisfy the following properties:

$$\mathbf{M}_i = \mathbf{M}_i^\top > 0 \tag{2.6}$$

$$\mathbf{q}^\top \mathbf{D}_i(\mathbf{v}_i)\mathbf{q} > 0 \quad \forall \mathbf{q} \neq \mathbf{0}, \quad \forall \boldsymbol{\nu}_i \in \mathbb{R}^3 \tag{2.7}$$

$$\mathbf{C}_i(\mathbf{v}_i) = -\mathbf{C}_i(\mathbf{v}_i)^\top \quad \forall \boldsymbol{\nu}_i \in \mathbb{R}^3 \tag{2.8}$$

It is noted that during maneuvering at forward speed, the assumption of a constant, symmetric, positive definite mass matrix may be violated due to added mass effects. The assumption will, however, still be used throughout the thesis.

2.4.2 Dynamical model including a constant environmental disturbance

The model (2.5) can be extended by including a constant environmental disturbance $\mathbf{b} = col(b_N, b_E, b_\psi) \in \mathbb{R}^3$ containing disturbance forces in the north and east directions and a disturbance moment in yaw. A disturbance of this kind will model the effect of steady ocean currents and mean wind with acceptable accuracy for control purposes. The extended model can be expressed as:

$$\dot{\boldsymbol{\eta}}_i = \mathbf{R}(\psi_i)\boldsymbol{\nu}_i \tag{2.9a}$$

$$\mathbf{M}_i\dot{\boldsymbol{\nu}}_i + \mathbf{D}_i(\boldsymbol{\nu}_i)\boldsymbol{\nu}_i + \mathbf{C}_i(\boldsymbol{\nu}_i)\boldsymbol{\nu}_i = \boldsymbol{\tau}_i + \mathbf{R}(\psi_i)^\top \mathbf{b} \tag{2.9b}$$

$$\dot{\mathbf{b}} = \mathbf{0} \tag{2.9c}$$

2.5 Communication topology

In order to control a group of vessels in formation, the vessels must be able to communicate. However, due to costs or other restrictions, it might not be desirable to have a line of communication between every pair of vessels. Such restrictions on communication, which can be used to enforce a decentralized versus a centralized design, can be introduced through a communication topology. For the first two control designs of this thesis, a communication topology will be specified through a communication graph, in accordance with Arcak (2007). Two nodes in the graph can exchange state information if and only if there is an edge between them. The graph will be explicitly stated through the incidence matrix $\mathbf{B} \in \mathbb{R}^{r\times p}$, where, r is the number of vessels, and p is the number of communication links (edges in the graph). The entries of $\mathbf{B}$ are defined as follows:

$$b_{ij} = \begin{cases} +1 & \text{if the } i\text{'th node is the positive end of the } j\text{'th communication link} \\ -1 & \text{if the } i\text{'th node is the negative end of the } j\text{'th communication link} \\ 0 & \text{if the } i\text{'th node is not a part of the } j\text{'th communication link} \end{cases} \tag{2.10}$$

An important thing to note is that the incidence matrix will be used to describe two-way communication paths between the nodes. If there exists a link between a pair of nodes, both can send and receive information. Hence, whether a vessel is at the positive or negative end of a link is of no importance.

An important assumption that will be utilized in the control designs is related to the notion of connectivity of a communication graph. A communication graph is connected if it is possible to get from any node in the graph to any other node by following the edges of the graph (where there are no restrictions on the direction you can travel along an edge). With regards to formation control, it is natural to require that the communication graph is connected for certain periods of time. After all, if the graph is disconnected for all time, the vessels are divided into different groups that cannot communicate with each other, making it impossible to coordinate the group as a whole. In Arcak (2007) and Ihle et al. (2007), results are obtained for the case where connectivity can be established in an integral sense, which allows for pointwise loss of connectivity in time. Herein, the control designs will be based on the assumption that the communication graph is connected for all time. Furthermore, it will be assumed that there are no cycles in the graph:

Assumption 1. *The communication graph is connected at all times, and it does not contain any cycles. Moreover, there exists at most one edge between any given pair of vertices.*

For a graph containing r vertices, an absence of cycles requires that there can be at most $r-1$ edges in the communication graph (assuming that only one edge can exist between any pair of vertices, this is indeed a necessary condition). Since connectivity requires that there must be at least $r-1$ edges in the communication graph, Assumption 1 implies that the communication graph contains exactly $r-1$ edges. As stated in Arcak (2007), the incidence matrix will have rank $r-1$ when the graph is connected. We thus have that the range space of $\mathbf{B}^\top$, denoted $\mathcal{R}(\mathbf{B}^\top)$, is equal to $\mathbb{R}^{r-1}$ whenever Assumption 1 is satisfied. This fact will be used to obtain global stability results for the first two control designs of Chapter 3.

2.6 Kronecker products

As stated in Arcak (2007), the Kronecker product between two matrices $\mathbf{A} \in \mathbb{R}^{m\times n}$ and $\mathbf{B} \in \mathbb{R}^{p\times q}$ is given by

$$\mathbf{A}\otimes\mathbf{B} = \begin{bmatrix} a_{11}\mathbf{B} & \dots & a_{1n}\mathbf{B} \\ \vdots & \ddots & \vdots \\ a_{m1}\mathbf{B} & \dots & a_{mn}\mathbf{B} \end{bmatrix} \in \mathbb{R}^{mp\times nq},$$

and satisfies the following properties:

$$(\mathbf{A}\otimes\mathbf{B})^\top = \mathbf{A}^\top\otimes\mathbf{B}^\top$$
$$(\mathbf{A}\otimes\mathbf{I}_p)(\mathbf{C}\otimes\mathbf{I}_p) = (\mathbf{AC})\otimes\mathbf{I}_p$$

Here, $\mathbf{I}_p \in \mathbb{R}^{p\times p}$ is the identity matrix, and $\mathbf{C}$ is assumed to be compatible for multiplication with $\mathbf{A}$.

Chapter 3

Formation Control Design

3.1 Introduction

This chapter is concerned with control design for the *Formation Control Problem*, which is chosen to consist of two distinct tasks. In the *Group Coordination Task*, the objective is is to get the vessels in the group to obtain specified relative positions in a formation reference frame $\mathcal{F}$, whose position and orientation with respect to the $\mathcal{E}$-frame may be arbitrary. The *Formation Mission Task* is concerned with getting the formation as a whole to fulfill its operational objective, which herein involves following a specified parameterized path at a specified speed. In accordance with Section 1.4, the task of group coordination is given the highest priority, and should be fulfilled sufficiently before the formation mission task is pursued.

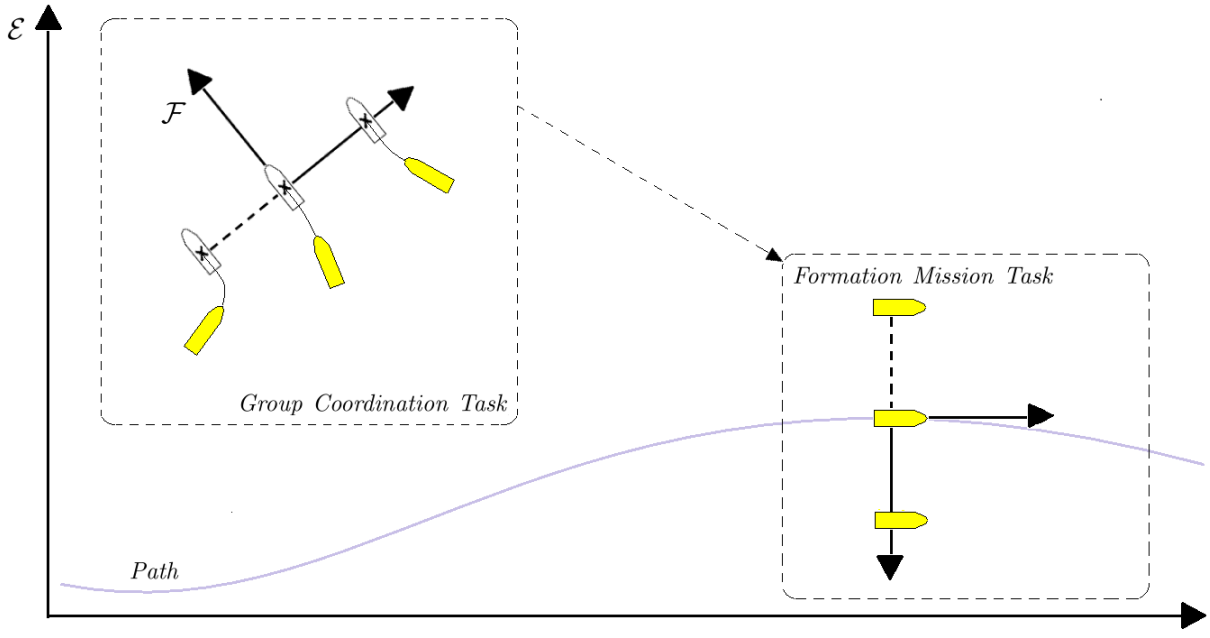

Figure 3.1: Illustration of the group coordination and formation mission tasks.

Three control designs solving the formation control problem will be presented. The first two designs are closely related and lay heavily within the cooperative approach described in Section 1.3.4. By controlling points offset from the vessels, group coordination is pursued through the group agreement protocols of Arcak (2007), while path following is targeted through the maneuvering methodology of Skjetne (2005).

The third design is is in the vein of the virtual structure approach, targeting group coordination through the generic maneuvering methodology, and path following through the helmsman-like LOS algorithm presented in Skjetne et al. (2011).

3.2 Design 1: Formation control using group agreement protocols

In the first design, the decentralized group agreement protocols of Arcak (2007) will be combined with ideas from the maneuvering methodology of Skjetne (2005) to solve the formation control problem. The design has been altered slightly from the version presented in the conference paper in Appendix D. Instead of transforming the dynamical models of the vessels into the $\mathcal{E}$-frame prior to performing the control design, the model (2.5) is utilized directly, resulting in control laws where the damping gain matrix for each vessel is specified in the $\mathcal{B}$-frame instead of the $\mathcal{E}$-frame.

3.2.1 Setup

Consider a group of r vessels to be controlled in formation, and let each vessel in the formation be identified by a unique identifier in the index set $\mathcal{I} = \{1, \ldots, r\}$. The desired configuration of each vessel in the formation is given by a possibly time-varying *configuration vector* in the local formation reference frame $\mathcal{F}$, denoted $\mathbf{l}_i(t) := col(x_{ci}(t), y_{ci}(t), \psi_{ci}(t))$. Each vessel is now assigned an individual formation reference frame $\mathcal{F}_i$, which moves with the vessel in such a way that the generalized position of the vessel relative to $\mathcal{F}_i$ is equal to the formation configuration vector. The orientation and position of origin of $\mathcal{F}_i$ in the $\mathcal{E}$-frame is thus given by

$$\mathbf{x_0}_i(\boldsymbol{\eta}_i, t) := \boldsymbol{\eta}_i - \mathbf{R}\left(\psi_i - \psi_{ci}(t)\right)\mathbf{l}_i(t), \tag{3.1}$$

where $\mathbf{x_0}_i = col(x_{0i}, y_{0i}, \psi_{0i})$ is the FRP for Vessel i. Through this setup, group coordination is achieved when all $\mathcal{F}_i$, $i \in \mathcal{I}$, are synchronized into a common $\mathcal{F}$, that is, if $\mathbf{x_0}_1 = \mathbf{x_0}_2 = \ldots = \mathbf{x_0}_r$.

Assumption 2. *The configuration vectors $\mathbf{l}_i(t) \in \mathcal{C}^2$, and $\exists\ l_{max} < \infty$ such that $\forall i \in \mathcal{I}$ and $\forall t \geq t_0$, then* $\max\{|\mathbf{l}_i(t)|, |\dot{\mathbf{l}}_i(t)|\} \leq l_{max}$.

To address the formation mission task, the strategy is that one vessel, denoted as the *acting leader* of the formation, will ensure path following. When all vessels are coordinated, this will indirectly ensure that the formation as a whole executes its path following mission. Without loss of generality, Vessel 1 is set as the acting leader, and path following is targeted as a maneuvering problem involving a geometric task and a dynamic task.

The geometric task is to get the FRP of the acting leader to converge to and follow the desired curve given by the set of points

$$\mathcal{P} = \{\boldsymbol{x} \in \mathbb{R}^3 : \exists \theta \text{ s.t. } \mathbf{x} = \mathbf{p}_d(\theta)\}, \tag{3.2}$$

where $\mathbf{p}_d(\theta) := col(x_d(\theta), y_d(\theta), \psi_d(\theta))$, with $(x_d(\cdot), y_d(\cdot))$ sufficiently smooth functions parameterized by the scalar variable θ, and

$$\psi_d(\theta) = \arctan\left(\frac{y_d^\theta(\theta)}{x_d^\theta(\theta)}\right) \tag{3.3}$$

chosen as the direction of the tangential vector to the path in each point $(x_d(\theta), y_d(\theta))$.[1]

The dynamic task is represented by a desired speed assignment $v_s(\theta, t)$ for $\dot{\theta}$, which typically is designed to set up a constant speed in [m/s] for the formation along the path.

Assumption 3. *The path $\mathbf{p}_d(\theta) \in \mathcal{C}^2$, and the speed assignment $v_s(\theta, t) \in \mathcal{C}^1$. There exists $d < \infty$ such that $\forall \theta \in \mathbb{R}$ and $\forall t \geq t_0$, then* $\max\{|\mathbf{p}_d^\theta(\theta)|, |v_s(\theta, t)|\} \leq d$.

[1] To ensure correct quadrant mapping, a four quadrant version of the arctan$(\cdot)$ function should be used for implementation, e.g. the atan2 function in Matlab.

3.2.2 Problem statement

The control problem can now be formally stated by the following two objectives:

Group coordination objective: To develop synchronization control laws to ensure that

$$\lim_{t\to\infty} |\mathbf{x_0}_i(t) - \mathbf{x_0}_j(t)| = 0 \quad \forall i,j \in \mathcal{I}. \tag{3.4}$$

Formation mission objective: To develop a maneuvering control law to ensure that

$$\lim_{t\to\infty} |\mathbf{x_{01}}(t) - \mathbf{p}_d(\theta(t))| = 0, \tag{3.5}$$

$$\lim_{t\to\infty} |\dot{\theta}(t) - v_s(\theta(t),t)| = 0. \tag{3.6}$$

As mentioned earlier, the coordination objective is of primary concern and should be achieved before the mission objective is pursued. The main reason for this is that having the vessels in formation is a measure for avoiding inter-vessel collision, especially during the transients when converging to the path.

3.2.3 Control design

3.2.3.1 Group coordination task

In order to design control laws to achieve group coordination, the passivity-based group agreement protocols presented in Arcak (2007) are used. For the vessels with dynamics (2.5) and outputs (3.1), the protocols are used to achieve (3.4) and

$$\lim_{t\to\infty} |\dot{\mathbf{x}}_{\mathbf{0}i}(t) - \mathbf{v}_d(t)| = 0 \quad \forall i \in \mathcal{I}, \tag{3.7}$$

where $\mathbf{v}_d(t)$ is a common velocity input to all vessels that later will be used as a degree-of-freedom to solve the formation mission task.

Establishing passivity: Motivated by the outline in Arcak (2007), the first step of the control design is to construct partial control laws that transform the vessel dynamics (2.5) to strictly state passive dynamical systems from auxiliary control inputs $\boldsymbol{\alpha}_i$ to the outputs[2]

$$\boldsymbol{\zeta}_i := \mathbf{R}(\psi_i)^\top (\dot{\mathbf{x}}_{\mathbf{0}i} - \mathbf{v}_d) \quad i \in \mathcal{I}. \tag{3.8}$$

Defining $\mathbf{f}_{1i}(\boldsymbol{\eta}_i, t) := \mathbf{R}\left(\psi_i - \psi_{ci}(t)\right)\mathbf{l}_i(t)$ and $\mathbf{f}_{2i}(\boldsymbol{\eta}_i, \boldsymbol{\nu}_i, \mathbf{v}_d, t) := \mathbf{R}(\psi_i)^\top(\dot{\mathbf{f}}_{1i} + \mathbf{v}_d)$, $\boldsymbol{\zeta}_i$ can be alternatively expressed as

$$\begin{aligned}\boldsymbol{\zeta}_i &= \mathbf{R}(\psi_i)^\top(\dot{\boldsymbol{\eta}}_i - \dot{\mathbf{f}}_{1i} - \mathbf{v}_d)\\ &= \boldsymbol{\nu}_i - \mathbf{f}_{2i},\end{aligned}$$

yielding the dynamics

$$\begin{aligned}\mathbf{M}_i\dot{\boldsymbol{\zeta}}_i &= \mathbf{M}_i\dot{\boldsymbol{\nu}}_i - \mathbf{M}_i\dot{\mathbf{f}}_{2i}\\ &= \boldsymbol{\tau}_i - \mathbf{D}_i(\boldsymbol{\nu}_i)\boldsymbol{\zeta}_i - \mathbf{C}_i(\boldsymbol{\nu}_i)\boldsymbol{\zeta}_i - \mathbf{D}_i(\boldsymbol{\nu}_i)\mathbf{f}_{2i} - \mathbf{C}_i(\boldsymbol{\nu}_i)\mathbf{f}_{2i} - \mathbf{M}_i\dot{\mathbf{f}}_{2i}\end{aligned}$$

Choosing the control inputs as

$$\boldsymbol{\tau}_i = \mathbf{D}_i(\boldsymbol{\nu}_i)\mathbf{f}_{2i} + \mathbf{C}_i(\boldsymbol{\nu}_i)\mathbf{f}_{2i} + \mathbf{M}_i\dot{\mathbf{f}}_{2i} - \mathbf{K_d}_i\boldsymbol{\zeta}_i + \boldsymbol{\alpha}_i, \quad \mathbf{K_d}_i = \mathbf{K_d}_i^\top > 0, \tag{3.9}$$

gives the desired passivity properties. To show this, the following positive definite and radially unbounded functions are utilized:

$$S_{\zeta i}(\boldsymbol{\zeta}_i) := \frac{1}{2}\boldsymbol{\zeta}_i^\top\mathbf{M}_i\boldsymbol{\zeta}_i \tag{3.10}$$

[2]This deviates slightly from the framework in Arcak (2007), where the outputs are set as $\boldsymbol{\zeta}_i := \dot{\mathbf{x}}_{\mathbf{0}i} - \mathbf{v}_d$.

Taking time derivatives and using the properties (2.7),(2.8) yields

$$\begin{aligned}\dot{S}_{\zeta i} &= \boldsymbol{\zeta}_i^\top \mathbf{M}_i \dot{\boldsymbol{\zeta}}_i \\ &= \boldsymbol{\zeta}_i^\top \left(-\mathbf{D}_i(\boldsymbol{\nu}_i)\boldsymbol{\zeta}_i - \mathbf{K}_{\mathbf{d}i}\boldsymbol{\zeta}_i - \mathbf{C}_i(\boldsymbol{\nu}_i)\boldsymbol{\zeta}_i + \boldsymbol{\alpha}_i\right) \\ &\leq -\boldsymbol{\zeta}_i^\top \mathbf{K}_{\mathbf{d}i}\boldsymbol{\zeta}_i + \boldsymbol{\zeta}_i^\top \boldsymbol{\alpha}_i,\end{aligned}$$

which proves the claim.

Synchronization: To complete the first part of the control design, we need to specify the auxiliary control inputs $\boldsymbol{\alpha}_i$. These functions will enable the vessels to synchronize in the limit. Motivated by Arcak (2007), the functions are chosen as

$$\boldsymbol{\alpha}_i = -\mathbf{R}(\psi_i)^\top \left(\sum_{k=1}^{p} b_{ik}\boldsymbol{\gamma}_k(\mathbf{z}_k)\right) \quad i \in \mathcal{I}, \tag{3.11}$$

where $\mathbf{B} = \{b_{ij}\} \in \mathbb{R}^{r\times p}$ is the incidence matrix of the communication graph[3]. For the k'th link connecting vessels with indexes m and n, $\mathbf{z}_k$ is the synchronization error between the vessels corresponding to

$$\mathbf{z}_k := \sum_{i=1}^{r} b_{ik}\mathbf{x}_{\mathbf{0}i} = \begin{cases} \mathbf{x}_{\mathbf{0}m} - \mathbf{x}_{\mathbf{0}n} & \text{if } m \text{ is the positive end} \\ \mathbf{x}_{\mathbf{0}n} - \mathbf{x}_{\mathbf{0}m} & \text{if } m \text{ is the negative end} \end{cases} \tag{3.12}$$

Furthermore, we have that

$$\boldsymbol{\gamma}_k(\mathbf{z}_k) = \left(\frac{\partial P_k(\mathbf{z}_k)}{\partial \mathbf{z}_k}\right)^\top \qquad \in \mathbb{R}^3, \tag{3.13}$$

where according to Arcak (2007), the functions $P_k : \mathbb{R}^3 \mapsto \mathbb{R}$ shall satisfy:

$$P_k \in C^2 \tag{3.14a}$$

$$P_k(\mathbf{z}_k) > 0 \quad \forall \mathbf{z}_k \neq \mathbf{0} \tag{3.14b}$$

$$P_k(\mathbf{z}_k) \to \infty \text{ as } |\mathbf{z}_k| \to \infty \tag{3.14c}$$

$$\mathbf{z}_k^\top \left(\frac{\partial P_k(\mathbf{z}_k)}{\partial \mathbf{z}_k}\right)^\top > 0 \quad \forall \mathbf{z}_k \neq \mathbf{0}. \tag{3.14d}$$

Examining (3.11) shows that the synchronizing control input for each vessel consists of feedback from the synchronization errors between the vessel and its "neighbors" in the communication topology. This corresponds to a decentralized design that necessitates only limited inter-vessel communication.

3.2.3.2 Formation mission task

Define $\mathbf{q}$ as the path following error between the FRP of the acting leader and its desired position $\mathbf{p}_d(\theta)$ on the path:

$$\mathbf{q}(\mathbf{x}_{\mathbf{0}1}, \theta) := \mathbf{x}_{\mathbf{0}1} - \mathbf{p}_d(\theta), \quad \mathbf{q} \in \mathbb{R}^3. \tag{3.15}$$

Since $\dot{\mathbf{x}}_{\mathbf{0}1} = \mathbf{R}(\psi_1)\boldsymbol{\zeta}_1 + \mathbf{v}_d$, the dynamics of $\mathbf{q}$ becomes

$$\dot{\mathbf{q}} = \mathbf{v}_d - \mathbf{p}_d^\theta(\theta)\dot{\theta} + \mathbf{R}(\psi_1)\boldsymbol{\zeta}_1,$$

where $\boldsymbol{\zeta}_1$ is the synchronization velocity error (3.8) for the acting leader. In the next step, control laws for $\mathbf{v}_d$ and $\dot{\theta}$ will be designed in order to solve (3.5) and (3.6). The design will be based on the certainty equivalence $\boldsymbol{\zeta}_1 = \mathbf{0}$, while a thorough analysis is given in Section 3.2.4.

[3] According to Assumption 1 in Section 2.5, the number of columns in $\mathbf{B}$ must be $p = r - 1$.

Maneuvering control design: To stabilize $\{\mathbf{q} = 0\}$, we select a Hurwitz matrix $\mathbf{A} \in \mathbb{R}^{3\times3}$ together with $\mathbf{P} = \mathbf{P}^\top > \mathbf{0}$ satisfying $\mathbf{PA} + \mathbf{A}^\top\mathbf{P} = -\mathbf{Q}$ for a given $\mathbf{Q} = \mathbf{Q}^\top > 0$, and consider the CLF

$$V_q(\mathbf{x_{01}}, \theta) = \mathbf{q}(\mathbf{x_{01}}, \theta)^\top \mathbf{P}\mathbf{q}(\mathbf{x_{01}}, \theta). \tag{3.16}$$

A simple choice for $\mathbf{v}_d$ and $\dot{\theta}$ is

$$\begin{aligned} \mathbf{v}_d &= \mathbf{A}\mathbf{q}(\mathbf{x_{01}}, \theta) + \mathbf{p}_d^\theta(\theta) v_s(\theta, t), \\ \dot{\theta} &= v_s(\theta, t). \end{aligned}$$

This choice stabilizes the path-following error $\{\mathbf{q} = 0\}$ through $\dot{\mathbf{q}} = \mathbf{A}\mathbf{q}$ (also verified by $\dot{V}_q = -\mathbf{q}^\top\mathbf{Q}\mathbf{q}$) for $\boldsymbol{\zeta}_1 = \mathbf{0}$. Additionally, it satisfies the speed assignment along the path (3.6) identically. However, the above control law has some severe flaws. The most notable is that the vessels will continuously receive a commanded velocity that drives them towards the path, irrespective of how well they are coordinated. To remedy this problem and ensure that coordination is handled with higher priority than path following, the terms $\mathbf{A}\mathbf{q}$ and $v_s(\theta, t)$ in the maneuvering control law will be weighted by functions that map the synchronization errors into scalar weight signals. These signals should vanish for large synchronization errors and be equal to unity when synchronized. Effectively, this means that the vessels will "forget the path" while synchronizing. To this end, the functions $\sigma_k : \mathbb{R}_{\geq 0} \mapsto \mathbb{R}_{>0}$, $k = 1, 2$, are introduced, which should be continuously differentiable, monotonically decreasing, and satisfy

$$\sigma_k(0) = 1 \tag{3.17a}$$

$$\lim_{s\to\infty} \sigma_k(s) = 0. \tag{3.17b}$$

As input to these functions, we use $|\mathbf{z}|_{L_1}^2 := \mathbf{z}^\top\mathbf{L}_1\mathbf{z}$, where $\mathbf{z} = col(\mathbf{z}_1, \ldots, \mathbf{z}_p)$, $\mathbf{z} \in \mathbb{R}^{3p}$, and $\mathbf{L}_1 = \mathbf{L}_1^\top \geq 0$ is a weight matrix used to tune the gains for position and orientation errors[4] in $\mathbf{z}$. To enable control of the transient movement towards the path after the vessels have synchronized, the term $v_s(\theta, t)$ will be scaled with an additional function that maps the path following error $\mathbf{q}$ to a scalar weight signal. This function can be chosen to have the same properties as the functions $\sigma_k(\cdot)$, or equal to unity (the effect of this choice will be discussed later). This is formalized by introducing the function $\beta : \mathbb{R}_{\geq 0} \mapsto \mathbb{R}_{>0}$, which should be $\mathcal{C}^1$, monotonically decreasing, and satisfy

$$\beta(0) = 1 \tag{3.18}$$

As input to the function , we use $|\mathbf{q}|_{L_2}^2 := \mathbf{q}^\top\mathbf{L}_2\mathbf{q}$, where $\mathbf{L}_2 = \mathbf{L}_2^\top \geq 0$ is a weight matrix. With these *activation functions* defined, the maneuvering control law is assigned as

$$\mathbf{v}_d = \sigma_1(|\mathbf{z}|_{L_1}^2)\mathbf{A}\mathbf{q}(\mathbf{x_{01}}, \theta) + \sigma_2(|\mathbf{z}|_{L_1}^2)\beta(|\mathbf{q}|_{L_2}^2)\mathbf{p}_d^\theta(\theta) v_s(\theta, t) \tag{3.19}$$

$$\dot{\theta} = \sigma_2(|\mathbf{z}|_{L_1}^2)\beta(|\mathbf{q}|_{L_2}^2) v_s(\theta, t) - \omega, \tag{3.20}$$

where ω is a free input used to shape the transient movement of $\mathbf{p}_d(\theta)$. In the path following error $\mathbf{q}$, the closed-loop dynamics now become

$$\dot{\mathbf{q}} = \sigma_1(|\mathbf{z}|_{L_1}^2)\mathbf{A}\mathbf{q} + \mathbf{p}_d^\theta(\theta)\omega + \mathbf{R}(\psi_1)\boldsymbol{\zeta}_1 \tag{3.21}$$

Motivated by the gradient optimization designs in Skjetne (2005), ω is assigned as

$$\omega = \mu(\theta) V_q^\theta(\mathbf{x_{01}}, \theta) = -2\mu(\theta)\mathbf{q}(\mathbf{x_{01}}, \theta)^\top \mathbf{P}\mathbf{p}_d^\theta(\theta), \tag{3.22}$$

where in contrast to Skjetne (2005), $\mu(\theta) > 0$ is designed as a function of θ to allow normalization with respect to path parameterization. This ensures that the speed of the gradient minimization is independent of how a certain path is parameterized (see Section 3.2.6 for an example of how this is done).

[4] The gains should be selected to normalize the position and orientation errors in $|\mathbf{z}|_{L_1}^2$. See Section 3.2.5.4 for details.

Assumption 4. *The gain $\mu(\theta) \in \mathcal{C}^1$, and $\exists \mu_{max} < \infty$ so that $\forall \theta \in \mathbb{R}$, then $0 < \mu(\theta) \leq \mu_{max}$.*

Differentiating (3.16) with respect to time now yields

$$\begin{aligned} \dot{V}_q &= -\sigma_1(|\mathbf{z}|_{L_1}^2)\mathbf{q}^\top \mathbf{Q}\mathbf{q} + 2\mathbf{q}^\top \mathbf{P}\mathbf{p}_d^\theta(\theta)\omega + 2\mathbf{q}^\top \mathbf{P}\mathbf{R}(\psi_1)\boldsymbol{\zeta}_1 \\ &= -\sigma_1(|\mathbf{z}|_{L_1}^2)\mathbf{q}^\top \mathbf{Q}\mathbf{q} - \mu(\theta)V_q^\theta(\mathbf{x}_{\mathbf{0}1}, \theta)^2 + 2\mathbf{q}^\top \mathbf{P}\mathbf{R}(\psi_1)\boldsymbol{\zeta}_1 \\ &\leq -\sigma_1(|\mathbf{z}|_{L_1}^2)\mathbf{q}^\top \mathbf{Q}\mathbf{q} + 2\mathbf{q}^\top \mathbf{P}\mathbf{R}(\psi_1)\boldsymbol{\zeta}_1 \end{aligned} \tag{3.23}$$

For $\mathbf{z}$ confined to compact sets by the control design for group coordination, it follows for $\boldsymbol{\zeta}_1 = \mathbf{0}$ that (3.5) is satisfied by (3.15). Furthermore, (3.6) is satisfied as $\mathbf{z}(t) \to \mathbf{0}$. A detailed analysis of stability for the complete closed-loop system is provided in Section 3.2.4.

Operation phases: The activation functions $\sigma_k(\cdot)$ were introduced to enable the desired priority levels between the group coordination and formation mission tasks, resulting in an operation effectively divided into a coordination phase and a path following phase.

- **Coordination phase**: By proper design, the functions $\sigma_1(|\mathbf{z}|_{L_1}^2)$ and $\sigma_2(|\mathbf{z}|_{L_1}^2)$ can attain arbitrarily small values for $|\mathbf{z}|_L \geq c$, where c is a set threshold value. This ensures that the common velocity input (3.19) to each vessel is close to zero when the synchronization errors are large. As the synchronization errors typically are large in the beginning of an operation, the result is a low-speed coordination phase where the vessels positions themselves relatively to the group without paying any attention to the path following objective. During this phase, the dynamics of θ is approximately reduced to

  $$\dot{\theta} \approx -\mu(\theta)V_q^\theta(\mathbf{x}_{\mathbf{0}1}, \theta),$$

  which shows that the point $\mathbf{p}_d(\theta(t))$ will move to a favorable position along the path by minimizing $\theta \mapsto V_q(\mathbf{x}_{\mathbf{0}1}, \theta)$, and wait there until the group becomes coordinated.

- **Path following phase**: After the vessels are sufficiently coordinated, the path following phase is initiated by a collective movement towards the path. This comes as a result of the functions $\sigma_1(|\mathbf{z}|_{L_1}^2)$ and $\sigma_2(|\mathbf{z}|_{L_1}^2)$ approaching unity, thereby activating the maneuvering feedback and feed-forward terms in the common velocity input (3.19). The transient behavior during this phase can be manipulated through shaping of the function $\beta(\cdot)$. The first option is to design $\beta(\cdot)$ so that the function vanishes for large inputs, thereby sharing the properties of the activation functions $\sigma_1(\cdot), \sigma_2(\cdot)$. Through proper tuning, $\beta(|\mathbf{q}|_{L_2}^2)$ can then attain arbitrarily small values for $|\mathbf{q}|_{L_2} \geq c$, where c is a chosen threshold value. The dynamics of θ will then remain $\dot{\theta} \approx -\mu(\theta)V_q^\theta(\mathbf{x}_{\mathbf{0}1}, \theta)$ during the transient motion towards the path, while the common velocity input will satisfy $\mathbf{v}_d \approx \mathbf{A}\mathbf{q}$. The result is a strong separation between the geometric and dynamic tasks of the formation mission objective, where collaboration between the common velocity input and the movement of $\mathbf{p}_d(\theta)$ will make the formation take the shortest way to the path, prior to initiation of forward movement along the path. The second option for $\beta(\cdot)$ is choosing the function identically equal to unity. This will drive $\mathbf{p}_d(\theta)$ along the path according to $v_s(\theta, t)$ immediately after the vessels have established the formation. The result is a maneuvering design along the lines of Skjetne (2005), where the gradient optimization is the sole provider of separation between the geometric and dynamic tasks.

3.2.4 Stability analysis

3.2.4.1 Preliminary definitions and properties

Define

$$\mathbf{x_0} := col(\mathbf{x_0}_1, \ldots, \mathbf{x_0}_r) \quad \in \mathbb{R}^{3r} \tag{3.24}$$

$$\boldsymbol{\psi} := col(\psi_1, \ldots, \psi_r) \quad \in \mathbb{R}^{r} \tag{3.25}$$

$$\bar{\boldsymbol{\nu}} := col(\boldsymbol{\nu}_1, \ldots, \boldsymbol{\nu}_r) \quad \in \mathbb{R}^{3r} \tag{3.26}$$

$$\bar{\mathbf{R}}(\boldsymbol{\psi}) := diag\left(\mathbf{R}(\psi_1), \ldots, \mathbf{R}(\psi_r)\right) \quad \in \mathbb{R}^{3r\times 3r} \tag{3.27}$$

$$\boldsymbol{\alpha}(\mathbf{z}, \boldsymbol{\psi}) := col\left(\boldsymbol{\alpha}_1(\mathbf{z}, \psi_1), \ldots, \boldsymbol{\alpha}_r(\mathbf{z}, \psi_r)\right) \quad \in \mathbb{R}^{3r} \tag{3.28}$$

$$\boldsymbol{\gamma}(\mathbf{z}) := col(\boldsymbol{\gamma}_1(\mathbf{z}_1), \ldots, \boldsymbol{\gamma}_p(\mathbf{z}_p)) \quad \in \mathbb{R}^{3p} \tag{3.29}$$

$$\boldsymbol{\zeta} := col(\boldsymbol{\zeta}_1, \ldots, \boldsymbol{\zeta}_r) \quad \in \mathbb{R}^{3r} \tag{3.30}$$

$$\Upsilon := \mathbf{1}_r \otimes \mathbf{v_d} \quad \in \mathbb{R}^{3r}, \tag{3.31}$$

where, $\mathbf{1}_r \in \mathbb{R}^r$ is the vector of ones. From the definition of $\boldsymbol{\zeta}_i$ and equations (3.11), (3.12), it is verified that the vectors $\mathbf{x_0}$, $\mathbf{z}$, and $\boldsymbol{\alpha}$ satisfy

$$\dot{\mathbf{x}}_\mathbf{0} = \bar{\mathbf{R}}(\boldsymbol{\psi})\boldsymbol{\zeta} + \Upsilon, \tag{3.32}$$

$$\mathbf{z} = (\mathbf{B}^\top \otimes \mathbf{I}_3)\mathbf{x_0}, \tag{3.33}$$

$$\boldsymbol{\alpha}(\mathbf{z}, \boldsymbol{\psi}) = -\bar{\mathbf{R}}(\boldsymbol{\psi})^\top(\mathbf{B} \otimes \mathbf{I}_3)\boldsymbol{\gamma}(\mathbf{z}), \tag{3.34}$$

where $\mathbf{I}_3 \in \mathbb{R}^{3\times 3}$ is the identity matrix. Furthermore, since the sum of entries in any column of $\mathbf{B}$ is equal to zero, the basis for the nullspace $\mathcal{N}(\mathbf{B}^\top \otimes \mathbf{I}_3)$ is

$$\left\{\mathbf{u} \in \mathbb{R}^{3r} : \mathbf{u} = \mathbf{1}_r \otimes \mathbf{c}, \quad \mathbf{c} \in \mathbb{R}^3\right\}, \tag{3.35}$$

from which it follows

$$(\mathbf{B}^\top \otimes \mathbf{I}_3)\Upsilon = \mathbf{0}. \tag{3.36}$$

A consequence of the connectivity assumption on the communication graph is the following lemma:

Lemma 1. *For a connected communication graph with r nodes, p edges and index set $\mathcal{I}$, then $\forall i, j \in \mathcal{I}$ there exists $\mathbf{K}_{ij} = [a_1\mathbf{I}_3, a_2\mathbf{I}_3, \ldots, a_p\mathbf{I}_3] \in \mathbb{R}^{3\times 3p}$, with $a_l \in \{-1, 0, 1\}$, $l = 1 \ldots p$, such that*

$$\mathbf{x_0}_i - \mathbf{x_0}_j = \mathbf{K}_{ij}\mathbf{z}.$$

Proof. See Appendix C.1. □

3.2.4.2 Closed-loop system

In terms of the error variables in the system, the closed-loop dynamics are given by

$$\mathbf{M}_i\dot{\boldsymbol{\zeta}}_i = -\mathbf{C}_i(\boldsymbol{\nu}_i)\boldsymbol{\zeta}_i - \mathbf{D}_i(\boldsymbol{\nu}_i)\boldsymbol{\zeta}_i - \mathbf{K_d}_i\boldsymbol{\zeta}_i + \boldsymbol{\alpha}_i(\mathbf{z}, \psi_i), \quad i \in \mathcal{I} \tag{3.37}$$

$$\dot{\mathbf{z}} = (\mathbf{B}^\top \otimes \mathbf{I}_3)\bar{\mathbf{R}}(\boldsymbol{\psi})\boldsymbol{\zeta} \tag{3.38}$$

$$\dot{\mathbf{q}} = \sigma_1(|\mathbf{z}|^2_{L_1})\mathbf{A}\mathbf{q} - 2\mu(\theta)\mathbf{p}_d^\theta(\theta)\mathbf{q}^\top\mathbf{P}\mathbf{p}_d^\theta(\theta) + \mathbf{R}(\psi_1)\boldsymbol{\zeta}_1 \tag{3.39}$$

$$\dot{\theta} = \sigma_2(|\mathbf{z}|^2_{L_1})\beta(|\mathbf{q}|^2_{L_2})v_s(\theta, t) + 2\mu(\theta)\mathbf{q}^\top\mathbf{P}\mathbf{p}_d^\theta(\theta). \tag{3.40}$$

Utilizing Lemma 1, it is verified that ψ_i can be expressed as

$$\begin{aligned}\psi_i &= \psi_{0i} + \psi_{ci}(t)\\ &= \mathbf{e}^\top\left(\mathbf{K}_{i1}\mathbf{z} + \mathbf{q} + \mathbf{p}_d(\theta)\right) + \psi_{ci}(t) \quad \big|\mathbf{e} = col(0, 0, 1)\end{aligned}$$

Furthermore, we have that

$$\begin{aligned}\boldsymbol{\nu}_i &= \boldsymbol{\zeta}_i + \mathbf{f}_{2i} \\ &= \boldsymbol{\zeta}_i + \mathbf{R}(\psi_i)^\top \left(\mathbf{v}_d + \mathbf{R}(\psi_i - \psi_{ci}(t)) \left(\dot{\mathbf{l}}_i(t) + \mathbf{Sl}_i(t) \left(\mathbf{e}^\top \boldsymbol{\nu}_i - \dot{\psi}_{ci}(t)\right)\right)\right),\end{aligned}$$

which after rearranging yields

$$\boldsymbol{\nu}_i = (\mathbf{I}_3 - \mathbf{R}(\psi_{ci}(t))^\top \mathbf{Sl}_i(t)\mathbf{e}^\top)^{-1} \left(\boldsymbol{\zeta}_i + \mathbf{R}(\psi_i)^\top \mathbf{v}_d + \mathbf{R}(\psi_{ci}(t))^\top \left(\dot{\mathbf{l}}_i(t) - \mathbf{Sl}_i(t)\dot{\psi}_{ci}(t)\right)\right), \tag{3.41}$$

where it is easily verified that

$$(\mathbf{I}_3 - \mathbf{R}(\psi_{ci}(t))^\top \mathbf{Sl}_i(t)\mathbf{e}^\top)^{-1} = (\mathbf{I}_3 + \mathbf{R}(\psi_{ci}(t))^\top \mathbf{Sl}_i(t)\mathbf{e}^\top)$$

By defining

$$\boldsymbol{\chi} := col(\mathbf{z}, \boldsymbol{\zeta}, \mathbf{q}) \quad \in \mathbb{R}^{3(p+r+1)}, \tag{3.42}$$

we can thus write the closed-loop dynamics compactly as

$$\begin{bmatrix}\dot{\boldsymbol{\chi}} \\ \dot{\theta}\end{bmatrix} = \begin{bmatrix}\mathbf{f}_\chi(t, \boldsymbol{\chi}, \theta) \\ f_\theta(t, \boldsymbol{\chi}, \theta)\end{bmatrix} =: \mathbf{F}(t, \boldsymbol{\chi}, \theta). \tag{3.43}$$

Note that in general, the closed-loop error dynamics are valid for $(\mathbf{z}, \boldsymbol{\zeta}, \mathbf{q}, \theta) \in \{\mathcal{R}\big(\mathbf{B}^\top \otimes \mathbf{I}_3\big) \times \mathbb{R}^{3r} \times \mathbb{R}^3 \times \mathbb{R}\}$. From Assumption 1, however, we have that $\mathcal{R}(\mathbf{B}^\top) = \mathbb{R}^p$, which implies that $\mathcal{R}\big(\mathbf{B}^\top \otimes \mathbf{I}_3\big) = \mathbb{R}^{3p}$. This means that the stated closed-loop dynamics are valid over the entire state space, which enables a global stability result.

The main result for the first design is stated in the following theorem:

Theorem 1. *Under assumptions 1 – 4, the control laws laws* (3.9)*,* (3.19)*,* (3.20)*, and* (3.22) *render the closed-loop system* (3.43) *forward complete and the set* $\mathcal{A} = \{(\boldsymbol{\chi}, \theta, t) : \ \boldsymbol{\chi} = 0\}$ *UGAS. This solves the control objectives* (3.4)*,* (3.5)*, and* (3.6)*.*

3.2.4.3 Proof of Theorem 1

Forward completeness: Define the function

$$V_{z,\zeta}(\boldsymbol{\chi}) := \sum_{k=1}^{p} P_k(\mathbf{z}_k) + \sum_{i=1}^{r} S_{\zeta_i}(\boldsymbol{\zeta}_i) \tag{3.44}$$

Since this function is both positive definite and radially unbounded in $(\mathbf{z}, \boldsymbol{\zeta})$, by Khalil (2002; Lemma 4.3) there exists class-$\mathcal{K}_\infty$ functions ϕ_1, ϕ_2 so that

$$\phi_1(|(\mathbf{z}, \boldsymbol{\zeta})|) \leq V_{z,\zeta} \leq \phi_2(|(\mathbf{z}, \boldsymbol{\zeta})|). \tag{3.45}$$

Differentiating (3.44) yields

$$\begin{aligned}\dot{V}_{z,\zeta} &= \left[\frac{\partial}{\partial \mathbf{z}} \left(\sum_{k=1}^{p} P_k(\mathbf{z}_k)\right)\right] \dot{\mathbf{z}} + \sum_{i=1}^{r} \dot{S}_{\zeta,i} \\ &\leq \boldsymbol{\gamma}(\mathbf{z})^\top (\mathbf{B}^\top \otimes \mathbf{I}_3) \bar{\mathbf{R}}(\boldsymbol{\psi}) \boldsymbol{\zeta} + \sum_{i=1}^{r} (-\boldsymbol{\zeta}_i^\top \mathbf{K}_{\mathbf{d}i} \boldsymbol{\zeta}_i + \boldsymbol{\zeta}_i^\top \boldsymbol{\alpha}_i) \\ &= \left(\bar{\mathbf{R}}(\boldsymbol{\psi})^\top (\mathbf{B} \otimes \mathbf{I}_3) \boldsymbol{\gamma}(\mathbf{z})\right)^\top \boldsymbol{\zeta} + \sum_{i=1}^{r} (-\boldsymbol{\zeta}_i^\top \mathbf{K}_{\mathbf{d}i} \boldsymbol{\zeta}_i + \boldsymbol{\zeta}_i^\top \boldsymbol{\alpha}_i) \\ &= -\boldsymbol{\alpha}^\top \boldsymbol{\zeta} - \sum_{i=1}^{r} (\boldsymbol{\zeta}_i^\top \mathbf{K}_{\mathbf{d}i} \boldsymbol{\zeta}_i) + \boldsymbol{\zeta}^\top \boldsymbol{\alpha} \\ &= -\sum_{i=1}^{r} (\boldsymbol{\zeta}_i^\top \mathbf{K}_{\mathbf{d}i} \boldsymbol{\zeta}_i) \leq 0\end{aligned} \tag{3.46}$$

Since $\dot{V}_{z,\zeta} \leq 0$, this implies for all t in the maximum interval of existence $[t_0, T)$, that $V_{z,\zeta}(t) \leq V_{z,\zeta}(t_0)$. Combining this with (3.45) yields

$$\left|\left(\mathbf{z}(t), \boldsymbol{\zeta}(t)\right)\right| \leq \phi_3\left(\left|\left(\mathbf{z}(t_0), \boldsymbol{\zeta}(t_0)\right)\right|\right) \tag{3.47}$$

where $\phi_3(\cdot) := \phi_1^{-1} \circ \phi_2(\cdot) \in \mathcal{K}_\infty$.

Next, consider the positive definite, radially unbounded function (3.16) satisfying

$$\lambda_{min,P}|\mathbf{q}|^2 \leq V_q \leq \lambda_{max,P}|\mathbf{q}|^2. \tag{3.48}$$

On the time interval $[t_0, T)$, the bounds (3.47) and the fact that $\sigma_1(\cdot)$ is monotonically decreasing give a lower bound on $\sigma_1(|\mathbf{z}(t)|_{L_1}^2)$ according to

$$\sigma_1(|\mathbf{z}(t)|_{L_1}^2) \geq \sigma_1\left(||\mathbf{L}_1||\phi_3\left(\left|\left(\mathbf{z}(t_0), \boldsymbol{\zeta}(t_0)\right)\right|\right)^2\right) =: \epsilon_1. \tag{3.49}$$

From (3.23) we then get the following over $[t_0, T)$, noting that $||\mathbf{R}(\psi)|| = 1 \; \forall \psi \in \mathbb{R}$:

$$\begin{aligned}
\dot{V}_q &\leq -\epsilon_1 \mathbf{q}^\top \mathbf{Q}\mathbf{q} + 2\mathbf{q}^\top \mathbf{P}\mathbf{R}(\psi_1)\boldsymbol{\zeta}_1 \\
&\leq -\epsilon_1 \lambda_{min,Q}|\mathbf{q}|^2 + 2|\mathbf{q}||\mathbf{P}||\boldsymbol{\zeta}_1| \\
&\leq -\frac{1}{2}\epsilon_1 \lambda_{min,Q}|\mathbf{q}|^2 \quad \forall |\mathbf{q}| \geq \frac{4||\mathbf{P}||}{\epsilon_1 \lambda_{min,Q}}|\boldsymbol{\zeta}_1|
\end{aligned}$$

For

$$|\mathbf{q}| \geq \frac{4||\mathbf{P}||\phi_3\left(\left|\left(\mathbf{z}(t_0), \boldsymbol{\zeta}(t_0)\right)\right|\right)}{\epsilon_1 \lambda_{min,Q}} =: \epsilon_2,$$

we are thus guaranteed $\dot{V}_q \leq 0$, which yields

$$\begin{aligned}
V_q(t) &\leq \max\{V_q(\mathbf{q}(t_0)), \sup_{|\mathbf{q}|=\epsilon_2} V_q(\mathbf{q})\} \\
&\leq V_q(\mathbf{q}(t_0)) + \sup_{|\mathbf{q}|=\epsilon_2} V_q(\mathbf{q}) \\
&\leq \lambda_{max,P}|\mathbf{q}(t_0)|^2 + \lambda_{max,P}\epsilon_2^2 \quad \forall t \in [t_0, T).
\end{aligned}$$

From this, we finally get uniform upper bounds for $|\mathbf{q}(t)|$ over the time interval $[t_0, T)$:

$$|\mathbf{q}(t)| \leq \sqrt{\frac{\lambda_{max,P}}{\lambda_{min,P}}}\left(|\mathbf{q}(t_0)| + \epsilon_2\right) \tag{3.50}$$

Combining this with assumptions 3 and 4, we achieve a uniform upper bound for $|\dot{\theta}|$ over $[t_0, T)$, which shows that there cannot be a finite escape time for the system (3.43), i.e. $T = +\infty$. By a locally Lipschitz property of the closed-loop system, it is concluded that the solutions $\theta(t)$ and $\boldsymbol{\chi}(t)$ exist and are continuous functions over $[t_0, \infty)$.

For the remainder of the analysis, θ will be treated as an external input, continuous in time, that enters the dynamics of $\boldsymbol{\chi}$. Stability of the origin of

$$\dot{\boldsymbol{\chi}} = \mathbf{f}(t, \boldsymbol{\chi}), \tag{3.51}$$

where $\mathbf{f}(t, \boldsymbol{\chi}) := \mathbf{f}_\chi(t, \boldsymbol{\chi}, \theta(t))$, will be investigated by the means of the Nested Matrosov Theorem for time-varying systems, presented in Loria et al. (2005). The theorem is included in Appendix A.1 for the sake of self-containment.

Uniform Global Stability: To apply the Nested Matrosov Theorem, UGS of the origin is first established. By forward completeness of the closed-loop system, the bounds in (3.47) and (3.50) hold $\forall t \geq t_0$. Since $|\boldsymbol{\chi}| \leq |(\mathbf{z}, \boldsymbol{\zeta})| + |\mathbf{q}|$, $|\boldsymbol{\chi}| \geq |(\mathbf{z}, \boldsymbol{\zeta})|$, and $|\boldsymbol{\chi}| \geq |\mathbf{q}|$, we have that

$$\begin{aligned}
&|\boldsymbol{\chi}(t)| \leq \phi_3\left(\left|\left(\mathbf{z}(t_0), \boldsymbol{\zeta}(t_0)\right)\right|\right) + \\
&\sqrt{\frac{\lambda_{max,P}}{\lambda_{min,P}}}\left[|\mathbf{q}(t_0)| + \frac{4||\mathbf{P}||\phi_3\left(\left|\left(\mathbf{z}(t_0), \boldsymbol{\zeta}(t_0)\right)\right|\right)}{\epsilon_1 \lambda_{min,Q}}\right] \\
&\leq \phi_3\left(|\boldsymbol{\chi}(t_0)|\right) + \\
&\sqrt{\frac{\lambda_{max,P}}{\lambda_{min,P}}}\left[|\boldsymbol{\chi}(t_0)| + \frac{4||\mathbf{P}||\phi_3\left(|\boldsymbol{\chi}(t_0)|\right)}{\lambda_{min,Q}\sigma_1\left(||\mathbf{L}_1||\phi_3\left(|\boldsymbol{\chi}(t_0)|\right)^2\right)}\right] \\
&=: \phi_4(|\boldsymbol{\chi}(t_0)|)
\end{aligned}$$

Since $\phi_3(\cdot) \in \mathcal{K}^\infty$ and $\sigma_1(\cdot)$ is monotonically decreasing and strictly positive, we have that $\phi_4(\cdot) \in \mathcal{K}^\infty$, which shows that the origin is UGS.

Uniform Global Asymptotic Stability: Defining

$$V_0(\boldsymbol{\chi}) := V_{z,\zeta}(\boldsymbol{\chi}), \tag{3.52}$$

we have from (3.46) that

$$\dot{V}_0(t, \boldsymbol{\chi}) \leq \sum_{i=1}^{r} (-\boldsymbol{\zeta}_i^\top \mathbf{K}_{\mathbf{d}_i} \boldsymbol{\zeta}_i) =: Y_0(\boldsymbol{\chi}) \leq 0 \quad \forall \boldsymbol{\chi}, \tag{3.53}$$

where it is noted that $Y_0(\boldsymbol{\chi}) = 0$ implies $\boldsymbol{\zeta} = \mathbf{0}$. Now, define the first auxiliary function[5]

$$V_1(t, \boldsymbol{\chi}) := \mathbf{z}^\top (\mathbf{B} \otimes \mathbf{I}_3)^\ddagger \bar{\mathbf{R}}(\boldsymbol{\psi}) \bar{\mathbf{M}} \boldsymbol{\zeta}, \tag{3.54}$$

where

$$\bar{\mathbf{M}} := diag(\mathbf{M}_1, \ldots, \mathbf{M}_r) \quad \in \mathbb{R}^{3r \times 3r}, \tag{3.55}$$

and $(\mathbf{B} \otimes \mathbf{I}_3)^\ddagger \in \mathbb{R}^{3p \times 3r}$ is the Moore-Penrose pseudo-inverse of $(\mathbf{B} \otimes \mathbf{I}_3)$ satisfying

$$(\mathbf{B} \otimes \mathbf{I}_3)(\mathbf{B} \otimes \mathbf{I}_3)^\ddagger (\mathbf{B} \otimes \mathbf{I}_3) = (\mathbf{B} \otimes \mathbf{I}_3)$$

Differentiating (3.54) with respect to time yields

$$\begin{aligned}
\dot{V}_1(t, \boldsymbol{\chi}) &= \boldsymbol{\zeta}^\top \bar{\mathbf{R}}(\boldsymbol{\psi})^\top (\mathbf{B} \otimes \mathbf{I}_3)(\mathbf{B} \otimes \mathbf{I}_3)^\ddagger \bar{\mathbf{R}}(\boldsymbol{\psi}) \bar{\mathbf{M}} \boldsymbol{\zeta} \\
&\quad + \mathbf{z}^\top (\mathbf{B} \otimes \mathbf{I}_3)^\ddagger \left(\dot{\bar{\mathbf{R}}}(\boldsymbol{\psi}, \bar{\boldsymbol{\nu}}) \bar{\mathbf{M}} \boldsymbol{\zeta} + \bar{\mathbf{R}}(\boldsymbol{\psi}) \bar{\mathbf{M}} \dot{\boldsymbol{\zeta}}\right) \\
&=: Y_1(\boldsymbol{\chi}, \boldsymbol{\phi}(t, \boldsymbol{\chi}))
\end{aligned}$$

Here, all time dependent terms of $\dot{V}_1(t, \boldsymbol{\chi})$ have been collected in the vector $\boldsymbol{\phi}(t, \boldsymbol{\chi})$, defined as

$$\boldsymbol{\phi}(t, \boldsymbol{\chi}) := col(\bar{\mathbf{R}}(\boldsymbol{\psi})\boldsymbol{\zeta}, \bar{\mathbf{R}}(\boldsymbol{\psi})\bar{\mathbf{M}}\boldsymbol{\zeta}, \dot{\bar{\mathbf{R}}}(\boldsymbol{\psi}, \bar{\boldsymbol{\nu}})\bar{\mathbf{M}}\boldsymbol{\zeta}, \bar{\mathbf{R}}(\boldsymbol{\psi})\bar{\mathbf{M}}\dot{\boldsymbol{\zeta}}) \tag{3.56}$$

Evaluating $Y_1(\boldsymbol{\chi}, \boldsymbol{\phi}(t, \boldsymbol{\chi}))$ at $\boldsymbol{\zeta} = \mathbf{0}$, and using (3.37) yields:

$$\begin{aligned}
Y_1(\boldsymbol{\chi}, \boldsymbol{\phi}(t, \boldsymbol{\chi}))\Big|_{\boldsymbol{\zeta}=0} &= \mathbf{z}^\top (\mathbf{B} \otimes \mathbf{I}_3)^\ddagger \bar{\mathbf{R}}(\boldsymbol{\psi}) (\bar{\mathbf{M}} \dot{\boldsymbol{\zeta}})\Big|_{\boldsymbol{\zeta}=0} \\
&= \mathbf{z}^\top (\mathbf{B} \otimes \mathbf{I}_3)^\ddagger \bar{\mathbf{R}}(\boldsymbol{\psi}) \boldsymbol{\alpha}(\mathbf{z}, \boldsymbol{\psi}) \\
&= -\mathbf{z}^\top (\mathbf{B} \otimes \mathbf{I}_3)^\ddagger \bar{\mathbf{R}}(\boldsymbol{\psi}) \bar{\mathbf{R}}(\boldsymbol{\psi})^\top (\mathbf{B} \otimes \mathbf{I}_3) \boldsymbol{\gamma}(\mathbf{z}) \\
&= -\mathbf{x_0}^\top (\mathbf{B} \otimes \mathbf{I}_3)(\mathbf{B} \otimes \mathbf{I}_3)^\ddagger (\mathbf{B} \otimes \mathbf{I}_3) \boldsymbol{\gamma}(\mathbf{z}) \\
&= -\mathbf{x_0}^\top (\mathbf{B} \otimes \mathbf{I}_3) \boldsymbol{\gamma}(\mathbf{z}) \\
&= -\mathbf{z}^\top \boldsymbol{\gamma}(\mathbf{z}) < 0 \quad \forall \mathbf{z} \neq \mathbf{0}
\end{aligned}$$

[5]The time dependency of this function is due to the heading angles of the vessels being time dependent after the change of variables, as shown in Section 3.2.4.2.

The last inequality follows from the definition of $\boldsymbol{\gamma}_k(\mathbf{z}_k)$ in (3.13) and the properties listed in (3.14). Now, define the second auxiliary function

$$V_2(\boldsymbol{\chi}) := V_q(\mathbf{q}) \tag{3.57}$$

which satisfies

$$\dot{V}_2 \leq -\sigma_1(|\mathbf{z}|_{L_1}^2)\mathbf{q}^\top\mathbf{Q}\mathbf{q} + 2\mathbf{q}^\top\mathbf{P}\mathbf{R}(\psi_1)\boldsymbol{\zeta}_1 =: Y_2(\boldsymbol{\chi}, \boldsymbol{\phi}(t,\boldsymbol{\chi})) \tag{3.58}$$

Evaluating $Y_2(\boldsymbol{\chi}, \boldsymbol{\phi}(t,\boldsymbol{\chi}))$ at $\boldsymbol{\zeta}, \mathbf{z} = \mathbf{0}$ yields

$$Y_2(\boldsymbol{\chi})\Big|_{\boldsymbol{\zeta},\mathbf{z}=\mathbf{0}} = -\mathbf{q}^\top\mathbf{Q}\mathbf{q} < 0 \quad \forall \mathbf{q} \neq \mathbf{0}$$

It will now be shown that all assumptions of Theorem A.1 are fulfilled.

1: The origin of (3.51) has been shown to UGS, and Assumption 1 of Theorem A.1 is thus satisfied.

2: By continuity of $\theta(t)$ and the smoothness assumptions on $\mathbf{p}_d(\theta)$, $P_k(\mathbf{z}_k)$, and $\mathbf{l}_i(t)$, we have that $V_0(\boldsymbol{\chi})$,$V_1(t,\boldsymbol{\chi})$,$V_2(\boldsymbol{\chi})$, $\frac{\partial V_0(\boldsymbol{\chi})}{\partial \boldsymbol{\chi}}$,$\frac{\partial V_1(t,\boldsymbol{\chi})}{\partial \boldsymbol{\chi}}$,$\frac{\partial V_2(\boldsymbol{\chi})}{\partial \boldsymbol{\chi}}$ are continuous on any set $[a,b]\times D$, where $[a,b] \subset [t_0,\infty)$, $D \subset \mathbb{R}^{3(p+r+1)}$. By Khalil (2002; Lemma 3.2), the functions $V_i(t,\boldsymbol{\chi})$ are thus locally Lipschitz over $[t_0,\infty)\times\mathbb{R}^{3(r+p+1)}$. Since $Y_0(\boldsymbol{\chi}), Y_1(\boldsymbol{\chi},\boldsymbol{\phi}), Y_2(\boldsymbol{\chi},\boldsymbol{\phi})$ are continuous in their arguments, the only thing left to show for Assumption 2 of Theorem A.1 to be satisfied is that there exists uniform upper bounds on $|V_i(t,\boldsymbol{\chi})|$ and $|\boldsymbol{\phi}(t,\boldsymbol{\chi})|$ for any given upper bound on $|\boldsymbol{\chi}|$. Uniform upper bounds on $|V_0(\boldsymbol{\chi})|, |V_2(\boldsymbol{\chi})|$ follows from (3.45) and (3.48), while bounds on $|V_1(t,\boldsymbol{\chi})|$ is established by using the Cauchy-Schwarz inequality, noting that the norm of the block-diagonal matrix $\bar{\mathbf{R}}(\boldsymbol{\psi})$ is uniformly upper bounded by the property $||\mathbf{R}(\psi)|| \equiv 1$. To see that the bound on $|\boldsymbol{\phi}(t,\boldsymbol{\chi})|$ holds, first note that the norms of $\boldsymbol{\nu}_i$, $i \in \mathcal{I}$, are bounded for bounded $|\boldsymbol{\chi}|$ by (3.41) and assumptions 2 – 3. Uniform upper bounds on $|\dot{\bar{\mathbf{R}}}(\psi_i,\boldsymbol{\nu}_i)| = |\mathbf{R}(\psi_i)\mathbf{S}\mathbf{e}^\top\boldsymbol{\nu}_i|$ follows, which in turn shows that $|\dot{\bar{\mathbf{R}}}(\boldsymbol{\psi},\bar{\boldsymbol{\nu}})\bar{\mathbf{M}}\boldsymbol{\zeta}|$ is uniformly upper bounded. Since $|\bar{\mathbf{R}}(\boldsymbol{\psi})\boldsymbol{\zeta}|$, $|\bar{\mathbf{R}}(\boldsymbol{\psi})\bar{\mathbf{M}}\boldsymbol{\zeta}|$ and $|\bar{\mathbf{R}}(\boldsymbol{\psi})\bar{\mathbf{M}}\dot{\boldsymbol{\zeta}}|$ also are uniformly upper bounded for bounded $|\boldsymbol{\chi}|$ (the latter follows from (3.37) and the bounds on $|\boldsymbol{\nu}_i|$), it is concluded that a uniform upper bound on $|\boldsymbol{\phi}(t,\boldsymbol{\chi})|$ can be established for any given upper bound on $|\boldsymbol{\chi}|$. Assumption 2 of Theorem A.1 is thus satisfied.

3: Since

$$\begin{aligned} Y_0(\boldsymbol{\chi}) \leq 0 \quad & \forall \boldsymbol{\chi}, \\ Y_0(\boldsymbol{\chi}) = 0 \Rightarrow Y_1(\boldsymbol{\chi},\boldsymbol{\phi}(t,\boldsymbol{\chi})) \leq 0 \quad & \forall \boldsymbol{\chi},\boldsymbol{\phi}, \\ Y_0(\boldsymbol{\chi}), Y_1(\boldsymbol{\chi},\boldsymbol{\phi}(t,\boldsymbol{\chi})) = 0 \Rightarrow Y_2(\boldsymbol{\chi},\boldsymbol{\phi}(t,\boldsymbol{\chi})) \leq 0 \quad & \forall \boldsymbol{\chi},\boldsymbol{\phi}, \end{aligned}$$

assumption 3 is satisfied.

4: Since

$$\begin{aligned} Y_0(\boldsymbol{\chi}) = 0 &\Rightarrow \boldsymbol{\zeta} = \mathbf{0}, \\ Y_1(\boldsymbol{\chi},\boldsymbol{\phi}(t,\boldsymbol{\chi}))\Big|_{\boldsymbol{\zeta}=\mathbf{0}} = 0 &\Rightarrow \mathbf{z} = \mathbf{0}, \\ Y_2(\boldsymbol{\chi},\boldsymbol{\phi}(t,\boldsymbol{\chi}))\Big|_{\boldsymbol{\zeta},\mathbf{z}=\mathbf{0}} = 0 &\Rightarrow \mathbf{q} = \mathbf{0}, \end{aligned}$$

we have that $Y_0(\boldsymbol{\chi}), Y_1(\boldsymbol{\chi},\boldsymbol{\phi}(t,\boldsymbol{\chi})), Y_2(\boldsymbol{\chi},\boldsymbol{\phi}(t,\boldsymbol{\chi})) = 0$ together imply $\boldsymbol{\chi} = \mathbf{0}$. Assumption 4 is thus satisfied.

All assumptions of Theorem A.1 is satisfied, and UGAS for the origin of (3.51) is concluded. Noting that $|(\boldsymbol{\chi}, \theta, t)|_{\mathcal{A}} = |\boldsymbol{\chi}|$, this proves UGAS for the set $\mathcal{A}$.

Fulfillment of control objectives: We now have that

$$\lim_{t\to\infty} (|\mathbf{z}(t)|, |\boldsymbol{\zeta}(t)|, |\mathbf{q}(t)|) = 0$$

By the definition of $\mathbf{q}$, the control objective (3.5) is satisfied. Fulfillment of (3.4) and (3.6) follows from Lemma 1 and the closed loop dynamics of θ in (3.40), respectively. The reader is referred to Appendix C.2 for a formal proof of this last statement. □

3.2.5 Practical considerations

3.2.5.1 Notes on implementation

The control design is summarized in Table 3.1

Control laws	$\boldsymbol{\tau}_i = \mathbf{D}_i(\boldsymbol{\nu}_i)\mathbf{f}_{2i} + \mathbf{C}_i(\boldsymbol{\nu}_i)\mathbf{f}_{2i} + \mathbf{M}_i\dot{\mathbf{f}}_{2i} - \mathbf{K}_{\mathbf{d}i}(\boldsymbol{\nu}_i - \mathbf{f}_{2i}) + \boldsymbol{\alpha}_i(\mathbf{z}, \psi_i)$
Internal dynamic variables	$\dot{\theta} = \sigma_2(\lvert\mathbf{z}\rvert^2_{L_1})\beta(\lvert\mathbf{q}\rvert^2_{L_2})v_s(\theta,t) + 2\mu(\theta)\mathbf{q}^\top\mathbf{P}\mathbf{p}_d^\theta(\theta)$
Parameters	$\mathbf{K}_{\mathbf{d}i} = \mathbf{K}_{\mathbf{d}i}^T > 0$ $\mathbf{A}$ Hurwitz $\mathbf{P} = \mathbf{P}^T > 0$ satisfying $\mathbf{PA} + \mathbf{A}^\top\mathbf{P} = -\mathbf{Q}$ for some $\mathbf{Q} = \mathbf{Q}^\top > 0$ $\mathbf{L}_1 = \mathbf{L}_1^\top \geq 0$, $\mathbf{L}_2 = \mathbf{L}_2^\top \geq 0$
Signals	$\boldsymbol{\alpha}_i(\mathbf{z}, \psi_i)$ is given jointly by (3.11)–(3.14) $\mathbf{q} = \mathbf{x}_{\mathbf{0}j^*} - \mathbf{p}_d(\theta)$ ($j^* \in \mathcal{I}$ is the index of the assigned acting leader) $\mathbf{x}_{\mathbf{0}i} = \boldsymbol{\eta}_i - \mathbf{f}_{1i}$ $\mathbf{z} = (\mathbf{B}^\top \otimes \mathbf{I}_3)\mathbf{x}_\mathbf{0}$ ($\mathbf{B}$ is the incidence matrix, $\mathbf{x}_\mathbf{0} = col(\mathbf{x}_{\mathbf{0}1}, \ldots, \mathbf{x}_{\mathbf{0}r})$) $\mathbf{f}_{1i} = \mathbf{R}(\psi_i - \psi_{ci}(t))\,\mathbf{l}_i(t), \qquad (\mathbf{l}_i(t) = col(x_{ci}(t), y_{ci}(t), \psi_{ci}(t)))$ $\dot{\mathbf{f}}_{1i} = \mathbf{R}(\psi_i - \psi_{ci})\big(\mathbf{S}\mathbf{l}_i(\dot{\psi}_i - \dot{\psi}_{ci}) + \dot{\mathbf{l}}_i\big)$ ($\mathbf{S}$ is given in Section 2.4.1) $\ddot{\mathbf{f}}_{1i} = \mathbf{R}(\psi_i - \psi_{ci})\big(\mathbf{S}\mathbf{l}_i(\ddot{\psi}_i - \ddot{\psi}_{ci}) + \mathbf{S}^2\mathbf{l}_i(\dot{\psi}_i - \dot{\psi}_{ci})^2 + 2\mathbf{S}\dot{\mathbf{l}}_i(\dot{\psi}_i - \dot{\psi}_{ci}) + \ddot{\mathbf{l}}_i\big)$ $\mathbf{f}_{2i} = \mathbf{R}(\psi_i)^\top(\dot{\mathbf{f}}_{1i} + \mathbf{v}_d)$ $\dot{\mathbf{f}}_{2i} = \mathbf{S}^\top\mathbf{f}_{2i}\dot{\psi}_i + \mathbf{R}(\psi_i)^\top(\ddot{\mathbf{f}}_{1i} + \dot{\mathbf{v}}_d)$ $\mathbf{v_d} = \sigma_1(\lvert\mathbf{z}\rvert^2_{L_1})\mathbf{Aq} + \sigma_2(\lvert\mathbf{z}\rvert^2_{L_1})\beta(\lvert\mathbf{q}\rvert^2_{L_2})\mathbf{p}_d^\theta(\theta)v_s(\theta,t)$ $\lvert\mathbf{z}\rvert^2_{L_1} = \mathbf{z}^\top\mathbf{L}_1\mathbf{z}$, $\lvert\mathbf{q}\rvert^2_{L_2} = \mathbf{q}^\top\mathbf{L}_2\mathbf{q}$ $\dot{\mathbf{v}}_\mathbf{d} = \left[\mathbf{A}\sigma_1(\lvert\mathbf{z}\rvert^2_{L_1}) + \sigma_2(\lvert\mathbf{z}\rvert^2_{L_1})\mathbf{p}_d^\theta(\theta)v_s(\theta,t)\frac{\partial\left(\beta(\lvert\mathbf{q}\rvert^2_{L_2})\right)}{\partial(\lvert\mathbf{q}\rvert^2_{L_2})}2\mathbf{q}^\top\mathbf{L}_2\right](\dot{\mathbf{x}}_{\mathbf{0}j^*} - \mathbf{p}_d^\theta(\theta)\dot{\theta})$ $+\left[\mathbf{Aq}\frac{\partial\left(\sigma_1(\lvert\mathbf{z}\rvert^2_{L_1})\right)}{\partial(\lvert\mathbf{z}\rvert^2_{L_1})}2\mathbf{z}^\top\mathbf{L}_1 + \beta(\lvert\mathbf{q}\rvert^2_{L_2})\mathbf{p}_d^\theta(\theta)v_s(\theta,t)\frac{\partial\left(\sigma_2(\lvert\mathbf{z}\rvert^2_{L_1})\right)}{\partial(\lvert\mathbf{z}\rvert^2_{L_1})}2\mathbf{z}^\top\mathbf{L}_1\right]\dot{\mathbf{z}}$ $+\sigma_2(\lvert\mathbf{z}\rvert^2_{L_1})\beta(\lvert\mathbf{q}\rvert^2_{L_2})\left(\mathbf{p}_d^{\theta^2}(\theta)v_s(\theta,t) + \mathbf{p}_d^\theta(\theta)v_s^\theta(\theta,t)\right)\dot{\theta}$ $+\sigma_2(\lvert\mathbf{z}\rvert^2_{L_1})\beta(\lvert\mathbf{q}\rvert^2_{L_2})\mathbf{p}_d^\theta(\theta)v_s^t(\theta,t)$ $\mathbf{p_d}(\theta) = col(x_d(\theta), y_d(\theta), \psi_d(\theta))$ $\psi_d(\theta) = \arctan(\frac{y_d^\theta(\theta)}{x_d^\theta(\theta)})$ $\psi_d^\theta = \frac{y_d^{\theta^2}x_d^\theta - x_d^{\theta^2}y_d^\theta}{(x_d^\theta)^2+(y_d^\theta)^2}$ $\psi_d^{\theta^2} = \frac{(y_d^{\theta^3}x_d^\theta - x_d^{\theta^3}y_d^\theta)((x_d^\theta)^2+(y_d^\theta)^2) - 2(y_d^{\theta^2}x_d^\theta - x_d^{\theta^2}y_d^\theta)(x_d^\theta x_d^{\theta^2} + y_d^\theta y_d^{\theta^2})}{((x_d^\theta)^2+(y_d^\theta)^2)^2}$

Table 3.1: Design 1 summarized

Calculation of accelerations during simulations: From the expression for $\dot{\mathbf{f}}_{2i}$ stated in Table 3.1, it is seen that the individual control laws require access to the yaw acceleration $\ddot{\psi}_i$. For simulations of the closed loop system, it may seem like this gives rise to algebraic loops, as the generalized control vector $\boldsymbol{\tau}_i$ depends on the yaw acceleration, which naturally depends on $\boldsymbol{\tau}_i$. It turns out that there are no algebraic loops. First of all, note that the yaw acceleration can be written as

$$\ddot{\psi}_i = \mathbf{e}^\top\dot{\boldsymbol{\nu}}_i \quad (\mathbf{e} = col(0,0,1))$$

Divide $\dot{\mathbf{f}}_{2i}$ into two terms, where one is dependent and the other is independent on $\dot{\boldsymbol{\nu}}_i$:

$$\begin{aligned}
\dot{\mathbf{f}}_{2i} &= \mathbf{S}^\top \mathbf{f}_{2i}\dot{\psi}_i + \mathbf{R}(\psi_i)^\top(\ddot{\mathbf{f}}_{1i} + \dot{\mathbf{v}}_d) \\
&= \mathbf{S}^\top \mathbf{f}_{2i}\dot{\psi}_i + \mathbf{R}(\psi_i)^\top \Big(\dot{\mathbf{v}}_d + \mathbf{R}(\psi_i - \psi_{ci})\big(\mathbf{S}\mathbf{l}_i(\ddot{\psi}_i - \ddot{\psi}_{ci}) + \mathbf{S}^2\mathbf{l}_i(\dot{\psi}_i - \dot{\psi}_{ci})^2 + 2\mathbf{S}\dot{\mathbf{l}}_i(\dot{\psi}_i - \dot{\psi}_{ci}) + \ddot{\mathbf{l}}_i\big)\Big) \\
&= \mathbf{R}(\psi_{ci}(t))^\top \mathbf{S}\mathbf{l}_i(t)\mathbf{e}^\top \dot{\boldsymbol{\nu}}_i + \mathbf{S}^\top \mathbf{f}_{2i}\dot{\psi}_i + \mathbf{R}(\psi_i)^\top \dot{\mathbf{v}}_d \\
&+ \mathbf{R}(\psi_{ci}(t))^\top \Big(-\mathbf{S}\mathbf{l}_i\ddot{\psi}_{ci}(t) + \mathbf{S}^2\mathbf{l}_i(\dot{\psi}_i - \dot{\psi}_{ci}(t))^2 + 2\mathbf{S}\dot{\mathbf{l}}_i(\dot{\psi}_i - \dot{\psi}_{ci}(t)) + \ddot{\mathbf{l}}_i(t)\Big) \\
&= \mathbf{R}(\psi_{ci}(t))^\top \mathbf{S}\mathbf{l}_i(t)\mathbf{e}^\top \dot{\boldsymbol{\nu}}_i + \mathbf{f}_{3i}
\end{aligned}$$

Here, the property $\mathbf{R}(\psi_i)^\top\mathbf{R}(\psi_i - \psi_{ci}) = \mathbf{R}(\psi_i)^\top\mathbf{R}(\psi_{ci} - \psi_i)^\top = \mathbf{R}(\psi_{ci})^\top$ has been used, and

$$\mathbf{f}_{3i} := \mathbf{S}^\top \mathbf{f}_{2i}\dot{\psi}_i + \mathbf{R}(\psi_i)^\top \dot{\mathbf{v}}_d + \mathbf{R}(\psi_{ci}(t))^\top \Big(-\mathbf{S}\mathbf{l}_i\ddot{\psi}_{ci}(t) + \mathbf{S}^2\mathbf{l}_i(\dot{\psi}_i - \dot{\psi}_{ci}(t))^2 + 2\mathbf{S}\dot{\mathbf{l}}_i(\dot{\psi}_i - \dot{\psi}_{ci}(t)) + \ddot{\mathbf{l}}_i(t)\Big) \tag{3.59}$$

The following is now obtained in closed loop:

$$\begin{aligned}
\mathbf{M}_i\dot{\boldsymbol{\nu}}_i &= -\mathbf{C}_i(\boldsymbol{\nu}_i)\boldsymbol{\nu}_i - \mathbf{D}_i(\boldsymbol{\nu}_i)\boldsymbol{\nu}_i + \boldsymbol{\tau}_i \\
&= -\mathbf{C}_i(\boldsymbol{\nu}_i)(\boldsymbol{\nu}_i - \mathbf{f}_{2i}) - \mathbf{D}_i(\boldsymbol{\nu}_i)(\boldsymbol{\nu}_i - \mathbf{f}_{2i}) + \mathbf{M}_i\dot{\mathbf{f}}_{2i} - \mathbf{K}_{\mathbf{d}i}(\boldsymbol{\nu}_i - \mathbf{f}_{2i}) + \boldsymbol{\alpha}_i(\mathbf{z}, \psi_i) \\
&= -\mathbf{C}_i(\boldsymbol{\nu}_i)(\boldsymbol{\nu}_i - \mathbf{f}_{2i}) - \mathbf{D}_i(\boldsymbol{\nu}_i)(\boldsymbol{\nu}_i - \mathbf{f}_{2i}) + \mathbf{M}_i\mathbf{R}(\psi_{ci}(t))^\top \mathbf{S}\mathbf{l}_i(t)\mathbf{e}^\top \dot{\boldsymbol{\nu}}_i + \mathbf{M}_i\mathbf{f}_{3i} \\
&- \mathbf{K}_{\mathbf{d}i}(\boldsymbol{\nu}_i - \mathbf{f}_{2i}) + \boldsymbol{\alpha}_i(\mathbf{z}, \psi_i)
\end{aligned}$$

Rearranging yields

$$\begin{aligned}
\dot{\boldsymbol{\nu}}_i = \big(\mathbf{I}_3 - \mathbf{R}(\psi_{ci}(t))^\top \mathbf{S}\mathbf{l}_i(t)\mathbf{e}^\top\big)^{-1} \mathbf{M}_i^{-1}\Big(&- \mathbf{C}_i(\boldsymbol{\nu}_i)(\boldsymbol{\nu}_i - \mathbf{f}_{2i}) - \mathbf{D}_i(\boldsymbol{\nu}_i)(\boldsymbol{\nu}_i - \mathbf{f}_{2i}) + \mathbf{M}_i\mathbf{f}_{3i} \\
&- \mathbf{K}_{\mathbf{d}i}(\boldsymbol{\nu}_i - \mathbf{f}_{2i}) + \boldsymbol{\alpha}_i(\mathbf{z}, \psi_i)\Big),
\end{aligned} \tag{3.60}$$

where it is noted that the inverse of $\big(\mathbf{I}_3 - \mathbf{R}(\psi_{ci}(t))^\top \mathbf{S}\mathbf{l}_i(t)\mathbf{e}^\top\big)$ always exists and is given by

$$\big(\mathbf{I}_3 - \mathbf{R}(\psi_{ci}(t))^\top \mathbf{S}\mathbf{l}_i(t)\mathbf{e}^\top\big)^{-1} = \big(\mathbf{I}_3 + \mathbf{R}(\psi_{ci}(t))^\top \mathbf{S}\mathbf{l}_i(t)\mathbf{e}^\top\big) \tag{3.61}$$

It is recommended that Equation (3.60) is used during simulations to avoid any warnings of algebraic loops from the simulation software.

Proper handling of orientation error signals: The vectors $\mathbf{z}_k$, $k = 1 \dots p$, and $\mathbf{q}$ contain orientation errors between local FRPs, and between the FRP of the acting leader and $\psi_d(\theta)$, respectively. Due to the $\mathcal{S}^1$ symmetry of orientation variables (i.e. $\psi \pm 2\pi n$, $n \in \mathbb{N}$ represents the same physical orientation), situations can arise where the value of the orientation error variables are larger in magnitude than the physical orientation errors they correspond to (this is the case for any error larger than π in magnitude), which in turn can result in misplaced control efforts. This is especially a problem for the control of $\mathbf{q}$ through the common velocity input (3.19), as a discontinuous four quadrant version of the arctan$(\cdot)$ function typically is used to calculate $\psi_d(\theta)$ in a practical implementation. A way to circumvent these problems is to modify the numerical representation for one of the two orientation variables before calculating the corresponding orientation error, so that the magnitude of the error is guaranteed to be less than or equal to π in magnitude. Algorithm 1 has been developed by the author for this purpose. It is recommended that the algorithm is applied to the orientation errors in both $\mathbf{q}$ and $\mathbf{z}_k$, $k = 1 \dots p$, wherever they appear in the control system.

Algorithm 1 Orientation handler

INPUT: $\psi, \psi_d \in \mathcal{S}^1$.
OUTPUT: $\psi_{out} = \psi + 2\pi n^*$, where $n^* \in \{\ldots, -3, -2, -1, 0, 1, 2, 3, \ldots\}$ is calculated so that $|\psi_{out} - \psi_d|$ is minimized.
PROCEDURE:
if $|\psi - \psi_d| > \pi$ **then**
  $a = \text{floor}(\left|\frac{\psi - \psi_d}{\pi}\right|)$
  $n = \text{floor}\left(\left|\frac{a-1}{2}\right|\right)$
  if $\psi > \psi_d$ **then**
    $\psi_{out} = \psi - (n+1)2\pi$
  else
    $\psi_{out} = \psi + (n+1)2\pi$
  end if
else
  $\psi_{out} = \psi$
end if

3.2.5.2 Choosing the functions $P_k(\mathbf{z}_k)$

A wide range of choices for $P_k(\mathbf{z}_k)$ satisfy the requirements in (3.14). However, as the synchronization terms $\boldsymbol{\alpha}_i(\mathbf{z}, \psi_i)$ in the vessel control laws are given by weighted sums of the gradients of these functions, some choices are more natural than others. The author finds the following to be appropriate for most applications:

$$P_k(\mathbf{z}_k) = \frac{1}{2}\left(a_k z_{k1}^2 + a_k z_{k2}^2 + b_k z_{k3}^2\right), \quad a_k, b_k > 0, \quad (\mathbf{z}_k = col(z_{k1}, z_{k2}, z_{k3})), \tag{3.62}$$

This corresponds to

$$\begin{aligned} \boldsymbol{\gamma}_k(\mathbf{z}_k) &= P_k^{\mathbf{z}_k}(\mathbf{z}_k)^\top \\ &= \mathbf{A}_k \mathbf{z}_k, \qquad \mathbf{A}_k = diag(a_k, a_k, b_k), \end{aligned}$$

which gives synchronization through proportional control terms. Another possible choice is to achieve synchronization through a combination of proportional and third degree terms, corresponding to

$$P_k(\mathbf{z}_k) = \frac{1}{2}\left(a_k z_{k1}^2 + a_k z_{k2}^2 + b_k z_{k3}^2 + a_k^* z_{k1}^4 + a_k^* z_{k2}^4 + b_k^* z_{k3}^4\right), \quad a_k, b_k, a_k^*, b_k^* > 0 \tag{3.63}$$

3.2.5.3 Choosing the activation functions

Since the only requirements to the activation functions $\sigma_1(\cdot)$,$\sigma_2(\cdot)$ are that they are continuously differentiable, monotonically decreasing and satisfy (3.17) (where it is noted that the last of the two properties in (3.17) can be relaxed), they can easily be tailored through e.g. sketching techniques. A lot of flexibility can, however, also be found in analytical functions, where the author identifies the following as a good starting point:

$$\sigma_k(s) = a^{-bs}, \qquad a > 1, b > 0 \tag{3.64}$$

3.2.5.4 Choosing the tuning matrix $\mathbf{L}_1$

The matrix $\mathbf{L}_1$ should be tuned so that the activation functions $\sigma_1(|\mathbf{z}|_{L_1}^2)$,$\sigma_2(|\mathbf{z}|_{L_1}^2)$ respond well to both position and orientation errors in $\mathbf{z}$. To illustrate the importance of this, consider a transversal straight line formation with three ships, where the desired inter-vessel spacing is equal to a. From a configuration where the vessels are perfectly synchronized, rotate one of the vessels an angle $-\frac{\pi}{2}[rad]$ while moving it so that the position of its local FRP remains synchronized with the other FRPs:

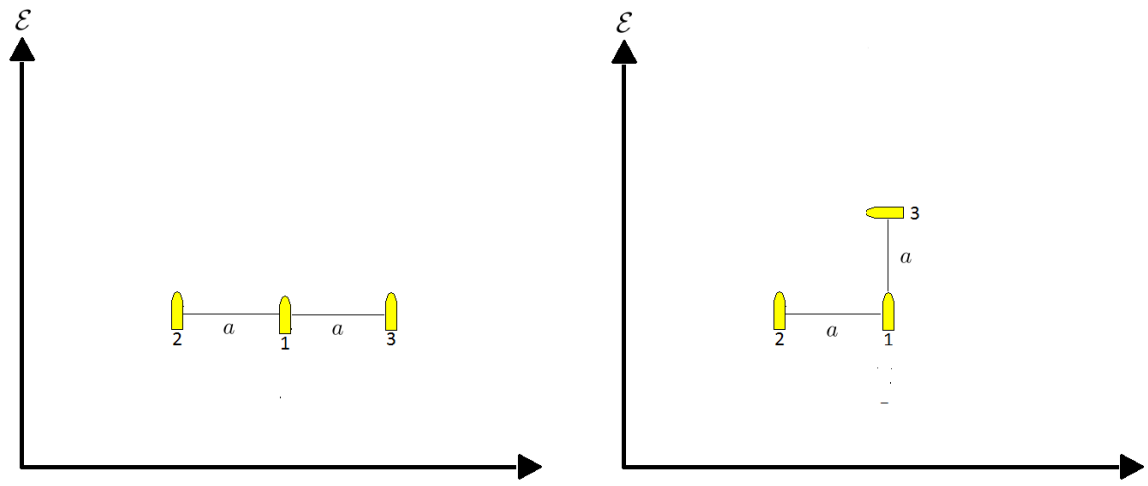

(a) Perfectly synchronized formation

(b) Configuration after moving vessel 3

Figure 3.2:

Despite the fact that the vessels are clearly out of formation in Figure 3.2(b), we have that $|\mathbf{z}|_\infty = \frac{\pi}{2}$, which is small in the context of position errors. If $\mathbf{L}_1$ is chosen as e.g. the identity matrix, the path following phase of an operation can consequently be initiated prematurely. To avoid such problems, the elements in $\mathbf{L}_1$ corresponding to orientation errors should be chosen considerably larger than those corresponding to position errors.

3.2.6 Simulations

To illustrate the main properties of the first design, three simulation cases will be shown. Three vessels with dynamics given in Appendix B are considered, where the desired formation structure (initially) is given by $\mathbf{l}_1 = col(0, 80, 0)$, $\mathbf{l}_2 = col(0, 0, 0)$, $\mathbf{l}_3 = col(0, -80, 0)$. This corresponds to a transversal line formation where a common heading angle is desired for all the ships. The communication topology is chosen according to two communication links, where Vessel 1 is the positive end of both links. Vessel 3 is set as the active leader. The parameterized path is chosen as an ellipse according to the parameterization

$$x_d(\theta) = R_1 \cos(k\theta)$$
$$y_d(\theta) = -R_2 \sin(k\theta),$$

with $R_1 = 800[m]$, $R_2 = 600[m]$, $k = \frac{1}{800}$. The control parameters are chosen as $\mathbf{K_{d}}_i = 10^4 \times diag(6.5, 6.5, 1300)$, $\mathbf{A} = diag(-0.02, -0.02, -0.03)$, $\mathbf{P} = \frac{3}{2} \times 10^{-2} \times diag(1, 1, 10^{-5})$, $\mathbf{L}_1 = diag(\mathbf{L}_0, \mathbf{L}_0)$, $\mathbf{L}_0 = diag(1, 1, 2500)$. The functions $P_k(\mathbf{z}_k)$ are chosen as in (3.62) with $a_k = 3000$, $b_k = 6 \times 10^5$, and $\sigma_1(s) = \sigma_2(s) = e^{-2.5s}$. Finally, $v_s(\theta, t)$ and $\mu(\theta)$ are chosen as $v_s(\theta, t) = \frac{U_d(t)}{\sqrt{x_d^\theta(\theta)^2 + x_y^\theta(\theta)^2}}$, $\mu(\theta) = \frac{1}{\sqrt{x_d^\theta(\theta)^2 + x_y^\theta(\theta)^2}}$, corresponding to a desired speed in $[m/s]$ along the path according to $U_d(t)$, and normalization of the gradient optimization with respect to the specific path parameterization. It is noted that no saturations have been implemented in the simulation model, so that the response times may be somewhat unrealistic.

3.2.6.1 Case 1

In the first simulation case, the function $\beta(|\mathbf{q}|^2_{L_2})$ is chosen according to $\beta(|\mathbf{q}|^2_{L_2}) \equiv 1$, so that $v_s(\theta, t)$ will drive $\mathbf{p}_d(\theta)$ along the path immediately after the vessels have synchronized. To illustrate the possibilities for formation reconfigurations and time-varying speed assignments along the path, the formation configuration vectors of the first and third vessels transition according to

$$\begin{aligned} \mathbf{l}_1^{start} &= col(0, 80, 0) \Rightarrow \mathbf{l}_1^{end} = col(0, 40, 0), \\ \mathbf{l}_3^{start} &= col(0, -80, 0) \Rightarrow \mathbf{l}_3^{end} = col(0, -40, 0), \end{aligned} \tag{3.65}$$

while the desired speed along the path transitions according to

$$U_d^{start} = 3[m/s] \Rightarrow U_d^{end} = 8[m/s]$$

during the simulation. This is done by feeding the new formation vectors and along-path speed as step inputs to third and second order reference filters at $t = 500[s]$ and $t = 600[s]$, respectively. The initial states of the system are chosen according to[6] $\boldsymbol{\eta}_{10} = col(80.3, 831, -\frac{7\pi}{30})$, $\boldsymbol{\eta}_{20} = col(27.6, 782.1, -\frac{\pi}{3})$, $\boldsymbol{\eta}_{30} = col(-94.3, 753.3, -\frac{\pi}{2})$, $\boldsymbol{\nu}_{10}, \boldsymbol{\nu}_{20}, \boldsymbol{\nu}_{30} = \mathbf{0}$, $\theta_0 = 4200$.

[6] The initial vessel positions where actually calculated by perturbing the vessels out of formation with respect to an FRF placed outside the path. This is the reason for the decimal-point precision.

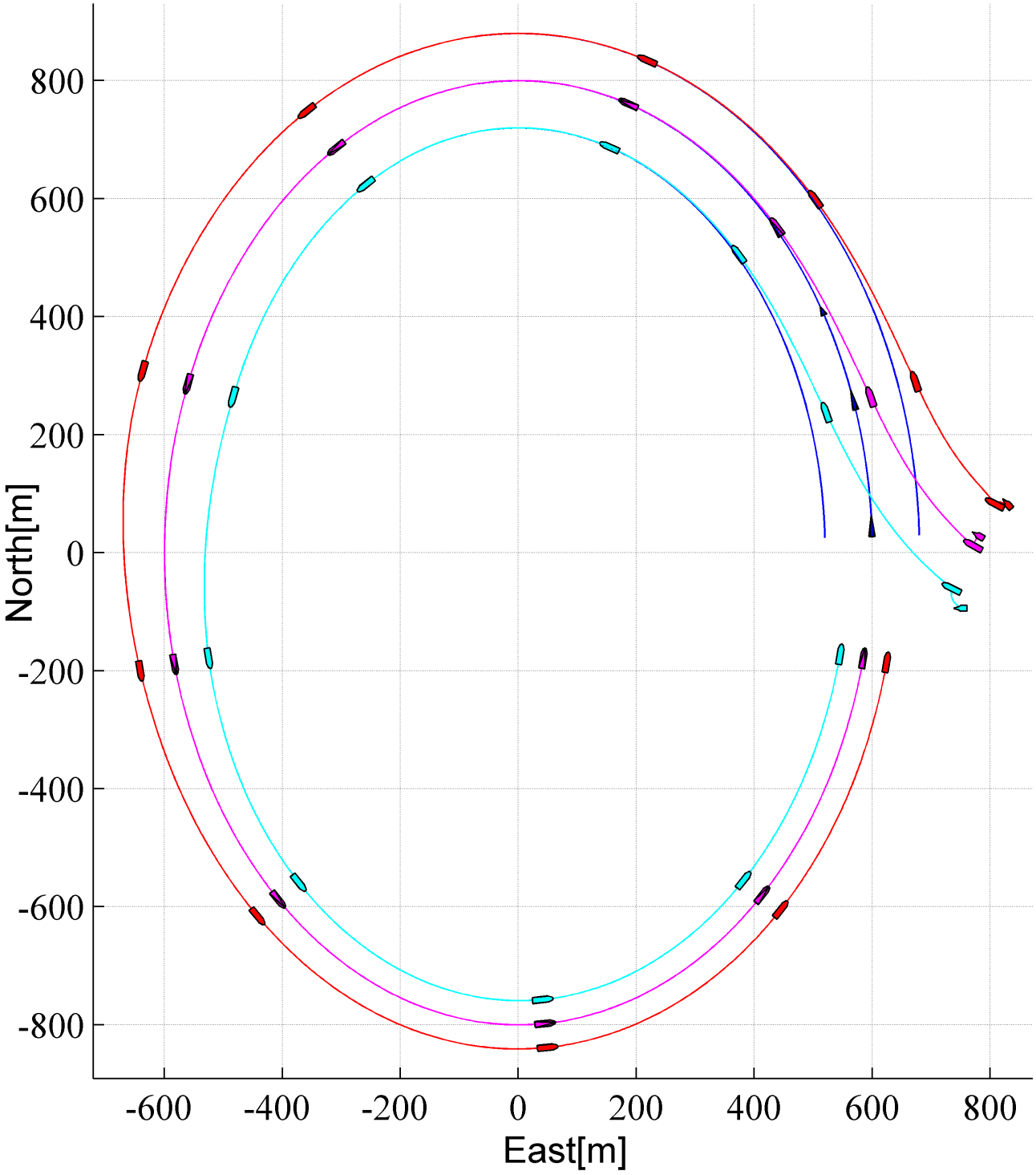

Figure 3.3: North-east position plot for the three vessels. The red, purple and blue ships correspond to vessels 1,2,3, respectively. The black arrow on the path indicates the position and orientation contained in $\mathbf{p}_d(\theta)$. Initial positions are indicated by smaller-sized ships and arrow.

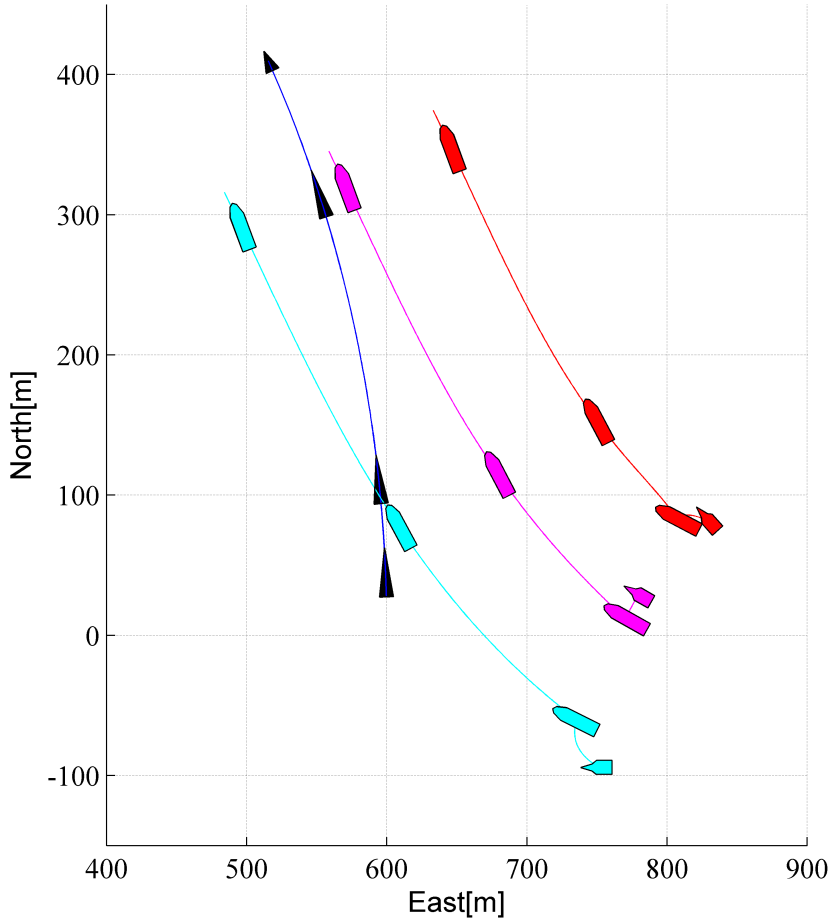

Figure 3.4: Close-up of coordination and transient motion towards the path.

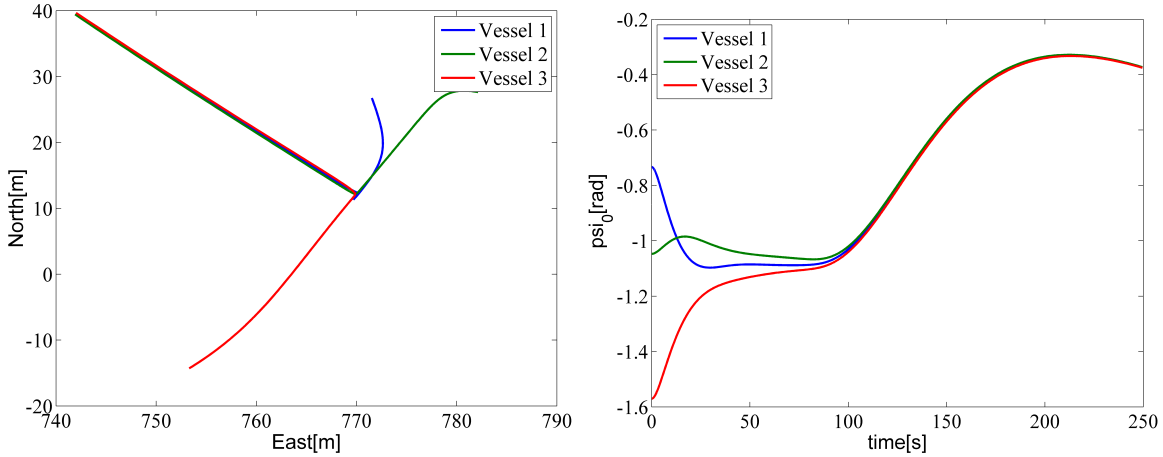

(a) North-east position plot of the position vectors $col(x_{0i}, y_{0i})$ contained in $\mathbf{x_{0}}_i$.

(b) Time series of ψ_{0i} for the three vessels.

Figure 3.5: Plot showing synchronization of $\mathbf{x_{0}}_i$, $i = 1, 2, 3$.

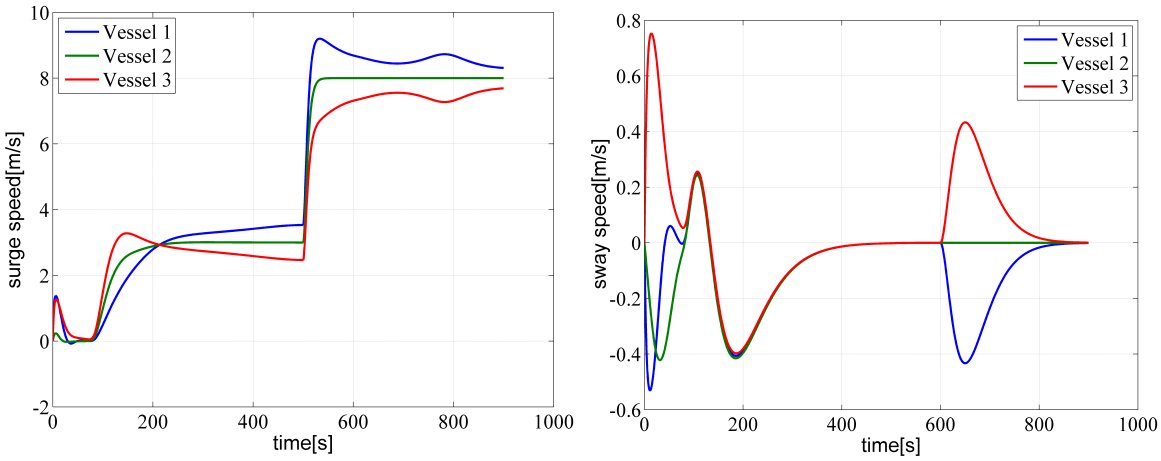

(a) Surge velocities

(b) Sway velocities

Figure 3.6: Surge and sway velocities for the three vessels

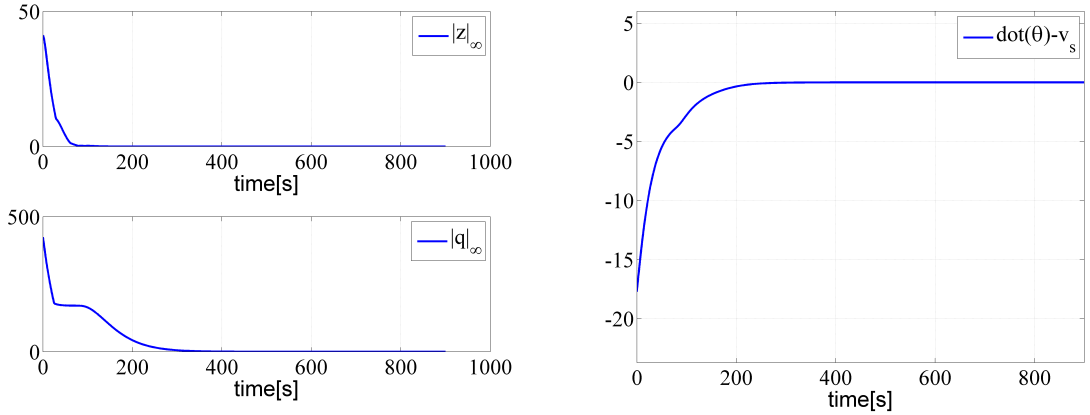

(a) Plot showing $|\mathbf{z}(t)|_\infty$ and $|\mathbf{q}(t)|_\infty$. At end of simulation, magnitudes are in the order of $O(10^{-6})$ and $O(10^{-5})$, respectively

(b) Plot showing $\left(\dot{\theta}(t) - v_s(\theta(t), t)\right)$. At end of simulation, magnitudes are in the order of $O(10^{-7})$.

Figure 3.7: Time series of error variables in the system

Figures 3.3 and 3.7 clearly demonstrate that the design is able to fulfill the group coordination and formation mission tasks of the formation control problem. Fulfillment of the dynamic assignment along the path is also seen from the surge speed of the second vessel in Figure 3.6(a), as the generalized position vector of the vessel coincides with $\mathbf{p}_d(\theta)$ on the path through the specified formation configuration. The prioritization between the coordination and path following tasks is evident in figures 3.5 and 3.7(a), where it is seen that the vessels synchronize before they start moving towards the path. During synchronization, $\mathbf{p}_d(\theta)$ moves to minimize $\mathbf{q}$, as seen in Figure 3.4 and the initial transient of $|\mathbf{q}(t)|_\infty$ in Figure 3.7(a). This is a result of the gradient optimization incorporated in the update law for θ.

When the desired formation structure starts narrowing in at $t = 600[s]$, it is seen from Figure 3.6(b) that vessels 1 and 3 start utilizing sway motion. The reason is that the desired relative heading angles in the formation configuration vectors satisfy $\psi_{ci}(t) \equiv 0$ as a result of the way the transition (3.65) was implemented. Consequently, the orientation of the vessels are restricted to the path-tangential direction whenever they are synchronized and follow the path, thereby forcing the vessels to use sway motion to reconfigure the formation. A more clever way to reconfigure the formation would be to dynamically adjust $\psi_{ci}(t)$ so that surge and yaw motion could be used exclusively. An algorithm for doing this is

developed for the third design in Section 3.4.5.2.

3.2.6.2 Case 2

To demonstrate the effect $\beta(|\mathbf{q}|^2_{L_2})$ has on the transient behavior in the path following phase, the function is now changed from $\beta(|\mathbf{q}|^2_{L_2}) \equiv 1$ to $\beta(|\mathbf{q}|^2_{L_2}) = e^{-0.025|\mathbf{q}|^2_{L_2}}$, thereby satisfying the properties of an activation function. The matrix $\mathbf{L}_2$ is chosen equal to the identity matrix, and the initial states of the system is chosen as $\boldsymbol{\eta}_{10} = col(88.9, 936, -\frac{13\pi}{30})$,$\boldsymbol{\eta}_{20} = col(41.6, 857.9, -\frac{\pi}{3})$,$\boldsymbol{\eta}_{30} = col(-57.9, 770.4, -\frac{\pi}{6})$, $\boldsymbol{\nu}_{10}, \boldsymbol{\nu}_{20}, \boldsymbol{\nu}_{30} = \mathbf{0}$, $\theta_0 = 4000$.

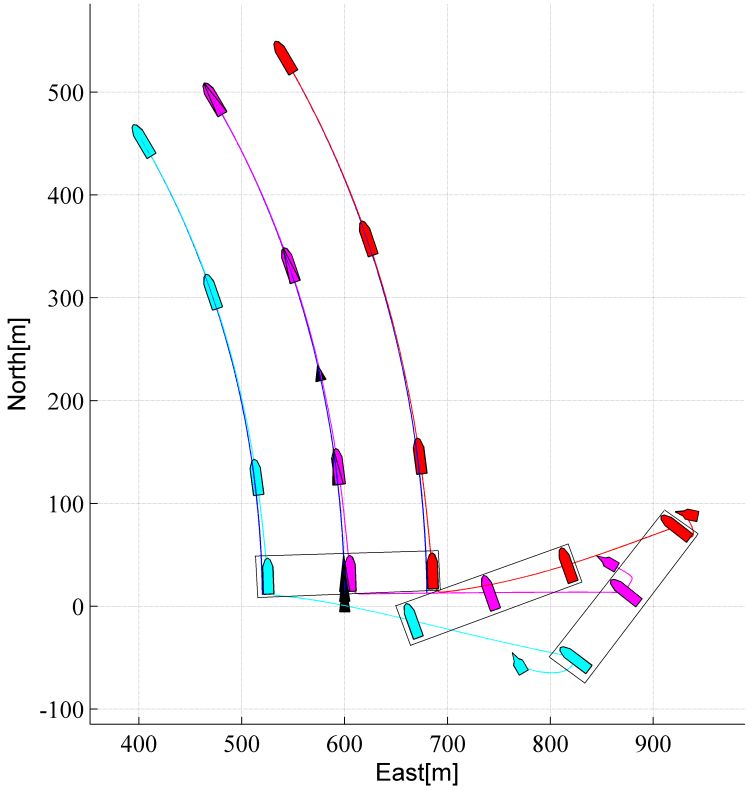

Figure 3.8: North-east position plot for the three vessels.

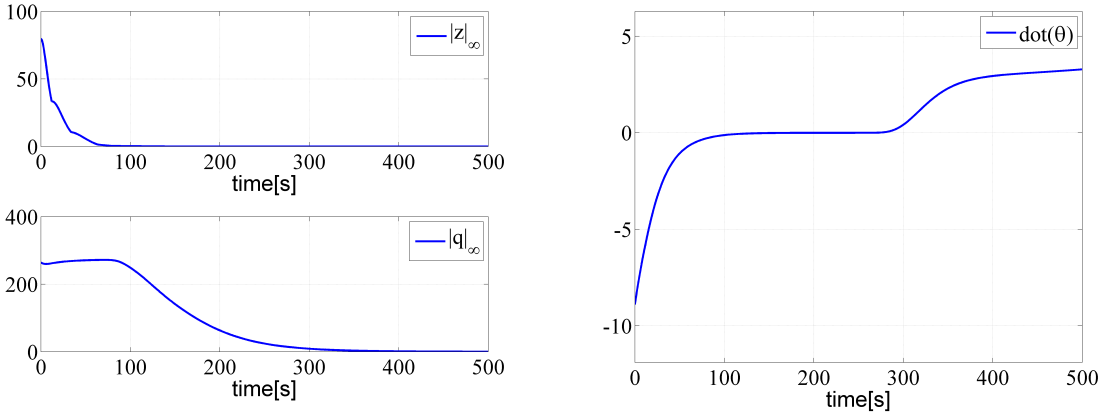

(a) Plot showing $|\mathbf{z}(t)|_\infty$ and $|\mathbf{q}(t)|_\infty$.

(b) Plot showing $\dot{\theta}(t)$.

Figure 3.9: Time series of relevant system states

As seen from Figure 3.9, $\dot{\theta}(t) \approx 0$ between $t \approx 100[s]$ and $t \approx 300[s]$, which corresponds with the time-interval where $|\mathbf{q}(t)|_\infty$ converges to zero. The effect is seen in Figure 3.8, where $\mathbf{p}_d(\theta)$ remains stationary while the formation converges to the path, after which forward motion is initiated. It is also seen that the formation uses significant sideways motion to converge to the path, which is quite inefficient. This illustrates one of the limitations of the first control design, as discussed in the next section.

3.2.6.3 Case 3

The feedback term $\sigma_1(|\mathbf{z}|^2_{L_1})\mathbf{A}\mathbf{q}(\mathbf{x_{01}}, \theta)$ in the common velocity input (3.19) is the mechanism that ensures path-convergence for the formation. As the common velocity input is given relative to the $\mathcal{E}$-frame, this corresponds to *independent* control of the position and orientation of the acting leaders FRP towards $\mathbf{p}_d(\theta)$. Although this is a valid approach from a theoretical point of view, it does not take into consideration that positive surge motion is preferred for marine surface vessels with regards to efficiency of motion. Situations can thus occur where the control system for each vessel induces considerable motion in sway (and in some extreme cases, motion in the negative surge direction) to steer the formation towards the path. A typical scenario where such problems can arise is when the vessels establish the formation far from the path. This will be demonstrated in the following. To illustrate another drawback of the design, which is sensitivity to initial heading angles, the initial configuration of the vessels are chosen to correspond perfectly to the desired line formation in terms of position, but where one of the vessels are rotated a little more than $90[deg]$ relative to the others. More specifically, the initial positions are chosen according to

$$\boldsymbol{\eta}_{i0} = col(0, 1350, -\frac{\pi}{3}) + \mathbf{R}\left(-\frac{\pi}{3}\right)(\mathbf{l}_i + \boldsymbol{\epsilon}_i),$$

where $\boldsymbol{\epsilon}_1 = col(0, 0, \frac{5\pi}{8})$, $\boldsymbol{\epsilon}_2 = \boldsymbol{\epsilon}_3 = \mathbf{0}$. The initial velocities are set as the zero-vector. It is noted that the function $\beta(|\mathbf{q}|^2_{L_2})$ has been reset to $\beta(|\mathbf{q}|^2_{L_2}) \equiv 1$ in the simulation.

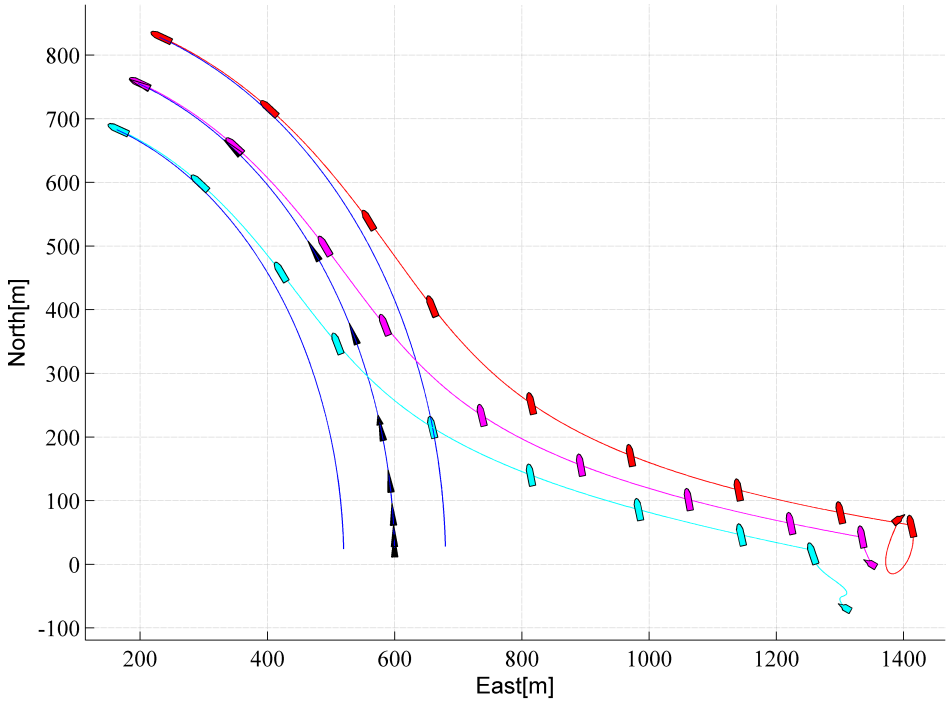

Figure 3.10: North-east position plot for the three vessels.

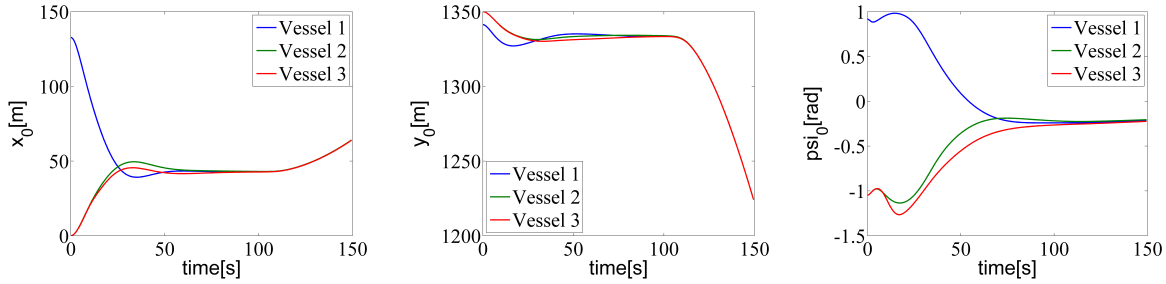

(a) Time series of x_{0i} for the three vessels..

(b) Time series of y_{0i} for the three vessels.

(c) Time series of ψ_{0i} for the three vessels.

Figure 3.11: Plot showing synchronization of $\mathbf{x_{0}}_i$, $i = 1, 2, 3$.

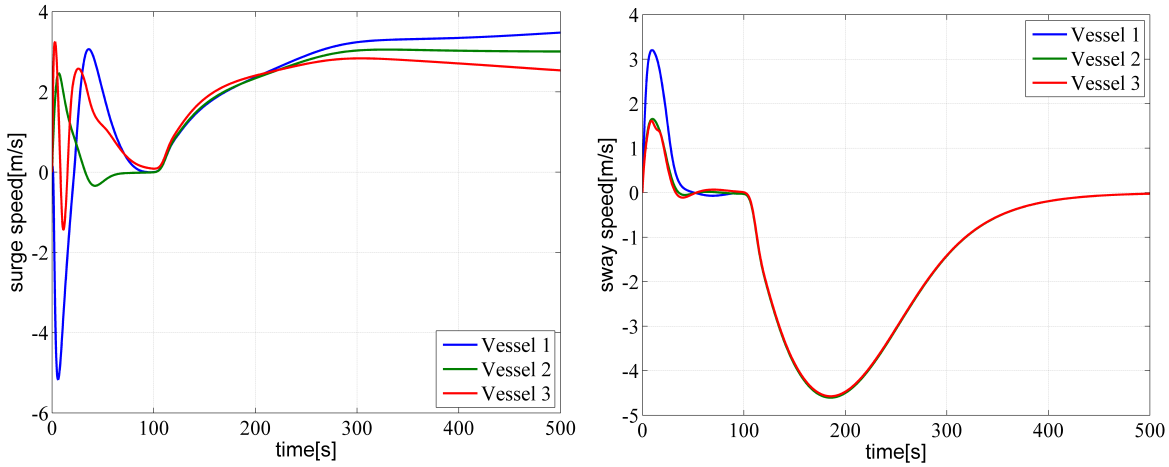

(a) Surge velocities

(b) Sway velocities

Figure 3.12: Surge and sway velocities for the three vessels

Although the vessels initially are very close to satisfying the specified formation configuration from a practical point of view, the control system interprets the situation otherwise. Since the position of a vessels local FRP is given relative to its body-fixed reference frame, the initial difference in heading angles introduce a large initial synchronization error between the *positions* of the FRPs (Figure 3.11(a)). As a result, the control system induces both translational and rotational motions to eliminate the errors, rather than just rotating Vessel 1 to obtain perfect synchronization. This causes a very inefficient and dangerous transient response (Figure 3.10). After the vessels have synchronized, the orientation of the formation turns out to be close to the targeted path-tangential orientation. The independent control of orientation and position in the common velocity input sees to that this orientation is reached quickly, without any consideration to where the formation is located with respect to the path. This results in sideways motion towards the path requiring significant sway velocities from the vessels (Figure 3.12(b)).

3.3 Design 2: Closed-loop guidance and control design

The design presented in Section 3.2 can be implemented and used directly as high-level controllers on real vessels. However, traveling in formation will typically only be one of many different operational modes for candidate vessels. Having a bank of separate controllers for every operational mode is not an optimal design choice, as it will require implementation of safe switching solutions, as well as more work with respect to integration and testing. A more intelligent way to approach vessel diversity is to follow the modular principles of the guidance, navigation, and control framework. The different operational modes are realized by designing a bank of guidance systems that will be used to feed reference signals to a separate control module. The control module contains a small bank of select controllers (e.g. one for dynamic positioning/low-speed maneuvering, one one for high-speed transit) that are designed to follow arbitrary reference signals, and that may have been optimized with regards to factors such as handling environmental disturbances and taking into account properties of the low-level actuator controllers. By following this modular approach, the operational performance can be increased, and costs can be reduced.

In this section, the first design will be adapted to the modular principles of guidance, navigation, and control. The approach will be to construct a *formation guidance system* that will generate reference signals for tracking controllers, also to be designed, that are used by the vessels to be controlled in formation. The motivation is to create a control system that addresses some of the shortcomings of the first design, specifically the required access to yaw accelerations and the omission of bias environmental forces in the vessel models.

3.3.1 Guidance system design aspects and approach

There are many aspects to consider when designing a guidance system. Arguably, the most important ones are related to feasibility of the generated reference signals and the behavior during vessel failures:

- **Feasibility:** A guidance system should generate reference signals that are feasible for the vessel to follow during normal operational conditions.
- **Robustness:** A guidance system should be robust in the sense that it is well behaved in the case of vessel failures. This involves slowing down or stopping the propagation of the reference signals sent to the control module when the vessel is incapable of following them, thereby avoiding aggravation of issues related to saturation of actuators, and enabling smooth recovery when the failure is remedied.

In order to obtain the desired properties, a closed-loop guidance system that utilizes feedback from relevant states of the vessels and that takes into account reigning maneuverability constraints, should be designed. Herein, a model-based approach will be used to achieve this. The guidance system for each vessel is chosen to consist of a dynamical model[7] of the vessel, corresponding to a *virtual vessel*, which is simulated in closed loop with an extension of the formation controllers designed in Section 3.2. The accelerations, velocities and positions that result from the simulations are then fed to tracking controllers as reference signals. Since the proposed guidance scheme is model-based, feasibility of the reference signals can be achieved implicitly through proper tuning of the guidance controllers (i.e. not overly aggressive), and explicitly by including saturations in the virtual vessel models.

Due to the desired closed-loop nature of the guidance system, the design will not be performed entirely separately from the design of the tracking controllers. Instead, preliminary designs will be established for each system, before they are combined to yield the final details.

[7]Depending on the available real-time computational resources, the vessel models used in the guidance systems may include all terms of the models presented in section 2.4.1, or only a subset of the terms (e.g. non-linear damping, centripetal/Coriolis forces are omitted).

3.3.2 Setup and problem statement

Consider r vessels to be controlled in formation, and assign to each of them a unique identifier in the index set $\mathcal{I} = \{1, \ldots, r\}$. A virtual vessel is assigned to each real vessel, and given the same identifier in the set $\mathcal{I}$. To avoid ambiguities, a subscript "v" is added to the position and velocity vectors (and their entries) and model matrices corresponding to the virtual vessels. The control design will be based on the following models for the real and virtual vessels:

$$\dot{\boldsymbol{\eta}}_i = \mathbf{R}(\psi_i)\boldsymbol{\nu}_i \tag{3.66a}$$

$$\mathbf{M}_i\dot{\boldsymbol{\nu}}_i + \mathbf{D}_i(\boldsymbol{\nu}_i)\boldsymbol{\nu}_i + \mathbf{C}_i(\boldsymbol{\nu}_i)\boldsymbol{\nu}_i = \boldsymbol{\tau}_i + \mathbf{R}(\psi_i)^\top \mathbf{b} \tag{3.66b}$$

$$\dot{\mathbf{b}} = \mathbf{0} \tag{3.66c}$$

$$\dot{\boldsymbol{\eta}}_{vi} = \mathbf{R}(\psi_{vi})\boldsymbol{\nu}_{vi} \tag{3.67a}$$

$$\mathbf{M}_{vi}\dot{\boldsymbol{\nu}}_{vi} + \mathbf{D}_{vi}(\boldsymbol{\nu}_{vi})\boldsymbol{\nu}_{vi} + \mathbf{C}_{vi}(\boldsymbol{\nu}_{vi})\boldsymbol{\nu}_{vi} = \boldsymbol{\tau}_{vi}, \tag{3.67b}$$

Note that the mass, damping, and centripetal/Coriolis matrices of the virtual vessels can be chosen differently from those of the corresponding real vessels. Moreover, note that the real vessels are assumed to be subjected to an unknown, constant environmental disturbance in the $\mathcal{E}$-frame.

Motivated by the design in Section 3.2, we define the FRPs of the virtual vessels as

$$\mathbf{x}_{0i}(\boldsymbol{\eta}_{vi}, t) := \boldsymbol{\eta}_{vi} - \mathbf{R}\left(\psi_{vi} - \psi_{ci}(t)\right)\mathbf{l}_i(t) \tag{3.68}$$

Without loss of generality, we assign the virtual vessel with index $i = 1$ as the acting leader in the formation guidance system. For a given path $\mathbf{p}_d(\theta)$ and a desired dynamic assignment $v_s(\theta, t)$ for $\dot{\theta}$, the problem of getting the real vessels to travel in formation and fulfill the path following mission objective can through this setup be formally stated by the following three control objectives:

Tracking objective: To develop tracking control laws for the real vessels to ensure that

$$\lim_{t\to\infty} |\boldsymbol{\eta}_i(t) - \boldsymbol{\eta}_{vi}(t)| = 0 \quad \forall i \in \mathcal{I} \tag{3.69}$$

Group coordination objective: To develop synchronization control laws for the virtual vessels to ensure that

$$\lim_{t\to\infty} |\mathbf{x}_{0i}(t) - \mathbf{x}_{0j}(t)| = 0 \quad \forall i, j \in \mathcal{I}. \tag{3.70}$$

Formation mission objective: To develop a maneuvering control law for the virtual vessels to ensure that

$$\lim_{t\to\infty} |\mathbf{x}_{01}(t) - \mathbf{p}_d(\theta(t))| = 0, \tag{3.71}$$

$$\lim_{t\to\infty} |\dot{\theta}(t) - v_s(\theta(t), t)| = 0. \tag{3.72}$$

3.3.3 Preliminary tracking control design

Adaptive tracking controllers that are to be used by the real vessels to achieve (3.69) will be the focus of this section. The method of vectorial backstepping forms the basis of the design procedure, which is performed in two steps.

Step 1: Define $\mathbf{s}_{1i}$ as the generalized position error between i'th real and virtual vessels expressed in the $\mathcal{B}$-frame of the real vessel, and $\mathbf{s}_{2i}$ as the velocity error between the i'th vessel and a virtual control input $\boldsymbol{\nu}_{ri}$:

$$\mathbf{s}_{1i} := \mathbf{R}(\psi_i)^\top(\boldsymbol{\eta}_i - \boldsymbol{\eta}_{vi}) \tag{3.73}$$

$$\mathbf{s}_{2i} := \boldsymbol{\nu}_i - \boldsymbol{\nu}_{ri} \tag{3.74}$$

Differentiating (3.73) with respect to time yields

$$\begin{aligned}\dot{\mathbf{s}}_{1i} &= \mathbf{S}^\top \mathbf{s}_{1i}\dot{\psi}_i + \mathbf{R}(\psi_i)^\top(\mathbf{R}(\psi_i)\boldsymbol{\nu}_i - \dot{\boldsymbol{\eta}}_{vi}) \\ &= \mathbf{S}^\top \mathbf{s}_{1i}\dot{\psi}_i + \boldsymbol{\nu}_i - \mathbf{R}(\psi_i)^\top\dot{\boldsymbol{\eta}}_{vi} \\ &= \mathbf{S}^\top \mathbf{s}_{1i}\dot{\psi}_i + \mathbf{s}_{2i} + \boldsymbol{\nu}_{ri} - \mathbf{R}(\psi_i)^\top\dot{\boldsymbol{\eta}}_{vi}\end{aligned}$$

Define the positive definite, radially unbounded CLF

$$V_{1i}(\mathbf{s}_{1i}) = \frac{1}{2}\mathbf{s}_{1i}^\top \mathbf{K}_{pi}\mathbf{s}_{1i}, \tag{3.75}$$

where

$$\mathbf{K}_{pi} = diag(k_p, k_p, k_\psi), \qquad k_p, k_\psi > 0 \tag{3.76}$$

Taking time derivatives yields

$$\begin{aligned}\dot{V}_{1i} &= \mathbf{s}_{1i}^\top \mathbf{K}_{pi}\mathbf{S}^\top \mathbf{s}_{1i}\dot{\psi}_i + \mathbf{s}_{1i}^\top \mathbf{K}_{pi}(\boldsymbol{\nu}_{ri} - \mathbf{R}(\psi_i)^\top\dot{\boldsymbol{\eta}}_{vi}) + \mathbf{s}_{1i}^\top \mathbf{K}_{pi}\mathbf{s}_{2i} \\ &= \mathbf{s}_{1i}^\top \mathbf{K}_{pi}(\boldsymbol{\nu}_{ri} - \mathbf{R}(\psi_i)^\top\dot{\boldsymbol{\eta}}_{vi}) + \mathbf{s}_{1i}^\top \mathbf{K}_{pi}\mathbf{s}_{2i},\end{aligned}$$

where the last step follows from $\mathbf{K}_{pi}\mathbf{S}^\top$ being skew-symmetric by the assignment (3.76). The virtual control input is chosen as

$$\boldsymbol{\nu}_{ri} = -\boldsymbol{\Lambda}_i\mathbf{s}_{1i} + \boldsymbol{\delta}_i, \tag{3.77}$$

where $\boldsymbol{\Lambda}_i$ is chosen to satisfy $\mathbf{K}_{pi}\boldsymbol{\Lambda}_i > 0$, and $\boldsymbol{\delta}_i$ is an auxiliary control input to be chosen in the final design (see Section 3.3.5). This yields

$$\dot{V}_{1i} = -\mathbf{s}_{1i}^\top \mathbf{K}_{pi}\boldsymbol{\Lambda}_i\mathbf{s}_{1i} + \mathbf{s}_{1i}^\top \mathbf{K}_{pi}(\boldsymbol{\delta}_i - \mathbf{R}(\psi_i)^\top\dot{\boldsymbol{\eta}}_{vi}) + \mathbf{s}_{1i}^\top \mathbf{K}_{pi}\mathbf{s}_{2i}$$

Step 2: From (3.74), the dynamics of $\mathbf{s}_{2i}$ becomes

$$\begin{aligned}\mathbf{M}_i\dot{\mathbf{s}}_{2i} &= \mathbf{M}_i\dot{\boldsymbol{\nu}}_i - \mathbf{M}_i\dot{\boldsymbol{\nu}}_{ri} \\ &= \boldsymbol{\tau}_i + \mathbf{R}(\psi_i)^\top\mathbf{b} - \mathbf{D}_i(\boldsymbol{\nu}_i)\mathbf{s}_{2i} - \mathbf{C}_i(\boldsymbol{\nu}_i)\mathbf{s}_{2i} - \mathbf{D}_i(\boldsymbol{\nu}_i)\boldsymbol{\nu}_{ri} - \mathbf{C}_i(\boldsymbol{\nu}_i)\boldsymbol{\nu}_{ri} - \mathbf{M}_i\dot{\boldsymbol{\nu}}_{ri}\end{aligned}$$

Define the second CLF

$$V_{2i}(\mathbf{s}_{1i}, \mathbf{s}_{2i}, \tilde{\mathbf{b}}_i) = V_{1i}(\mathbf{s}_{1i}) + \frac{1}{2}\mathbf{s}_{2i}^\top\mathbf{M}_i\mathbf{s}_{2i} + \frac{1}{2}\tilde{\mathbf{b}}_i^\top\boldsymbol{\Gamma}_i^{-1}\tilde{\mathbf{b}}_i, \tag{3.78}$$

where $\boldsymbol{\Gamma}_i = \boldsymbol{\Gamma}_i^\top > 0$, and $\tilde{\mathbf{b}}_i$ is the bias estimation error for the i'th tracking controller:

$$\tilde{\mathbf{b}}_i := \hat{\mathbf{b}}_i - \mathbf{b} \tag{3.79}$$

Taking time derivatives of (3.78) and using the fact that $\mathbf{C}_i(\boldsymbol{\nu}_i)$ is skew-symmetric yields

$$\begin{aligned}\dot{V}_{2i} = &-\mathbf{s}_{1i}^\top \mathbf{K}_{pi}\boldsymbol{\Lambda}_i\mathbf{s}_{1i} + \mathbf{s}_{1i}^\top \mathbf{K}_{pi}(\boldsymbol{\delta}_i - \mathbf{R}(\psi_i)^\top\dot{\boldsymbol{\eta}}_{vi}) + \tilde{\mathbf{b}}_i^\top\left(\boldsymbol{\Gamma}_i^{-1}\dot{\hat{\mathbf{b}}}_i - \mathbf{R}(\psi_i)\mathbf{s}_{2i}\right) \\ &+ \mathbf{s}_{2i}^\top\left(\mathbf{K}_{pi}\mathbf{s}_{1i} + \boldsymbol{\tau}_i + \mathbf{R}(\psi_i)^\top\hat{\mathbf{b}}_i - \mathbf{D}_i(\boldsymbol{\nu}_i)\mathbf{s}_{2i} - \mathbf{D}_i(\boldsymbol{\nu}_i)\boldsymbol{\nu}_{ri} - \mathbf{C}_i(\boldsymbol{\nu}_i)\boldsymbol{\nu}_{ri} - \mathbf{M}_i\dot{\boldsymbol{\nu}}_{ri}\right)\end{aligned}$$

Choosing

$$\boldsymbol{\tau}_i = -\mathbf{K}_{pi}\mathbf{s}_{1i} - \mathbf{R}(\psi_i)^\top\hat{\mathbf{b}}_i + \mathbf{D}_i(\boldsymbol{\nu}_i)\boldsymbol{\nu}_{ri} + \mathbf{C}_i(\boldsymbol{\nu}_i)\boldsymbol{\nu}_{ri} + \mathbf{M}_i\dot{\boldsymbol{\nu}}_{ri} - \mathbf{K}_{\mathbf{d}i}\mathbf{s}_{2i}, \quad \mathbf{K}_{\mathbf{d}i} = \mathbf{K}_{\mathbf{d}i}^\top > 0 \tag{3.80}$$

$$\dot{\hat{\mathbf{b}}}_i = \boldsymbol{\Gamma}_i\mathbf{R}(\psi_i)\mathbf{s}_{2i}, \tag{3.81}$$

yields

$$\begin{aligned}\dot{V}_{2i} &= -\mathbf{s}_{1i}^\top \mathbf{K}_{pi}\boldsymbol{\Lambda}_i\mathbf{s}_{1i} - \mathbf{s}_{2i}^\top(\mathbf{D}_i(\boldsymbol{\nu}_i) + \mathbf{K}_{\mathbf{d}i})\mathbf{s}_{2i} + \mathbf{s}_{1i}^\top \mathbf{K}_{pi}(\boldsymbol{\delta}_i - \mathbf{R}(\psi_i)^\top\dot{\boldsymbol{\eta}}_{vi}) \\ &\leq -\mathbf{s}_{1i}^\top \mathbf{K}_{pi}\boldsymbol{\Lambda}_i\mathbf{s}_{1i} - \mathbf{s}_{2i}^\top \mathbf{K}_{\mathbf{d}i}\mathbf{s}_{2i} + \mathbf{s}_{1i}^\top \mathbf{K}_{pi}(\boldsymbol{\delta}_i - \mathbf{R}(\psi_i)^\top\dot{\boldsymbol{\eta}}_{vi})\end{aligned}$$

3.3.4 Preliminary guidance control design

Define

$$\boldsymbol{\zeta}_i := \mathbf{R}(\psi_{vi})^\top (\dot{\mathbf{x}}_{\mathbf{0}i} - \mathbf{v}_d) \quad i \in \mathcal{I}, \tag{3.82}$$

where $\mathbf{x}_{\mathbf{0}i}$ is given in (3.68). Following the outline in Section 3.2.3.1, the closed-loop dynamics in $\boldsymbol{\zeta}_i$ become

$$\begin{aligned}\mathbf{M}_{vi}\dot{\boldsymbol{\zeta}}_i &= \mathbf{M}_{vi}\dot{\boldsymbol{\nu}}_{vi} - \mathbf{M}_{vi}\dot{\mathbf{f}}_{2i} \\ &= \boldsymbol{\tau}_{vi} - \mathbf{D}_{vi}(\boldsymbol{\nu}_{vi})\boldsymbol{\zeta}_i - \mathbf{C}_{vi}(\boldsymbol{\nu}_{vi})\boldsymbol{\zeta}_i - \mathbf{D}_{vi}(\boldsymbol{\nu}_{vi})\mathbf{f}_{2i} - \mathbf{C}_{vi}(\boldsymbol{\nu}_{vi})\mathbf{f}_{2i} - \mathbf{M}_{vi}\dot{\mathbf{f}}_{2i},\end{aligned}$$

where $\mathbf{f}_{2i}(\boldsymbol{\eta}_{vi}, \boldsymbol{\nu}_{vi}, \mathbf{v}_d, t) := \mathbf{R}(\psi_{vi})^\top(\dot{\mathbf{f}}_{1i} + \mathbf{v}_d)$, and $\mathbf{f}_{1i}(\boldsymbol{\eta}_{vi}, t) := \mathbf{R}\left(\psi_{vi} - \psi_{ci}(t)\right)\mathbf{l}_i(t)$. The virtual control laws are now chosen as an extension of the control laws in Section 3.2.3.1, where we include an extra auxiliary control input $\boldsymbol{\delta}_{vi}$ that is to be designed later:

$$\boldsymbol{\tau}_{vi} = \mathbf{D}_{vi}(\boldsymbol{\nu}_{vi})\mathbf{f}_{2i} + \mathbf{C}_{vi}(\boldsymbol{\nu}_{vi})\mathbf{f}_{2i} + \mathbf{M}_{vi}\dot{\mathbf{f}}_{2i} - \mathbf{K}_{\mathbf{d}vi}\boldsymbol{\zeta}_i + \boldsymbol{\alpha}_i + \boldsymbol{\delta}_{vi}, \quad \mathbf{K}_{\mathbf{d}vi} = \mathbf{K}_{\mathbf{d}vi}^\top > 0, \tag{3.83}$$

The motivation behind $\boldsymbol{\delta}_{vi}$ is to have an attraction term in the virtual vessel control law which will "pull" the virtual vessels towards their corresponding real vessels, thereby creating a closed-loop guidance system. Considering the positive definite, radially unbounded functions

$$S_{\zeta i}(\boldsymbol{\zeta}_i) := \frac{1}{2}\boldsymbol{\zeta}_i^\top \mathbf{M}_{vi}\boldsymbol{\zeta}_i, \tag{3.84}$$

and taking time derivatives yields (using the properties (2.7),(2.8))

$$\begin{aligned}\dot{S}_{\zeta i} &= \boldsymbol{\zeta}_i^\top \mathbf{M}_{vi}\dot{\boldsymbol{\zeta}}_i \\ &= \boldsymbol{\zeta}_i^\top \left(-\mathbf{D}_{vi}(\boldsymbol{\nu}_{vi})\boldsymbol{\zeta}_i - \mathbf{K}_{\mathbf{d}vi}\boldsymbol{\zeta}_i - \mathbf{C}_{vi}(\boldsymbol{\nu}_{vi})\boldsymbol{\zeta}_i + \boldsymbol{\alpha}_i + \boldsymbol{\delta}_{vi}\right) \\ &\leq -\boldsymbol{\zeta}_i^\top \mathbf{K}_{\mathbf{d}vi}\boldsymbol{\zeta}_i + \boldsymbol{\zeta}_i^\top \boldsymbol{\alpha}_i + \boldsymbol{\zeta}_i^\top \boldsymbol{\delta}_{vi},\end{aligned}$$

To finalize the preliminary guidance design, the synchronization terms $\boldsymbol{\alpha}_i$ and the maneuvering control laws $\mathbf{v}_d$ and $\dot{\theta}$ are chosen in accordance with Section 3.2.3.1:

$$\boldsymbol{\alpha}_i = -\mathbf{R}(\psi_{vi})^\top \left(\sum_{k=1}^{p} b_{ik}\boldsymbol{\gamma}_k(\mathbf{z}_k)\right) \quad i \in \mathcal{I}, \tag{3.85}$$

$$\mathbf{v}_d = \sigma_1(|\mathbf{z}|^2_{L_1})\mathbf{A}\mathbf{q}(\mathbf{x}_{\mathbf{0}1}, \theta) + \sigma_2(|\mathbf{z}|^2_{L_1})\beta(|\mathbf{q}|^2_{L_2})\mathbf{p}_d^\theta(\theta)v_s(\theta, t) \tag{3.86}$$

$$\dot{\theta} = \sigma_2(|\mathbf{z}|^2_{L_1})\beta(|\mathbf{q}|^2_{L_2})v_s(\theta, t) + 2\mu(\theta)\mathbf{q}^\top \mathbf{P}\mathbf{p}_d^\theta(\theta), \tag{3.87}$$

3.3.5 Final control design

In the following, all definitions from Section 3.2.4.1 are adopted, while some additional definitions are made:

$$\boldsymbol{\psi}_v := col(\psi_{v1}, \ldots, \psi_{vr}) \quad \in \mathbb{R}^r \tag{3.88}$$

$$\bar{\boldsymbol{\nu}}_v := col(\boldsymbol{\nu}_{v1}, \ldots, \boldsymbol{\nu}_{vr}) \quad \in \mathbb{R}^{3r} \tag{3.89}$$

$$\mathbf{s}_1 := col(\mathbf{s}_{1i}, \ldots, \mathbf{s}_{1r}) \quad \in \mathbb{R}^{3r} \tag{3.90}$$

$$\mathbf{s}_2 := col(\mathbf{s}_{2i}, \ldots, \mathbf{s}_{2r}) \quad \in \mathbb{R}^{3r} \tag{3.91}$$

$$\tilde{\mathbf{b}} := col(\tilde{\mathbf{b}}_1, \ldots, \tilde{\mathbf{b}}_r) \quad \in \mathbb{R}^{3r} \tag{3.92}$$

Consider the positive definite, radially unbounded CLF

$$V(\mathbf{z}, \boldsymbol{\zeta}, \mathbf{s}_1, \mathbf{s}_2, \tilde{\mathbf{b}}) := \sum_{k=1}^{p} P_k(\mathbf{z}_k) + \sum_{i=1}^{r} S_{\zeta_i}(\boldsymbol{\zeta}_i) + \sum_{i=1}^{r} V_{2i}(\mathbf{s}_{1i}, \mathbf{s}_{2i}, \tilde{\mathbf{b}}_i), \tag{3.93}$$

Taking time derivatives yields

$$\begin{aligned}\dot{V} &= \left[\frac{\partial}{\partial \mathbf{z}}\left(\sum_{k=1}^{p} P_k(\mathbf{z}_k)\right)\right]\dot{\mathbf{z}} + \sum_{i=1}^{r}(\dot{S}_{\zeta,i} + \dot{V}_{2i}) \\ &\leq \boldsymbol{\gamma}(\mathbf{z})^\top(\mathbf{B}^\top \otimes \mathbf{I}_3)\bar{\mathbf{R}}(\boldsymbol{\psi}_v)\boldsymbol{\zeta} \\ &+ \sum_{i=1}^{r}\left(-\boldsymbol{\zeta}_i^\top \mathbf{K}_{\mathbf{d}vi}\boldsymbol{\zeta}_i + \boldsymbol{\zeta}_i^\top \boldsymbol{\alpha}_i + \boldsymbol{\zeta}_i^\top \boldsymbol{\delta}_{vi} - \mathbf{s}_{1i}^\top \mathbf{K}_{pi}\boldsymbol{\Lambda}_i\mathbf{s}_{1i} - \mathbf{s}_{2i}^\top \mathbf{K}_{\mathbf{d}i}\mathbf{s}_{2i} + \mathbf{s}_{1i}^\top \mathbf{K}_{pi}(\boldsymbol{\delta}_i - \mathbf{R}(\psi_i)^\top \dot{\boldsymbol{\eta}}_{vi})\right) \\ &= -\boldsymbol{\alpha}^\top\boldsymbol{\zeta} + \boldsymbol{\zeta}^\top\boldsymbol{\alpha} + \sum_{i=1}^{r}\left(-\boldsymbol{\zeta}_i^\top \mathbf{K}_{\mathbf{d}vi}\boldsymbol{\zeta}_i + \boldsymbol{\zeta}_i^\top \boldsymbol{\delta}_{vi} - \mathbf{s}_{1i}^\top \mathbf{K}_{pi}\boldsymbol{\Lambda}_i\mathbf{s}_{1i} - \mathbf{s}_{2i}^\top \mathbf{K}_{\mathbf{d}i}\mathbf{s}_{2i} + \mathbf{s}_{1i}^\top \mathbf{K}_{pi}(\boldsymbol{\delta}_i - \mathbf{R}(\psi_i)^\top \dot{\boldsymbol{\eta}}_{vi})\right)\end{aligned}$$

Since $\boldsymbol{\zeta}_i = \mathbf{R}(\psi_{vi})^\top(\dot{\mathbf{x}}_{\mathbf{0}i} - \mathbf{v}_d) = \mathbf{R}(\psi_{vi})^\top\left(\dot{\boldsymbol{\eta}}_{vi} - \dot{\mathbf{f}}_{1i} - \mathbf{v}_d\right)$, we get that

$$\dot{V} \leq \sum_{i=1}^{r}\left(-\boldsymbol{\zeta}_i^\top \mathbf{K}_{\mathbf{d}vi}\boldsymbol{\zeta}_i - \mathbf{s}_{1i}^\top \mathbf{K}_{pi}\boldsymbol{\Lambda}_i\mathbf{s}_{1i} - \mathbf{s}_{2i}^\top \mathbf{K}_{\mathbf{d}i}\mathbf{s}_{2i} + \boldsymbol{\delta}_{vi}^\top \mathbf{R}(\psi_{vi})^\top\left(\dot{\boldsymbol{\eta}}_{vi} - \dot{\mathbf{f}}_{1i} - \mathbf{v}_d\right) + \mathbf{s}_{1i}^\top \mathbf{K}_{pi}(\boldsymbol{\delta}_i - \mathbf{R}(\psi_i)^\top \dot{\boldsymbol{\eta}}_{vi})\right)$$

Choosing

$$\boldsymbol{\delta}_{vi} = \mathbf{R}(\psi_{vi})^\top \mathbf{R}(\psi_i)\mathbf{K}_{pi}\mathbf{s}_{1i}, \tag{3.94}$$

$$\boldsymbol{\delta}_i = \mathbf{R}(\psi_i)^\top\left(\dot{\mathbf{f}}_{1i} + \mathbf{v}_d\right), \tag{3.95}$$

finally yields

$$\dot{V} \leq \sum_{i=1}^{r}\left(-\boldsymbol{\zeta}_i^\top \mathbf{K}_{\mathbf{d}vi}\boldsymbol{\zeta}_i - \mathbf{s}_{1i}^\top \mathbf{K}_{pi}\boldsymbol{\Lambda}_i\mathbf{s}_{1i} - \mathbf{s}_{2i}^\top \mathbf{K}_{\mathbf{d}i}\mathbf{s}_{2i}\right) \leq 0 \tag{3.96}$$

From (3.94) and the definition of $\mathbf{s}_{1i}$ in (3.73), it is seen that the guidance control law for each virtual vessel now contains a proportional term pulling it towards the corresponding real vessel. Compared to the proportional terms in the tracking control laws, the magnitudes of the forces/moments are the same, while the directions are reversed in the $\mathcal{E}$-frame. In the case of a failure on one of the real vessels, the proportional guidance control term will ensure that the corresponding virtual vessel does not drift far away. However, as the other terms in the guidance control law try to get the virtual vessel into formation with the other virtual vessels, there will be a "battle" between the terms. The solution is thus not the most elegant way to achieve guidance system robustness, but it is certainly better than an open-loop solution. It is also noted that in a traditional backstepping tracking control design, $\boldsymbol{\delta}_i$ would have been chosen as $\boldsymbol{\delta}_i = \mathbf{R}(\psi_i)^\top \dot{\boldsymbol{\eta}}_{vi}$, corresponding to feedforward from the velocity of the target to be followed. The choice (3.95) instead involves feedforward from the desired velocity of the virtual ships, which they achieve when coordinated.

3.3.6 Stability analysis

3.3.6.1 Closed-loop system

In terms of the error variables in the system, the closed-loop dynamics are given by

$$\mathbf{M}_{vi}\dot{\boldsymbol{\zeta}}_i = -(\mathbf{C}_{vi}(\boldsymbol{\nu}_{vi}) + \mathbf{D}_{vi}(\boldsymbol{\nu}_{vi}) + \mathbf{K}_{\mathbf{d}vi})\boldsymbol{\zeta}_i + \boldsymbol{\alpha}_i(\mathbf{z}, \psi_{vi}) + \mathbf{R}(\psi_{vi})^\top \mathbf{R}(\psi_i)\mathbf{K}_{pi}\mathbf{s}_{1i}, \quad i \in \mathcal{I} \tag{3.97}$$

$$\dot{\mathbf{z}} = (\mathbf{B}^\top \otimes \mathbf{I}_3)\bar{\mathbf{R}}(\boldsymbol{\psi}_v)\boldsymbol{\zeta} \tag{3.98}$$

$$\dot{\mathbf{q}} = \sigma_1(|\mathbf{z}|^2_{L_1})\mathbf{A}\mathbf{q} - 2\mu(\theta)\mathbf{p}_d^\theta(\theta)\mathbf{q}^\top \mathbf{P}\mathbf{p}_d^\theta(\theta) + \mathbf{R}(\psi_{v1})\boldsymbol{\zeta}_1 \tag{3.99}$$

$$\dot{\theta} = \sigma_2(|\mathbf{z}|^2_{L_1})\beta(|\mathbf{q}|^2_{L_2})v_s(\theta, t) + 2\mu(\theta)\mathbf{q}^\top \mathbf{P}\mathbf{p}_d^\theta(\theta). \tag{3.100}$$

$$\dot{\mathbf{s}}_{1i} = \mathbf{S}^\top \mathbf{s}_{1i}(\mathbf{e}^\top \boldsymbol{\nu}_i) - \boldsymbol{\Lambda}_i\mathbf{s}_{1i} + \mathbf{s}_{2i} - \mathbf{R}(\psi_i)^\top \mathbf{R}(\psi_{vi})\boldsymbol{\zeta}_i, \quad \mathbf{e} = col(0, 0, 1), \quad i \in \mathcal{I} \tag{3.101}$$

$$\mathbf{M}_i\dot{\mathbf{s}}_{2i} = -\mathbf{K}_{pi}\mathbf{s}_{1i} - \mathbf{R}(\psi_i)^\top \tilde{\mathbf{b}}_i - (\mathbf{D}_i(\boldsymbol{\nu}_i) + \mathbf{C}_i(\boldsymbol{\nu}_i) + \mathbf{K}_{\mathbf{d}i})\mathbf{s}_{2i}, \quad i \in \mathcal{I} \tag{3.102}$$

$$\dot{\tilde{\mathbf{b}}}_i = \mathbf{\Gamma}_i \mathbf{R}(\psi_i)\mathbf{s}_{2i} \tag{3.103}$$

Following the outline in Section 3.2.4.2, ψ_{vi} and $\boldsymbol{\nu}_{vi}$ can be expressed as

$$\psi_{vi} = \mathbf{e}^\top \left(\mathbf{K}_{i1}\mathbf{z} + \mathbf{q} + \mathbf{p_d}(\theta)\right) + \psi_{ci}(t) \tag{3.104}$$

$$\boldsymbol{\nu}_{vi} = (\mathbf{I}_3 - \mathbf{R}(\psi_{ci}(t))^\top \mathbf{Sl}_i(t)\mathbf{e}^\top)^{-1} \left(\boldsymbol{\zeta}_i + \mathbf{R}(\psi_{vi})^\top \mathbf{v}_d + \mathbf{R}(\psi_{ci}(t))^\top \left(\dot{\mathbf{l}}_i(t) - \mathbf{Sl}_i(t)\dot{\psi}_{ci}(t)\right)\right) \tag{3.105}$$

Furthermore, we have that ψ_i and $\boldsymbol{\nu}_i$ can be expressed as

$$\begin{aligned}\psi_i &= \mathbf{e}^\top \mathbf{s}_{1i} + \psi_{vi} \\ &= \mathbf{e}^\top \left(\mathbf{s}_{1i} + \mathbf{K}_{i1}\mathbf{z} + \mathbf{q} + \mathbf{p_d}(\theta)\right) + \psi_{ci}(t)\end{aligned} \tag{3.106}$$

$$\begin{aligned}\boldsymbol{\nu}_i &= \mathbf{s}_{2i} - \mathbf{\Lambda}_i \mathbf{s}_{1i} + \mathbf{R}(\psi_i)^\top \left(\dot{\mathbf{f}}_{1i} + \mathbf{v}_d\right) \\ &= \mathbf{s}_{2i} - \mathbf{\Lambda}_i \mathbf{s}_{1i} + \mathbf{R}(\psi_i)^\top \left(\mathbf{v}_d + \mathbf{R}(\psi_{vi} - \psi_{ci}(t)) \left(\dot{\mathbf{l}}_i(t) + \mathbf{Sl}_i(t)(\mathbf{e}^\top \boldsymbol{\nu}_{vi} - \dot{\psi}_{ci}(t))\right)\right)\end{aligned} \tag{3.107}$$

By defining

$$\boldsymbol{\chi} := col(\mathbf{z}, \boldsymbol{\zeta}, \mathbf{q}, \mathbf{s}_1, \mathbf{s}_2, \tilde{\mathbf{b}}) \quad \in \mathbb{R}^{3p+12r+3}, \tag{3.108}$$

the closed-loop system can thus be written compactly as

$$\begin{bmatrix}\dot{\boldsymbol{\chi}} \\ \dot{\theta}\end{bmatrix} = \begin{bmatrix}\mathbf{f}_\chi(t, \boldsymbol{\chi}, \theta) \\ f_\theta(t, \boldsymbol{\chi}, \theta)\end{bmatrix} =: \mathbf{F}(t, \boldsymbol{\chi}, \theta). \tag{3.109}$$

The main result for the second design is given in Theorem 2.

Theorem 2. *Under assumptions 1 – 4, the tracking control laws* (3.80)–(3.81) *and guidance control laws* (3.83),(3.86),(3.87) *render the closed-loop system* (3.109) *forward complete and the set* $\mathcal{A} = \{(\boldsymbol{\chi}, \theta, t) : \ \boldsymbol{\chi} = 0\}$ *UGAS. This solves the control objectives* (3.69)–(3.72).

3.3.6.2 Proof of Theorem 2

Forward Completeness: Consider the positive definite, radially unbounded function $V(\mathbf{z}, \boldsymbol{\zeta}, \mathbf{s}_1, \mathbf{s}_2, \tilde{\mathbf{b}})$ defined in (3.93). By Khalil (2002; Lemma 4.3) there exists class-$\mathcal{K}_\infty$ functions ϕ_1, ϕ_2 such that

$$\phi_1(|(\mathbf{z}, \boldsymbol{\zeta}, \mathbf{s}_1, \mathbf{s}_2, \tilde{\mathbf{b}})|) \leq V(\mathbf{z}, \boldsymbol{\zeta}, \mathbf{s}_1, \mathbf{s}_2, \tilde{\mathbf{b}}) \leq \phi_2(|(\mathbf{z}, \boldsymbol{\zeta}, \mathbf{s}_1, \mathbf{s}_2, \tilde{\mathbf{b}})|). \tag{3.110}$$

Since $\dot{V} \leq 0$ (see (3.96)), this implies for all t in the maximum interval of existence $[t_0, T)$, that $V(t) \leq V(t_0)$. Combining this with (3.110) yields

$$\left|\left(\mathbf{z}(t), \boldsymbol{\zeta}(t), \mathbf{s}_1(t), \mathbf{s}_2(t), \tilde{\mathbf{b}}(t)\right)\right| \leq \phi_3\left(\left|\left(\mathbf{z}(t_0), \boldsymbol{\zeta}(t_0), \mathbf{s}_1(t_0), \mathbf{s}_2(t_0), \tilde{\mathbf{b}}(t_0)\right)\right|\right) \tag{3.111}$$

where $\phi_3(\cdot) := \phi_1^{-1} \circ \phi_2(\cdot) \in \mathcal{K}_\infty$. Defining

$$\epsilon_1 := \sigma_1\left(||\mathbf{L}_1|| \phi_3\left(\left|\left(\mathbf{z}(t_0), \boldsymbol{\zeta}(t_0), \mathbf{s}_1(t_0), \mathbf{s}_2(t_0), \tilde{\mathbf{b}}(t_0)\right)\right|\right)^2\right), \tag{3.112}$$

$$\epsilon_2 := \frac{4||\mathbf{P}|| \phi_3\left(\left|\left(\mathbf{z}(t_0), \boldsymbol{\zeta}(t_0), \mathbf{s}_1(t_0), \mathbf{s}_2(t_0), \tilde{\mathbf{b}}(t_0)\right)\right|\right)}{\epsilon_1 \lambda_{min,Q}}, \tag{3.113}$$

and following the outline in Section 3.2.4.3 yields the following bounds on $|\mathbf{q}(t)|$ over $[t_0, T)$:

$$|\mathbf{q}(t)| \leq \sqrt{\frac{\lambda_{max,P}}{\lambda_{min,P}}} \left(|\mathbf{q}(t_0)| + \epsilon_2\right) \tag{3.114}$$

Combining this with assumptions 3 and 4, a uniform upper bound for $|\dot{\theta}|$ is achieved over $[t_0, T)$, which shows that there cannot be a finite escape time for the system (3.109), i.e. $T = +\infty$. By a locally

Lipschitz property of the closed-loop system, it is concluded that the solutions $\theta(t)$ and $\boldsymbol{\chi}(t)$ exist and are continuous functions over $[t_0, \infty)$.

As in the proof of Theorem 1, θ will from now on be treated as an external input, continuous in time, that enters the dynamics of $\boldsymbol{\chi}$ Stability of the origin of

$$\dot{\boldsymbol{\chi}} = \mathbf{f}(t, \boldsymbol{\chi}), \tag{3.115}$$

where $\mathbf{f}(t, \boldsymbol{\chi}) := \mathbf{f}_\chi(t, \boldsymbol{\chi}, \theta(t))$, will be investigated by the means of Theorem A.1.

Uniform Global Stability: By forward completeness of the closed-loop system, the bounds in (3.111) and (3.114) hold $\forall t \geq t_0$. Since

$$\begin{aligned}
|\boldsymbol{\chi}| &\leq |\big(\mathbf{z}, \boldsymbol{\zeta}, \mathbf{s}_1, \mathbf{s}_2, \tilde{\mathbf{b}}\big)| + |\mathbf{q}|, \\
|\boldsymbol{\chi}| &\geq |\big(\mathbf{z}, \boldsymbol{\zeta}, \mathbf{s}_1, \mathbf{s}_2, \tilde{\mathbf{b}}\big)|, \\
|\boldsymbol{\chi}| &\geq |\mathbf{q}|,
\end{aligned}$$

we have that

$$\begin{aligned}
&|\boldsymbol{\chi}(t)| \leq \phi_3\left(\left|\big(\mathbf{z}(t_0), \boldsymbol{\zeta}(t_0), \mathbf{s}_1(t_0), \mathbf{s}_2(t_0), \tilde{\mathbf{b}}(t_0)\big)\right|\right) + \\
&\sqrt{\frac{\lambda_{max,P}}{\lambda_{min,P}}}\left[|\mathbf{q}(t_0)| + \frac{4||\mathbf{P}||\phi_3\left(\left|\big(\mathbf{z}(t_0), \boldsymbol{\zeta}(t_0), \mathbf{s}_1(t_0), \mathbf{s}_2(t_0), \tilde{\mathbf{b}}(t_0)\big)\right|\right)}{\epsilon_1 \lambda_{min,Q}}\right] \\
&\leq \phi_3\left(|\boldsymbol{\chi}(t_0)|\right) + \sqrt{\frac{\lambda_{max,P}}{\lambda_{min,P}}}\left[|\boldsymbol{\chi}(t_0)| + \frac{4||\mathbf{P}||\phi_3\left(|\boldsymbol{\chi}(t_0)|\right)}{\lambda_{min,Q}\sigma_1\left(||\mathbf{L}_1||\phi_3\left(|\boldsymbol{\chi}(t_0)|\right)^2\right)}\right] \\
&=: \phi_4(|\boldsymbol{\chi}(t_0)|)
\end{aligned}$$

Since $\phi_3(\cdot) \in \mathcal{K}^\infty$ and $\sigma_1(\cdot)$ is monotonically decreasing and strictly positive, we have that $\phi_4(\cdot) \in \mathcal{K}^\infty$, which shows that the origin is UGS.

Uniform Global Asymptotic Stability: Define

$$V_0(\boldsymbol{\chi}) := V(\mathbf{z}, \boldsymbol{\zeta}, \mathbf{s}_1, \mathbf{s}_2, \tilde{\mathbf{b}}), \tag{3.116}$$

From (3.96), we have that

$$\dot{V}_0(t, \boldsymbol{\chi}) \leq \sum_{i=1}^{r}\left(-\boldsymbol{\zeta}_i^\top \mathbf{K}_{\mathbf{d}vi}\boldsymbol{\zeta}_i - \mathbf{s}_{1i}^\top \mathbf{K}_{pi}\boldsymbol{\Lambda}_i\mathbf{s}_{1i} - \mathbf{s}_{2i}^\top \mathbf{K}_{\mathbf{d}i}\mathbf{s}_{2i}\right) =: Y_0(\boldsymbol{\chi}) \leq 0 \quad \forall \boldsymbol{\chi}, \tag{3.117}$$

where it is noted that $Y_0(\boldsymbol{\chi}) = 0$ implies $\boldsymbol{\zeta}, \mathbf{s}_1, \mathbf{s}_2 = \mathbf{0}$. Now, define the first auxiliary function

$$V_1(t, \boldsymbol{\chi}) := \mathbf{z}^\top (\mathbf{B} \otimes \mathbf{I}_3)^\ddagger \bar{\mathbf{R}}(\boldsymbol{\psi}_v)\bar{\mathbf{M}}_v\boldsymbol{\zeta}, \tag{3.118}$$

where

$$\bar{\mathbf{M}}_v := diag(\mathbf{M}_{v1}, \ldots, \mathbf{M}_{vr}) \quad \in \mathbb{R}^{3r\times 3r}, \tag{3.119}$$

$(\mathbf{B} \otimes \mathbf{I}_3)^\ddagger \in \mathbb{R}^{3p\times 3r}$ is the Moore-Penrose pseudo-inverse of $(\mathbf{B} \otimes \mathbf{I}_3)$ satisfying

$$(\mathbf{B} \otimes \mathbf{I}_3)(\mathbf{B} \otimes \mathbf{I}_3)^\ddagger(\mathbf{B} \otimes \mathbf{I}_3) = (\mathbf{B} \otimes \mathbf{I}_3),$$

and it is once again noted that all definitions from Section 3.2.4.1 have been adopted. Differentiating (3.118) with respect to time yields

$$\begin{aligned}
\dot{V}_1(t, \boldsymbol{\chi}) &= \boldsymbol{\zeta}^\top \bar{\mathbf{R}}(\boldsymbol{\psi}_v)^\top (\mathbf{B} \otimes \mathbf{I}_3)(\mathbf{B} \otimes \mathbf{I}_3)^\ddagger \bar{\mathbf{R}}(\boldsymbol{\psi}_v)\bar{\mathbf{M}}_v\boldsymbol{\zeta} \\
&\quad + \mathbf{z}^\top (\mathbf{B} \otimes \mathbf{I}_3)^\ddagger\big(\dot{\bar{\mathbf{R}}}(\boldsymbol{\psi}_v, \bar{\boldsymbol{\nu}}_v)\bar{\mathbf{M}}_v\boldsymbol{\zeta} + \bar{\mathbf{R}}(\boldsymbol{\psi}_v)\bar{\mathbf{M}}_v\dot{\boldsymbol{\zeta}}\big) \\
&=: Y_1(\boldsymbol{\chi}, \boldsymbol{\phi}(t, \boldsymbol{\chi}))
\end{aligned}$$

Here, all time dependent terms of $\dot{V}_1(t,\boldsymbol{\chi})$ are included in a function $\boldsymbol{\phi}(t,\boldsymbol{\chi})$ that will be specified later on. Evaluating $Y_1(\boldsymbol{\chi},\boldsymbol{\phi}(t,\boldsymbol{\chi}))$ at $\boldsymbol{\zeta},\mathbf{s}_1,\mathbf{s}_2=\mathbf{0}$ and using (3.97) yields

$$\begin{aligned}
Y_1(\boldsymbol{\chi},\boldsymbol{\phi}(t,\boldsymbol{\chi}))\Big|_{\boldsymbol{\zeta},\mathbf{s}_1,\mathbf{s}_2=0} &= \mathbf{z}^\top(\mathbf{B}\otimes\mathbf{I}_3)^\ddagger\bar{\mathbf{R}}(\boldsymbol{\psi}_v)(\bar{\mathbf{M}}_v\dot{\boldsymbol{\zeta}})\Big|_{\boldsymbol{\zeta},\mathbf{s}_1,\mathbf{s}_2=0}\\
&= \mathbf{z}^\top(\mathbf{B}\otimes\mathbf{I}_3)^\ddagger\bar{\mathbf{R}}(\boldsymbol{\psi}_v)\boldsymbol{\alpha}(\mathbf{z},\boldsymbol{\psi}_v)\\
&= -\mathbf{z}^\top(\mathbf{B}\otimes\mathbf{I}_3)^\ddagger\bar{\mathbf{R}}(\boldsymbol{\psi}_v)\bar{\mathbf{R}}(\boldsymbol{\psi}_v)^\top(\mathbf{B}\otimes\mathbf{I}_3)\boldsymbol{\gamma}(\mathbf{z})\\
&= -\mathbf{x_0}^\top(\mathbf{B}\otimes\mathbf{I}_3)(\mathbf{B}\otimes\mathbf{I}_3)^\ddagger(\mathbf{B}\otimes\mathbf{I}_3)\boldsymbol{\gamma}(\mathbf{z})\\
&= -\mathbf{x_0}^\top(\mathbf{B}\otimes\mathbf{I}_3)\boldsymbol{\gamma}(\mathbf{z})\\
&= -\mathbf{z}^\top\boldsymbol{\gamma}(\mathbf{z})<0 \quad \forall\mathbf{z}\neq\mathbf{0}
\end{aligned}$$

The last inequality follows from the definition of $\boldsymbol{\gamma}_k(\mathbf{z}_k)$ in (3.13) and the properties listed in (3.14).

Define the second auxiliary function

$$V_2(\boldsymbol{\chi}) := \mathbf{q}^\top\mathbf{P}\mathbf{q}, \tag{3.120}$$

which satisfies

$$\dot{V}_2 \leq -\sigma_1(|\mathbf{z}|_{L_1}^2)\mathbf{q}^\top\mathbf{Q}\mathbf{q} + 2\mathbf{q}^\top\mathbf{P}\mathbf{R}(\psi_{v1})\boldsymbol{\zeta}_1 =: Y_2(\boldsymbol{\chi},\boldsymbol{\phi}(t,\boldsymbol{\chi})) \tag{3.121}$$

Evaluating $Y_2(\boldsymbol{\chi},\boldsymbol{\phi}(t,\boldsymbol{\chi}))$ at $\boldsymbol{\zeta},\mathbf{s}_1,\mathbf{s}_2,\mathbf{z}=\mathbf{0}$ yields

$$Y_2(\boldsymbol{\chi})\Big|_{\boldsymbol{\zeta},\mathbf{s}_1,\mathbf{s}_2,\mathbf{z}=\mathbf{0}} = -\mathbf{q}^\top\mathbf{Q}\mathbf{q}<0 \quad \forall\mathbf{q}\neq\mathbf{0}$$

Define

$$\begin{aligned}
\bar{\mathbf{M}} &:= diag(\mathbf{M}_1,\ldots,\mathbf{M}_r) \quad \in\mathbb{R}^{3r\times 3r},\\
\bar{\boldsymbol{\Gamma}} &:= diag(\boldsymbol{\Gamma}_1,\ldots,\boldsymbol{\Gamma}_r) \quad \in\mathbb{R}^{3r\times 3r},
\end{aligned}$$

and let the third and final auxiliary function be given by

$$V_3(t,\boldsymbol{\chi}) := \tilde{\mathbf{b}}^\top\bar{\mathbf{R}}(\boldsymbol{\psi})\bar{\mathbf{M}}\mathbf{s}_2, \tag{3.122}$$

Taking time derivatives yields

$$\begin{aligned}
\dot{V}_3(t,\boldsymbol{\chi}) &= \mathbf{s}_2^\top\bar{\mathbf{R}}(\boldsymbol{\psi})^\top\bar{\boldsymbol{\Gamma}}\bar{\mathbf{R}}(\boldsymbol{\psi})\bar{\mathbf{M}}\mathbf{s}_2 + \tilde{\mathbf{b}}^\top\left(\dot{\bar{\mathbf{R}}}(\boldsymbol{\psi},\bar{\boldsymbol{\nu}})\bar{\mathbf{M}}\mathbf{s}_2 + \bar{\mathbf{R}}(\boldsymbol{\psi})\bar{\mathbf{M}}\dot{\mathbf{s}}_2\right)\\
&=: Y_3(\boldsymbol{\chi},\boldsymbol{\phi}(t,\boldsymbol{\chi})),
\end{aligned}$$

Evaluating $Y_3(\boldsymbol{\chi},\boldsymbol{\phi}(t,\boldsymbol{\chi}))$ at $\boldsymbol{\zeta},\mathbf{s}_1,\mathbf{s}_2,\mathbf{z},\mathbf{q}=\mathbf{0}$ and using (3.102) yields

$$\begin{aligned}
Y_3(\boldsymbol{\chi},\boldsymbol{\phi}(t,\boldsymbol{\chi}))\Big|_{\boldsymbol{\zeta},\mathbf{s}_1,\mathbf{s}_2,\mathbf{z},\mathbf{q}=0} &= \tilde{\mathbf{b}}^\top\bar{\mathbf{R}}(\boldsymbol{\psi})(\bar{\mathbf{M}}\dot{\mathbf{s}}_2)\Big|_{\boldsymbol{\zeta},\mathbf{s}_1,\mathbf{s}_2,\mathbf{z},\mathbf{q}=0}\\
&= -\tilde{\mathbf{b}}^\top\bar{\mathbf{R}}(\boldsymbol{\psi})\bar{\mathbf{R}}(\boldsymbol{\psi})^\top\tilde{\mathbf{b}}\\
&= -\tilde{\mathbf{b}}^\top\tilde{\mathbf{b}}<0 \quad \forall\tilde{\mathbf{b}}\neq\mathbf{0}
\end{aligned}$$

It will now be shown that all assumptions of Theorem A.1 are satisfied.

1: The origin of (3.115) has been shown to be UGS, and Assumption 1 is thus satisfied.

2: We have established that $\theta(t)$ is a continuous function of time $\forall t\geq t_0$. Combining this with the smoothness assumptions on $\mathbf{p}_d(\theta)$, $P_k(\mathbf{z}_k)$, and $\mathbf{l}_i(t)$, it is verified that $V_0(\boldsymbol{\chi})$,$V_1(t,\boldsymbol{\chi})$,$V_2(\boldsymbol{\chi})$,$V_3(t,\boldsymbol{\chi})$, $\frac{\partial V_0(\boldsymbol{\chi})}{\partial\boldsymbol{\chi}}$, $\frac{\partial V_1(t,\boldsymbol{\chi})}{\partial\boldsymbol{\chi}}$, $\frac{\partial V_2(\boldsymbol{\chi})}{\partial\boldsymbol{\chi}}$, $\frac{\partial V_3(t,\boldsymbol{\chi})}{\partial\boldsymbol{\chi}}$ are continuous on any set $[a,b]\times D$, where $[a,b]\subset[t_0,\infty)$, $D\subset\mathbb{R}^{3p+12r+3)}$. Consequently, the functions $V_i(t,\boldsymbol{\chi})$ are locally Lipschitz continuous over $[t_0,\infty)\times\mathbb{R}^{3p+12r+3)}$ by Khalil

(2002; Lemma 3.2).

Collecting all time dependent terms appearing in the expressions for $Y_i(\boldsymbol{\chi}, \boldsymbol{\phi}(t,\boldsymbol{\chi}))$ yields[8]

$$\boldsymbol{\phi}(t,\boldsymbol{\chi}) := col(\bar{\mathbf{R}}(\boldsymbol{\psi}_v)\boldsymbol{\zeta}, \bar{\mathbf{R}}(\boldsymbol{\psi}_v)\bar{\mathbf{M}}_v\boldsymbol{\zeta}, \dot{\bar{\mathbf{R}}}(\boldsymbol{\psi}_v, \bar{\boldsymbol{\nu}}_v)\bar{\mathbf{M}}_v\boldsymbol{\zeta}, \bar{\mathbf{R}}(\boldsymbol{\psi}_v)\bar{\mathbf{M}}_v\dot{\boldsymbol{\zeta}}, \bar{\mathbf{R}}(\boldsymbol{\psi})\mathbf{s}_2, \bar{\mathbf{R}}(\boldsymbol{\psi})\bar{\mathbf{M}}\mathbf{s}_2, \dot{\bar{\mathbf{R}}}(\boldsymbol{\psi}, \bar{\boldsymbol{\nu}})\bar{\mathbf{M}}\mathbf{s}_2, \bar{\mathbf{R}}(\boldsymbol{\psi})\bar{\mathbf{M}}\dot{\mathbf{s}}_2)$$

It is verified that $Y_0(\boldsymbol{\chi}), Y_1(\boldsymbol{\chi},\boldsymbol{\phi}), Y_2(\boldsymbol{\chi},\boldsymbol{\phi}), Y_3(\boldsymbol{\chi},\boldsymbol{\phi})$ are continuous in their arguments. The only thing left to show for Assumption 2 of Theorem A.1 to be satisfied is that there exist uniform upper bounds on $|V_i(t,\boldsymbol{\chi})|$ and $|\boldsymbol{\phi}(t,\boldsymbol{\chi})|$ for any given upper bound on $|\boldsymbol{\chi}|$. Uniform upper bounds on $|V_0(\boldsymbol{\chi})|, |V_2(\boldsymbol{\chi})|$ follows from (3.110) and $\lambda_{min,P}|\mathbf{q}|^2 \leq V_2(\boldsymbol{\chi}) \leq \lambda_{max,P}|\mathbf{q}|^2$, while bounds on $|V_1(t,\boldsymbol{\chi})|, |V_3(t,\boldsymbol{\chi})|$ are established by using the Cauchy-Schwarz inequality, noting that the norm of the block-diagonal matrices $\bar{\mathbf{R}}(\boldsymbol{\psi}), \bar{\mathbf{R}}(\boldsymbol{\psi}_v)$ are uniformly upper bounded by the property $||\mathbf{R}(\psi)|| \equiv 1$. To see that the bound on $|\boldsymbol{\phi}(t,\boldsymbol{\chi})|$ holds, first note that the norms of $\boldsymbol{\nu}_{vi}$, $i \in \mathcal{I}$, are uniformly upper bounded for bounded $|\boldsymbol{\chi}|$ by (3.105) and assumptions 2 – 3. By (3.107), this in turn gives uniform upper bounds on $|\boldsymbol{\nu}_i|$, $i \in \mathcal{I}$. Uniform upper bounds on $|\dot{\mathbf{R}}(\psi_{vi}, \boldsymbol{\nu}_{vi})| = |\mathbf{R}(\psi_{vi})\mathbf{S}\mathbf{e}^\top\boldsymbol{\nu}_{vi}|$ and $|\dot{\mathbf{R}}(\psi_i, \boldsymbol{\nu}_i)| = |\mathbf{R}(\psi_i)\mathbf{S}\mathbf{e}^\top\boldsymbol{\nu}_i|$ follows, which in turn shows that $|\dot{\bar{\mathbf{R}}}(\boldsymbol{\psi}_v, \bar{\boldsymbol{\nu}}_v)\bar{\mathbf{M}}_v\boldsymbol{\zeta}|$ and $|\dot{\bar{\mathbf{R}}}(\boldsymbol{\psi}, \bar{\boldsymbol{\nu}})\bar{\mathbf{M}}\mathbf{s}_2|$ are uniformly upper bounded for bounded $|\boldsymbol{\chi}|$. The bounds on $\boldsymbol{\nu}_{vi}$ and $\boldsymbol{\nu}_i$ also yield uniform upper bounds on $|\bar{\mathbf{R}}(\boldsymbol{\psi})\bar{\mathbf{M}}\dot{\mathbf{s}}_2|$ and $|\bar{\mathbf{R}}(\boldsymbol{\psi}_v)\bar{\mathbf{M}}_v\dot{\boldsymbol{\zeta}}|$ through (3.97) and (3.102). Since $|\bar{\mathbf{R}}(\boldsymbol{\psi}_v)\boldsymbol{\zeta}|, |\bar{\mathbf{R}}(\boldsymbol{\psi}_v)\bar{\mathbf{M}}_v\boldsymbol{\zeta}|, |\bar{\mathbf{R}}(\boldsymbol{\psi})\mathbf{s}_2|, |\bar{\mathbf{R}}(\boldsymbol{\psi})\bar{\mathbf{M}}\mathbf{s}_2|$ also are uniformly upper bounded for bounded $|\boldsymbol{\chi}|$, it is concluded that a uniform upper bound on $|\boldsymbol{\phi}(t,\boldsymbol{\chi})|$ can be established for any given upper bound on $|\boldsymbol{\chi}|$. Assumption 2 of Theorem A.1 is thus satisfied.

3: Since

$$\begin{aligned}
Y_0(\boldsymbol{\chi}) \leq 0 \quad &\forall \boldsymbol{\chi}, \\
Y_0(\boldsymbol{\chi}) = 0 \Rightarrow Y_1(\boldsymbol{\chi}, \boldsymbol{\phi}(t,\boldsymbol{\chi})) \leq 0 \quad &\forall \boldsymbol{\chi}, \boldsymbol{\phi}, \\
Y_0(\boldsymbol{\chi}), Y_1(\boldsymbol{\chi}, \boldsymbol{\phi}(t,\boldsymbol{\chi})) = 0 \Rightarrow Y_2(\boldsymbol{\chi}, \boldsymbol{\phi}(t,\boldsymbol{\chi})) \leq 0 \quad &\forall \boldsymbol{\chi}, \boldsymbol{\phi}, \\
Y_0(\boldsymbol{\chi}), Y_1(\boldsymbol{\chi}, \boldsymbol{\phi}(t,\boldsymbol{\chi})), Y_2(\boldsymbol{\chi}, \boldsymbol{\phi}(t,\boldsymbol{\chi})) = 0 \Rightarrow Y_3(\boldsymbol{\chi}, \boldsymbol{\phi}(t,\boldsymbol{\chi})) \leq 0 \quad &\forall \boldsymbol{\chi}, \boldsymbol{\phi},
\end{aligned}$$

assumption 3 is satisfied.

4: Since

$$\begin{aligned}
Y_0(\boldsymbol{\chi}) = 0 &\Rightarrow \mathbf{s}_1, \mathbf{s}_2, \boldsymbol{\zeta} = \mathbf{0}, \\
Y_1(\boldsymbol{\chi}, \boldsymbol{\phi}(t,\boldsymbol{\chi}))\Big|_{\mathbf{s}_1,\mathbf{s}_2,\boldsymbol{\zeta}=\mathbf{0}} &= 0 \Rightarrow \mathbf{z} = \mathbf{0}, \\
Y_2(\boldsymbol{\chi}, \boldsymbol{\phi}(t,\boldsymbol{\chi}))\Big|_{\mathbf{s}_1,\mathbf{s}_2,\boldsymbol{\zeta},\mathbf{z}=\mathbf{0}} &= 0 \Rightarrow \mathbf{q} = \mathbf{0}, \\
Y_3(\boldsymbol{\chi}, \boldsymbol{\phi}(t,\boldsymbol{\chi}))\Big|_{\mathbf{s}_1,\mathbf{s}_2,\boldsymbol{\zeta},\mathbf{z},\mathbf{q}=\mathbf{0}} &= 0 \Rightarrow \tilde{\mathbf{b}} = \mathbf{0},
\end{aligned}$$

we have that $Y_0(\boldsymbol{\chi}), Y_1(\boldsymbol{\chi}, \boldsymbol{\phi}(t,\boldsymbol{\chi})), Y_2(\boldsymbol{\chi}, \boldsymbol{\phi}(t,\boldsymbol{\chi})), Y_3(\boldsymbol{\chi}, \boldsymbol{\phi}(t,\boldsymbol{\chi})) = 0$ together imply $\boldsymbol{\chi} = \mathbf{0}$. Assumption 4 is thus satisfied.

All assumptions of Theorem A.1 are satisfied, and it is concluded that the origin of (3.115) is UGAS. Since $|(\boldsymbol{\chi}, \theta, t)|_{\mathcal{A}} = |\boldsymbol{\chi}|$, this proves UGAS for the set $\mathcal{A}$.

Fulfillment of control objectives: We now have that

$$\lim_{t\to\infty} (|\mathbf{z}(t)|, |\boldsymbol{\zeta}(t)|, |\mathbf{q}(t)|, |\mathbf{s}_1(t)|, |\mathbf{s}_2(t)|, |\tilde{\mathbf{b}}(t)|) = 0$$

[8] The time dependencies arise from the fact that the heading and velocities of the virtual and real ships are time-dependent after the change of variables. See Section 3.3.6.1.

By the definition of $\mathbf{q}$ and $\mathbf{s}_{1i}$, the control objectives (3.69),(3.71) are fulfilled. Fulfillment of (3.70),(3.72) follows from Lemma 1 and the closed-loop dynamics of θ in (3.100). The reader is referred to Appendix C.2 for a formal proof of this last statement. □

3.3.7 Notes on implementation

The control design is summarized in Table 3.2.

Control laws, real vessels	$\boldsymbol{\tau}_i = -\mathbf{K}_{pi}\mathbf{R}(\psi_i)^\top(\boldsymbol{\eta}_i - \boldsymbol{\eta}_{vi}) - \mathbf{R}(\psi_i)^\top\hat{\mathbf{b}}_i + \mathbf{D}_i(\boldsymbol{\nu}_i)\boldsymbol{\nu}_{ri} + \mathbf{C}_i(\boldsymbol{\nu}_i)\boldsymbol{\nu}_{ri} + \mathbf{M}_i\dot{\boldsymbol{\nu}}_{ri} - \mathbf{K}_{\mathbf{d}i}(\boldsymbol{\nu}_i - \boldsymbol{\nu}_{ri})$
Control laws, virtual vessels	$\boldsymbol{\tau}_{vi} = \mathbf{D}_{vi}(\boldsymbol{\nu}_{vi})\mathbf{f}_{2i} + \mathbf{C}_{vi}(\boldsymbol{\nu}_{vi})\mathbf{f}_{2i} + \mathbf{M}_{vi}\dot{\mathbf{f}}_{2i} - \mathbf{K}_{\mathbf{d}vi}(\boldsymbol{\nu}_{vi} - \mathbf{f}_{2i}) + \boldsymbol{\alpha}_i(\mathbf{z}, \psi_{vi}) + \boldsymbol{\delta}_{vi}$
Internal dynamic variables	$\dot{\theta} = \sigma_2(\lvert\mathbf{z}\rvert^2_{L_1})\beta(\lvert\mathbf{q}\rvert^2_{L_2})v_s(\theta,t) + 2\mu(\theta)\mathbf{q}^\top\mathbf{P}\mathbf{p}_d^\theta(\theta)$ (see Table 3.1 for details) $\dot{\hat{\mathbf{b}}}_i = \boldsymbol{\Gamma}_i\mathbf{R}(\psi_i)(\boldsymbol{\nu}_i - \boldsymbol{\nu}_{ri})$ $\dot{\boldsymbol{\eta}}_{vi} = \mathbf{R}(\psi_{vi})\boldsymbol{\nu}_{vi}$ $\dot{\boldsymbol{\nu}}_{vi} = \mathbf{M}_{vi}^{-1}(\boldsymbol{\tau}_{vi} - \mathbf{D}_{vi}(\boldsymbol{\nu}_{vi})\boldsymbol{\nu}_{vi} - \mathbf{C}_{vi}(\boldsymbol{\nu}_{vi})\boldsymbol{\nu}_{vi})$
Parameters	$\mathbf{K}_{\mathbf{d}i} = \mathbf{K}_{\mathbf{d}i}^\top > 0$ $\mathbf{K}_{\mathbf{d}vi} = \mathbf{K}_{\mathbf{d}vi}^\top > 0$ $\mathbf{K}_{pi} = diag(k_p, k_p, k_\psi), \qquad k_p, k_\psi > 0$ $\boldsymbol{\Gamma}_i = \boldsymbol{\Gamma}_i^\top > 0$ $\boldsymbol{\Lambda}_i$ satisfying $\mathbf{K}_{pi}\boldsymbol{\Lambda}_i > 0$ $\mathbf{A}$ Hurwitz $\mathbf{P} = \mathbf{P}^T > 0$ satisfying $\mathbf{P}\mathbf{A} + \mathbf{A}^\top\mathbf{P} = -\mathbf{Q}$ for some $\mathbf{Q} = \mathbf{Q}^\top > 0$
Signals	$\mathbf{v}_d = \sigma_1(\lvert\mathbf{z}\rvert^2_{L_1})\mathbf{A}\mathbf{q} + \sigma_2(\lvert\mathbf{z}\rvert^2_{L_1})\beta(\lvert\mathbf{q}\rvert^2_{L_2})\mathbf{p}_d^\theta(\theta)v_s(\theta,t)$ (see Table 3.1 for details) $\boldsymbol{\delta}_{vi} = \mathbf{R}(\psi_{vi})^\top\mathbf{R}(\psi_i)\mathbf{K}_{pi}\mathbf{R}(\psi_i)^\top(\boldsymbol{\eta}_i - \boldsymbol{\eta}_{vi})$ $\boldsymbol{\alpha}_i$ is given by (3.85), where all involved functions and variables are in accordance with the first control design, noting that for this design, $\mathbf{x}_{\mathbf{0}i} = \boldsymbol{\eta}_{vi} - \mathbf{f}_{1i}$. $\boldsymbol{\nu}_{ri} = -\boldsymbol{\Lambda}_i\mathbf{R}(\psi_i)^\top(\boldsymbol{\eta}_i - \boldsymbol{\eta}_{vi}) + \mathbf{R}(\psi_i)^\top\left(\dot{\mathbf{f}}_{1i} + \mathbf{v}_d\right)$ $\dot{\boldsymbol{\nu}}_{ri} = -\boldsymbol{\Lambda}_i\left(\mathbf{S}^\top\mathbf{R}(\psi_i)^\top(\boldsymbol{\eta}_i - \boldsymbol{\eta}_{vi})\dot{\psi}_i + \boldsymbol{\nu}_i - \mathbf{R}(\psi_i)^\top\dot{\boldsymbol{\eta}}_{vi}\right)$ $+\mathbf{S}^\top\mathbf{R}(\psi_i)^\top\left(\dot{\mathbf{f}}_{1i} + \mathbf{v}_d\right)\dot{\psi}_i + \mathbf{R}(\psi_i)^\top\left(\ddot{\mathbf{f}}_{1i} + \dot{\mathbf{v}}_d\right)$ $\mathbf{f}_{2i} = \mathbf{R}(\psi_{vi})^\top(\dot{\mathbf{f}}_{1i} + \mathbf{v}_d)$ $\mathbf{f}_{1i} = \mathbf{R}\left(\psi_{vi} - \psi_{ci}(t)\right)\mathbf{l}_i(t)$ See Table 3.1 for $\dot{\mathbf{f}}_{2i}$, $\ddot{\mathbf{f}}_{1i}$,$\dot{\mathbf{v}}_d$, replacing all occurrences of ψ_i, $\dot{\psi}_i$, $\ddot{\psi}_i$ with ψ_{vi}, $\dot{\psi}_{vi}$, $\ddot{\psi}_{vi}$, respectively.

Table 3.2: Design 2 summarized

It is noted that all considerations presented in Section 3.2.5 are applicable to this design. The accelerations of the virtual vessels should be calculated as in (3.60), with the obvious modifications due to the change of notation and the extra term $\boldsymbol{\delta}_{vi}$ in the virtual vessel control laws. Furthermore, all orientation error variables in the system should be handled in accordance with the proposed algorithm.

3.3.8 Simulation

The purpose of this simulation is to show that the closed-loop guidance and control design manages to achieve group coordination and path following for the vessels despite the presence of an unknown, constant environmental disturbance in the $\mathcal{E}$-frame. Three vessels with dynamics given in Appendix B are considered, where the desired formation configuration is given by $\mathbf{l}_1 = col(0, 90, 0)$, $\mathbf{l}_2 = col(0, 0, 0)$, $\mathbf{l}_3 = col(0, -90, 0)$. The path is chosen as a circle according to the parameterization

$$x_d(\theta) = R\cos(k\theta),$$
$$y_d(\theta) = -R\sin(k\theta),$$

where $R = 800[m]$, $k = \frac{1}{800}$. The virtual vessel models are chosen equal to the models of the real vessels. Furthermore, the communication topology, acting leader and control parameters for the virtual vessels are chosen in accordance with Section (3.2.6), with the exception of $\mathbf{K}_{\mathbf{d}vi} = 10^4 \times diag(5, 5, 1000)$, $\sigma_1(s) = \sigma_2(s) = e^{-0.25s}$. The function $\beta(\cdot)$ is chosen equal to unity, and the desired along-path speed is set to $U_d(t) \equiv 4[m/s]$. The control parameters for the real vessels are chosen as $\mathbf{K}_{\mathbf{d}i} = 10^4 \times diag(5, 5, 2)$, $\mathbf{K}_{pi} = 10^3 \times diag(3, 3, 60)$, $\mathbf{\Gamma}_i = 10^4 \times diag(3, 3, 80)$, $\mathbf{\Lambda}_i = 10^{-1}\mathbf{I}_3$.

The initial states for the system are chosen as $\boldsymbol{\eta}_{10} = col(-106.1, 627.8, \frac{5\pi}{12})$, $\boldsymbol{\eta}_{20} = col(-45.3, 561.3, \frac{\pi}{4})$, $\boldsymbol{\eta}_{10} = col(49.5, 472.2, \frac{\pi}{2})$, $\boldsymbol{\nu}_{10}, \boldsymbol{\nu}_{20}, \boldsymbol{\nu}_{30}, \hat{\mathbf{b}}_1, \hat{\mathbf{b}}_2, \hat{\mathbf{b}}_3 = \mathbf{0}$, $\theta_0 = 3300$, where the initial positions and velocities of the virtual vessels are set equal to those of the corresponding real vessels. Finally, the environmental disturbance is chosen as $\mathbf{b} = col(-10^5, 10^5, 10^6)$. It is noted that no saturations have been implemented in the simulation model, so that the response times are somewhat unrealistic.

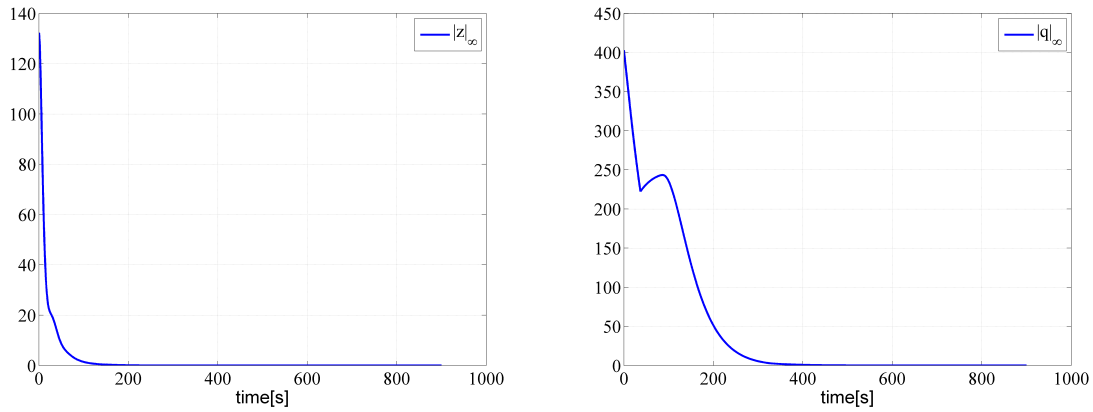

(a) $|\mathbf{z}(t)|_\infty$ (b) $|\mathbf{q}(t)|_\infty$

Figure 3.14: Time series of $|\mathbf{z}(t)|_\infty$ and $|\mathbf{q}(t)|_\infty$. At end of simulation, magnitudes are in the order of $O(10^{-7})$ and $O(10^{-5})$, respectively.

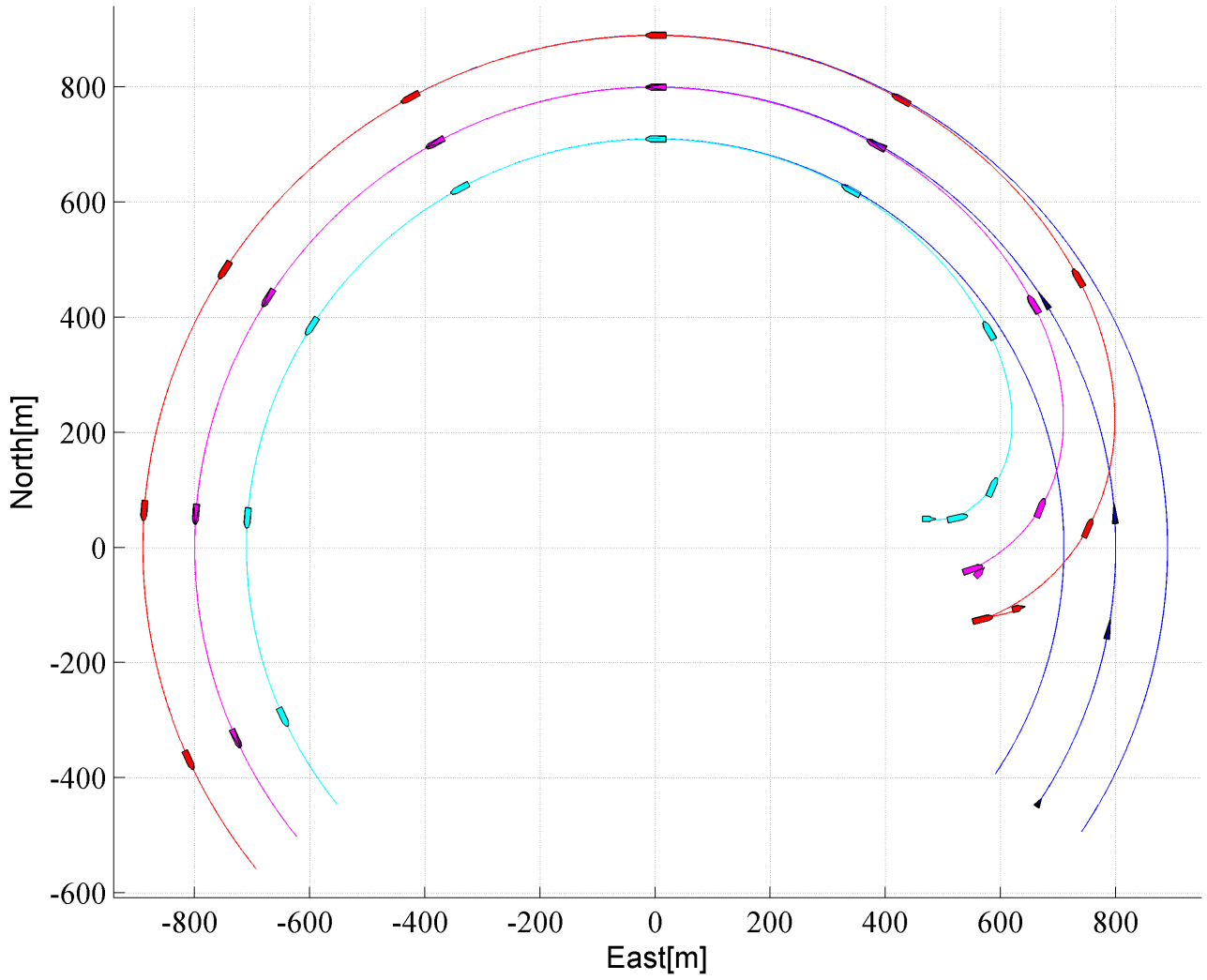

Figure 3.13: North-east position plot for the three vessels. The red, purple and blue ships correspond to vessels 1,2,3, respectively. The black arrow on the path indicates the position and orientation contained in $\mathbf{p}_d(\theta)$. Initial positions are indicated by smaller-sized ships and arrow.

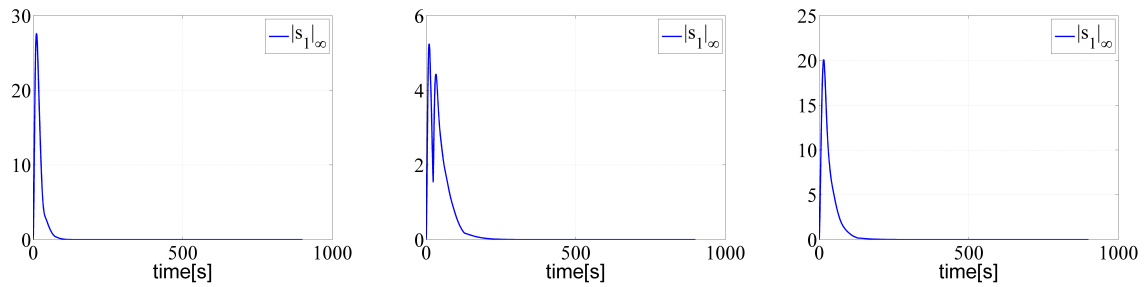

(a) Vessel 1 (b) Vessel 2 (c) Vessel 3

Figure 3.15: Plots showing $|\mathbf{s}_{1i}(t)|_\infty$ for the three vessels. At end of simulation, magnitudes are in the order of $O(10^{-7})$.

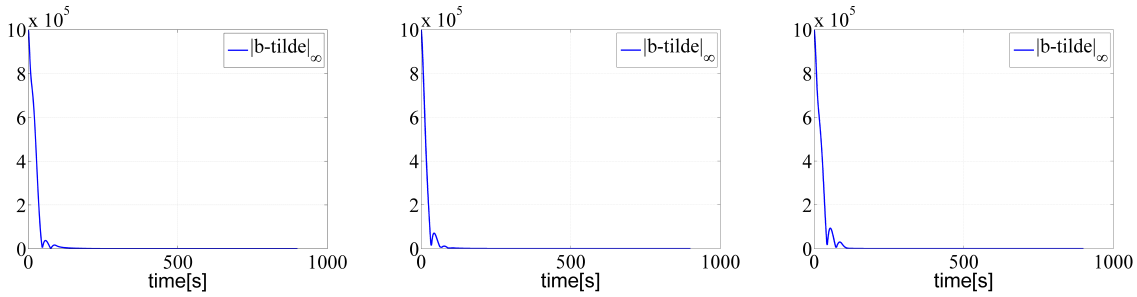

(a) Vessel 1 (b) Vessel 2 (c) Vessel 3

Figure 3.16: Plots showing $|\tilde{\mathbf{b}}_i(t)|_\infty$ for the three vessels. At end of simulation, magnitudes are in the order of $O(10^{-2})$

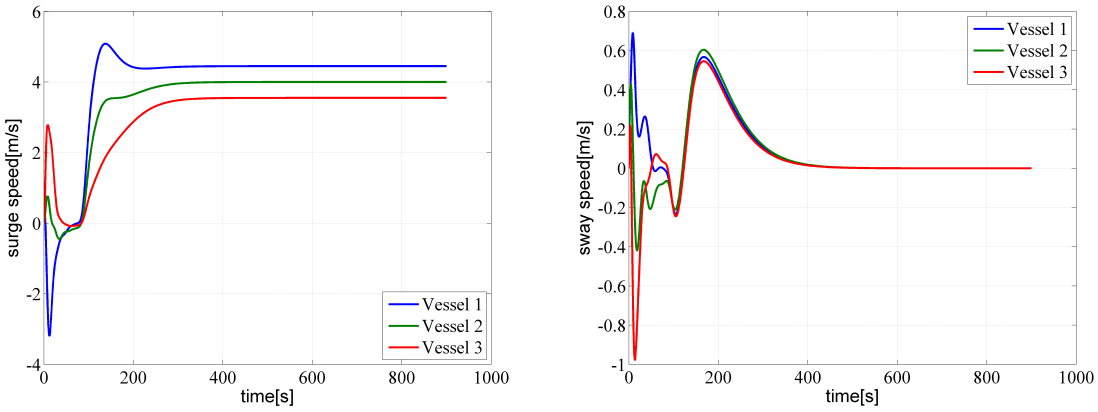

(a) Surge velocities (b) Sway velocities

Figure 3.17: Surge and sway velocities for the three vessels

After an initial transient caused by the unknown environmental disturbance, the real vessels track the positions of the virtual vessels (Figure 3.15), which in turn ensures group coordination and path following (Figure 3.14). Fulfillment of the dynamic assignment along the path is evident from figure 3.17(a), where it is seen that the surge speed of Vessel 2 converges to the desired speed $U_d = 4[m/s]$. Figure 3.16 demonstrates the effectiveness of the bias estimators in the control system.

3.4 Design 3: Generic maneuvering design using a LOS approach

The control designs of sections 3.2 and 3.3 have accomplished path following for the formation through independent control of its position and orientation in the $\mathcal{E}$-frame. Although this is a valid approach from a theoretical point of view, the transient motion towards the path can become rather unpractical for the vessels, as demonstrated in Section 3.2.6.3. In this third and final control design, path following will be targeted through the line-of-sight(LOS) algorithm presented in Skjetne et al. (2011), ensuring a practical and predictable transient motion towards the path. The design will also depart from the group agreement protocols used in the previous designs, instead following the generic maneuvering methodology to solve the formation control problem.

3.4.1 The LOS algorithm

Consider a vessel with generalized position $\boldsymbol{\eta} = col(\mathbf{p}, \psi)$, $\mathbf{p} = col(x, y)$, in the $\mathcal{E}$-frame, with dynamics given by

$$\dot{\boldsymbol{\eta}} = \mathbf{R}(\psi)\boldsymbol{\nu}, \tag{3.123}$$

where $\boldsymbol{\nu} = col(u, v, r)$. For a parameterized path given by the set of points

$$\mathcal{P} = \{\mathbf{x} \in \mathbb{R}^2 : \quad \exists \theta \in \mathbb{R} \quad s.t. \quad \mathbf{x} = \mathbf{p}_d(\theta)\},$$

where $\mathbf{p}_d(\theta) := col(x_d(\theta), y_d(\theta))$ is a sufficiently smooth function, the LOS algorithm directs the course angle of the vessel in such a way that it guarantees convergence to the path provided perfect tracking and a non-zero lower bound on the magnitude of motion. For a vessel not experiencing any sideslip (i.e. zero deviation between the course and heading angles), this translates to a reference signal ψ_{los} for the heading angle that accomplishes path following through positive surge motion. As the LOS algorithm actually will be used to direct the motion of an FRF in this design, sideslip is of no relevance in the following.

For a given value of θ, introduce a path-tangential reference frame with origin located at $\mathbf{p}_d(\theta)$. The orientation of the reference frame is given by

$$\psi_d(\theta) = \arctan\left(\frac{y_d^\theta(\theta)}{x_d^\theta(\theta)}\right) \tag{3.124}$$

The position of the vessel relative to the origin of the frame can be expressed in path-tangential coordinates according to

$$\boldsymbol{\epsilon}(\mathbf{p}, \theta) = col(s(\mathbf{p}, \theta), e(\mathbf{p}, \theta)) = \mathbf{R}_{2D}(\psi_d(\theta))^\top(\mathbf{p} - \mathbf{p}_d(\theta)), \tag{3.125}$$

where $s(\mathbf{p}, \theta)$ and $e(\mathbf{p}, \theta)$ are termed the along-track and cross-track errors, respectively, and

$$\mathbf{R}_{2D}(\psi_d(\theta)) = \begin{bmatrix} \cos(\psi_d(\theta)) & -\sin(\psi_d(\theta)) \\ \sin(\psi_d(\theta)) & \cos(\psi_d(\theta)) \end{bmatrix} \tag{3.126}$$

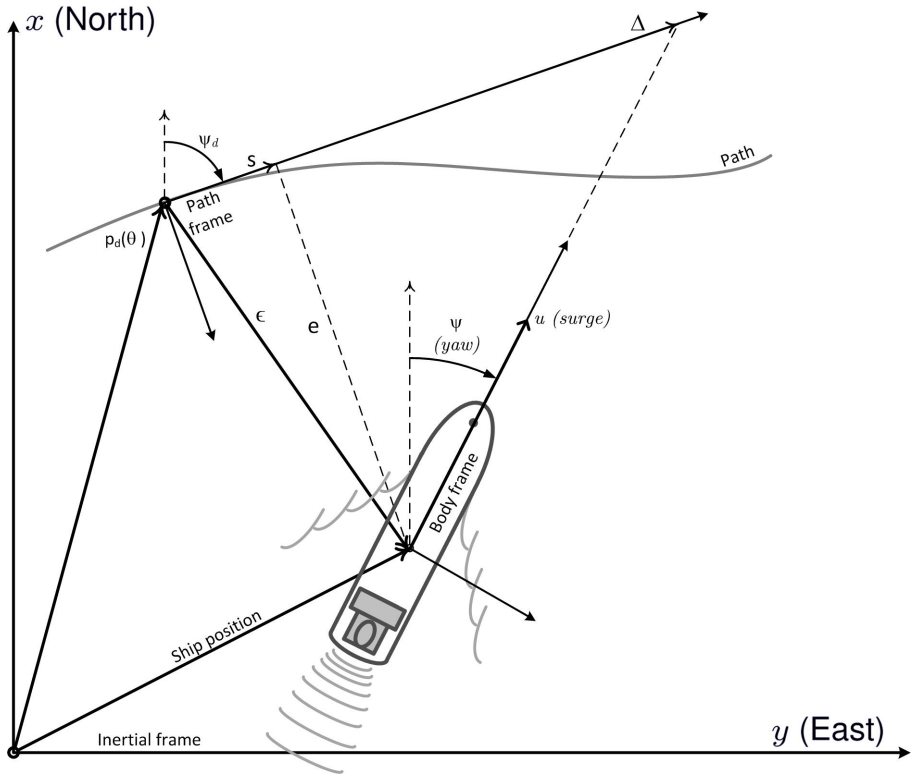

Figure 3.18: Illustration of the LOS algorithm in the case of zero sideslip. Courtesy of Skjetne et al. (2011)

Let the surge speed of the vessel be given by $u = U_d(t) > 0$, and define

$$V(\mathbf{p}, \theta) = \frac{1}{2}\boldsymbol{\epsilon}(\mathbf{p}, \theta)^\top \boldsymbol{\epsilon}(\mathbf{p}, \theta) \tag{3.127}$$

In accordance with Skjetne et al. (2011), the LOS algorithm can now be summarized as

$$\psi_{los}(\mathbf{p}, \theta) = \psi_d(\theta) + \arctan\left(\frac{-e(\mathbf{p}, \theta)}{\Delta}\right), \tag{3.128}$$

$$\dot{\theta} = f_\theta^*(\mathbf{p}, \theta, t), \tag{3.129}$$

$$f_\theta^*(\mathbf{p}, \theta, t) = \frac{\Delta}{\sqrt{\Delta^2 + e(\mathbf{p}, \theta)^2}} \frac{U_d(t)}{|\mathbf{p}_d^\theta(\theta)|} - \omega_s(\mathbf{p}, \theta), \tag{3.130}$$

$$\begin{aligned} \omega_s(\mathbf{p}, \theta) &= \frac{\mu_\theta}{|\mathbf{p}_d^\theta(\theta)|} V^\theta(\mathbf{p}, \theta) \\ &= -\mu_\theta \frac{\mathbf{p}_d^\theta(\theta)^\top}{|\mathbf{p}_d^\theta(\theta)|}(\mathbf{p} - \mathbf{p}_d(\theta)) \\ &= -\mu_\theta s(\mathbf{p}, \theta), \end{aligned} \tag{3.131}$$

where $\Delta, \mu_\theta > 0$. It is seen that the algorithm points the vessel towards a point located a distance Δ along the x-axis of the path-tangential frame. Furthermore, it is seen that the dynamic update law for θ incorporates gradient optimization in addition to a feedback term from the surge speed of the vessel.

The stability properties of the LOS algorithm is derived in Skjetne et al. (2011). It turns out that the algorithm solves a maneuvering problem given by the geometric and dynamic tasks

$$\lim_{t \to \infty} |\boldsymbol{\eta}(t) - \boldsymbol{\eta}_d(\theta)| = 0,$$
$$\lim_{t \to \infty} |\dot{\theta}(t) - v_s(\theta(t), t)| = 0,$$

where $\boldsymbol{\eta}_d(\theta) = col(\mathbf{p}_d(\theta), \psi_d(\theta))$, and $v_s(\theta(t), t) = \frac{U_d(t)}{|\mathbf{p}_d^\theta(\theta)|}$. The result is summarized in the following proposition

Proposition 1. *Let the parameterization $\theta \mapsto \mathbf{p}_d(\theta)$ be absolutely continuous, bounded, and such that $\exists(p_1, p_2) > 0$ s.t. $\forall\theta \in \mathbb{R}, p_1 \leq |\mathbf{p}_d^\theta(\theta)| \leq p_2$. For the system (3.123) with motion constrained to $\psi(t) \equiv \psi_{los}(\mathbf{p}(t), \theta(t))$, $u(t) \equiv U_d(t) \geq u_0 > 0$, $v(t) \equiv 0$, the LOS algorithm (3.128)–(3.131) renders the set*

$$\mathcal{A} = \{(\boldsymbol{\eta}, \theta) : \boldsymbol{\eta} = \boldsymbol{\eta}_d(\theta)\}$$

UGAS and ULES.

Proof. See Skjetne et al. (2011). □

Proposition 1 clearly shows the effectiveness of the LOS algorithm.

3.4.2 Setup and problem statement

In the previous designs, a cooperative approach was utilized to ensure that the vessels established the specified formation structure. This was done by making the vessels obtain their formation configuration vectors in an implicit formation reference frame $\mathcal{F}$ resulting from an agreement of local FRFs. Motivated by the approach of the first formation control design in Skjetne (2005), the position and orientation of $\mathcal{F}$ will be stated explicitly in this design. Contrary to Skjetne (2005), however, the frame will not be constrained to move along a parameterized path, but rather be allowed to evolve over the entire state space. To this end, we define the FRP of $\mathcal{F}$ as

$$\boldsymbol{\zeta} := col(\mathbf{p}_\zeta, \zeta_3) \quad \in \mathbb{R}^3, \tag{3.132}$$

where

$$\mathbf{p}_\zeta = col(x_\zeta, y_\zeta) \quad \in \mathbb{R}^2 \tag{3.133}$$

contains the position of the origin of the FRF, and ζ_3 contains its orientation relative to the $\mathcal{E}$-frame.

Consider r vessels with dynamics given by (2.5) that is to be controlled in formation, and assign to each of them a unique identifier in the index set $\mathcal{I} = \{1, \ldots, r\}$. The desired formation is specified as a set of configuration vectors

$$\mathbf{l}_i(t) = col(x_{ci}(t), y_{ci}(t), \psi_{ci}(t)), \quad i \in \mathcal{I}$$

that is to be attained relative to $\mathcal{F}$. This yields a desired generalized position vector for each vessel according to

$$\boldsymbol{\eta}_{di}(\boldsymbol{\zeta}, t) = \boldsymbol{\zeta} + \mathbf{R}(\zeta_3)\mathbf{l}_i(t), \quad i \in \mathcal{I}, \tag{3.134}$$

where $\mathbf{R}(\cdot)$ is the rotation matrix in yaw. When the vessels have established the formation by reaching their desired generalized positions, we want the formation to utilize the LOS algorithm to pursue path following. In light of the generic maneuvering methodology, this can be fulfilled by letting the algorithm dictate the trajectories of $\boldsymbol{\zeta}$ when a certain manifold is reached. By defining

$$\bar{\boldsymbol{\eta}} := col(\boldsymbol{\eta}_1, \ldots, \boldsymbol{\eta}_r) \quad \in \mathbb{R}^{3r}, \tag{3.135}$$

$$\bar{\boldsymbol{\nu}} := col(\boldsymbol{\nu}_1, \ldots, \boldsymbol{\nu}_r) \quad \in \mathbb{R}^{3r}, \tag{3.136}$$

$$\bar{\boldsymbol{\eta}}_d(\boldsymbol{\zeta}, t) := col(\boldsymbol{\eta}_{d1}(\boldsymbol{\zeta}, t), \ldots, \boldsymbol{\eta}_{dr}(\boldsymbol{\zeta}, t)) \quad \in \mathbb{R}^{3r}, \tag{3.137}$$

a natural choice for the manifold is

$$\mathcal{A} = \{(\bar{\boldsymbol{\eta}}, \bar{\boldsymbol{\nu}}, \boldsymbol{\zeta}, \theta, t) : \bar{\boldsymbol{\eta}} = \bar{\boldsymbol{\eta}}_d(\boldsymbol{\zeta}, t), \zeta_3 = \psi_{los}(\mathbf{p}_\zeta, \theta)\}, \tag{3.138}$$

where t has been included in the system state vector by adhering to

$$\dot{t} = 1 \qquad t(0) = t_0 \tag{3.139}$$

Remark 2. *To separate the explicit time from the internal time-variable in the system, the explicit time will from this point on be denoted t^*, so that $t(t^*) = t^* + t_0 \ \forall t^* \geq 0$, in accordance with* (3.139).

The desired dynamics for $\mathcal{F}$ on the manifold $\mathcal{A}$ is given by the motion constraints in Proposition 1. By defining

$$\mathbf{f}_p(\zeta_3, t) = \begin{bmatrix} \cos(\zeta_3) \\ \sin(\zeta_3) \end{bmatrix} U_d(t), \tag{3.140}$$

where $U_d(t)$ is a desired surge speed for $\mathcal{F}$, the control objectives can through this setup be expressed as the following geometric and dynamic tasks:

Geometric task:

$$\lim_{t^* \to \infty} |\bar{\boldsymbol{\eta}}(t^*) - \bar{\boldsymbol{\eta}}_d(\boldsymbol{\zeta}(t^*), t(t^*))| = 0 \tag{3.141}$$

$$\lim_{t^* \to \infty} |\zeta_3(t^*) - \psi_{los}(\mathbf{p}_\zeta(t^*), \theta(t^*))| = 0 \tag{3.142}$$

Dynamic task:

$$\lim_{t^* \to \infty} |\dot{\mathbf{p}}_\zeta(t^*) - \mathbf{f}_p(\zeta_3(t^*), t(t^*))| = 0, \tag{3.143}$$

Since we want to separate the pursuit of group coordination and path following, (3.141) is given higher priority than (3.142) and (3.143). This can prevent initiation of the collective movement towards the path before the vessels are sufficiently close to being in formation, in accordance with the efforts of the previous control designs.

It is finally noted that satisfying (3.142) and (3.143) does not provide a formal guarantee that $\mathcal{F}$ will converge to the path, as applying Proposition 1 would require $\dot{\mathbf{p}}_\zeta(t^*) \equiv \mathbf{f}_p(\zeta_3(t^*), t(t^*))$, $\zeta_3(t^*) \equiv \psi_{los}(\mathbf{p}_\zeta(t^*), \theta(t^*))$. However, based on the intuitive nature of the LOS algorithm and its proven effectiveness in theory and practice, the author finds fulfillment of (3.142) and (3.143) to be sufficient "proof" of path convergence for any practical application.

3.4.3 Control design

A backstepping procedure similar to the formation control design in Skjetne (2005) will be used to achieve the control objectives (3.141)–(3.143). The design will be presented after the dynamics of $\boldsymbol{\zeta}$ and θ have been specified.

3.4.3.1 Specification of FRP and path-variable dynamics

In a straight forward maneuvering design, the dynamics of $\boldsymbol{\zeta}$ and θ would be chosen as

$$\dot{\boldsymbol{\zeta}} = \mathbf{f}_\zeta^*(\boldsymbol{\zeta}, \theta, t) - \boldsymbol{\omega}_\zeta \tag{3.144}$$

$$\dot{\theta} = f_\theta^*(\mathbf{p}_\zeta, \theta, t) - \omega_\theta, \tag{3.145}$$

where $\boldsymbol{\omega}_\zeta$ and ω_θ would end up providing gradient optimization of the Lyapunov function used in the design, and $\mathbf{f}_\zeta^*(\boldsymbol{\zeta}, \theta, t)$, $f_\theta^*(\mathbf{p}_\zeta, \theta, t)$ are nominal terms that would be chosen in accordance with the desired dynamics on the specified manifold. In our case, this would amount to choosing $f_\theta^*(\mathbf{p}_\zeta, \theta, t)$ as in (3.130),

$$\mathbf{f}_\zeta^*(\boldsymbol{\zeta}, \theta, t) = \begin{bmatrix} \mathbf{f}_p(\zeta_3, t) \\ f_{\zeta_3}^*(\boldsymbol{\zeta}, \theta, t)) \end{bmatrix}, \tag{3.146}$$

where $\mathbf{f}_p(\zeta_3, t)$ is given by (3.140), and

$$f_{\zeta_3}^*(\boldsymbol{\zeta}, \theta, t) = -k_{\zeta_3}(\zeta_3 - \psi_{los}(\mathbf{p}_\zeta, \theta)) + \psi_{los}^{\mathbf{p}_\zeta}(\mathbf{p}_\zeta, \theta)\mathbf{f}_p(\zeta_3, t) + \psi_{los}^{\theta}(\mathbf{p}_\zeta, \theta) f_\theta^*(\mathbf{p}_\zeta, \theta, t), \quad k_{\zeta_3} > 0, \tag{3.147}$$

where a stabilizing term is included in (3.147) to enable fulfillment of (3.142).

The dynamics of $\boldsymbol{\zeta}$ and θ will be assigned slightly different from (3.144)–(3.147). First of all, ω_θ will be omitted. The reason is that the LOS algorithm already incorporates a very intuitive gradient optimization term in $f^*_\theta(\mathbf{p}_\zeta, \theta, t)$ that will work as a minimizer of the distance between the path-tangential frame and $\mathbf{p}_\zeta$. Including additional gradient optimization through a new Lyapunov function could pollute this nice feature, resulting in an unpredictable and less intuitive transient response for θ.

Due to our desire for a clear-cut separation between the group coordination and formation mission tasks, $\mathbf{f}_p(\zeta_3, t)$ and $f^*_{\zeta_3}(\boldsymbol{\zeta}, \theta, t)$ in (3.146) will also be altered slightly from their preliminary specifications in (3.140) and (3.147). As it is the desired surge speed function $U_d(t)$ that will dictate the magnitude of motion of $\mathcal{F}$ towards the path, and the stabilizing term in (3.147) that will drive the orientation of $\mathcal{F}$ towards the LOS angle, "deactivating" them when the vessels are out of formation will provide the desired separation and prioritization. This is formalized by scaling the terms with activation functions $\sigma_k : \mathbb{R}_{\geq 0} \mapsto \mathbb{R}_{>0}$, $k = 1, 2$, which should be continuously differentiable, monotonically decreasing, and satisfy

$$\sigma_k(0) = 1 \qquad k = 1, 2 \tag{3.148a}$$

$$\lim_{s\to\infty} \sigma_1(s) = 0. \tag{3.148b}$$

$$\sigma_2(s) \geq \epsilon \quad \forall s \in \mathbb{R}_{\geq 0}, \qquad 1 >> \epsilon > 0 \tag{3.148c}$$

The positive lower bound the second activation function in (3.148c) is introduced due to technicalities in the backstepping procedure. As ϵ can be chosen arbitrarily close to zero, this does not have any practical implications (i.e. it can be chosen so that $\lim_{s\to\infty} \sigma_2(s) \approx 0$). As input to the activation functions, we use $|\bar{\boldsymbol{\eta}} - \bar{\boldsymbol{\eta}}_d(\boldsymbol{\zeta}, t)|^2_L := (\bar{\boldsymbol{\eta}} - \bar{\boldsymbol{\eta}}_d(\boldsymbol{\zeta}, t))^\top \mathbf{L} (\bar{\boldsymbol{\eta}} - \bar{\boldsymbol{\eta}}_d(\boldsymbol{\zeta}, t))$, where $\mathbf{L} = \mathbf{L}^\top \geq 0$ is a weight matrix used to tune the gains for position and orientation errors in $(\bar{\boldsymbol{\eta}} - \bar{\boldsymbol{\eta}}_d(\boldsymbol{\zeta}, t))$.

With these notes in mind, the dynamics of $\boldsymbol{\zeta}$ and θ are chosen as

$$\dot{\boldsymbol{\zeta}} = \mathbf{f}_\zeta(\boldsymbol{\zeta}, \bar{\boldsymbol{\eta}}, \theta, t) - \boldsymbol{\omega}_\zeta, \tag{3.149}$$

$$\dot{\theta} = f_\theta(\boldsymbol{\zeta}, \bar{\boldsymbol{\eta}}, \theta, t), \tag{3.150}$$

where

$$f_\theta(\boldsymbol{\zeta}, \bar{\boldsymbol{\eta}}, \theta, t) = \frac{\Delta}{\sqrt{\Delta^2 + e(\mathbf{p}_\zeta, \theta)^2}} \frac{U_d(t)\sigma_1\left(|\bar{\boldsymbol{\eta}} - \bar{\boldsymbol{\eta}}_d(\boldsymbol{\zeta}, t)|^2_L\right)}{|\mathbf{p}^\theta_d(\theta)|} + \mu_\theta \frac{\mathbf{p}^\theta_d(\theta)^\top}{|\mathbf{p}^\theta_d(\theta)|}(\mathbf{p}_\zeta - \mathbf{p}_d(\theta)), \tag{3.151}$$

$$\mathbf{f}_\zeta(\boldsymbol{\zeta}, \bar{\boldsymbol{\eta}}, \theta, t) = \begin{bmatrix} \mathbf{f}_{p\zeta}(\boldsymbol{\zeta}, \bar{\boldsymbol{\eta}}, t) \\ f_{\zeta_3}(\boldsymbol{\zeta}, \bar{\boldsymbol{\eta}}, \theta, t)) \end{bmatrix}, \tag{3.152}$$

$$\mathbf{f}_{p\zeta}(\boldsymbol{\zeta}, \bar{\boldsymbol{\eta}}, t) = \begin{bmatrix} \cos(\zeta_3) \\ \sin(\zeta_3) \end{bmatrix} U_d(t)\sigma_1\left(|\bar{\boldsymbol{\eta}} - \bar{\boldsymbol{\eta}}_d(\boldsymbol{\zeta}, t)|^2_L\right), \tag{3.153}$$

$$f_{\zeta_3}(\boldsymbol{\zeta}, \bar{\boldsymbol{\eta}}, \theta, t)) = -k_{\zeta_3}\sigma_2\left(|\bar{\boldsymbol{\eta}} - \bar{\boldsymbol{\eta}}_d(\boldsymbol{\zeta}, t)|^2_L\right)(\zeta_3 - \psi_{los}(\mathbf{p}_\zeta, \theta)) + \psi^{\mathbf{p}_\zeta}_{los}(\mathbf{p}_\zeta, \theta)\mathbf{f}_{p\zeta}(\boldsymbol{\zeta}, \bar{\boldsymbol{\eta}}, t) + \psi^\theta_{los}(\mathbf{p}_\zeta, \theta) f_\theta(\boldsymbol{\zeta}, \bar{\boldsymbol{\eta}}, \theta, t), \tag{3.154}$$

and $\boldsymbol{\omega}_\zeta$ is to be designed during the backstepping procedure.

3.4.3.2 Backstepping design

Step 1: Define

$$\mathbf{z}_{1i}(\boldsymbol{\eta}_i, \boldsymbol{\zeta}, t) := \boldsymbol{\eta}_i - \boldsymbol{\eta}_{di}(\boldsymbol{\zeta}, t) \qquad i \in \mathcal{I}, \tag{3.155}$$

$$\mathbf{z}_{2i}(\boldsymbol{\zeta}, \bar{\boldsymbol{\eta}}, \boldsymbol{\nu}_i, \theta, t) := \boldsymbol{\nu}_i - \boldsymbol{\alpha}_i(\boldsymbol{\zeta}, \bar{\boldsymbol{\eta}}, \theta, t) \quad i \in \mathcal{I}, \tag{3.156}$$

where $\boldsymbol{\alpha}_i(\boldsymbol{\zeta}, \bar{\boldsymbol{\eta}}, \theta, t)$, $i \in \mathcal{I}$, are virtual control inputs to be designed. Differentiating (3.155) with respect to time yields

$$\begin{aligned}\dot{\mathbf{z}}_{1i} &= \mathbf{R}(\psi_i)\boldsymbol{\nu}_i - \boldsymbol{\eta}_{di}^{\boldsymbol{\zeta}}(\boldsymbol{\zeta}, t)\mathbf{f}_{\boldsymbol{\zeta}}(\boldsymbol{\zeta}, \bar{\boldsymbol{\eta}}, \theta, t) - \boldsymbol{\eta}_{di}^{t}(\boldsymbol{\zeta}, t) + \boldsymbol{\eta}_{di}^{\boldsymbol{\zeta}}(\boldsymbol{\zeta}, t)\boldsymbol{\omega}_{\boldsymbol{\zeta}} \\ &= \mathbf{R}(\psi_i)(\mathbf{z}_{2i} + \boldsymbol{\alpha}_i) - \boldsymbol{\eta}_{di}^{\boldsymbol{\zeta}}(\boldsymbol{\zeta}, t)\mathbf{f}_{\boldsymbol{\zeta}}(\boldsymbol{\zeta}, \bar{\boldsymbol{\eta}}, \theta, t) - \boldsymbol{\eta}_{di}^{t}(\boldsymbol{\zeta}, t) + \boldsymbol{\eta}_{di}^{\boldsymbol{\zeta}}(\boldsymbol{\zeta}, t)\boldsymbol{\omega}_{\boldsymbol{\zeta}}\end{aligned}$$

Select Hurwitz matrices $\mathbf{A}_{1i}$ and corresponding symmetric, positive definite matrices $\mathbf{P}_{1i}$ satisfying $\mathbf{P}_{1i}\mathbf{A}_{1i} + \mathbf{A}_{1i}^{\top}\mathbf{P}_{1i} = -\mathbf{Q}_{1i}$ for some $\mathbf{Q}_{1i} = \mathbf{Q}_{1i}^{\top} > 0$. Defining the radially unbounded, positive definite CLF

$$V_1(\bar{\boldsymbol{\eta}}, \boldsymbol{\zeta}, t) := \sum_{i \in \mathcal{I}} \mathbf{z}_{1i}(\boldsymbol{\eta}_i, \boldsymbol{\zeta}, t)^{\top}\mathbf{P}_{1i}\mathbf{z}_{1i}(\boldsymbol{\eta}_i, \boldsymbol{\zeta}, t), \tag{3.157}$$

and differentiating with respect to time yields

$$\dot{V}_1 = \sum_{i \in \mathcal{I}} 2\mathbf{z}_{1i}^{\top}\mathbf{P}_{1i}\Big[\mathbf{R}(\psi_i)(\mathbf{z}_{2i} + \boldsymbol{\alpha}_i) - \boldsymbol{\eta}_{di}^{\boldsymbol{\zeta}}(\boldsymbol{\zeta}, t)\mathbf{f}_{\boldsymbol{\zeta}}(\boldsymbol{\zeta}, \bar{\boldsymbol{\eta}}, \theta, t) - \boldsymbol{\eta}_{di}^{t}(\boldsymbol{\zeta}, t) + \boldsymbol{\eta}_{di}^{\boldsymbol{\zeta}}(\boldsymbol{\zeta}, t)\boldsymbol{\omega}_{\boldsymbol{\zeta}}\Big]$$

Choosing

$$\boldsymbol{\alpha}_i(\boldsymbol{\zeta}, \bar{\boldsymbol{\eta}}, \theta, t) = \mathbf{R}(\psi_i)^{\top}\Big(\boldsymbol{\eta}_{di}^{\boldsymbol{\zeta}}(\boldsymbol{\zeta}, t)\mathbf{f}_{\boldsymbol{\zeta}}(\boldsymbol{\zeta}, \bar{\boldsymbol{\eta}}, \theta, t) + \boldsymbol{\eta}_{di}^{t}(\boldsymbol{\zeta}, t) + \mathbf{A}_{1i}\mathbf{z}_{1i}(\boldsymbol{\eta}_i, \boldsymbol{\zeta}, t)\Big) \qquad i \in \mathcal{I}, \tag{3.158}$$

yields

$$\dot{V}_1 = \sum_{i \in \mathcal{I}}\big(-\mathbf{z}_{1i}^{\top}\mathbf{Q}_{1i}\mathbf{z}_{1i} + 2\mathbf{z}_{1i}^{\top}\mathbf{P}_{1i}\mathbf{R}(\psi_i)\mathbf{z}_{2i}\big) + \Big(\sum_{i \in \mathcal{I}} 2\mathbf{z}_{1i}^{\top}\mathbf{P}_{1i}\boldsymbol{\eta}_{di}^{\boldsymbol{\zeta}}(\boldsymbol{\zeta}, t)\Big)\boldsymbol{\omega}_{\boldsymbol{\zeta}}$$

Before we move on to the next step of the backstepping procedure, it is noted that by defining

$$\boldsymbol{\psi} := col(\psi_1, \ldots, \psi_r) \qquad \in \mathbb{R}^r, \tag{3.159}$$

$$\bar{\mathbf{R}}(\boldsymbol{\psi}) := diag(\mathbf{R}(\psi_1), \ldots, \mathbf{R}(\psi_r)) \qquad \in \mathbb{R}^{3r \times 3r}, \tag{3.160}$$

the time derivatives of $\boldsymbol{\alpha}_i$ can be expressed as

$$\dot{\boldsymbol{\alpha}}_i = \boldsymbol{\delta}_i(\boldsymbol{\zeta}, \bar{\boldsymbol{\eta}}, \bar{\boldsymbol{\nu}}, \theta, t) - \boldsymbol{\alpha}_i^{\boldsymbol{\zeta}}(\boldsymbol{\zeta}, \bar{\boldsymbol{\eta}}, \theta, t)\boldsymbol{\omega}_{\boldsymbol{\zeta}} \qquad i \in \mathcal{I}, \tag{3.161}$$

where

$$\begin{aligned}\boldsymbol{\delta}_i(\boldsymbol{\zeta}, \bar{\boldsymbol{\eta}}, \bar{\boldsymbol{\nu}}, \theta, t) =& \boldsymbol{\alpha}_i^{\boldsymbol{\zeta}}(\boldsymbol{\zeta}, \bar{\boldsymbol{\eta}}, \theta, t)\mathbf{f}_{\boldsymbol{\zeta}}(\boldsymbol{\zeta}, \bar{\boldsymbol{\eta}}, \theta, t) + \boldsymbol{\alpha}_i^{\theta}(\boldsymbol{\zeta}, \bar{\boldsymbol{\eta}}, \theta, t)\mathbf{f}_{\theta}(\boldsymbol{\zeta}, \bar{\boldsymbol{\eta}}, \theta, t) \\ &+ \boldsymbol{\alpha}_i^{\bar{\boldsymbol{\eta}}}(\boldsymbol{\zeta}, \bar{\boldsymbol{\eta}}, \theta, t)\bar{\mathbf{R}}(\boldsymbol{\psi})\bar{\boldsymbol{\nu}} + \boldsymbol{\alpha}_i^{t}(\boldsymbol{\zeta}, \bar{\boldsymbol{\eta}}, \theta, t), \qquad i \in \mathcal{I}\end{aligned} \tag{3.162}$$

Step 2: From (3.156) and (3.161), the dynamics of $\mathbf{z}_{2i}$ become

$$\begin{aligned}\dot{\mathbf{z}}_{2i} &= \dot{\boldsymbol{\nu}}_i - \boldsymbol{\delta}_i(\boldsymbol{\zeta}, \bar{\boldsymbol{\eta}}, \bar{\boldsymbol{\nu}}, \theta, t) + \boldsymbol{\alpha}_i^{\boldsymbol{\zeta}}(\boldsymbol{\zeta}, \bar{\boldsymbol{\eta}}, \theta, t)\boldsymbol{\omega}_{\boldsymbol{\zeta}} \\ &= \mathbf{M}_i^{-1}\big(\boldsymbol{\tau}_i - \mathbf{D}_i(\boldsymbol{\nu}_i)(\mathbf{z}_{2i} + \boldsymbol{\alpha}_i(\boldsymbol{\zeta}, \bar{\boldsymbol{\eta}}, \theta, t)) - \mathbf{C}_i(\boldsymbol{\nu}_i)(\mathbf{z}_{2i} + \boldsymbol{\alpha}_i(\boldsymbol{\zeta}, \bar{\boldsymbol{\eta}}, \theta, t))\big) \\ &\quad - \boldsymbol{\delta}_i(\boldsymbol{\zeta}, \bar{\boldsymbol{\eta}}, \bar{\boldsymbol{\nu}}, \theta, t) + \boldsymbol{\alpha}_i^{\boldsymbol{\zeta}}(\boldsymbol{\zeta}, \bar{\boldsymbol{\eta}}, \theta, t)\boldsymbol{\omega}_{\boldsymbol{\zeta}}\end{aligned}$$

Defining the CLF

$$V_2(\boldsymbol{\zeta}, \bar{\boldsymbol{\eta}}, \bar{\boldsymbol{\nu}}, \theta, t) = V_1(\bar{\boldsymbol{\eta}}, \boldsymbol{\zeta}, t) + \sum_{i \in \mathcal{I}} \mathbf{z}_{2i}(\boldsymbol{\zeta}, \bar{\boldsymbol{\eta}}, \boldsymbol{\nu}_i, \theta, t)^{\top}\mathbf{M}_i\mathbf{z}_{2i}(\boldsymbol{\zeta}, \bar{\boldsymbol{\eta}}, \boldsymbol{\nu}_i, \theta, t), \tag{3.163}$$

and differentiating with respect to time yields (omitting some argument lists)

$$\begin{aligned}\dot{\mathbf{V}}_2 =& \sum_{i \in \mathcal{I}}\big(-\mathbf{z}_{1i}^{\top}\mathbf{Q}_{1i}\mathbf{z}_{1i}\big) + \Big(\sum_{i \in \mathcal{I}} 2\mathbf{z}_{1i}^{\top}\mathbf{P}_{1i}\boldsymbol{\eta}_{di}^{\boldsymbol{\zeta}}(\boldsymbol{\zeta}, t)\Big)\boldsymbol{\omega}_{\boldsymbol{\zeta}} \\ &+ \sum_{i \in \mathcal{I}} 2\mathbf{z}_{2i}^{\top}\Big[\mathbf{R}(\psi_i)^{\top}\mathbf{P}_{1i}\mathbf{z}_{1i} + \boldsymbol{\tau}_i - (\mathbf{D}_i(\boldsymbol{\nu}_i) + \mathbf{C}_i(\boldsymbol{\nu}_i))(\mathbf{z}_{2i} + \boldsymbol{\alpha}_i) - \mathbf{M}_i\boldsymbol{\delta}_i + \mathbf{M}_i\boldsymbol{\alpha}_i^{\boldsymbol{\zeta}}(\boldsymbol{\zeta}, \bar{\boldsymbol{\eta}}, \theta, t)\boldsymbol{\omega}_{\boldsymbol{\zeta}}\Big]\end{aligned}$$

Choosing the control inputs as

$$\boldsymbol{\tau}_i = -\mathbf{R}(\psi_i)^\top \mathbf{P}_{1i}\mathbf{z}_{1i} - \mathbf{K}_{di}\mathbf{z}_{2i} + \mathbf{D}_i(\boldsymbol{\nu}_i)\boldsymbol{\alpha}_i + \mathbf{C}_i(\boldsymbol{\nu}_i)\boldsymbol{\alpha}_i + \mathbf{M}_i\boldsymbol{\delta_i} \qquad i \in \mathcal{I}, \tag{3.164}$$

where $\mathbf{K}_{di} = \mathbf{K}_{di}^\top > 0$, yields (using properties (2.7),(2.8))

$$\dot{V}_2 \leq -\sum_{i\in\mathcal{I}} \left(\mathbf{z}_{1i}^\top \mathbf{Q}_{1i}\mathbf{z}_{1i} + 2\mathbf{z}_{2i}^\top \mathbf{K}_{di}\mathbf{z}_{2i}\right) + \left(\sum_{i\in\mathcal{I}} \left(2\mathbf{z}_{1i}^\top \mathbf{P}_{1i}\boldsymbol{\eta}_{di}^{\boldsymbol{\zeta}}(\boldsymbol{\zeta},t) + 2\mathbf{z}_{2i}^\top \mathbf{M}_i\boldsymbol{\alpha}_i^{\boldsymbol{\zeta}}(\boldsymbol{\zeta},\bar{\boldsymbol{\eta}},\theta,t)\right)\right)\boldsymbol{\omega}_\zeta$$

Step 3: Introduce the error variable

$$\tilde{\zeta}_3(\boldsymbol{\zeta},\theta) := \zeta_3 - \psi_{los}(\mathbf{p}_\zeta,\theta), \tag{3.165}$$

and define the candidate Lyapunov function

$$V_3(\boldsymbol{\zeta},\bar{\boldsymbol{\eta}},\bar{\boldsymbol{\nu}},\theta,t) = V_2(\boldsymbol{\zeta},\bar{\boldsymbol{\eta}},\bar{\boldsymbol{\nu}},\theta,t) + \frac{\rho}{2}\tilde{\zeta}_3^2, \quad \rho > 0 \tag{3.166}$$

Taking time derivatives and using (3.149)–(3.154) yields

$$\begin{aligned}
\dot{V}_3 &= \dot{V}_2 + \rho\tilde{\zeta}_3\Big[f_{\zeta_3}(\boldsymbol{\zeta},\bar{\boldsymbol{\eta}},\theta,t)) - \mathbf{h}_3^\top\boldsymbol{\omega}_\zeta - \psi_{los}^{\mathbf{p}_\zeta}(\mathbf{p}_\zeta,\theta)\big(\mathbf{f}_{p\zeta}(\boldsymbol{\zeta},\bar{\boldsymbol{\eta}},t) - \mathbf{I}_{2\times 3}\boldsymbol{\omega}_\zeta\big) \\
&\quad - \psi_{los}^{\theta}(\mathbf{p}_\zeta,\theta)f_\theta(\boldsymbol{\zeta},\bar{\boldsymbol{\eta}},\theta,t)\Big] \qquad \mathbf{h}_3 = col(0,0,1), \quad \mathbf{I}_{2\times 3} = \begin{bmatrix}1 & 0 & 0\\ 0 & 1 & 0\end{bmatrix} \\
&\leq -\sum_{i\in\mathcal{I}} \left(\mathbf{z}_{1i}^\top \mathbf{Q}_{1i}\mathbf{z}_{1i} + 2\mathbf{z}_{2i}^\top \mathbf{K}_{di}\mathbf{z}_{2i}\right) - \rho k_{\zeta_3}\sigma_2\left(|\bar{\boldsymbol{\eta}} - \bar{\boldsymbol{\eta}}_d(\boldsymbol{\zeta},t)|_L^2\right)\tilde{\zeta}_3^2 \\
&\quad + \left[\sum_{i\in\mathcal{I}} \left(2\mathbf{z}_{1i}^\top \mathbf{P}_{1i}\boldsymbol{\eta}_{di}^{\boldsymbol{\zeta}}(\boldsymbol{\zeta},t) + 2\mathbf{z}_{2i}^\top \mathbf{M}_i\boldsymbol{\alpha}_i^{\boldsymbol{\zeta}}(\boldsymbol{\zeta},\bar{\boldsymbol{\eta}},\theta,t)\right) + \rho\tilde{\zeta}_3\left(\psi_{los}^{\mathbf{p}_\zeta}(\mathbf{p}_\zeta,\theta)\mathbf{I}_{2\times 3} - \mathbf{h}_3^\top\right)\right]\boldsymbol{\omega}_\zeta
\end{aligned}$$

It is easily verified that

$$V_3^{\boldsymbol{\zeta}}(\boldsymbol{\zeta},\bar{\boldsymbol{\eta}},\bar{\boldsymbol{\nu}},\theta,t) = \sum_{i\in\mathcal{I}} \left(-2\mathbf{z}_{1i}^\top \mathbf{P}_{1i}\boldsymbol{\eta}_{di}^{\boldsymbol{\zeta}}(\boldsymbol{\zeta},t) - 2\mathbf{z}_{2i}^\top \mathbf{M}_i\boldsymbol{\alpha}_i^{\boldsymbol{\zeta}}(\boldsymbol{\zeta},\bar{\boldsymbol{\eta}},\theta,t)\right) + \rho\tilde{\zeta}_3\left(\mathbf{h}_3^\top - \psi_{los}^{\mathbf{p}_\zeta}(\mathbf{p}_\zeta,\theta)\mathbf{I}_{2\times 3}\right), \tag{3.167}$$

which shows that

$$\begin{aligned}
\dot{V}_3 &\leq -\sum_{i\in\mathcal{I}} \left(\mathbf{z}_{1i}^\top \mathbf{Q}_{1i}\mathbf{z}_{1i} + 2\mathbf{z}_{2i}^\top \mathbf{K}_{di}\mathbf{z}_{2i}\right) - \rho k_{\zeta_3}\sigma_2\left(|\bar{\boldsymbol{\eta}} - \bar{\boldsymbol{\eta}}_d(\boldsymbol{\zeta},t)|_L^2\right)\tilde{\zeta}_3^2 - V_3^{\boldsymbol{\zeta}}(\boldsymbol{\zeta},\bar{\boldsymbol{\eta}},\bar{\boldsymbol{\nu}},\theta,t)\boldsymbol{\omega}_\zeta, \\
&\leq -\sum_{i\in\mathcal{I}} \left(\mathbf{z}_{1i}^\top \mathbf{Q}_{1i}\mathbf{z}_{1i} + 2\mathbf{z}_{2i}^\top \mathbf{K}_{di}\mathbf{z}_{2i}\right) - \rho k_{\zeta_3}\epsilon\tilde{\zeta}_3^2 - V_3^{\boldsymbol{\zeta}}(\boldsymbol{\zeta},\bar{\boldsymbol{\eta}},\bar{\boldsymbol{\nu}},\theta,t)\boldsymbol{\omega}_\zeta,
\end{aligned}$$

where the last transition follows from (3.148c). At this point, a natural way to proceed would be to utilize the gradient assignment $\boldsymbol{\omega}_\zeta = \mu_\zeta V_3^{\boldsymbol{\zeta}}(\boldsymbol{\zeta},\bar{\boldsymbol{\eta}},\bar{\boldsymbol{\nu}},\theta,t)^\top$ for some $\mu_\zeta > 0$, making $\dot{V}_3$ negative definite in our error variables. However, due to some technicalities in the stability proof of Section 3.4.4.4, $\boldsymbol{\omega}_\zeta$ will instead be chosen as the output of a first order reference filter that is fed $\mu_\zeta V_3^{\boldsymbol{\zeta}}(\boldsymbol{\zeta},\bar{\boldsymbol{\eta}},\bar{\boldsymbol{\nu}},\theta,t)^\top$ as input, resulting in a filtered gradient assignment. To formalize this, we select a matrix $\mathbf{A}_\zeta = \mathbf{A}_\zeta^\top > 0$, and assign

$$\dot{\boldsymbol{\omega}}_\zeta = -\mathbf{A}_\zeta\boldsymbol{\omega}_\zeta + \mathbf{A}_\zeta\mu_\zeta V_3^{\boldsymbol{\zeta}}(\boldsymbol{\zeta},\bar{\boldsymbol{\eta}},\bar{\boldsymbol{\nu}},\theta,t)^\top \tag{3.168}$$

Intuitively speaking, the filtered gradient law will retain the optimization qualities of the pure gradient assignment $\boldsymbol{\omega}_\zeta = \mu_\zeta V_3^{\boldsymbol{\zeta}}(\boldsymbol{\zeta},\bar{\boldsymbol{\eta}},\bar{\boldsymbol{\nu}},\theta,t)^\top$ provided the reference filter is tuned aggressively (i.e. $\mathbf{A}_\zeta$ is chosen large).

Remark 3. *Note that the mass matrices of the vessels are included in $V_3^{\boldsymbol{\zeta}}(\boldsymbol{\zeta},\bar{\boldsymbol{\eta}},\bar{\boldsymbol{\nu}},\theta,t)$. By following the approach of the formation control designs in Skjetne (2005), these matrices can be replaced by tunable matrices $\mathbf{P}_{2i} = \mathbf{P}_{2i}^\top > 0$, resulting in increased flexibility with respect to tuning of the gradient optimization. The downside is that the corresponding control laws must cancel the terms $\mathbf{D}_i(\boldsymbol{\nu}_i)\boldsymbol{\nu}_i, \mathbf{C}_i(\boldsymbol{\nu}_i)\boldsymbol{\nu}_i$ in the vessel dynamics.*

Extending the candidate function (3.166) into the Lyapunov function

$$V_4(\boldsymbol{\zeta}, \bar{\boldsymbol{\eta}}, \bar{\boldsymbol{\nu}}, \boldsymbol{\omega}_\zeta, \theta, t) = V_3(\boldsymbol{\zeta}, \bar{\boldsymbol{\eta}}, \bar{\boldsymbol{\nu}}, \theta, t) + \frac{1}{2\mu_\zeta} \boldsymbol{\omega}_\zeta^\top \mathbf{A}_\zeta^{-1} \boldsymbol{\omega}_\zeta, \tag{3.169}$$

and differentiating with respect to time finally yields

$$\begin{aligned}
\dot{V}_4 \leq & -\sum_{i \in \mathcal{I}} \left(\mathbf{z}_{1i}^\top \mathbf{Q}_{1i} \mathbf{z}_{1i} + 2\mathbf{z}_{2i}^\top \mathbf{K}_{di} \mathbf{z}_{2i} \right) - \rho k_{\zeta_3} \epsilon \tilde{\zeta}_3^2 - V_3^{\boldsymbol{\zeta}}(\boldsymbol{\zeta}, \bar{\boldsymbol{\eta}}, \bar{\boldsymbol{\nu}}, \theta, t) \boldsymbol{\omega}_\zeta \\
& - \frac{1}{\mu_\zeta} \boldsymbol{\omega}_\zeta^\top \boldsymbol{\omega}_\zeta + \boldsymbol{\omega}_\zeta^\top V_3^{\boldsymbol{\zeta}}(\boldsymbol{\zeta}, \bar{\boldsymbol{\eta}}, \bar{\boldsymbol{\nu}}, \theta, t)^\top \\
= & -\sum_{i \in \mathcal{I}} \left(\mathbf{z}_{1i}^\top \mathbf{Q}_{1i} \mathbf{z}_{1i} + 2\mathbf{z}_{2i}^\top \mathbf{K}_{di} \mathbf{z}_{2i} \right) - \rho k_{\zeta_3} \epsilon \tilde{\zeta}_3^2 - \frac{1}{\mu_\zeta} \boldsymbol{\omega}_\zeta^\top \boldsymbol{\omega}_\zeta \\
\leq & \, 0
\end{aligned}$$

3.4.3.3 Operation phases

The activation functions $\sigma_k(\cdot)$ were included in (3.151), (3.153), and (3.154) to enable prioritization and separation between the task of establishing the formation, and the task of getting the formation to converge to the specified path. Through proper tuning of the system, this is achieved by effectively dividing an operation into two distinct phases:

Coordination phase: By design, the activation functions $\sigma_k\left(|\bar{\boldsymbol{\eta}} - \bar{\boldsymbol{\eta}}_d(\boldsymbol{\zeta}, t)|_L^2\right)$ can attain values arbitrarily close to zero for $|\bar{\boldsymbol{\eta}} - \bar{\boldsymbol{\eta}}_d(\boldsymbol{\zeta}, t)|_L \geq c$, where c is threshold that can define when the vessels are "out of formation". In the coordination phase, where the vessels are outside this threshold, the dynamics (3.151)–(3.154) consequently simplify to

$$\begin{aligned}
f_\theta(\boldsymbol{\zeta}, \bar{\boldsymbol{\eta}}, \theta, t) &\approx \mu_\theta s(\mathbf{p}_\zeta, \theta), \\
\mathbf{f}_{p\zeta}(\boldsymbol{\zeta}, \bar{\boldsymbol{\eta}}, t) &\approx 0, \\
f_{\zeta_3}(\boldsymbol{\zeta}, \bar{\boldsymbol{\eta}}, \theta, t)) &\approx \psi_{los}^{\mathbf{p}_\zeta}(\mathbf{p}_\zeta, \theta) \mathbf{f}_{p\zeta}(\boldsymbol{\zeta}, \bar{\boldsymbol{\eta}}, t) + \psi_{los}^{\theta}(\mathbf{p}_\zeta, \theta) f_\theta(\boldsymbol{\zeta}, \bar{\boldsymbol{\eta}}, \theta, t), \\
&\approx \mu_\theta \psi_{los}^{\theta}(\mathbf{p}_\zeta, \theta) s(\mathbf{p}_\zeta, \theta),
\end{aligned}$$

where the last transition follows from $|\psi_{los}^{\mathbf{p}_\zeta}(\mathbf{p}_\zeta, \theta)| \leq \frac{1}{\Delta}$ $\forall(\mathbf{p}_\zeta, \theta)$ (see Table 3.3 in Section 3.4.5.1). It is seen that the dynamics of θ reduce to a minimizer of the along-track distance $s(\mathbf{p}_\zeta, \theta)$. As the vessels are likely to require quite some time to reach their specified positions (in the order of minutes), there is no need for this optimization to be very fast. By choosing μ_θ small we can thus approximate[9]

$$\begin{aligned}
\dot{\boldsymbol{\zeta}} &= \mathbf{f}_\zeta(\boldsymbol{\zeta}, \bar{\boldsymbol{\eta}}, \theta, t) - \boldsymbol{\omega}_\zeta \\
&\approx -\boldsymbol{\omega}_\zeta
\end{aligned}$$

The result is that $\mathcal{F}$ will move to minimize the function $V_3(\boldsymbol{\zeta}, \bar{\boldsymbol{\eta}}, \bar{\boldsymbol{\nu}}, \theta, t)$ while the vessels use control efforts to obtain their specified positions relative to $\mathcal{F}$. Although the orientation error between $\mathcal{F}$ and the LOS angle is included in $V_3(\boldsymbol{\zeta}, \bar{\boldsymbol{\eta}}, \bar{\boldsymbol{\nu}}, \theta, t)$, the corresponding impact on the gradient optimization can be made arbitrarily small by choosing ρ small. The vessels and $\mathcal{F}$ will then collaborate in establishing the formation as quickly as possible without paying any attention to where the formation is established relative to the path, and the desired separation from the LOS path following phase is achieved.

[9] It is noted that $f_{\zeta_3}(\boldsymbol{\zeta}, \bar{\boldsymbol{\eta}}, \theta, t)) \approx \mu_\theta \psi_{los}^{\theta}(\mathbf{p}_\zeta, \theta) s(\mathbf{p}_\zeta, \theta)$ can cause some rotational motion for $\mathcal{F}$ during coordination. The effect can, however, be mitigated by ensuring a small initial along-track error through proper initialization of θ, and by choosing μ_θ small.

LOS path following phase: After the vessels have converged to their desired generalized positions relative to $\mathcal{F}$, the LOS path following phase is initiated as a result of the activation functions approaching unity in value. This activates the feedback in (3.154) turning $\mathcal{F}$ towards the LOS angle, as well as the desired forward motion $U_d(t)$ translating $\mathcal{F}$ in the direction of its x-axis. Through tuning of the gain k_{ζ_3} in (3.154) and the relative shaping of the two activation functions, the transient behavior in the path following phase can be manipulated. By Choosing k_{ζ_3} large and making sure that $\sigma_2\left(|\bar{\boldsymbol{\eta}} - \bar{\boldsymbol{\eta}}_d(\boldsymbol{\zeta}, t)|_L^2\right)$ approaches unity faster than $\sigma_1\left(|\bar{\boldsymbol{\eta}} - \bar{\boldsymbol{\eta}}_d(\boldsymbol{\zeta}, t)|_L^2\right)$, the time taken and distance traveled before the orientation of $\mathcal{F}$ reaches the LOS angle is likely to be shorter than if k_{ζ_3} is chosen small and $\sigma_1(\cdot), \sigma_2(\cdot)$ is tuned the other way around. The appropriate choice will depend on the maneuverability of the vessels and the specific formation configuration.

3.4.4 Stability analysis

3.4.4.1 Assumptions

The following assumptions are made:

Assumption 5. *The configuration vectors $\mathbf{l}_i(t) \in \mathcal{C}^2$, and $\exists\ l_{max} < \infty$ so that $\forall i \in \mathcal{I}$ and $\forall t \geq t_0$, then* $\max\{|\mathbf{l}_i(t)|, |\mathbf{l}_i^t(t)|\} \leq l_{max}$.

Assumption 6. *The desired speed function $U_d(t) \in \mathcal{C}^1$, and $\exists U_{max} < \infty$ such that $\forall t \geq t_0$*

$$0 < U_d(t) \leq U_{max}$$

Assumption 7. *The path $\mathbf{p}_d(\theta) \in \mathcal{C}^3$, and $\exists (p_1, p_2) > 0$ s.t. $\forall \theta \in \mathbb{R}$,*

$$p_1 \leq |\mathbf{p}_d^\theta(\theta)| \leq p_2$$

The reason for requiring $\mathbf{p}_d(\theta) \in \mathcal{C}^3$ is that the control laws for each vessels utilize the third derivatives of the path function through the feedforward signal (3.162).

Proposition 2. *By assumption 7, there exists constants $L_\theta, c_\theta > 0$ such that $\forall \theta \in \mathbb{R}$,*

$$|\mathbf{p}_d(\theta)| \leq L_\theta |\theta| + c_\theta$$

Proof. See Appendix C.3. □

3.4.4.2 Change of variables

Define

$$\mathbf{z}_1 := col(\mathbf{z}_{11}, \ldots, \mathbf{z}_{1r}) \qquad \in \mathbb{R}^{3r} \tag{3.170}$$

$$\mathbf{z}_2 := col(\mathbf{z}_{21}, \ldots, \mathbf{z}_{2r}) \qquad \in \mathbb{R}^{3r} \tag{3.171}$$

$$\mathbf{x} = col(\bar{\boldsymbol{\eta}}, \bar{\boldsymbol{\nu}}, \boldsymbol{\zeta}, \boldsymbol{\omega}_\zeta, \theta, t) \qquad \in \mathbb{R}^{6r+8} \tag{3.172}$$

$$\boldsymbol{\phi} = col(\mathbf{z}_1, \mathbf{z}_2, \tilde{\zeta}_3, \mathbf{p}_\zeta, \boldsymbol{\omega}_\zeta, \theta, t) \qquad \in \mathbb{R}^{6r+8} \tag{3.173}$$

In subsequent analysis, the diffeomorphism $\mathbf{x} \mapsto \boldsymbol{\phi}$ is applied. The change of variables is performed through the continuously differentiable map $\mathbf{T} : \mathbb{R}^{6r+8} \mapsto \mathbb{R}^{6r+8}$, where $\boldsymbol{\phi} = \mathbf{T}(\mathbf{x})$. The continuously differentiable inverse map $\mathbf{x} = \mathbf{T}^{-1}(\boldsymbol{\phi})$ is given implicitly by

$$\boldsymbol{\zeta}(\mathbf{p}_\zeta, \tilde{\zeta}_3, \theta) = \mathbf{I}_{3\times 2}\mathbf{p}_\zeta + \left(\tilde{\zeta}_3 + \psi_{los}(\mathbf{p}_\zeta, \theta)\right)\mathbf{h}_3, \tag{3.174}$$

$$\bar{\boldsymbol{\eta}}(\mathbf{z}_1, \mathbf{p}_\zeta, \tilde{\zeta}_3, \theta, t) = \mathbf{z}_1 + \bar{\boldsymbol{\eta}}_d\left(\boldsymbol{\zeta}(\mathbf{p}_\zeta, \tilde{\zeta}_3, \theta), t\right), \tag{3.175}$$

$$\bar{\boldsymbol{\nu}}(\mathbf{z}_1, \mathbf{z}_2, \mathbf{p}_\zeta, \tilde{\zeta}_3, \theta, t) = \mathbf{z}_2 + \bar{\boldsymbol{\alpha}}\left(\bar{\boldsymbol{\eta}}(\mathbf{z}_1, \mathbf{p}_\zeta, \tilde{\zeta}_3, \theta, t), \boldsymbol{\zeta}(\mathbf{p}_\zeta, \tilde{\zeta}_3, \theta), \theta, t\right), \tag{3.176}$$

where

$$\bar{\boldsymbol{\alpha}}(\boldsymbol{\zeta},\bar{\boldsymbol{\eta}},\theta,t) = col(\boldsymbol{\alpha}_1(\boldsymbol{\zeta},\bar{\boldsymbol{\eta}},\theta,t),\ldots,\boldsymbol{\alpha}_r(\boldsymbol{\zeta},\bar{\boldsymbol{\eta}},\theta,t)) \quad \in \mathbb{R}^{3r},$$
$$\mathbf{I}_{3\times 2} = \begin{bmatrix} 1 & 0 \\ 0 & 1 \\ 0 & 0 \end{bmatrix},$$
$$\mathbf{h}_3 = col(0,0,1)$$

It is noted that by assumptions 5–7, the diffeomorphism satisfies $\lim_{|\mathbf{x}|\to\infty} |\mathbf{T}(\mathbf{x})| = \infty$ (see Appendix C.4 for a proof of this statement), so that boundedness of $|\boldsymbol{\phi}|$ implies boundedness of $|\mathbf{x}|$.

3.4.4.3 Closed-loop system

The closed-loop system in our transformed variables is given by (omitting the argument lists of the original variables wherever they appear for convenience)

$$\dot{\mathbf{z}}_{1i} = \mathbf{A}_{1i}\mathbf{z}_{1i} + \mathbf{R}(\psi_i)\mathbf{z}_{2i} + \boldsymbol{\eta}_{di}^{\boldsymbol{\zeta}}(\boldsymbol{\zeta},t)\boldsymbol{\omega}_\zeta \qquad i \in \mathcal{I} \tag{3.177}$$
$$\dot{\mathbf{z}}_{2i} = \mathbf{M}_i^{-1}\left(-\mathbf{K}_{di}\mathbf{z}_{2i} - \mathbf{D}_i(\boldsymbol{\nu}_i)\mathbf{z}_{2i} - \mathbf{C}_i(\boldsymbol{\nu}_i)\mathbf{z}_{2i} - \mathbf{R}(\psi_i)^\top\mathbf{P}_{1i}\mathbf{z}_{1i}\right) + \boldsymbol{\alpha}_i^{\boldsymbol{\zeta}}(\boldsymbol{\zeta},\bar{\boldsymbol{\eta}},\theta,t)\boldsymbol{\omega}_\zeta \qquad i \in \mathcal{I} \tag{3.178}$$
$$\dot{\tilde{\zeta}}_3 = -k_{\zeta_3}\sigma_2\left(|\mathbf{z}_1|_L^2\right)\tilde{\zeta}_3 + \left(\psi_{los}^{\mathbf{p}_\zeta}(\mathbf{p}_\zeta,\theta)\mathbf{I}_{2\times 3} - \mathbf{h}_3^\top\right)\boldsymbol{\omega}_\zeta \tag{3.179}$$
$$\dot{\mathbf{p}}_\zeta = \begin{bmatrix}\cos(\zeta_3)\\ \sin(\zeta_3)\end{bmatrix} U_d(t)\sigma_1\left(|\mathbf{z}_1|_L^2\right) - \mathbf{I}_{2\times 3}\boldsymbol{\omega}_\zeta \tag{3.180}$$
$$\dot{\boldsymbol{\omega}}_\zeta = -\mathbf{A}_\zeta\boldsymbol{\omega}_\zeta + \mathbf{A}_\zeta\mu_\zeta V_3^{\boldsymbol{\zeta}}(\boldsymbol{\zeta},\bar{\boldsymbol{\eta}},\bar{\boldsymbol{\nu}},\theta,t)^\top \tag{3.181}$$
$$\dot{\theta} = \frac{\Delta}{\sqrt{\Delta^2 + e(\mathbf{p}_\zeta,\theta)^2}}\frac{U_d(t)\sigma_1\left(|\mathbf{z}_1|_L^2\right)}{|\mathbf{p}_d^\theta(\theta)|} + \mu_\theta\frac{\mathbf{p}_d^\theta(\theta)^\top}{|\mathbf{p}_d^\theta(\theta)|}(\mathbf{p}_\zeta - \mathbf{p}_d(\theta)) \tag{3.182}$$
$$\dot{t} = 1 \tag{3.183}$$

3.4.4.4 Main result

Theorem 3. *Under assumptions 5–7, the control system given jointly by the dynamical assignments* (3.149)–(3.154),(3.168)*, and the vessel control laws* (3.164)*, renders the set*

$$\mathcal{M} = \{(\mathbf{z}_1,\mathbf{z}_2,\tilde{\zeta}_3,\mathbf{p}_\zeta,\boldsymbol{\omega}_\zeta,\theta,t) \in \mathbb{R}^{6r+8} : \quad \mathbf{z}_1 = \mathbf{0}, \mathbf{z}_2 = \mathbf{0}, \boldsymbol{\omega}_\zeta = \mathbf{0}, \tilde{\zeta}_3 = 0\}$$

UGES, and solves the control objectives (3.141)–(3.143)*.*

Proof. The closed-loop system (3.177)–(3.183) can be restated on the form of the interconnected system (A.5) in Appendix A.2 by choosing $\mathbf{x}_1 = col(\mathbf{z}_1,\mathbf{z}_2,\tilde{\zeta}_3,\boldsymbol{\omega}_\zeta) \in \mathbb{R}^{6r+4}$, $\mathbf{x}_2 = col(\mathbf{p}_\zeta,\theta,t) \in \mathbb{R}^4$, and $(\mathbf{u}_1,\mathbf{u}_2) = \mathbf{0}$. With these choices in mind, the set $\mathcal{M}$ can be restated on the form (A.6), where the compact set $\mathcal{A}_1$ is given by the equilibrium point

$$\mathcal{A}_1 = \{(\mathbf{z}_1,\mathbf{z}_2,\tilde{\zeta}_3,\boldsymbol{\omega}_\zeta) \in \mathbb{R}^{6r+4} : \quad \mathbf{z}_1 = \mathbf{0}, \mathbf{z}_2 = \mathbf{0}, \boldsymbol{\omega}_\zeta = \mathbf{0}, \tilde{\zeta}_3 = 0\},$$

with corresponding distance function $|(\mathbf{z}_1,\mathbf{z}_2,\tilde{\zeta}_3,\boldsymbol{\omega}_\zeta)|_{\mathcal{A}_1} = |(\mathbf{z}_1,\mathbf{z}_2,\tilde{\zeta}_3,\boldsymbol{\omega}_\zeta)|$. We can thus examine stability of $\mathcal{M}$ through Theorem A.2.

The first step is to show that the sector bound (A.7) holds for the system. For $(\mathbf{z}_1,\mathbf{z}_2,\tilde{\zeta}_3,\boldsymbol{\omega}_\zeta)$ confined in

a compact set in which $|(\mathbf{z}_1, \mathbf{z}_2, \tilde{\zeta}_3, \boldsymbol{\omega}_\zeta)| \leq C$, we have that (utilizing assumptions 6–7 and Proposition 2)

$$\begin{aligned} |\dot{\mathbf{p}}_\zeta| &\leq U_{max} + C \\ |\dot{\theta}| &\leq \frac{U_{max}}{p_1} + \mu_\theta \left(|\mathbf{p}_\zeta| + L_\theta |\theta| + c_\theta\right) \\ |\dot{t}| &= 1 \end{aligned}$$

Since

$$\begin{aligned} |(\dot{\mathbf{p}}_\zeta, \dot{\theta}, \dot{t})| &\leq |\dot{\mathbf{p}}_\zeta| + |\dot{\theta}| + |\dot{t}|, \\ |\mathbf{p}_\zeta|, |\theta| &\leq |(\mathbf{p}_\zeta, \theta, t)|, \end{aligned}$$

this yields

$$|(\dot{\mathbf{p}}_\zeta, \dot{\theta}, \dot{t})| \leq \mu_\theta (L_\theta + 1) |(\mathbf{p}_\zeta, \theta, t)| + U_{max} + C + \frac{U_{max}}{p_1} + \mu_\theta c_\theta + 1,$$

which clearly shows that the sector bound (A.7) is satisfied.

Since the smooth function

$$V_4(\mathbf{z}_1, \mathbf{z}_2, \tilde{\zeta}_3, \boldsymbol{\omega}_\zeta) = \sum_{i \in \mathcal{I}} \left(\mathbf{z}_{1i}^\top \mathbf{P}_{1i} \mathbf{z}_{1i} + \mathbf{z}_{2i}^\top \mathbf{M}_i \mathbf{z}_{2i}\right) + \frac{\rho}{2} \tilde{\zeta}_3^2 + \frac{1}{2\mu_\zeta} \boldsymbol{\omega}_\zeta^\top \mathbf{A}_\zeta^{-1} \boldsymbol{\omega}_\zeta$$

satisfies

$$\begin{aligned} d_1 |(\mathbf{z}_1, \mathbf{z}_2, \tilde{\zeta}_3, \boldsymbol{\omega}_\zeta)|^2 \leq V_4(\mathbf{z}_1, \mathbf{z}_2, \tilde{\zeta}_3, \boldsymbol{\omega}_\zeta) \leq d_2 |(\mathbf{z}_1, \mathbf{z}_2, \tilde{\zeta}_3, \boldsymbol{\omega}_\zeta)|^2, \\ \dot{V}_4 \leq -d_3 |(\mathbf{z}_1, \mathbf{z}_2, \tilde{\zeta}_3, \boldsymbol{\omega}_\zeta)|^2, \end{aligned}$$

where

$$\begin{aligned} d_1 &= \min \left\{ \min_{i \in \mathcal{I}} \{\lambda_{min, P_{1i}}\}, \min_{i \in \mathcal{I}} \{\lambda_{min, M_i}\}, \frac{\rho}{2}, \frac{1}{2\mu_\zeta} \lambda_{min, A_\zeta^{-1}} \right\} > 0, \\ d_2 &= \max \left\{ \max_{i \in \mathcal{I}} \{\lambda_{max, P_{1i}}\}, \max_{i \in \mathcal{I}} \{\lambda_{max, M_i}\}, \frac{\rho}{2}, \frac{1}{2\mu_\zeta} \lambda_{max, A_\zeta^{-1}} \right\} > 0, \\ d_3 &= \min \left\{ \min_{i \in \mathcal{I}} \{\lambda_{min, Q_{1i}}\}, 2 \min_{i \in \mathcal{I}} \{\lambda_{min, K_{di}}\}, \rho k_{\zeta_3} \epsilon, \frac{1}{\mu_\zeta} \right\} > 0, \end{aligned}$$

UGES is concluded for the set $\mathcal{M}$ by Theorem A.2.

Having established UGES, it follows that $\lim_{t^* \to \infty} (|\mathbf{z}_1(t^*)|, |\mathbf{z}_2(t^*)|, |\tilde{\zeta}_3(t^*)|, |\boldsymbol{\omega}_\zeta(t^*)|) = 0$. From the definitions of $\mathbf{z}_1$ and $\tilde{\zeta}_3$, it follows that the control objectives (3.141)–(3.142) are fulfilled. Fulfillment of the control objective (3.143) follows from the closed-loop dynamics (3.180) and the property (3.148a). A formal proof of the last statement is given in Appendix C.5. □

3.4.5 Practical considerations

3.4.5.1 Notes on implementation

The control design is summarized in Table 3.3. When implementing the design, it is important to apply the orientation handler algorithm in Section 3.2.5.1 to all orientation error variables that are used in the control system (the third elements of the signals $\mathbf{z}_{1i}$, $i = 1 \dots r$, and $\tilde{\zeta}_3 = \zeta_3 - \psi_{los}(\mathbf{p}_\zeta, \theta)$).

3.4.5.2 Choosing relative heading angles in the formation configuration vectors

In the control designs of this thesis, a formation is specified as a set of relative position vectors and heading angles through the formation configuration vectors $\mathbf{l}_i(t) = col(x_{ci}(t), y_{ci}(t), \psi_{ci}(t))$. Although this rigorous formation specification can be useful for some operations, it might be a bit overkill for others. More specifically, it might be of interest to specify the formation as a set of relative positions without posing any restrictions on the relative heading angles. The vessels can then control their orientation in a manner that yields the most efficient and feasible motion within the moving formation. This might involve choosing orientations that enable the vessels to follow their designated positions by utilizing surge and yaw motion exclusively, as controlling motion in sway can become difficult at higher speeds[10].

When the LOS path following phase is initiated (see Section 3.4.3.3), the vessels will be in formation with respect to $\mathcal{F}$, which in turn will utilize surge and yaw motion exclusively to guide the formation towards the path. During this phase of the operation, the motion of the positions we want the vessels to track is consequently very predictable, enabling us to specify relative heading angles $\psi_{ci}(t)$ that allow pure surge and yaw motion for the vessels during tracking. A method for doing this will be presented in the following

The desired generalized positions for the vessels are given by

$$\boldsymbol{\eta}_{di}(\boldsymbol{\zeta}, t) = \boldsymbol{\zeta} + \mathbf{R}(\zeta_3)\mathbf{l}_i(t)$$

Separating this into desired positions and orientations yields

$$\mathbf{p}_{di} = \mathbf{p}_\zeta + \mathbf{R}_{2D}(\zeta_3)\mathbf{l}_{pi}(t), \tag{3.184}$$

$$\psi_{di} = \zeta_3 + \psi_{ci}(t), \tag{3.185}$$

where $\mathbf{l}_{pi}(t) = col(x_{ci}(t), y_{ci}(t))$, and $\mathbf{R}_{2D}(\cdot)$ is given in (3.126). Since $|\boldsymbol{\omega}|$ will be small after the coordination phase, we have that

$$\begin{aligned}\dot{\mathbf{p}}_{di} &= \dot{\mathbf{p}}_\zeta + \mathbf{R}_{2D}(\zeta_3)\left(\mathbf{S}_{2D}\mathbf{l}_{pi}(t)\dot{\zeta}_3 + \dot{\mathbf{l}}_{pi}(t)\right) \\ &\approx \mathbf{f}_{p\zeta}(\boldsymbol{\zeta}, \bar{\boldsymbol{\eta}}, t) + \mathbf{R}_{2D}(\zeta_3)\left(\mathbf{S}_{2D}\mathbf{l}_{pi}(t) f_{\zeta_3}(\boldsymbol{\zeta}, \bar{\boldsymbol{\eta}}, \theta, t) + \dot{\mathbf{l}}_{pi}(t)\right) =: \mathbf{v}^*_{di},\end{aligned}$$

where $\mathbf{S}_{2D}$ is given in Table 3.3. By directing the vessels along

$$\psi_{di} = \arctan\left(\frac{row(0,1)\mathbf{v}^*_{di}}{row(1,0)\mathbf{v}^*_{di}}\right), \tag{3.186}$$

during the LOS path following phase, they will thus be able to track $\mathbf{p}_{di}$ by utilizing surge and sway motion exclusively. By (3.185) this corresponds to

$$\psi_{ci} = \psi_{di} - \zeta_3, \tag{3.187}$$

[10] Due to the coupling between sway and yaw in the equations of motion, pure surge and yaw motion still requires control effort in sway. The most desirable choice for the orientations would enable the vessels to utilize forces/moments in surge/yaw exclusively while following the formation, making the motion applicable to underactuated vessels. This will, however, not be pursued further herein.

where it is noted that the orientation algorithm of Section 3.2.5.1 should be utilized when calculating the right hand side of the equation. To ensure that the heading configuration signals (3.187) are applied *after* the coordination phase, it is proposed that they are scaled with an activation function $\sigma_3(|\mathbf{z}_1|_L^2)$ satisfying the properties (3.148a)–(3.148b). By doing this, the signals will be close to zero during coordination, and the ships will thus synchronize their heading with the orientation of $\mathcal{F}$. Since the initial motion of $\mathcal{F}$ in the LOS path following phase will be positive along its x-axis, the corresponding initial values of $\psi_{ci} = \psi_{di} - \zeta_3$ will be close to zero, guaranteeing a smooth transition.

Since the control law for the i'th vessel requires signals for the first and second time derivatives of ψ_{ci}, the calculated signal should be passed through a fast, third order reference filter. This yields the algorithm

$$\begin{aligned}
\mathbf{v}_{di}^* &= \mathbf{f}_{p\zeta}(\boldsymbol{\zeta}, \bar{\boldsymbol{\eta}}, t) + \mathbf{R}_{2D}(\zeta_3)\left(\mathbf{S}_{2D}\mathbf{l}_{pi}(t) f_{\zeta_3}(\boldsymbol{\zeta}, \bar{\boldsymbol{\eta}}, \theta, t) + \dot{\mathbf{l}}_{pi}(t)\right) \\
\psi_{di} &= \arctan\left(\frac{row(0,1)\mathbf{v}_{di}^*}{row(1,0)\mathbf{v}_{di}^*}\right) \\
\psi_{ri} &= (\psi_{di} - \zeta_3)\sigma_3(|\mathbf{z}_1|_L^2) \\
\psi_{ci} &= \frac{\omega_l^3}{(s+\omega_l)^3}\psi_{ri}, \qquad \omega_l > 0
\end{aligned} \tag{3.188}$$

It is finally noted that by letting the time derivatives of ψ_{ci} be dependent on the states of the system, the stability result of Theorem 3 is no longer valid, as Assumption 5 no longer can be guaranteed. The algorithm has, however, proved itself in simulations, as demonstrated in Section 3.4.6.

Control laws	$\boldsymbol{\tau}_i = -\mathbf{R}(\psi_i)^\top \mathbf{P}_{1i}\mathbf{z}_{1i} - \mathbf{K}_{di}\mathbf{z}_{2i} + \mathbf{D}_i(\boldsymbol{\nu}_i)\boldsymbol{\alpha}_i + \mathbf{C}_i(\boldsymbol{\nu}_i)\boldsymbol{\alpha}_i + \mathbf{M}_i\boldsymbol{\delta}_i$
Internal dynamic variables	$\dot{\boldsymbol{\zeta}} = \mathbf{f}_\zeta(\boldsymbol{\zeta}, \bar{\boldsymbol{\eta}}, \theta, t) - \boldsymbol{\omega}_\zeta, \qquad \mathbf{f}_\zeta(\boldsymbol{\zeta}, \bar{\boldsymbol{\eta}}, \theta, t)$ is given in (3.152)–(3.154), $\boldsymbol{\zeta} = col(\mathbf{p}_\zeta, \zeta_3)$ $\dot{\theta} = f_\theta(\boldsymbol{\zeta}, \bar{\boldsymbol{\eta}}, \theta, t), \qquad f_\theta(\boldsymbol{\zeta}, \bar{\boldsymbol{\eta}}, \theta, t)$ is given in (3.151) $\dot{\boldsymbol{\omega}}_\zeta = -\mathbf{A}_\zeta\boldsymbol{\omega}_\zeta + \mathbf{A}_\zeta\mu_\zeta V_3^{\boldsymbol{\zeta}}(\boldsymbol{\zeta}, \bar{\boldsymbol{\eta}}, \bar{\boldsymbol{\nu}}, \theta, t)^\top$
Parameters	$\mathbf{K}_{di} = \mathbf{K}_{di}^\top > 0$ $\mathbf{A}_{1i}$ Hurwitz $\mathbf{P}_{1i} = \mathbf{P}_{1i}^\top > 0$ satisfying $\mathbf{P}_{1i}\mathbf{A}_{1i} + \mathbf{A}_{1i}^\top\mathbf{P}_{1i} = -\mathbf{Q}_{1i}$ for some $\mathbf{Q}_{1i} = \mathbf{Q}_{1i}^\top > 0$ $\mathbf{A}_\zeta = \mathbf{A}_\zeta^\top > 0$ $\mathbf{L} = \mathbf{L}^\top \geq 0 \qquad \mathbf{L} \in \mathbb{R}^{3r\times 3r}$ $\mu_\theta, \mu_\zeta, k_{\zeta_3}, \rho, \Delta > 0$
Signals	$\bar{\boldsymbol{\eta}} = col(\boldsymbol{\eta}_1, \ldots, \boldsymbol{\eta}_r)$ $\bar{\boldsymbol{\nu}} = col(\boldsymbol{\nu}_1, \ldots, \boldsymbol{\nu}_r)$ $\bar{\mathbf{R}}(\boldsymbol{\psi}) = diag(\mathbf{R}(\psi_1), \ldots, \mathbf{R}(\psi_r))$ $\mathbf{z}_1 = col(\mathbf{z}_{1i}, \ldots, \mathbf{z}_{1r})$ $\mathbf{z}_{1i} = \boldsymbol{\eta}_i - \boldsymbol{\eta}_{di}(\boldsymbol{\zeta}, t)$ $\mathbf{z}_{2i} = \boldsymbol{\nu}_i - \boldsymbol{\alpha}_i(\boldsymbol{\zeta}, \bar{\boldsymbol{\eta}}, \theta, t)$ $\lvert\mathbf{z}_1\rvert_L^2 = \lvert\bar{\boldsymbol{\eta}} - \bar{\boldsymbol{\eta}}_d(\boldsymbol{\zeta}, t)\rvert_L^2 = \mathbf{z}_1\mathbf{L}\mathbf{z}_1$ $\boldsymbol{\alpha}_i(\boldsymbol{\zeta}, \bar{\boldsymbol{\eta}}, \theta, t) = \mathbf{R}(\psi_i)^\top \left(\boldsymbol{\eta}_{di}^{\boldsymbol{\zeta}}(\boldsymbol{\zeta}, t)\mathbf{f}_\zeta(\boldsymbol{\zeta}, \bar{\boldsymbol{\eta}}, \theta, t) + \boldsymbol{\eta}_{di}^t(\boldsymbol{\zeta}, t) + \mathbf{A}_{1i}\mathbf{z}_{1i}\right)$ $\boldsymbol{\alpha}_i^{\boldsymbol{\zeta}}(\boldsymbol{\zeta}, \bar{\boldsymbol{\eta}}, \theta, t), \boldsymbol{\alpha}_i^{\bar{\boldsymbol{\eta}}}(\boldsymbol{\zeta}, \bar{\boldsymbol{\eta}}, \theta, t), \boldsymbol{\alpha}_i^\theta(\boldsymbol{\zeta}, \bar{\boldsymbol{\eta}}, \theta, t), \boldsymbol{\alpha}_i^t(\boldsymbol{\zeta}, \bar{\boldsymbol{\eta}}, \theta, t)$ are given in Appendix C.6 $\boldsymbol{\delta}_i = \boldsymbol{\alpha}_i^{\boldsymbol{\zeta}}(\boldsymbol{\zeta}, \bar{\boldsymbol{\eta}}, \theta, t)\mathbf{f}_\zeta(\boldsymbol{\zeta}, \bar{\boldsymbol{\eta}}, \theta, t) + \boldsymbol{\alpha}_i^\theta(\boldsymbol{\zeta}, \bar{\boldsymbol{\eta}}, \theta, t)\mathbf{f}_\theta(\boldsymbol{\zeta}, \bar{\boldsymbol{\eta}}, \theta, t)$ $+\boldsymbol{\alpha}_i^{\bar{\boldsymbol{\eta}}}(\boldsymbol{\zeta}, \bar{\boldsymbol{\eta}}, \theta, t)\bar{\mathbf{R}}(\boldsymbol{\psi})\bar{\boldsymbol{\nu}} + \boldsymbol{\alpha}_i^t(\boldsymbol{\zeta}, \bar{\boldsymbol{\eta}}, \theta, t)$ $\bar{\boldsymbol{\eta}}_d(\boldsymbol{\zeta}, t) = col(\boldsymbol{\eta}_{d1}(\boldsymbol{\zeta}, t), \ldots, \boldsymbol{\eta}_{dr}(\boldsymbol{\zeta}, t))$ $\boldsymbol{\eta}_{di}(\boldsymbol{\zeta}, t) = \boldsymbol{\zeta} + \mathbf{R}(\zeta_3)\mathbf{l}_i(t)$ $\boldsymbol{\eta}_{di}^{\boldsymbol{\zeta}}(\boldsymbol{\zeta}, t) = \mathbf{I}_3 + \mathbf{R}(\zeta_3)\mathbf{S}\mathbf{l}_i(t)\mathbf{h}_3^\top, \qquad \mathbf{h}_3 = col(0, 0, 1)$ $\boldsymbol{\eta}_{di}^t(\boldsymbol{\zeta}, t) = \mathbf{R}(\zeta_3)\mathbf{l}_i^t(t)$ $\psi_{los}(\mathbf{p}_\zeta, \theta) = \psi_d(\theta) + \arctan\left(\frac{-e(\mathbf{p}_\zeta, \theta)}{\Delta}\right)$ $\psi_{los}^{\mathbf{p}_\zeta}(\mathbf{p}_\zeta, \theta) = \frac{\Delta}{e(\mathbf{p}_\zeta, \theta)^2 + \Delta^2} row\left(\sin(\psi_d(\theta)), -\cos(\psi_d(\theta))\right)$ $\psi_{los}^\theta(\mathbf{p}_\zeta, \theta) = \psi_d^\theta(\theta) - \frac{\Delta}{e(\mathbf{p}_\zeta, \theta)^2 + \Delta^2} e^\theta(\mathbf{p}_\zeta, \theta)$ $e(\mathbf{p}_\zeta, \theta) = row(0, 1)\mathbf{R}_{2D}(\psi_d(\theta))^\top(\mathbf{p}_\zeta - \mathbf{p}_d(\theta))$ $e^\theta(\mathbf{p}_\zeta, \theta) = row(0, 1)\left(\mathbf{S}_{2D}^\top\mathbf{R}_{2D}(\psi_d(\theta))^\top(\mathbf{p}_\zeta - \mathbf{p}_d(\theta))\psi_d^\theta(\theta) - \mathbf{R}_{2D}(\psi_d(\theta))^\top\mathbf{p}_d^\theta(\theta)\right)$ $\mathbf{S}_{2D} = \begin{bmatrix} 0 & -1 \\ 1 & 0 \end{bmatrix}$ $\mathbf{p}_d(\theta) = col(x_d(\theta), y_d(\theta))$ $\psi_d(\theta) = \arctan\left(\frac{y_d^\theta(\theta)}{x_d^\theta(\theta)}\right)$ $\psi_d^\theta = \frac{y_d^{\theta 2} x_d^\theta - x_d^{\theta 2} y_d^\theta}{(x_d^\theta)^2 + (y_d^\theta)^2}$

Table 3.3: Control laws, design 3

3.4.6 Simulations

The author experienced some numerical problems when simulating the third design in closed loop. Utilizing fixed-step equation solvers in Matlab/Simulink caused the solutions to blow up, seemingly irrespective of how the control system was tuned. Switching to a standard variable-step integrator remedied this problem, but the solver used extremely short time-steps when integrating the system equations, resulting in very long execution times. The source of the problems seemed to be the gradient optimization, as setting $\boldsymbol{\omega}_\zeta \equiv \mathbf{0}$ yielded normal system behavior. Identifying the numerical difficulties as the characteristics of a stiff problem, a specialized solver for stiff system equations has been used in the following simulations. This has provided normal execution times, but as pointed out in the documentation of Matlab, lower accuracy is expected compared to the standard variable-step solver.

To demonstrate the third design, two simulation cases will be shown. Three vessels with dynamics given in Appendix B are considered. The path is chosen as a sine wave propagating along the positive y-axis of the $\mathcal{E}$-frame, with parameterization $x_d(\theta) = 100 + 100\sin(\frac{2\pi}{800}\theta)$, $y_d(\theta) = 100 + \theta$. The control parameters are chosen as $\mathbf{A}_{1i} = -10^{-3} \times diag(1,1,25)$, $\mathbf{P}_{1i} = 10^3 \times diag(2,2,150)$, $\mathbf{K}_{di} = 10^4 \times diag(5,5,60)$, $\mathbf{A}_\zeta = 10^3 \times \mathbf{I}_3$, $\mathbf{L} = diag(\mathbf{L}_0, \mathbf{L}_0, \mathbf{L}_0)$, $\mathbf{L}_0 = diag(1,1,1000)$, $\mu_\theta = 10^{-2}$, $\mu_\zeta = 2.1021 \times 10^{-5}$, $\rho = 10^{-4}$, $k_{\zeta_3} = 0.015$, $\Delta = 50$. The activation functions are chosen as[11] $\sigma_1(s) = \sigma_2(s) = e^{-0.2s}$. It is noted that no saturations have been implemented in the simulation model, so that the response times are somewhat unrealistic.

3.4.6.1 Case 1

In the first simulation case, the desired formation configuration is set according to $\mathbf{l}_1 = col(0, 80, 0)$, $\mathbf{l}_2 = col(0,0,0)$, $\mathbf{l}_3 = col(0,-80,0)$, which corresponds to a transversal line formation where the desired generalized position for Vessel 2 coincides with $\boldsymbol{\zeta}$. The desired speed for the formation is chosen as $U_d(t) \equiv 3[m/s]$, and the initial states are $\boldsymbol{\eta}_{10} = col(-760, 85, \frac{-3\pi}{4})$, $\boldsymbol{\eta}_{20} = col(-780, 200, \frac{-9\pi}{10})$, $\boldsymbol{\eta}_{30} = col(-745, 300, \frac{-7\pi}{6})$, $\boldsymbol{\zeta}_0 = col(-700, 180, -\pi)$, $\boldsymbol{\nu}_{10}, \boldsymbol{\nu}_{20}, \boldsymbol{\nu}_{30}, \boldsymbol{\omega}_{\zeta 0} = \mathbf{0}$, $\theta_0 = 10$.

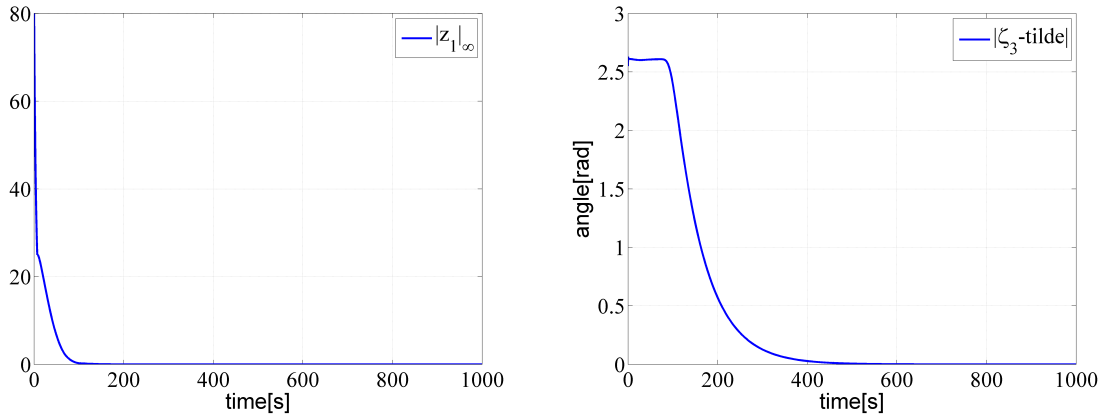

(a) $|\mathbf{z}_1(t)|_\infty$ (b) $|\tilde{\zeta}_3(t)|$

Figure 3.20: Time series of $|\mathbf{z}_1(t)|_\infty$ and $|\tilde{\zeta}_3(t)|$. At end of simulation, magnitudes are in the order of $O(10^{-4})$ and $O(10^{-5})$, respectively.

[11] This choice for $\sigma_2(\cdot)$ does not satisfy (3.148c). However, this is of no practical importance.

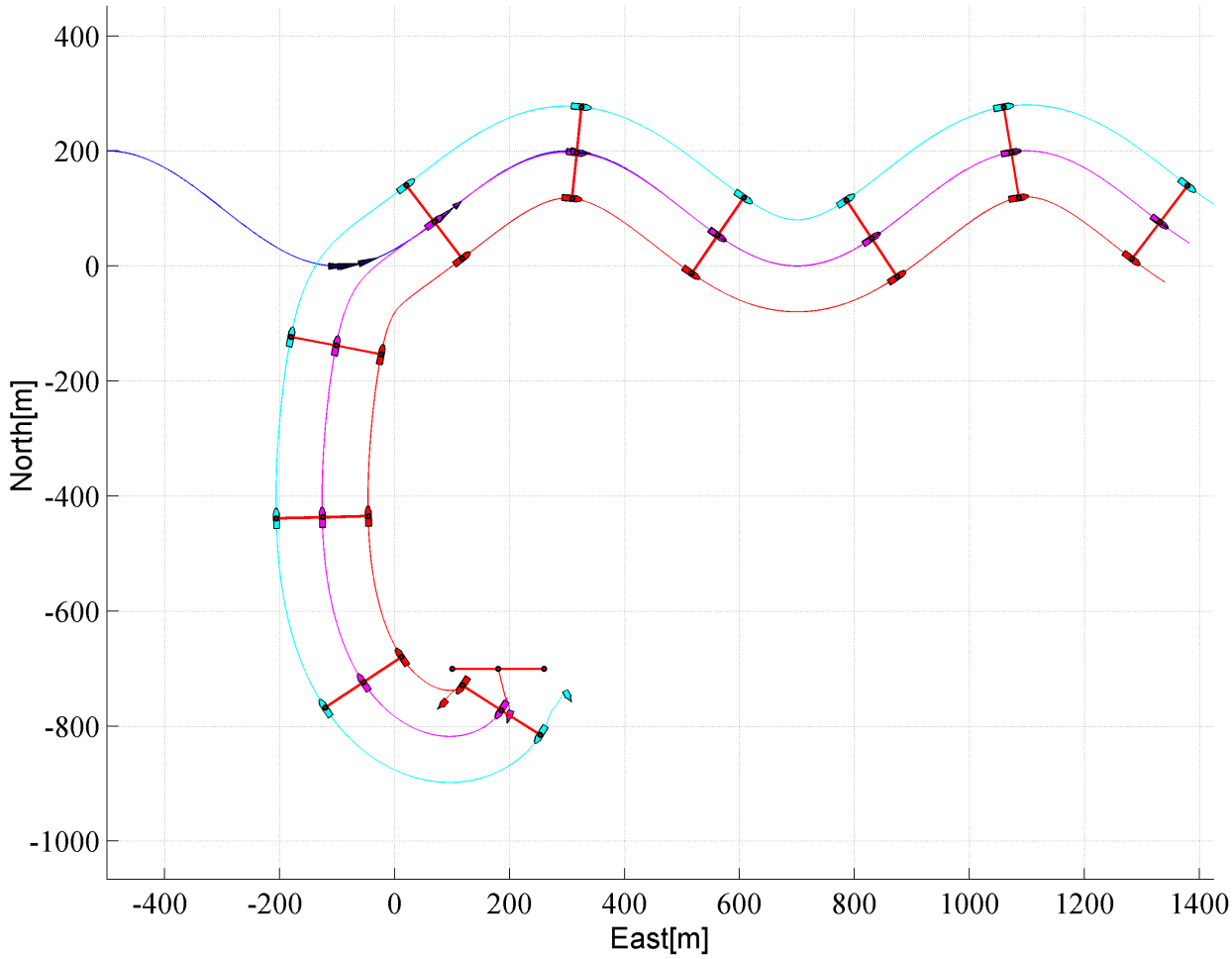

Figure 3.19: North-east position plot for the three vessels. The red, purple and blue ships correspond to vessels 1,2,3, respectively. The black arrow on the path indicates the position of $\mathbf{p}_d(\theta)$. The red bar with black dots represents the desired positions $\boldsymbol{\eta}_{di}$, $i = 1, 2, 3$, and the position of $\boldsymbol{\zeta}$ (equal to $\boldsymbol{\eta}_{d2}$). Initial positions are indicated by smaller-sized ships and arrow.

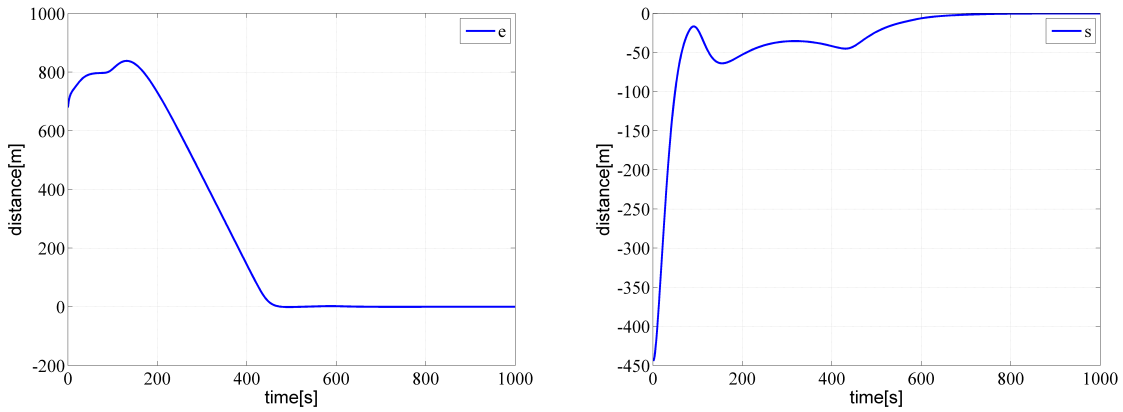

(a) $e(t)$ (b) $s(t)$

Figure 3.21: Time series of the cross-track and along-track errors $e(t)$ and $s(t)$. At end of simulation, magnitudes are in the order of $O(10^{-3})$ and $O(10^{-2})$, respectively.

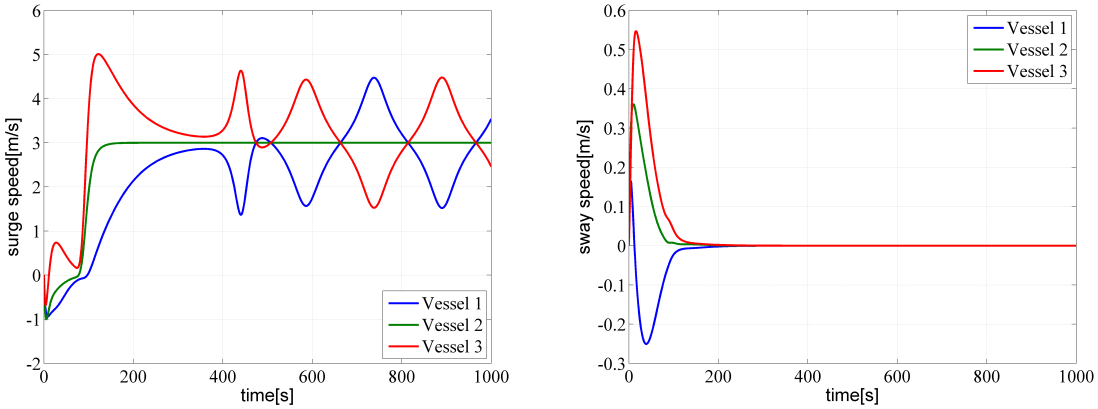

(a) Surge velocities

(b) Sway velocities

Figure 3.22: Surge and sway velocities for the three vessels

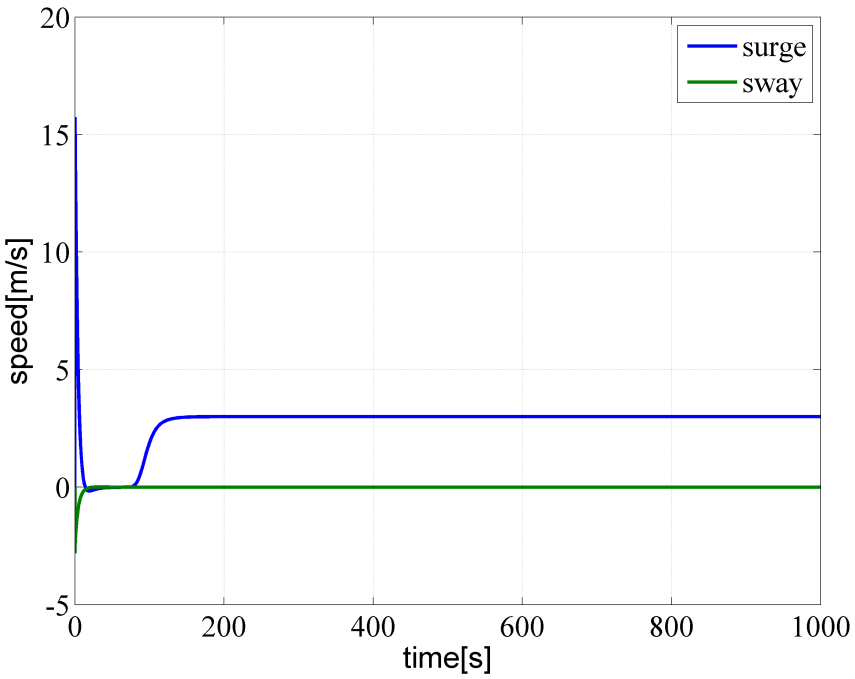

Figure 3.23: Surge and sway velocities for $\mathcal{F}$.

Figures 3.19, 3.20, and 3.23 clearly demonstrate that the proposed control system fulfills the control objectives (3.141)–(3.143). Separation between the tasks of group coordination and path following is also evident, as the desired motion (3.140) for $\mathcal{F}$ and convergence of $|\tilde{\zeta}_3(t)|$ is initiated *after* $|\mathbf{z}_1(t)|_\infty$ has converged. The effect of the gradient optimization can be seen by comparing figures 3.20(a), 3.22, and 3.23, as the initial rate of convergence for $|\mathbf{z}_1(t)|_\infty$ clearly exceeds the velocities of the vessels. It is also seen that the LOS steering algorithm ensures transient motion that is well suited for the vessels, despite the fact that the formation is established facing away from the path. The effectiveness of the algorithm with respect to path-convergence is verified in Figure 3.21.

3.4.6.2 Case 2

The purpose of this simulation is to demonstrate the algorithm proposed in Section 3.4.5.2 for ensuring pure surge and yaw motion for the vessels after group coordination. The initial formation configuration is chosen as a longitudinal line formation according to $\mathbf{l}_{p1} = col(-130, 0)$, $\mathbf{l}_{p2} = col(0, 0)$, $\mathbf{l}_{p3} = col(-65, 0)$. Due to the large x-components in these formation vectors, specifying $\psi_{ci}(t) \equiv 0$ would induce considerable sway motion for vessels 1 and 3 when moving in formation along a curved path. To illustrate the possibilities for formation reconfigurations, the configuration vectors gradually change through third order reference filters to $\mathbf{l}_{p1}^{new} = col(-40, 80)$, $\mathbf{l}_{p3}^{new} = col(-40, -80)$ after $t = 500[s]$. The parameter ω_l in (3.188) is chosen as $\omega_l = 100$, and the activation function $\sigma_3(\cdot)$ is chosen equal to $\sigma_1(\cdot)$. The desired speed for the formation is chosen as $U_d(t) \equiv 4[m/s]$, and the initial states for the system are $\boldsymbol{\eta}_{10} = col(-967.4, 95.3, \frac{11\pi}{60})$, $\boldsymbol{\eta}_{20} = col(-825.7, 107.4, \frac{\pi}{12})$, $\boldsymbol{\eta}_{30} = col(-900.4, 77, \frac{-\pi}{12})$, $\boldsymbol{\zeta}_0 = col(-780, 130, \frac{\pi}{12})$, $\boldsymbol{\nu}_{10}, \boldsymbol{\nu}_{20}, \boldsymbol{\nu}_{30}, \boldsymbol{\omega}_{\zeta 0} = \mathbf{0}$, $\theta_0 = -100$. It is noted that by including the algorithm (3.188) in the system, the closed-loop equations seemed to become even more stiff. To ensure feasible execution times for the simulation, the tolerance of the equation solver was relaxed in Matlab/Simulink.

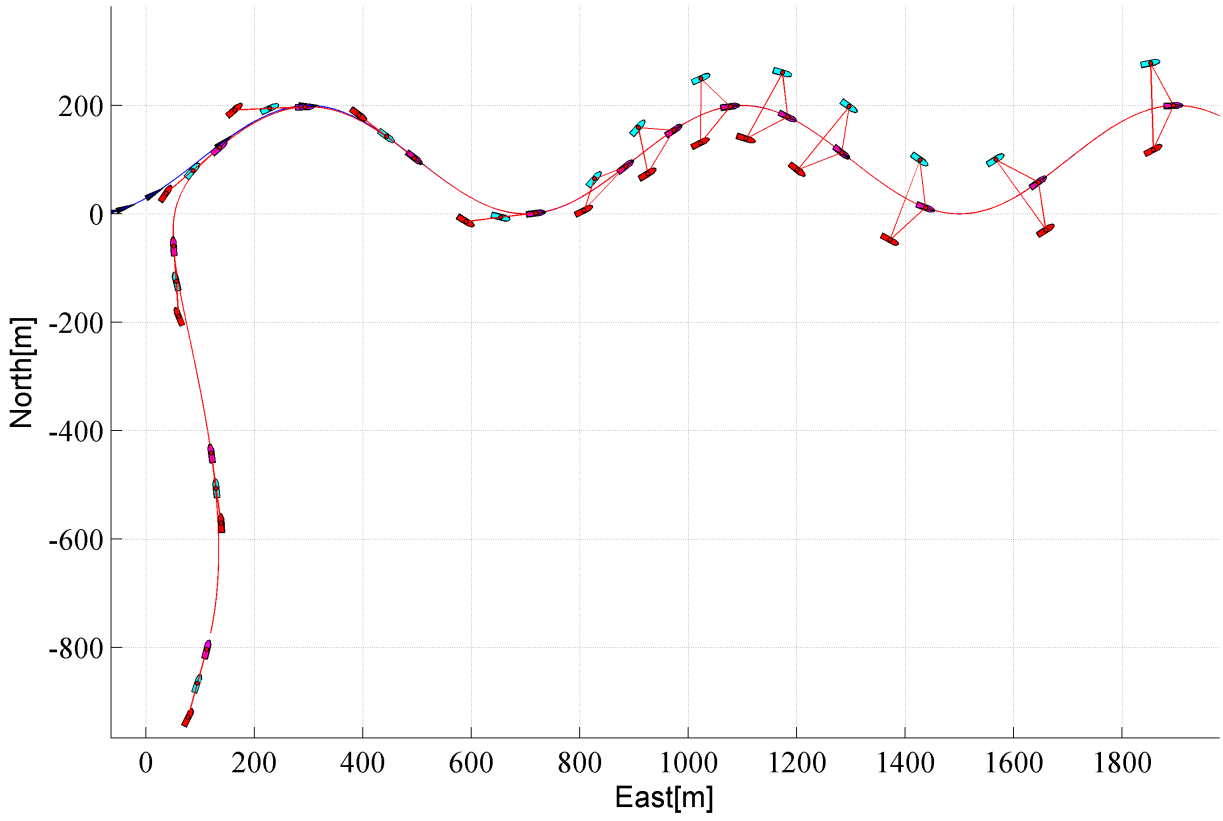

Figure 3.24: North-east position plot for the three vessels after the group coordination phase.

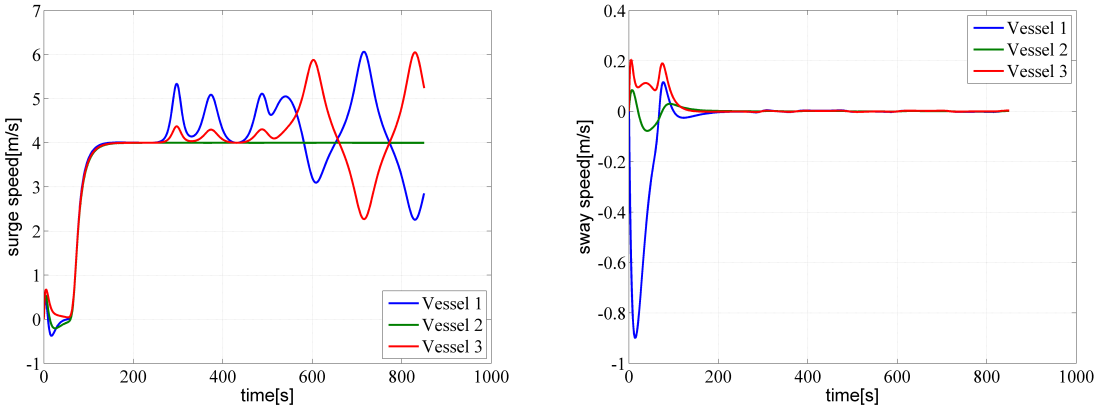

(a) Surge velocities

(b) Sway velocities

Figure 3.25: Surge and sway velocities for the three vessels

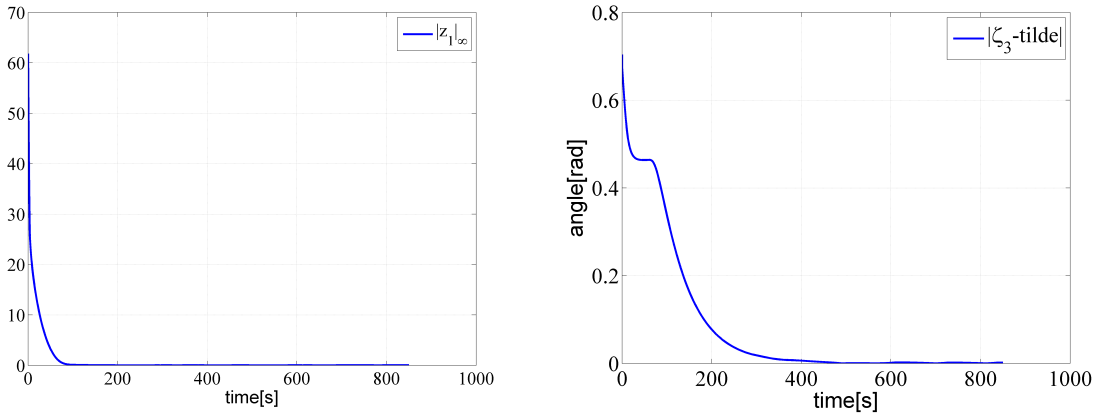

(a) $|\mathbf{z}_1(t)|_\infty$

(b) $|\tilde{\zeta}_3(t)|$

Figure 3.26: Time series of $|\mathbf{z}_1(t)|_\infty$ and $|\tilde{\zeta}_3(t)|$.

As seen from figures 3.25(b) and 3.26(a), the vessels move in formation without utilizing sway motion shortly after group coordination has been achieved. Figure 3.24 shows how the relative orientations of the vessels change dynamically to accommodate this behavior.

Chapter 4

Evaluation of control designs

In this chapter, the control designs of Chapter 3 will be evaluated against criteria that are important for formation control systems. In the end, the designs will be compared to one another in terms of advantages and disadvantages.

4.1 Evaluation criteria

The following aspects will be considered in the evaluation:

- **Communication requirements:** The possibility of extensive real-time communication between vessels is typically limited at sea. A good control design should take such restrictions into account and strive to limit the required inter-vessel communication.
- **Behavior during failure scenarios:** A formation control system should be well-behaved in the case of vessel failures. This includes mild failures such as saturations, and severe scenarios such as blackouts. The desired behavior during failure scenarios depends on operational philosophy. In some applications, it might be of interest to leave a failing vessel behind, while in others, maintaining the formation structure might be of utmost importance. Since the task of group coordination has been given the highest priority in the control designs of this thesis, the desired behavior during vessel failures will be defined by an ability to maintain the specified formation structure.
- **Collision avoidance capabilities:** Formation control deals with simultaneous control of multiple vessels. The danger of collisions during operations is thus of major concern. Ideally, a formation control system should include functionality that strives to avoid collisions during operations. This is important in the initial phase of an operation where the formation is established, during formation reconfigurations, and during failure scenarios.
- **Transient behavior during group coordination and path following:** The separation of group coordination and path following has shaped the overall transients of the proposed formation control systems. Transient behavior within the operational phases is, however, also of importance. In this respect, factors such as feasibility and efficiency of motion for the vessels should be considered.

4.2 Evaluation

4.2.1 Communication requirements

By following the framework of Arcak (2007), the first two control designs have to some extent incorporated limitations on inter-vessel communication through the use of a communication topology. Specifically, limitations on the communication required to obtain the synchronization terms in the control laws (the terms

$\boldsymbol{\alpha}_i$) have been incorporated. In this respect, the designs satisfy the notion of a decentralized solution. However, the control law for each vessel/virtual vessel requires access to more external signals than those required for calculation of the synchronization term, namely the common velocity input $\mathbf{v}_d$ and its time-derivative $\dot{\mathbf{v}}_d$. For the proposed solution of the formation mission task, $\mathbf{v}_d$ and $\dot{\mathbf{v}}_d$ incorporates feedback from the states of the vessels, as evident from Table 3.1. In the most general case, data must therefore be collected in real-time to calculate $\mathbf{v}_d$ and $\dot{\mathbf{v}}_d$, which in turn must be distributed back to the vessels. The result is a centralized control system requiring significant communication during operations.

The author has identified a way to circumvent the issues described above. By choosing the matrix $\mathbf{L}_1$ incorporated in the activation functions $\sigma_1(|\mathbf{z}|^2_{L_1}), \sigma_2(|\mathbf{z}|^2_{L_1})$ such that only the synchronization errors between the acting leader and its neighbors in the communication topology are required for calculating $|\mathbf{z}|^2_{L_1}$, the acting leader can calculate all terms required in $\mathbf{v}_d$ and $\dot{\mathbf{v}}_d$ locally while adhering to the restricted lines of communication[1]. The signals can subsequently be distributed to the acting leaders neighboring vessels in the communication topology, which in turn distribute the signals to their neighbors until all the vessels have received them. This approach yields a fully decentralized design, although there are some downsides. First of all, time-delays would be introduced into the system as a result of the stepwise distribution of $\mathbf{v}_d$ and $\dot{\mathbf{v}}_d$. For large groups of vessels spanning long distances, this could possibly deteriorate performance of the control system. Furthermore, choosing the matrix $\mathbf{L}_1$ as suggested can lead to situations where the path following phase is initiated prematurely, as the omitted synchronization errors lose influence on the activations functions $\sigma_1(|\mathbf{z}|^2_{L_1}), \sigma_2(|\mathbf{z}|^2_{L_1})$.

The third control design is very inefficient in terms of communication requirements. As seen in Table 3.3, the controller of each vessel requires access to the states of all the vessels in the group (through the signals $\boldsymbol{\alpha}_i, \boldsymbol{\delta}_i$), as does the update laws for the internal dynamic variables $\boldsymbol{\zeta}$, θ, $\boldsymbol{\omega}_\zeta$. To cope with these demands in a real-world implementation, communication links would have to be set up between each vessel and a central hub, resulting in a highly centralized system. With the exception of the workaround for the first two control designs, it is thus concluded that the communication requirements of the proposed control systems are extensive. In general, the author therefore recommends that the use of the designs is limited to small groups of vessels.

4.2.2 Behavior during vessel failures

In this section, simulations demonstrating how the three control designs behave during two different failure scenarios will be shown. The chosen scenarios correspond to surge speed saturation and a total loss of propulsion ('blackout') for a single vessel.

4.2.2.1 Velocity saturation scenario

In the following simulations, three vessels with dynamics given in Appendix B are considered. The desired formation structure is chosen according to $\mathbf{l}_1 = col(0, 80, 0)$, $\mathbf{l}_2 = col(0, 0, 0)$, and $\mathbf{l}_3 = col(0, -80, 0)$, and the path is chosen as the sine wave in Section 3.4.6. A saturation limit $u_{max} = 5[m/s]$ has been set for the surge speed of Vessel 3. To trigger the saturation, the desired speed for the formation change from $U_d = 2[m/s]$ to $U_d = 8[m/s]$ through a reference filter after $t = 500[s]$. The initial positions of the vessels are chosen as $\boldsymbol{\eta}_{10} = col(-70, 185, \frac{\pi}{10})$, $\boldsymbol{\eta}_{20} = col(-50, 140, 0)$, $\boldsymbol{\eta}_{30} = col(-80, 50, -\frac{\pi}{6})$, and the initial velocities are set equal to zero. All control parameters for designs 1,2 and 3 are set in accordance with sections 3.2.6 (Case 1), 3.3.8, and 3.4.6 (Case 1), respectively, with the exception of $\sigma_1(s) = \sigma_2(s) = e^{-0.25s}$ for Design 1. For the second design, the initial states of the virtual vessels are set equal to those of the corresponding real vessels, and the initial bias estimates are set as the zero-vector.

[1] It is noted that that the acting leader would calculate θ locally in such an approach.

Furthermore, the virtual vessel models are chosen equal to the models of the real vessels. For the third design, $\boldsymbol{\zeta}_0 = \boldsymbol{\eta}_{20}$, and $\boldsymbol{\omega}_{\zeta 0} = \mathbf{0}$. Finally, $\theta_0 = 0$.

Design 1: The following performance was achieved by the first design:

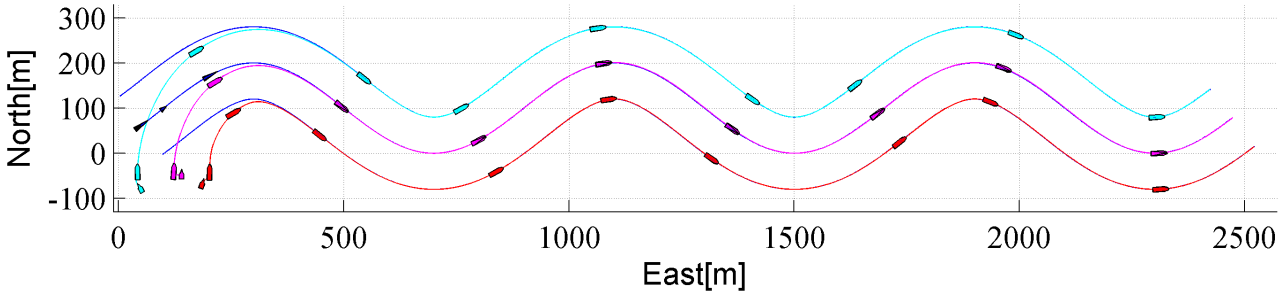

Figure 4.1: North-east position plot for the three vessels. The red, purple and blue ships correspond to vessels 1,2,3, respectively.

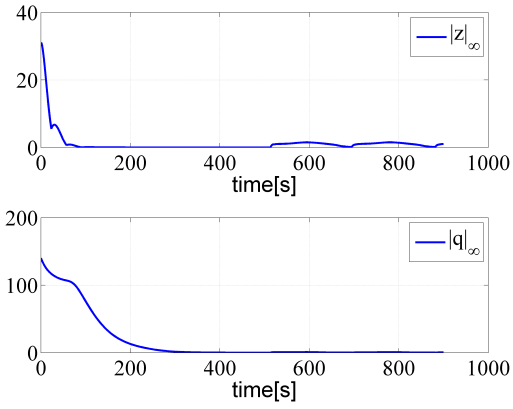

(a) Plot showing $|\mathbf{z}(t)|_\infty$ and $|\mathbf{q}(t)|_\infty$. After $t = 500(s)$, the magnitudes are lower than $|\mathbf{z}|_\infty^{max} = 1.6$ and $|\mathbf{q}|_\infty^{max} = 0.85$, respectively

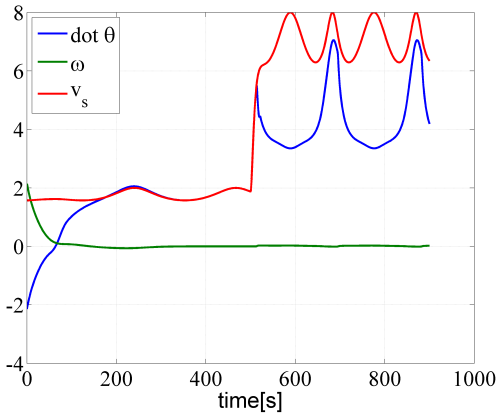

(b) Plot comparing $\dot{\theta}(t)$, $v_s(\theta(t), t)$, and $\omega(t)$

Figure 4.2: Time series of relevant system states

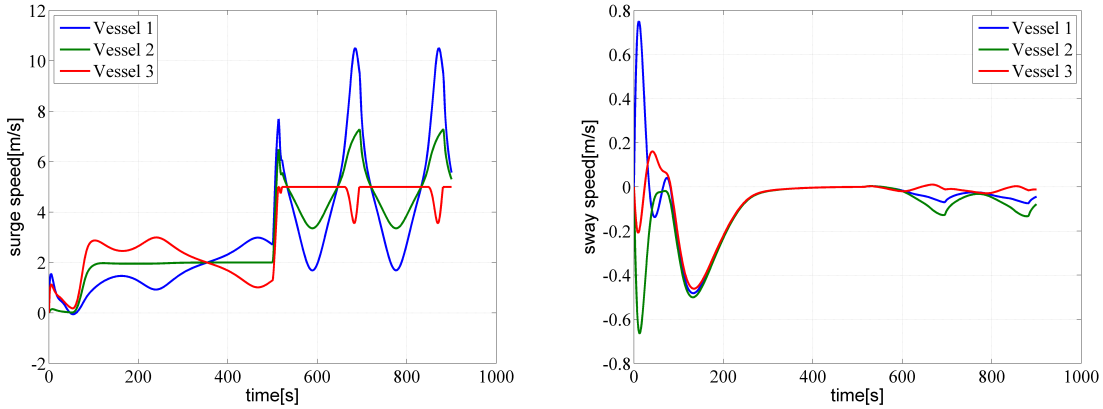

(a) Surge velocities

(b) Sway velocities

Figure 4.3: Surge and sway velocities for the three vessels

From figures 4.1 and 4.2(a), it is seen that both the formation keeping and path following capabilities of the group are maintained throughout the saturation scenario. Furthermore, the formation travels along the path at the maximum speed allowed by the saturating vessel (Figure 4.3(a)). This involves vessels 1 and 2 slowing down in the parts of the path where the commanded speed causes Vessel 3 to saturate, and speeding up when the vessel exits saturation. In Figure 4.2(b), it is shown how the propagation of θ slows down during the saturation scenario. It is interesting to see that the gradient optimization has little to no influence in this respect, so that the decrease in $\dot{\theta}(t)$ is attributed to the activation function $\sigma_2(|\mathbf{z}|^2_{L_1})$ decreasing the nominal term in (3.20). If the activation function had been tuned less aggressively, the gradient optimization would have played a more important role.

Design 2: For the second design, the saturation actually destabilized the closed-loop system. The source of the problem turned out to be the bias estimator of the saturating vessel charging up and causing oscillations. In the following simulation, the update law for bias estimator has simply been shut off after $t = 500[s]$. The result is an ideal response, only achievable in a practical setting if an effective fault-detection system is implemented.

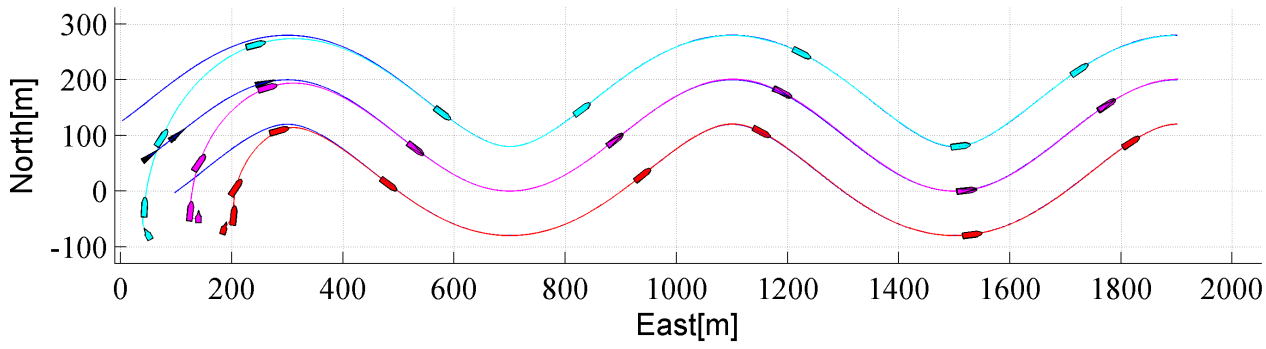

Figure 4.4: North-east position plot for the three vessels.

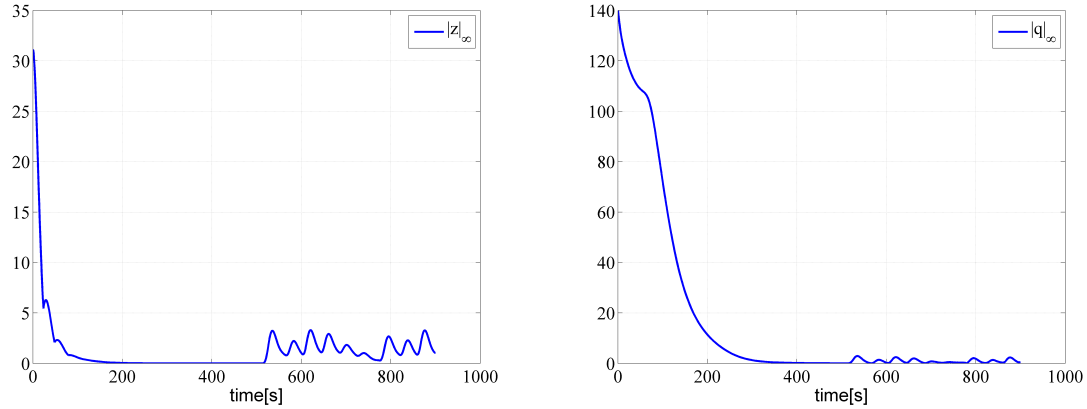

(a) $|\mathbf{z}(t)|_\infty$ (b) $|\mathbf{q}(t)|_\infty$

Figure 4.5: Time series of $|\mathbf{z}(t)|_\infty$ and $|\mathbf{q}(t)|_\infty$. After $t = 500(s)$, the magnitudes are lower than $|\mathbf{z}|_\infty^{max} = 3.3$ and $|\mathbf{q}|_\infty^{max} = 3.0$, respectively

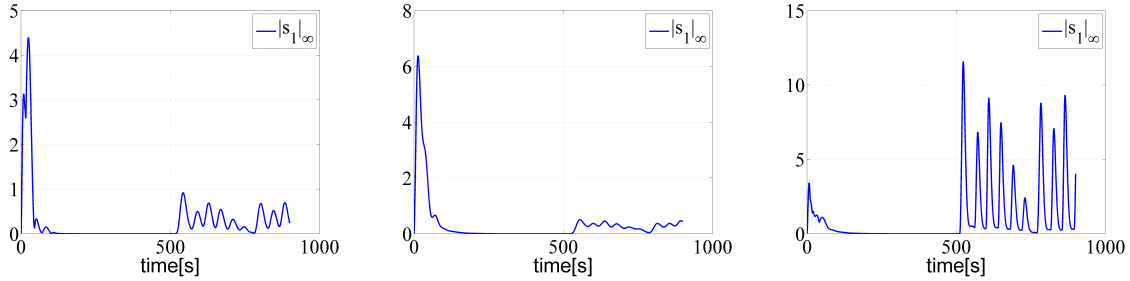

(a) Vessel 1 (b) Vessel 2 (c) Vessel 3

Figure 4.6: Plots showing $|\mathbf{s}_{1i}(t)|_\infty$ for the three vessels.

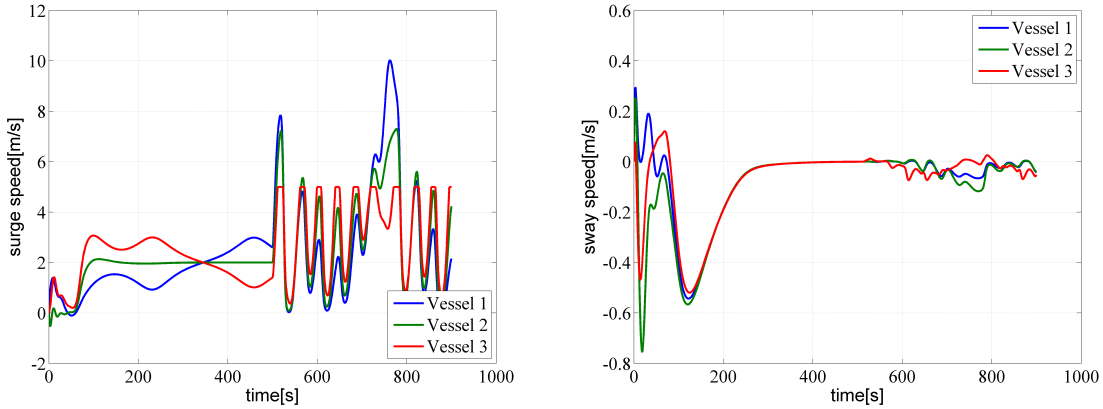

(a) Surge velocities (b) Sway velocities

Figure 4.7: Surge and sway velocities for the three vessels

Although synchronization and path following is maintained reasonably well by the virtual vessels during the saturation scenario (Figure 4.5), the tracking errors for Vessel 3 show that the real vessels are out of formation from time to time (Figure 4.6(c)). As the errors are small relative to the magnitude of the formation configuration vectors, this is hardly noticeable in Figure 4.4.

Compared to the response achieved by the first control design, the response of the second design is seen to be less smooth, involving oscillatory stop and start motion for the vessels (Figure 4.7(a)). This behavior can be attributed to conflicting efforts in the virtual vessel control laws, as explained in the end of Section 3.3.5. When Vessel 3 saturates, the corresponding virtual vessel does not slow down before the feedback term $\boldsymbol{\delta}_{v3}$ becomes sufficiently large relative to the synchronization and feedforward terms in its control law. This involves the tracking error reaching a certain threshold, where the magnitude depends on how the proportional gain matrix $\mathbf{K}_{p3}$ is tuned. After the virtual vessel has slowed down, causing synchronization errors that halt the rest of the formation, the saturating vessel catches up, causing the virtual vessels to resume to their commanded velocities. The process is then repeated.

Design 3: The following response was achieved by the third control design:

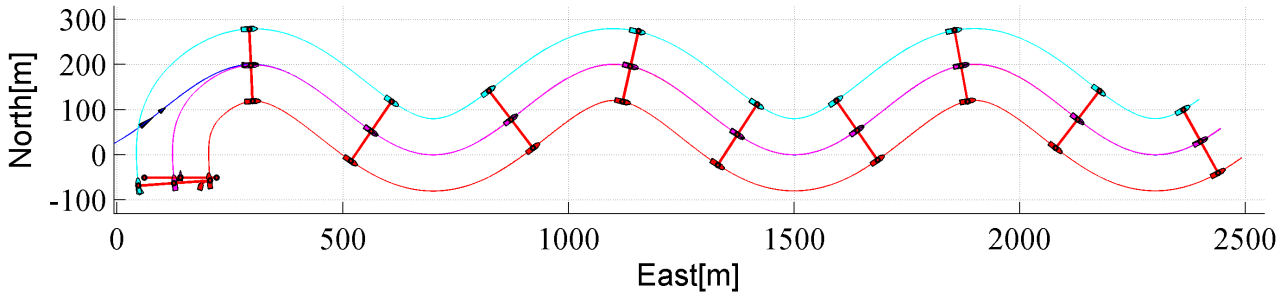

Figure 4.8: North-east position plot for the three vessels.

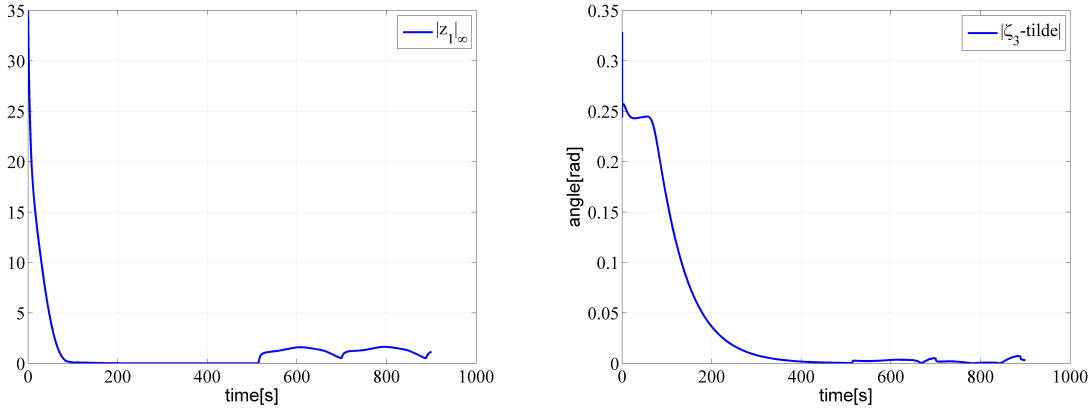

(a) $|\mathbf{z}_1(t)|_\infty$ (b) $|\tilde{\zeta}_3(t)|$

Figure 4.9: Time series of $|\mathbf{z}_1(t)|_\infty$ and $|\tilde{\zeta}_3(t)|$. After $t = 500[s]$, magnitudes are less than $|\mathbf{z}_1|_\infty^{max} = 1.65$ and $|\tilde{\boldsymbol{\zeta}}_3|^{max} = 0.01[rad]$, respectively.

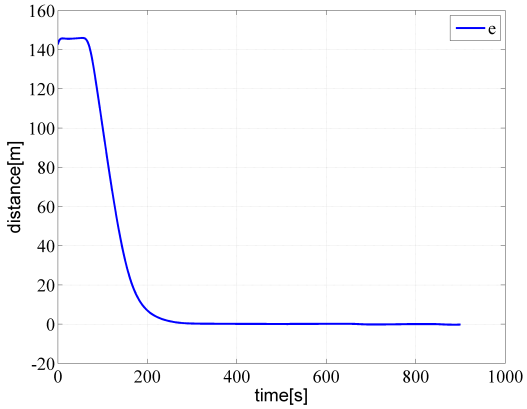

(a) $e(t)$

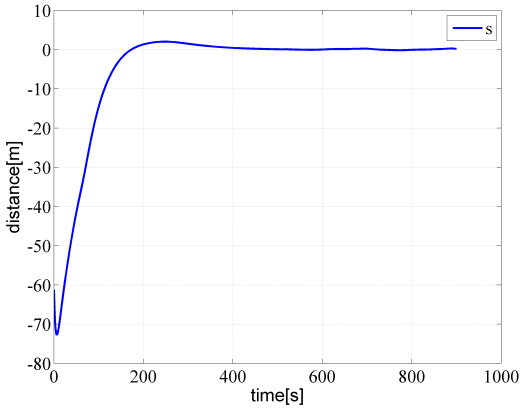

(b) $s(t)$

Figure 4.10: Time series of the cross-track and along-track errors $e(t)$ and $s(t)$. After $t = 500[s]$, magnitudes are less than $|s|^{max} = 0.35[m]$, $|e|^{max} = 0.3[m]$, respectively.

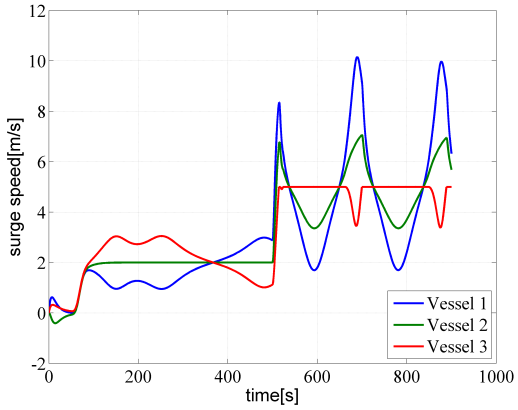

(a) Surge velocities

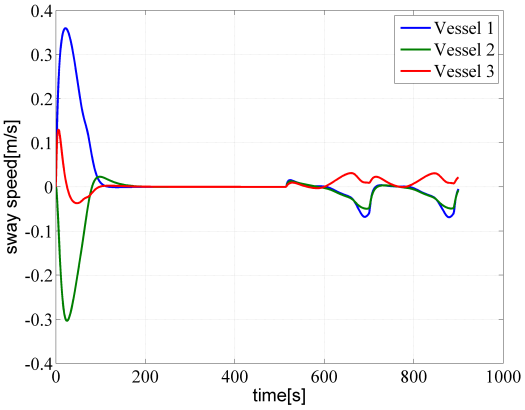

(b) Sway velocities

Figure 4.11: Surge and sway velocities for the three vessels

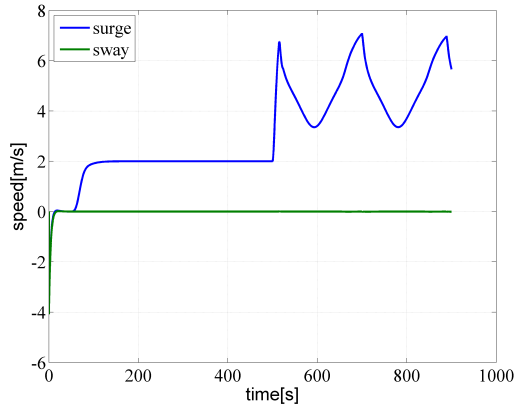

(a) surge/sway velocities for $\mathcal{F}$.

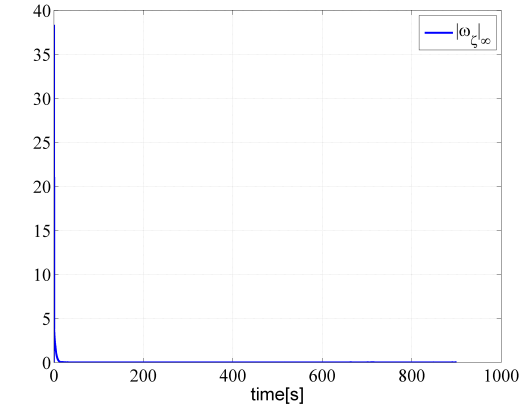

(b) $|\boldsymbol{\omega}_\zeta(t)|_\infty$

Figure 4.12: Time series of $|\boldsymbol{\omega}_\zeta(t)|_\infty$ and the surge and sway velocities for $\mathcal{F}$.

Figures 4.8, 4.9(a) and 4.10 show that group coordination and path following is maintained very nicely

throughout the saturation scenario. As in the response achieved by the first design, the formation travels along the path at the maximum speed allowed by the saturating vessel (Figure 4.11(a)). Comparing figures 4.12(a) and 4.12(b), it is seen that the gradient optimization has little influence on the motion of $\mathcal{F}$ after Vessel 3 starts saturating. The reason to why the reference frame moves slower than the commanded speed $U_d = 8[m/s]$ can thus be attributed to the activation function in the nominal dynamics of $\mathbf{p}_\zeta$.

4.2.2.2 Blackout scenario

In the following simulations, a 'blackout' is inflicted to Vessel 1 after $t = 550[s]$. This involves a loss of propulsion for the vessel (i.e. $\boldsymbol{\tau}_1 = \mathbf{0}$). All initial conditions and parameters for the three designs are in accordance with those used in the saturation scenarios. The desired speed for the formation is set as $U_d(t) \equiv 2[m/s]$. In order to achieve similar post-blackout behavior for the failing vessel in all simulations, the bias environmental disturbance is set equal to zero in the simulations for the second design.

Design 1: The following response was achieved by the first design:

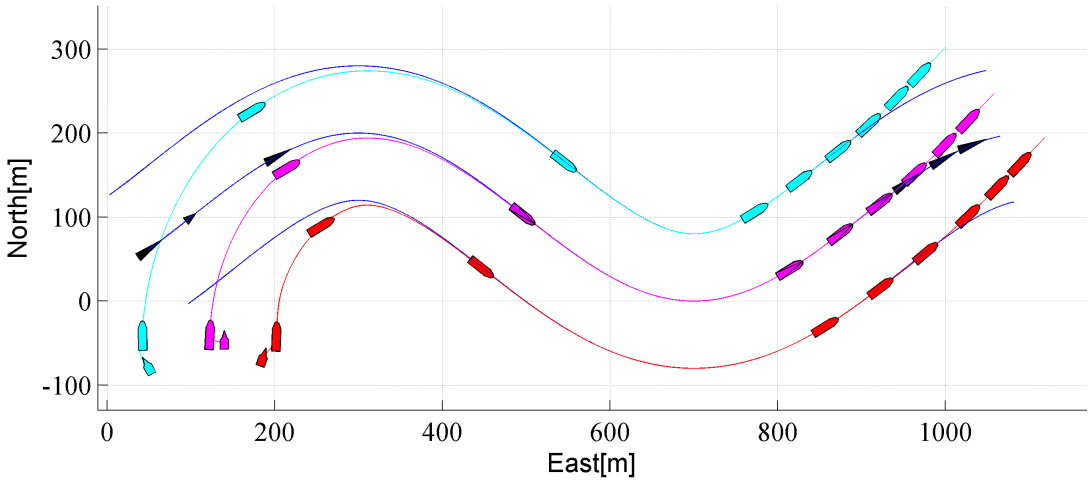

Figure 4.13: North-east position plot for the three vessels. The red, purple and blue ships correspond to vessels 1,2,3, respectively.

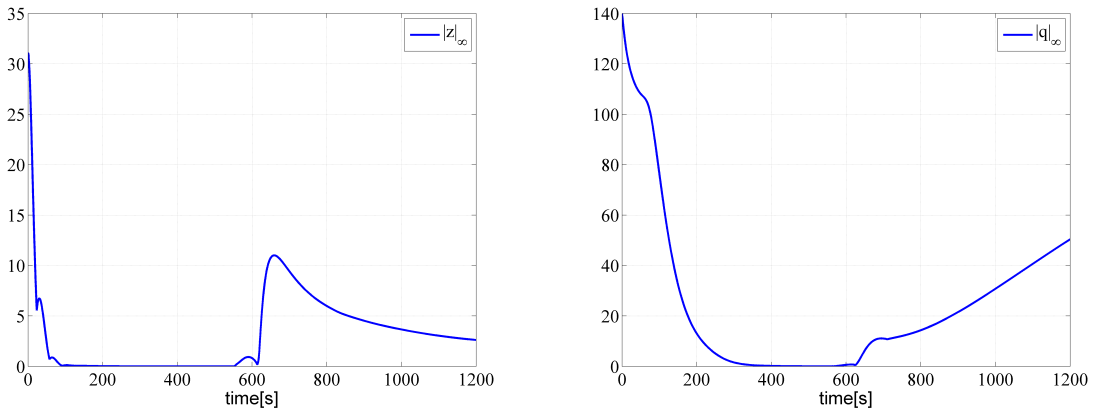

(a) $|\mathbf{z}(t)|_\infty$ (b) $|\mathbf{q}(t)|_\infty$

Figure 4.14: Time series of $|\mathbf{z}(t)|_\infty$ and $|\mathbf{q}(t)|_\infty$.

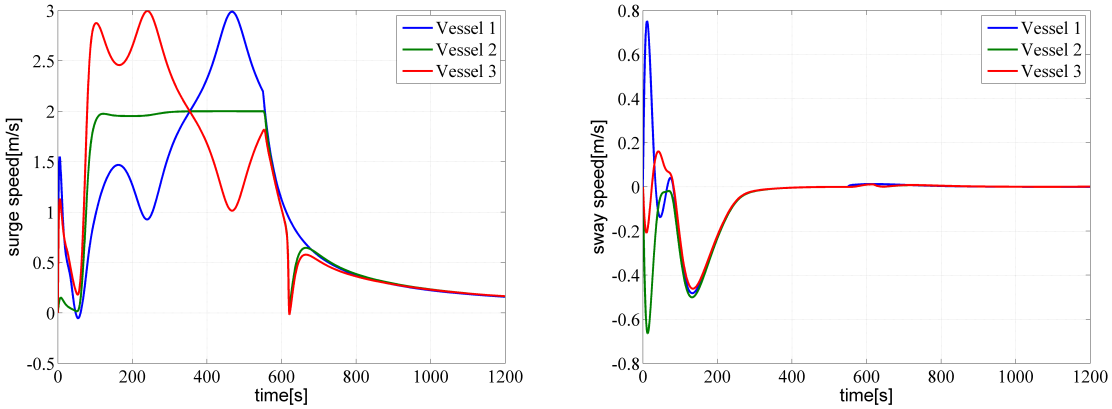

(a) Surge velocities

(b) Sway velocities

Figure 4.15: Surge and sway velocities for the three vessels

From figures 4.13 and 4.14(a), it is seen that the non-failing vessels manage to maintain the formation structure very nicely after the blackout. This comes as a result of the prioritization between the group coordination and formation mission tasks, as the non-failing vessels 'forget' about path following after the blackout, concentrating solely on decreasing the synchronization errors by following the failing vessel.

Design 2: The following response was achieved by the second control design:

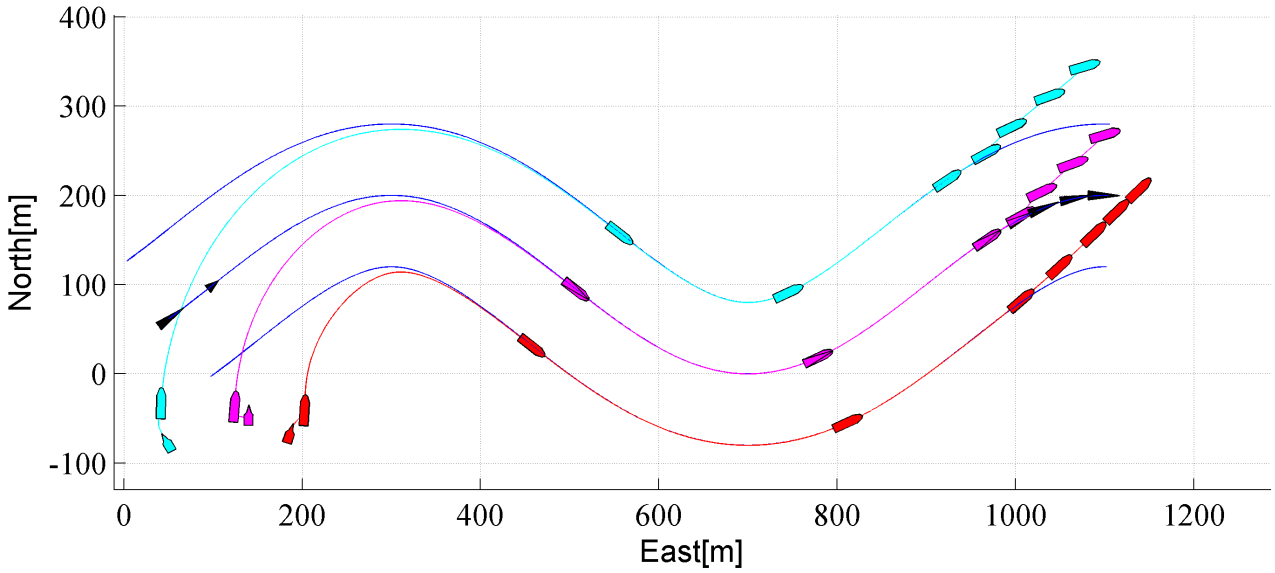

Figure 4.16: North-east position plot for the three vessels.

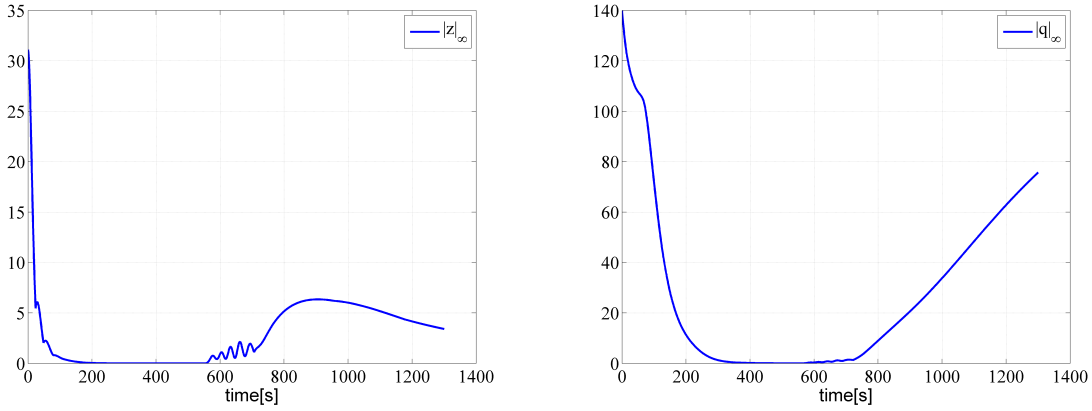

(a) $|\mathbf{z}(t)|_\infty$ (b) $|\mathbf{q}(t)|_\infty$

Figure 4.17: Time series of $|\mathbf{z}(t)|_\infty$ and $|\mathbf{q}(t)|_\infty$.

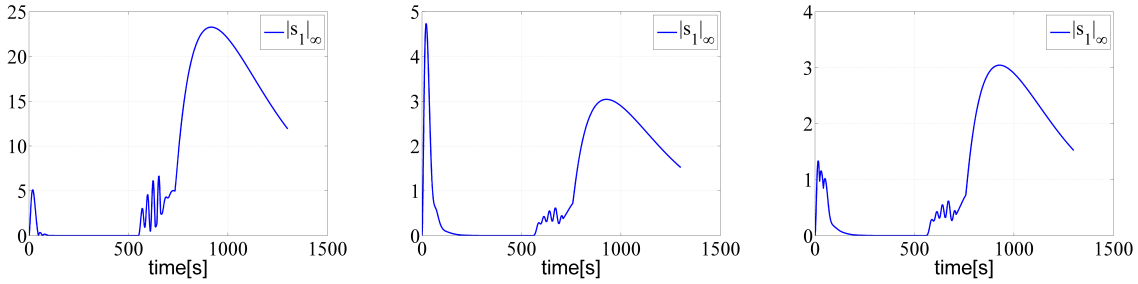

(a) Vessel 1 (b) Vessel 2 (c) Vessel 3

Figure 4.18: Plots showing $|\mathbf{s}_{1i}(t)|_\infty$ for the three vessels.

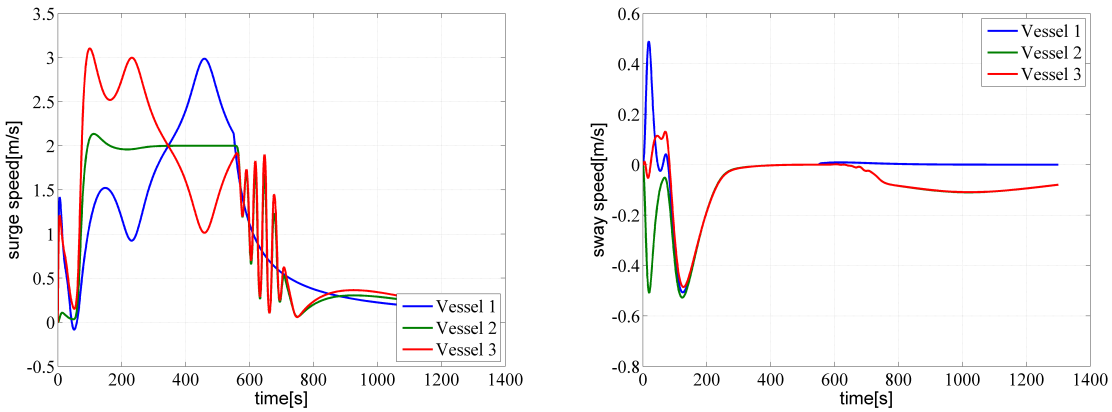

(a) Surge velocities (b) Sway velocities

Figure 4.19: Surge and sway velocities for the three vessels

From Figure 4.16, it is seen that the formation is maintained reasonably well after the blackout. Comparing figures 4.17(a) and 4.18, the coordination errors that arise are mainly attributed to the tracking error of Vessel 1. By increasing the proportional gain matrix involved in the feedback term $\boldsymbol{\delta}_{v1}$ of the virtual vessel control law, this tracking error can be reduced. From Figure 4.19(a), it is finally noted that the transient response after the blackout is less smooth than the response achieved by the first

control design. The explanation to the oscillatory behavior follows along the same lines as the explanation in the saturation scenario.

Design 3: The following response was achieved by the third control design:

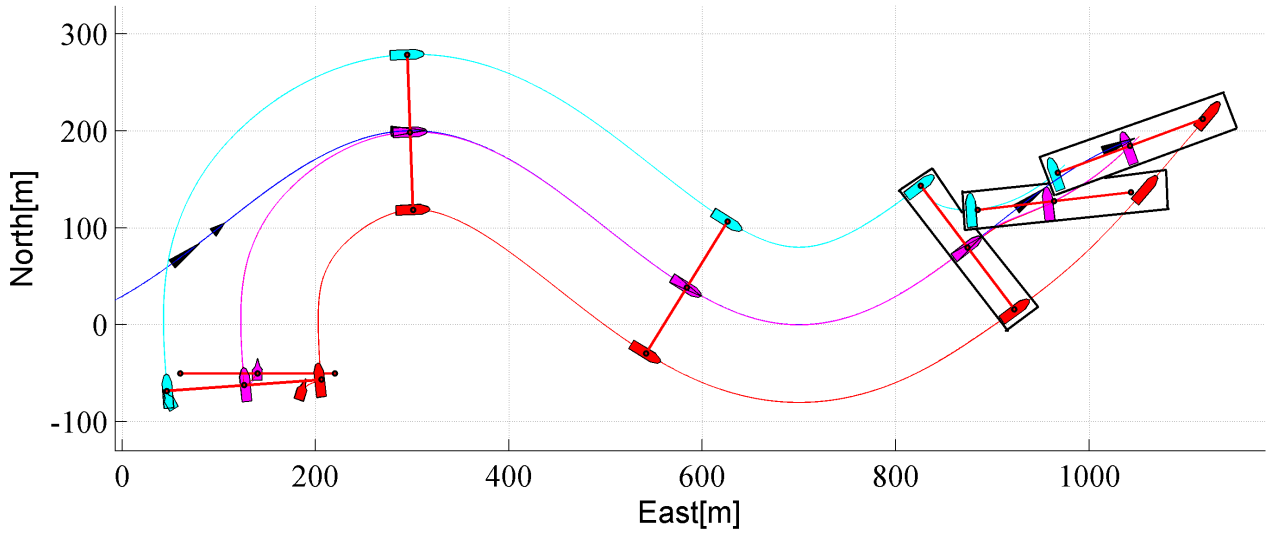

Figure 4.20: North-east position plot for the three vessels.

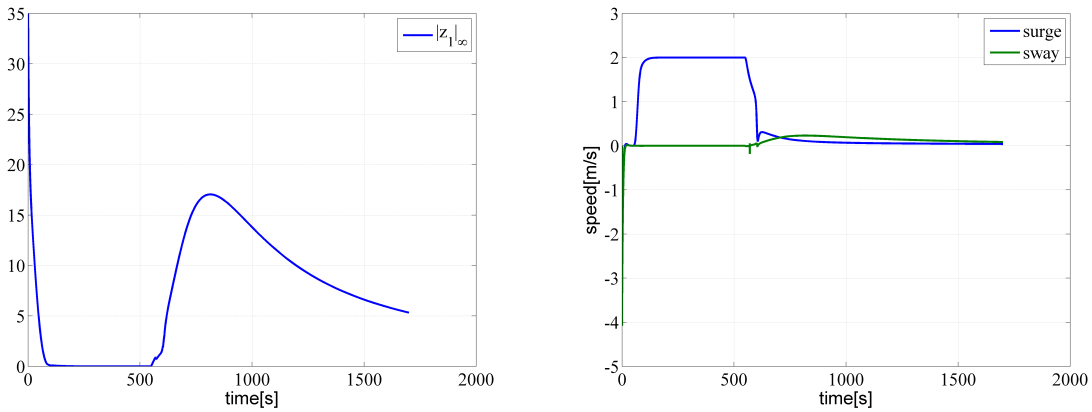

(a) $|\mathbf{z}_1(t)|_\infty$

(b) surge/sway velocities of $\mathcal{F}$.

Figure 4.21: Time series of $|\mathbf{z}_1(t)|_\infty$ and the surge/sway velocities of $\mathcal{F}$.

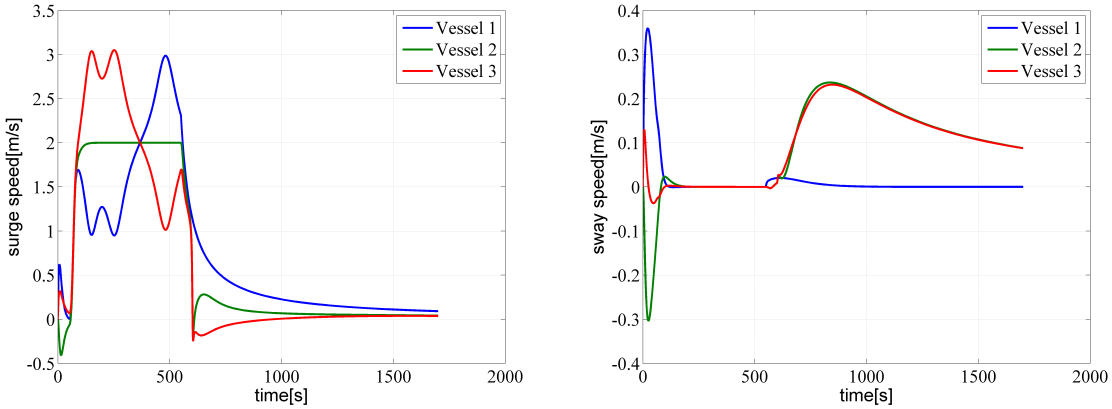

(a) Surge velocities

(b) Sway velocities

Figure 4.22: Surge and sway velocities for the three vessels

As seen in figures 4.20 and 4.21(a), the control system manages to maintain the formation well in terms of position after the blackout. The relative heading angles are, however, not maintained. The reason for this can be traced to the relative influence position and orientation errors have in the gradient optimization. By tuning the third elements of the matrices $\mathbf{P}_{1i}$ more aggressively, a response similar to those of the first two designs was achieved. There is an obvious downside to doing this, however, as the matrices also correspond to the proportional gains in the vessel control laws. In any case, the author finds the response presented here to be adequate, as keeping the positional errors under control is what is most important with respect to avoidance of collisions.

To summarize, the proposed control designs have been shown to be robust to individual vessel failures in general. With respect to surge velocity saturations, an equally good response was achieved for the first and third designs, where the group managed to stay in formation and follow the path at the maximum speed allowed by the saturating vessel. The second design did not perform well, however, as the bias estimator of the failing vessel destabilized the system. By turning off the estimator update law after the saturation was triggered, the control system displayed both formation-keeping and path following capabilities, although the response was less smooth than the responses achieved by the other designs. In the blackout scenario, the first design performed best in terms of maintaining the specified formation structure. The second design performed reasonably well, although the response was less smooth than the response achieved by the first design. Finally, the third design managed to keep the positional coordination errors under control, but failed to maintain the specified relative heading angles. However, as avoidance of collisions must be considered to be the primary goal during a blackout scenario, this is only of minor importance.

4.2.3 Collision avoidance capabilities

Explicit anti-collision functionality has not been included in the designs of this thesis. Consequently, collision-free operations cannot be guaranteed. The author identifies two main scenarios where collisions can occur for the designs; in the coordination phase of an operation due to unfortunate initial conditions, and during the path following phase due to vessel failures.

In the coordination phase, the vessels strive to obtain relative positions in accordance with the specified formation structure. If the initial positions of the vessels are such that a crossing of paths is inevitable in establishing the formation, collisions can occur. For the first two designs, it is important to ensure that the local FRPs are in close proximity initially to avoid dangerous transients. As demonstrated in

the third simulation case of Section 3.2.6, the initial heading angles of the vessels are just as important as the initial positions in this respect. In the third design, the gradient optimization incorporated in the equations of motion for the formation reference frame $\mathcal{F}$ can provide a safeguard to bad initial conditions. To illustrate this, consider the transversal straight line formation utilized throughout this thesis. If the initial position of Vessel 2 is at its desired position with respect to $\mathcal{F}$, the initial position of Vessel 1 is set at the desired position of Vessel 3, and vice versa, the resulting transient motion will almost certainly result in collisions if $\mathcal{F}$ is fixed. However, with the gradient optimization engaged and properly tuned, $\mathcal{F}$ will immediately rotate $\pi[rad]$ to minimize the positional errors. The vessels will subsequently only have to rotate $\pi[rad]$ to obtain their desired generalized positions, and collisions are avoided. A slow motion movie demonstrating this behavior has been included in the electronic version of this thesis.

After the coordination phase, the control designs will ensure that the vessels move as a single, rigid unit. Because of this, collisions can only occur in the case of vessel failures[2]. The separation and prioritization between the group coordination and formation mission tasks in the control designs effectively reduce the probability of collisions during such events, as demonstrated in Section 4.2.2. However, as vessel failures always incur some positional errors with respect to the desired formation structure, severe failures (e.g. blackouts) in formations involving close proximity between the vessels can still result in collisions.

4.2.4 Transient behavior during group coordination and path following

The three proposed designs have pursued group coordination through independent control of the position and orientation of the vessels in the $\mathcal{E}$-frame. Consequently, it is difficult to influence which modes of motion (surge,sway, yaw) the vessels use to establish the formation, and the efficiency of the response will mainly depend on initial conditions. In general, the efficiency of the transients is expected to decrease the more the vessels are out of formation initially, as undesirable modes of motion (e.g. pure sway translation, backing) possibly will be used over larger distances before the vessels reach a coordinated state. For the first and second designs, the initial orientations of the (virtual)vessels have a big impact on the transients of the coordination phase due to their influence on the initial positional synchronization errors between the local FRPs. As demonstrated in Section 3.2.6.3, this can lead to dangerous and inefficient responses in scenarios where little control effort is required to obtain coordination. The third design is not associated with such problems, as a guidance approach, where the vessels are controlled towards specified positions in an explicitly stated FRF, is used to achieve group coordination.

In the path following phase, the first and second designs utilize independent control of the position and orientation of the implicit formation reference frame $\mathcal{F}$ to fulfill the mission objective. Depending on the initial orientation and position of the formation relative to the path, this can result in inefficient motion for the vessels. Examples of scenarios associated with unfortunate transients are when the vessels coordinate far away and/or facing away from the path. By only utilizing (positive)surge and yaw motion for $\mathcal{F}$ to achieve path-convergence, the third design effectively avoid these problems. Overall, it is thus concluded that the third design outperforms the other two in terms of transient behavior within the operational phases.

4.3 Comparison of designs

The main advantages and disadvantages of the first, second, and third control designs are summarized in tables 4.1, 4.2, and 4.3, respectively.

[2]Naturally, collisions can also occur during formation reconfigurations. However, this will be attributed to poorly chosen signals for $\mathbf{l}_i(t)$, and not to the control system.

Advantages	**Disadvantages**
1: Possibility for fully decentralized operations. **2:** Best overall performance during individual vessel failure scenarios.	**1:** The controller of each vessel requires access to yaw acceleration (an IMU or observer is thus required). **2:** Transients during group coordination are very sensitive to initial heading angles, as they influence the initial positional synchronization errors. The result can be inefficient transient responses, as demonstrated in Section 3.2.6.3. **3:** Independent control of the position and orientation of the acting leaders FRP towards the path can result in inefficient transients in the path following phase.

Table 4.1: Advantages/disadvantages, Design 1

Advantages	**Disadvantages**
1: Solves the formation control problem for vessels subjected to an unknown, constant environmental disturbance in the $\mathcal{E}$-frame. **2:** Possibility for fully decentralized operations.	**1:** Worst overall performance during individual vessel failure scenarios. **2:** Transients during group coordination are very sensitive to initial heading angles (see Table 4.1). **3:** Independent control of the position and orientation of the acting leaders FRP towards the path can result in inefficient transients in the path following phase.

Table 4.2: Advantages/disadvantages, Design 2

Advantages	**Disadvantages**
1: LOS algorithm provides intuitive and feasible motion for the formation in the path following phase. **2:** Very good performance during individual vessel failure scenarios.	**1:** Numerical issues could complicate an implementation under hard, real-time constraints. **2:** Highly centralized.

Table 4.3: Advantages/disadvantages, Design 3

Overall, the author feels that the third design carries the greatest potential of the three. The main reason for this is that the design addresses all the problems related to inefficient transient responses for the first and second designs. Moreover, the similarities in approach with the established maneuvering designs in Skjetne (2005) opens the door to interesting extensions, for instance towards uncertain non-linear systems (e.g. systems that contain parametrical uncertainties or that are subjected to disturbances).

Chapter 5

Conclusion

This thesis has been concerned with formation control for fully actuated marine surface vessels. The *Formation Control Problem* has been defined in terms of two separate tasks; the *Group Coordination Task* and the *Formation Mission Task*. The former involves establishing a specified formation structure at an arbitrary location in the $\mathcal{E}$-frame, while the latter involves path following for the formation as a whole. Motivated by a desire to reduce the risk of collisions during path-convergence and vessel failure scenarios, separation and prioritization between the two tasks has been pursued. In Chapter 3, three different control designs have been derived, analyzed, and demonstrated through simulations. The first design utilizes the group coordination framework of Arcak (2007) to obtain group coordination, and the maneuvering methodology in Skjetne (2005) to achieve path following. The second design modifies the first design into a closed-loop guidance and control system, solving the formation control problem for vessels subjected to an unknown, constant environmental disturbance in the $\mathcal{E}$-frame. Finally, the third design solves the formation control problem through a generic maneuvering approach by exponentially stabilizing a manifold where the vessels are coordinated and the motion of the formation is in accordance with a helmsman-like LOS algorithm. In Chapter 4, the three designs have been evaluated with regards to important criteria that concerns formation control, and compared to one another in terms of advantages and disadvantages. The main findings are:

- In general, all three designs are centralized and require extensive communication during operations. There is a way to decentralize the first two designs, but doing so will introduce time-delays in the system. This could possibly deteriorate performance.
- In general, the designs demonstrate an ability to maintain formation structure during vessel failures[1]. During surge speed saturations, the first and third designs also maintain path following for the formation at the maximum speed allowed by the failing vessel.
- The designs do not contain any explicit anti-collision functionality, and collision-free operations can thus not be guaranteed. However, the formation-keeping abilities during vessel failure scenarios and the separation and prioritization between the group coordination and formation mission tasks effectively reduce the risk of accidents.
- Due to the practical nature of the LOS algorithm and the possibilities of generalizations according to the maneuvering designs in Skjetne (2005), the author believes that the third design has the greatest potential of the three.

Hopefully, the contributions of this thesis have provided a foundation for future endeavors in the exciting field of formation control. Some suggestions for future work is given in the following.

[1] Recall that the second design requires special handling of the bias estimator of the failing vessel in the case of surge speed saturation.

5.1 Recommendations for future work

- In order to determine the feasibility of the proposed method in Section 4.2.1 for decentralizing the first two designs, it should be investigated how time-delays affect the stability properties of the closed-loop systems.
- Efforts should be made to decentralize the third design. A possible approach is to synchronize multiple maneuvering systems in a decentralized manner, as done in Ihle et al. (2007) and the second formation control design in Skjetne (2005).
- The numerical issues encountered during simulations of the third design should be investigated, and if possible, resolved.
- Adapting the third design to more general non-linear systems along the lines of Skjetne (2005).
- Modifying the designs to allow for underactuated vessels, or vessels that become underactuated at higher speeds.
- Experiments (in model-scale) should be carried out to investigate how the designs behave in a practical setting.

Bibliography

Murat Arcak. Passivity as a design tool for group coordination. *IEEE Transactions on Automatic Control*, 52(8):1381–1390, 2007.

Filippo Arrichiello, Stefano Chiaverini, and Thor I. Fossen. Formation control of underactuated surface vessels using the null-space-based behavioral control. In *Proceedings of the 2006 IEEE/RSJ International Conference on Intelligent Robots and Systems*, pages 5942–5947, 2006.

He Bai, Murat Arcak, and John T. Wen. Adaptive design for reference velocity recovery in motion coordination. *Systems & Control Letters*, 57:602–610, 2008.

Tucker Balch and Ronald C. Arkin. Behavior-based formation control for multirobot teams. *IEEE Transactions on Robotics and Automation*, 14:926–939, 1998.

M. Breivik, M.V. Subbotin, and T.I. Fossen. Guided formation control for wheeled mobile robots. In *Proceedings of the 9th ICARCV*, 2006.

Morten Breivik. *Topics in Guided Motion Control of Marine Vehicles*. PhD thesis, NTNU, 2010.

Morten Breivik, Vegard E. Hovstein, and Thor I. Fossen. Ship formation control: A guided leader-follower approach. In *Proceedings of the 17th IFAC World Congress*, 2008.

Morten Breivik, Christian Holden, and Thor Inge Fossen. *Assignment 4 TTK4190: Dynamic Positioning Systems*. NTNU, 2010.

Jaydev P. Desai, James P. Ostrowski, and Vijay Kumar. Modeling and control of formations of nonholonomic mobile robots. *IEEE Transactions on Robotics and Automation*, 17(6):905–908, 2001.

Magnus Egerstedt and Xiaoming Hu. Formation constrained multi-agent control. *IEEE Transactions on Robotics and Automation*, 17:947–951, 2001.

Thor I. Fossen. *Guidance and Control of Marine Craft*. Draft copy, 2010.

Thor I. Fossen and Morten Breivik. Guidance laws for autonomous underwater vehicles. NTNU.

J. Ghommem, F. Mnif, G. Poisson, and N. Derbel. Nonlinear formation control of a group of underactuated ships. In *Proceedings of OCEANS 2007-Europe*, pages 1–8, 2007.

Ivar-Andrè F. Ihle, Murat Arcak, and Thor I. Fossen. Passivity-based designs for synchronized path-following. *Automatica*, 43:1508–1518, 2007.

Hassan K. Khalil. *NonLinear Systems*. Prentice Hall, 2002.

Erik Kyrkjebø and Kristin Y. Pettersen. Ship replenishment using synchronization control. In *Proceeding of the 6th IFAC Conference on Manoeuvring and Control of Marine Craft, Girona, Spain, September 2003*, pages 286–291, 2003.

Naomi Ehrich Leonard and Edward Fiorelli. Virtual leaders, artificial potentials and coordinated control of groups. *Proceedings of the 40th IEEE Conference on Decision and Control*, pages 2968–2973, 2001.

M. Anthony Lewis and Kar-Han Tan. High precision formation control of mobile robots using virtual structures. *Autonomous Robots*, 4:387–403, 1997.

Antonio Loria, Elena Panteley, Dobrivoje Popovic, and Andrew R. Teel. A nested matrosov theorem and persistancy of excitation for uniform convergence in stable nonautonomous systems. *IEEE Transactions on Automatic Control*, 50(2):183–198, 2005.

MaritimeQuest. Uss harry s. truman cvn-75 (ex-united states), 2010. URL `http://www.maritimequest.com/warship_directory/us_navy_pages/aircraft_carriers/uss_harry_s_truman_cvn_75_page_6.htm`. [Online; accessed 28-April-2011].

M. Mesbahi and F.Y. Hadaegh. Formation flying control of multiple spacecraft via graphs, matrix inequalities, and switching. In *Proceedings of the 1999 IEEE International Conference on Control Applications*, volume 2, pages 1211–1216, 1999.

Reza Olfati-Saber and Richard M. Murray. Distributed cooperative control of multiple vehicle formations using structural potential functions. In *Proceedings of the 15th IFAC World Congress*, 2002.

Reza Olfati-Saber and Richard M. Murray. Consensus protocols for networks of dynamic agents. In *Proceedings of the 2003 American Control Conference*, pages 951–956, 2003.

Wei Ren and Randal W. Beard. Decentralized scheme for spacecraft formation flying via the virtual structure approach. In *Proceedings of the 2003 American Control Conference*, pages 1746–1751, 2003.

Craig W. Reynolds. Flocks, herds and schools: A distributed behavioral model. *ACM SIGGRAPH Computer Graphics*, 21(4):25–34, 1987.

Renato Skejic, Morten Breivik, Thor I. Fossen, and Odd M. Faltinsen. Modelling and control of underwater replenishment operations in calm water. In *Proceedings of the 8th IFAC MCMC, Guarujá, Brazil*, pages 78–85, 2009.

Roger Skjetne. *The Maneuvering Problem*. PhD thesis, NTNU, 2005.

Roger Skjetne, Ulrik Jørgensen, and Andrew R. Teel. Line-of-sight path-following along regularly parameterized curves solved as a generic maneuvering problem. *Submitted to the 50th IEEE Conference on Decision and Control and European Control Conference*, 2011.

Wikipedia. Swarm — Wikipedia, the free encyclopedia, 2010a. URL `http://en.wikipedia.org/wiki/Swarm`. [Online; accessed 31-October-2010].

Wikipedia. Underway replenishment — Wikipedia, the free encyclopedia, 2010b. URL `http://en.wikipedia.org/wiki/Underway_replenishment`. [Online; accessed 27-October-2010].

Appendices

Appendix A

Stability theorems

A.1 Nested Matrosov Theorem

Consider the system

$$\dot{x} = F(t,x), \qquad x \in \mathbb{R}^n \tag{A.1}$$

Furthermore, define the set $\mathcal{B}^n(r)$ as

$$\mathcal{B}^n(r) = \{z \in \mathbb{R}^n : |z| \leq r\} \tag{A.2}$$

The nested Matrosov theorem presented in Loria et al. (2005) is as follows:

Theorem A.1. *Under the following assumptions the origin of* (A.1) *is UGAS.*

Assumption 1. *The origin of the system* (A.1) *is UGS.*

Assumption 2. *There exist integers $j, m > 0$ and for each $\Delta > 0$ there exist*

- *a number $\mu > 0$;*
- *locally Lipschitz continuous functions $V_i : \mathbb{R}_{\geq 0} \times \mathbb{R}^n \to \mathbb{R}$, $i \in \{1, \ldots, j\}$;*
- *a function $\phi : \mathbb{R}_{\geq 0} \times \mathbb{R}^n \to \mathbb{R}^m$;*
- *continuous functions $Y_i : \mathbb{R}^n \times \mathbb{R}^m \to \mathbb{R}$, $i \in \{1, \ldots, j\}$;*

such that, for almost all $(t,x) \in \mathbb{R}_{\geq 0} \times \mathcal{B}^n(\Delta)$, and all $i \in \{1, \ldots, j\}$

$$\max\{|V_i(t,x)|, |\phi(t,x)|\} \leq \mu \tag{A.3}$$

$$\dot{V}_i(t,x) \leq Y_i(x, \phi(t,x)). \tag{A.4}$$

Assumption 3. *For each integer $k \in \{1, \ldots, j\}$, we have that*[1]

A) $\{Y_i(z,\psi) = 0 \ \forall i \in \{1, \ldots, k-1\}$ *and all* $(z,\psi) \in \mathcal{B}^n(\Delta) \times \mathcal{B}^m(\mu)\}$

implies that

B) $\{Y_k(z,\psi) \leq 0, \ \forall (z,\psi) \in \mathcal{B}^n(\Delta) \times \mathcal{B}^m(\mu)\}$.

Assumption 4. *We have that the statement*

A) $\{Y_i(z,\psi) = 0 \ \forall i \in \{1, \ldots, j\}$, *and all* $(z,\psi) \in \mathcal{B}^n(\Delta) \times \mathcal{B}^m(\mu)\}$

implies that

B) $\{z = 0\}$

Proof. See Loria et al. (2005) □

[1] For the case $k = 1$ this assumption takes the form: "Statement B) holds with $k = 1$"

A.2 Partial set-stability for interconnected systems

The following is taken from Skjetne (2005; Appendix A.5).

Consider the interconnected system

$$\begin{aligned}\dot{\mathbf{x}}_1 &= \mathbf{f}_1(\mathbf{x}_1, \mathbf{x}_2, \mathbf{u}_1)\\ \dot{\mathbf{x}}_2 &= \mathbf{f}_2(\mathbf{x}_1, \mathbf{x}_2, \mathbf{u}_2)\end{aligned} \tag{A.5}$$

where $\mathbf{x}_1(t) \in \mathbb{R}^{n_1}$, $\mathbf{x}_2(t) \in \mathbb{R}^{n_2}$ are the states, $\mathbf{u}_1(t) \in \mathcal{U}_1 \subset \mathbb{R}^{m_1}$ and $\mathbf{u}_2(t) \in \mathcal{U}_2 \subset \mathbb{R}^{m_2}$ are inputs where $\mathcal{U}_1$, $\mathcal{U}_2$ are compact sets, and the vector fields $\mathbf{f}_1$,$\mathbf{f}_2$ are smooth. Theorem A.2 considers stability of the set

$$\mathcal{A} := \{(\mathbf{x}_1, \mathbf{x}_2) \in \mathbb{R}^{n_1} \times \mathbb{R}^{n_2} : |\mathbf{x}_1|_{\mathcal{A}_1} = 0\}, \tag{A.6}$$

where $\mathcal{A}_1 \subset \mathbb{R}^{n_1}$ is a compact set (for instance an equilibrium point $\mathbf{x}_1 = \mathbf{0}$). This gives, $|(\mathbf{x}_1, \mathbf{x}_2)|_{\mathcal{A}} = |\mathbf{x}_1|_{\mathcal{A}_1}$.

Lemma A.1. *If for each compact set $\mathcal{X} \subset \mathbb{R}^{n_1}$, there exists $L > 0$ and $c > 0$ such that*

$$|\mathbf{f}_2(\boldsymbol{\xi}, \mathbf{x}_2, \mathbf{v})| \leq L|\mathbf{x}_2| + c \qquad \forall \mathbf{x}_2 \in \mathbf{R}^{n_2}, \tag{A.7}$$

uniformly for all $(\boldsymbol{\xi}, \mathbf{v}) \in \mathcal{X} \times \mathcal{U}_2$, that is, $\mathbf{f}_2$ satisfies a sector growth condition in $\mathbf{x}_2$, then the system (A.5) *is finite escape-time detectable through $|(\mathbf{x}_1, \mathbf{x}_2)|_{\mathcal{A}}$.*

Proof. See Skjetne (2005; Appendix A.5) □

Theorem A.2. *Assume that the sector bound* (A.7) *in Lemma A.1 holds for the system* (A.5)*. If, in addition, there exists a smooth function $V : \mathbb{R}^{n_1} \times \mathbb{R}^{n_1} \mapsto \mathbb{R}_{\geq 0}$ and $\mathcal{K}_\infty$-functions α_i, $i = 1, \ldots, 4$, such that*

$$\alpha_1(|\mathbf{x}_1|_{\mathcal{A}_1}) \leq V(\mathbf{x}_1, \mathbf{x}_2) \leq \alpha_2(|\mathbf{x}_1|_{\mathcal{A}_1}) \tag{A.8}$$

and

$$V^{\mathbf{x}_1}(\mathbf{x}_1, \mathbf{x}_2)\mathbf{f}_1(\mathbf{x}_1, \mathbf{x}_2, \mathbf{u}_1) + V^{\mathbf{x}_2}(\mathbf{x}_1, \mathbf{x}_2)\mathbf{f}_2(\mathbf{x}_1, \mathbf{x}_2, \mathbf{u}_2) \leq -\alpha_3(|\mathbf{x}_1|_{\mathcal{A}_1}) + \alpha_4(|\mathbf{u}|) \tag{A.9}$$

hold, where $\mathbf{u} = (\mathbf{u}_1, \mathbf{u}_2) \in \mathcal{U}_1 \times \mathcal{U}_2$, then the system (A.5) *is Input-to-state stable with respect to the closed, 0-invariant set* (A.6)*. In the case when $\mathbf{u}_1, \mathbf{u}_2 = \mathbf{0}$, then the closed, forward invariant set* (A.6) *is UGAS with respect to* (A.5)*, and if $\alpha_i(|\mathbf{x}_1|_{\mathcal{A}_1}) = c_i|\mathbf{x}_1|^r_{\mathcal{A}_1}$ for $i = 1, 2, 3$, where c_1, c_2, c_3, r are strictly positive reals with $r \geq 1$, then* (A.6) *is UGES with respect to* (A.5)*.*

Proof. See Skjetne (2005; Appendix A.5). □

Appendix B

Vessel Simulation Model

The vessel model used for simulations in this thesis corresponds to that of the virtual ship 'MS The Waterfall' presented in Breivik et al. (2010). The model is given by

$$\dot{\boldsymbol{\eta}} = \mathbf{R}(\psi)\boldsymbol{\nu} \tag{B.1a}$$

$$\mathbf{M}\dot{\boldsymbol{\nu}} + \mathbf{D}(\boldsymbol{\nu})\boldsymbol{\nu} + \mathbf{C}(\boldsymbol{\nu})\boldsymbol{\nu} = \boldsymbol{\tau}, \tag{B.1b}$$

where the total mass matrix is constituted by rigid body and added mass matrices,

$$\mathbf{M} = \mathbf{M_R} + \mathbf{M_A} = \mathbf{M}^\top > \mathbf{0}, \tag{B.2}$$

and the damping is given by a combination of linear and non-linear terms:

$$\mathbf{D}(\boldsymbol{\nu}) = \mathbf{D}_L + \mathbf{D_u}|u| + \mathbf{D_v}|v| + \mathbf{D_r}|r| > \mathbf{0} \tag{B.3}$$

The numerical values for the different matrices are as follows:

$$\mathbf{M_R} = 10^7 \begin{bmatrix} 0.026267070914126 & 0 & 0 \\ 0 & 0.026267070914126 & -0.127532446870796 \\ 0 & -0.127532446870796 & 3.632552946785921 \end{bmatrix} \tag{B.4}$$

$$\mathbf{M_A} = 10^7 \begin{bmatrix} 0.001254155924657 & 0 & 0 \\ 0 & 0.050080510599731 & 0.053729323885923 \\ 0 & 0.053729323885923 & 3.058410000661727 \end{bmatrix} \tag{B.5}$$

$$\mathbf{D_L} = 10^6 \begin{bmatrix} 0.000024881864101 & 0 & 0 \\ 0 & 0.009865273373387 & 0.001374903311471 \\ 0 & 0.000710605692916 & 2.813354837263425 \end{bmatrix} \tag{B.6}$$

$$\mathbf{D_u} = 10^6 \begin{bmatrix} 0.002375323545585 & 0 & 0 \\ 0 & 0.008842970679035 & 0 \\ 0 & 0.111773504851143 & 6.047977827568305 \end{bmatrix} \tag{B.7}$$

$$\mathbf{D_v} = 10^7 \begin{bmatrix} 0 & 0 & 0 \\ 0 & 0.000282988598239 & 0.013494819354102 \\ 0 & 0 & 1.188650447871845 \end{bmatrix} \tag{B.8}$$

$$\mathbf{D_r} = 10^8 \begin{bmatrix} 0 & 0 & 0 \\ 0 & 0.009537450243184 & 0 \\ 0 & 0 & 1.562879800522891 \end{bmatrix} \tag{B.9}$$

Finally, the matrix $\mathbf{C}(\mathbf{v})$ can be calculated from the total mass matrix by following the procedure presented in Fossen (2010). For a mass matrix on the form

$$\begin{bmatrix} M_{11} & 0 & 0 \\ 0 & M_{22} & M_{23} \\ 0 & M_{23} & M_{33} \end{bmatrix},$$

the procedure reduces to

$$\mathbf{C}(\mathbf{v}) = \begin{bmatrix} 0 & 0 & -(M_{22}v + M_{23}r) \\ 0 & 0 & M_{11}u \\ (M_{22}v + M_{23}r) & -M_{11}u & 0 \end{bmatrix} \tag{B.10}$$

Appendix C

Calculations

C.1 Proof of Lemma 1

For $i = j$, $a_l = 0\ \forall l$ satisfies the claim. Assume now that $i \neq j$. As described in Section 2.5, connectivity means that it is possible to get from any node to any other node in the communication graph by following the edges (i.e. communication links) in the graph. Thus, there exists a non-cyclic path in the graph between nodes i and j. For a chosen non-cyclic path, let the index set $\mathcal{I}^* \subseteq \{1, \ldots, p\}$ contain the column-indexes in the incidence matrix corresponding to the edges along the path. For any edge with index $k \in \mathcal{I}^*$ connecting two nodes with indexes $m, n \in \mathcal{I}$, we have that $\mathbf{z}_k$ either equates to $(\mathbf{x_0}_m - \mathbf{x_0}_n)$ or $(\mathbf{x_0}_n - \mathbf{x_0}_m)$, depending on which node is the positive end of the link. Now, if there are any intermediate nodes along the chosen non-cyclic path between nodes i and j, they will be connected to two distinct edges along the path. By taking the sum $\sum_{l\in\mathcal{I}^*} a_l\mathbf{z}_l$ and performing a wise selection of $a_l \in \{-1, 1\}$ $\forall l \in \mathcal{I}^*$, we can thus cancel out the occurrence of $\mathbf{x_0}_m$ for any $m \neq (i, j)$ in the sum, ending up with $\sum_{l\in\mathcal{I}^*} a_l\mathbf{z}_l = \mathbf{x_0}_i - \mathbf{x_0}_j$. The result then follows by choosing $a_l = 0\ \forall l \notin \mathcal{I}^*$.

C.2 Further details on proofs of theorems 1 and 2

From UGAS of the targeted sets, it follows that

$$\lim_{t\to\infty} (|\mathbf{z}(t)|, |\mathbf{q}(t)|) = 0$$

From Lemma 1, we have that $\forall i, j \in \mathcal{I}$,

$$\mathbf{x_0}_i - \mathbf{x_0}_j = \mathbf{K}_{ij}\mathbf{z} \tag{C.1}$$

By taking time limits of the norm of (C.1), we readily get

$$0 \leq \lim_{t\to\infty} |\mathbf{x_0}_i(t) - \mathbf{x_0}_j(t)| \leq ||\mathbf{K}_{ij}||(\lim_{t\to\infty} |\mathbf{z}(t)|) = 0 \quad \forall i, j \in \mathcal{I}$$

By utilization of the squeeze law of limits, it is concluded that the group coordination objective is fulfilled.

Through our assignment of $\dot{\theta}$, we have that

$$\begin{aligned}\left|\dot{\theta} - v_s(\theta, t)\right| &= \left|v_s(\theta, t)\big(\sigma_2(|\mathbf{z}|^2_{L_1})\beta(|\mathbf{q}|^2_{L_2}) - 1\big) + 2\mu(\theta)\mathbf{q}^\top\mathbf{P}\mathbf{p}^\theta_d(\theta)\right| \\ &\leq \left|v_s(\theta, t)\big(\sigma_2(|\mathbf{z}|^2_{L_1})\beta(|\mathbf{q}|^2_{L_2}) - 1\big)\right| + \left|2\mu(\theta)\mathbf{q}^\top\mathbf{P}\mathbf{p}^\theta_d(\theta)\right|\end{aligned}$$

Using assumptions 3–4 yields

$$\left|\dot{\theta} - v_s(\theta, t)\right| \leq d\left|\big(\sigma_2(|\mathbf{z}|^2_{L_1})\beta(|\mathbf{q}|^2_{L_2}) - 1\big)\right| + 2\mu_{max}d||\mathbf{P}|||\mathbf{q}|$$

Now, since $0 \leq |\mathbf{z}|_{L_1}^2 \leq ||\mathbf{L}_1|||\mathbf{z}|^2$, and $0 \leq |\mathbf{q}|_{L_2}^2 \leq ||\mathbf{L}_2|||\mathbf{q}|^2$, we have that $\lim_{t\to\infty}\left(|\mathbf{z}(t)|_{L_1}^2, |\mathbf{q}(t)|_{L_2}^2\right) = 0$ by the squeeze law of limits. From continuity of the absolute value function and the functions $\sigma_2(\cdot), \beta(\cdot)$, we then get from elementary limit laws (also utilizing (3.17),(3.18))

$$\begin{aligned} 0 \leq \lim_{t\to\infty} \left|\dot{\theta}(t) - v_s(\theta(t),t)\right| &\leq d\left|\left(\sigma_2(\lim_{t\to\infty}|\mathbf{z}(t)|_{L_1}^2)\beta(\lim_{t\to\infty}|\mathbf{q}(t)|_{L_2}^2) - 1\right)\right| + 2\mu_{max}d||\mathbf{P}||\left(\lim_{t\to\infty}|\mathbf{q}(t)|\right) \\ &= d|1-1| + 0 = 0, \end{aligned}$$

By the squeeze law of limits, it follows that the dynamic task of the formation mission objective is fulfilled.

C.3 Proof of Proposition 2

Since $\mathbf{p}_d(\theta) = col(x_d(\theta), y_d(\theta))$ is continuously differentiable, we have from the mean value theorem of calculus that $\forall\theta_1, \theta_2 \in \mathbb{R}$, $\exists\theta_1^*, \theta_2^* \in (\theta_1, \theta_2)$ such that

$$\begin{aligned} x_d(\theta_1) - x_d(\theta_2) &= x_d^\theta(\theta_1^*)(\theta_1 - \theta_2) \\ y_d(\theta_1) - y_d(\theta_2) &= y_d^\theta(\theta_2^*)(\theta_1 - \theta_2) \end{aligned}$$

Taking absolute values, using the property

$$|x_d^\theta(\theta)|, |y_d^\theta(\theta)| \leq |\mathbf{p}_d^\theta(\theta)| \leq p_2 \quad \forall\theta \in \mathbb{R},$$

and choosing $\theta_1 = \theta$, $\theta_2 = 0$ yields

$$\begin{aligned} |x_d(\theta)| - |x_d(0)| \leq |x_d(\theta) - x_d(0)| \leq p_2|\theta| \Rightarrow |x_d(\theta)| \leq p_2|\theta| + |x_d(0)| \\ |y_d(\theta)| - |y_d(0)| \leq |y_d(\theta) - y_d(0)| \leq p_2|\theta| \Rightarrow |y_d(\theta)| \leq p_2|\theta| + |y_d(0)| \end{aligned}$$

We thus have that

$$\begin{aligned} |\mathbf{p}_d(\theta)| &\leq |x_d(\theta)| + |y_d(\theta)|, \\ &\leq 2p_2|\theta| + |x_d(0)| + |y_d(0)|, \end{aligned}$$

which proves the claim.

C.4 Proof of diffeomorphism property for the third design

The property $\lim_{|\mathbf{x}|\to\infty}|\mathbf{T}(\mathbf{x})| = \infty$, or rather $\lim_{r\to\infty}\inf_{|\mathbf{x}|\geq r}|\mathbf{T}(\mathbf{x})| = \infty$, implies that there cannot exist a trajectory for $\mathbf{x} \in \mathbb{R}^{6r+8}$ along which $|\mathbf{x}| \to \infty$ and $|\mathbf{T}(\mathbf{x})|$ remains bounded. It will now be shown through contradiction that no such trajectory can exist.

Suppose a trajectory $\mathcal{T}$ exists for $\mathbf{x}$ along which $|\mathbf{x}| \to \infty$ and $|\mathbf{T}(\mathbf{x})|$ remains bounded. Without loss of generality, let the trajectory be contained in a domain $D \subseteq \mathbb{R}^{6r+8}$. $\mathbf{T}(\mathbf{x})$ maps

$$\mathbf{x} := (\bar{\boldsymbol{\eta}}, \bar{\boldsymbol{\nu}}, \boldsymbol{\zeta}, \boldsymbol{\omega}_\zeta, \theta, t) \mapsto (\mathbf{z}_1, \mathbf{z}_2, \tilde{\zeta}_3, \mathbf{p}_\zeta, \boldsymbol{\omega}_\zeta, \theta, t) =: \boldsymbol{\phi},$$

i.e. $\boldsymbol{\phi} = \mathbf{T}(\mathbf{x})$. As $(\mathbf{p}_\zeta, \boldsymbol{\omega}_\zeta, \theta, t)$ is contained in both $\mathbf{x}$ and $\boldsymbol{\phi}$[1], $|(\mathbf{p}_\zeta, \boldsymbol{\omega}_\zeta, \theta, t)| \to \infty$ implies $|\mathbf{T}(\mathbf{x})| \to \infty$. Hence, $|(\mathbf{p}_\zeta, \boldsymbol{\omega}_\zeta, \theta, t)|$ must be bounded along $\mathcal{T}$, and we can correspondingly restrict D to a domain where $|(\mathbf{p}_\zeta, \boldsymbol{\omega}_\zeta, \theta, t)|$ is bounded. Since $\psi_{los}(\mathbf{p}_\zeta, \theta)$ is bounded within such a domain, we have that if $|\zeta_3| \to \infty$ along $\mathcal{T}$, $|\tilde{\zeta}_3| \to \infty$, and thus $|\mathbf{T}(x)| \to \infty$. Hence ζ_3 must also remain bounded along $\mathcal{T}$, which shows that D can be further restricted to a domain where $|(\boldsymbol{\zeta}, \boldsymbol{\omega}_\zeta, \theta, t)|$ is bounded. From Assumption

[1] Recall that $\boldsymbol{\zeta} := col(\mathbf{p}_\zeta, \zeta_3)$.

5 and (3.134), we have that $\bar{\boldsymbol{\eta}}_d(\boldsymbol{\zeta}, t)$ is bounded within such a domain. Consequently, if $|\bar{\boldsymbol{\eta}}| \to \infty$ along $\mathcal{T}$, $|\mathbf{z}_1| \to \infty$, and thus $|\mathbf{T}(\mathbf{x})| \to \infty$. Hence, $|\bar{\boldsymbol{\eta}}|$ must be bounded along $\mathcal{T}$, and D can thus be further restricted to a domain where $|(\boldsymbol{\zeta}, \bar{\boldsymbol{\eta}}, \boldsymbol{\omega}_\zeta, \theta, t)|$ is bounded. Using assumptions 5–7, it can be verified that (3.158) is bounded whenever $|(\boldsymbol{\zeta}, \bar{\boldsymbol{\eta}}, \boldsymbol{\omega}_\zeta, \theta, t)|$ is bounded. Hence, $|\bar{\boldsymbol{\nu}}| \to \infty$ along $\mathcal{T}$ implies $|\mathbf{z}_2| \to \infty$, and thus $|\mathbf{T}(\mathbf{x})| \to \infty$. This shows that $|\bar{\boldsymbol{\nu}}|$ must remain bounded along $\mathcal{T}$, which finally shows that D can be restricted to a domain where $|\mathbf{x}|$ is bounded. Since $\mathcal{T}$ is contained in D, this contradicts that $|\mathbf{x}| \to \infty$ along $\mathcal{T}$, which proves the stated claim.

C.5 Further details on the proof of Theorem 3

Since $0 \leq |\mathbf{z}_1|_L^2 \leq ||\mathbf{L}||\mathbf{z}_1|^2$, we have that $\lim_{t^* \to \infty} |\mathbf{z}_1(t^*)|_L^2 = 0$ by the squeeze law of limits. From the continuity of the absolute value function and $\sigma_1(\cdot)$, we then get the following from elementary limit laws (also utilizing (3.148a)):

$$
\begin{aligned}
|\dot{\mathbf{p}}_\zeta - \mathbf{f}_p(\zeta_3, t)| &= \left| \begin{bmatrix} \cos(\zeta_3) \\ \sin(\zeta_3) \end{bmatrix} U_d(t) \left(\sigma_1 \left(|\mathbf{z}_1|_L^2 \right) - 1 \right) - \mathbf{I}_{2\times 3} \boldsymbol{\omega}_\zeta \right| \\
&\leq U_{max} \left| \sigma_1 \left(|\mathbf{z}_1|_L^2 \right) - 1 \right| + ||\mathbf{I}_{2\times 3}|| |\boldsymbol{\omega}_\zeta| \\
&= U_{max} \left| \sigma_1 \left(|\mathbf{z}_1|_L^2 \right) - 1 \right| + |\boldsymbol{\omega}_\zeta| \\
&\Downarrow \\
0 \leq \lim_{t^* \to \infty} |\dot{\mathbf{p}}_\zeta(t^*) - \mathbf{f}_p(\zeta_3(t^*), t(t^*))| &\leq U_{max} \left| \sigma_1 \left(\lim_{t^* \to \infty} |\mathbf{z}_1(t^*)|_L^2 \right) - 1 \right| + \lim_{t^* \to \infty} |\boldsymbol{\omega}_\zeta(t^*)| \\
&= U_{max} |1 - 1| + 0 \\
&= 0
\end{aligned}
$$

By the squeeze law of limits, it is concluded that control objective (3.143) is fulfilled.

C.6 Feedforward signals for the third design

In the following, define

$$
\begin{aligned}
\mathbf{h}_1 &:= col(1, 0, 0), \\
\mathbf{h}_2 &:= col(0, 1, 0), \\
\mathbf{h}_3 &:= col(0, 0, 1), \\
\mathbf{I}_{2\times 3} &:= \begin{bmatrix} 1 & 0 & 0 \\ 0 & 1 & 0 \end{bmatrix}, \\
\mathbf{H}_i &:= \left[\mathbf{0}_{3\times 3}^{(1)}, \mathbf{0}_{3\times 3}^{(2)}, \ldots, \mathbf{0}_{3\times 3}^{(i-1)}, \mathbf{I}_{3\times 3}, \mathbf{0}_{3\times 3}^{(i+1)}, \ldots, \mathbf{0}_{3\times 3}^{(r)} \right] \quad \in \mathbb{R}^{3\times 3r}, \\
\mathbf{I}_{3r} &:= \mathbf{I}_{3r\times 3r},
\end{aligned}
$$

where $\mathbf{0}_{3\times 3} \in \mathbb{R}^{3\times 3}$ is the zero-matrix, and $\mathbf{I}_{3r\times 3r} \in \mathbb{R}^{3r\times 3r}$ is the identity matrix.

Calculation of $\boldsymbol{\alpha}_i^{\boldsymbol{\zeta}}(\boldsymbol{\zeta}, \bar{\boldsymbol{\eta}}, \theta, t)$

$$
\boldsymbol{\alpha}_i^{\boldsymbol{\zeta}}(\boldsymbol{\zeta}, \bar{\boldsymbol{\eta}}, \theta, t) = \mathbf{R}(\psi_i)^\top \left(\boldsymbol{\eta}_{di}^{\boldsymbol{\zeta}}(\boldsymbol{\zeta}, t) \mathbf{f}_{\boldsymbol{\zeta}}^{\boldsymbol{\zeta}}(\boldsymbol{\zeta}, \bar{\boldsymbol{\eta}}, \theta, t) + \boldsymbol{\eta}_{di}^{\boldsymbol{\zeta}, \zeta_3}(\boldsymbol{\zeta}, t) \mathbf{f}_\zeta(\boldsymbol{\zeta}, \bar{\boldsymbol{\eta}}, \theta, t) \mathbf{h}_3^\top + \boldsymbol{\eta}_{di}^{t, \boldsymbol{\zeta}}(\boldsymbol{\zeta}, t) - \mathbf{A}_{1i} \boldsymbol{\eta}_{di}^{\boldsymbol{\zeta}}(\boldsymbol{\zeta}, t) \right), \tag{C.2}
$$

where

$$
\boldsymbol{\eta}_{di}^{t, \boldsymbol{\zeta}}(\boldsymbol{\zeta}, t) = \mathbf{R}(\zeta_3) \mathbf{S} \mathbf{l}_i^t(t) \mathbf{h}_3^\top \tag{C.3}
$$

$$
\boldsymbol{\eta}_{di}^{\boldsymbol{\zeta}, \zeta_3}(\boldsymbol{\zeta}, t) = \mathbf{R}(\zeta_3) \mathbf{S}^2 \mathbf{l}_i(t) \mathbf{h}_3^\top \tag{C.4}
$$

$$\mathbf{f}_{\zeta}^{\boldsymbol{\zeta}}(\boldsymbol{\zeta},\bar{\boldsymbol{\eta}},\theta,t) = col\left(\mathbf{f}_{p\zeta}^{\boldsymbol{\zeta}}(\boldsymbol{\zeta},\bar{\boldsymbol{\eta}},t), f_{\zeta_3}^{\boldsymbol{\zeta}}(\boldsymbol{\zeta},\bar{\boldsymbol{\eta}},\theta,t)\right) \tag{C.5}$$

$$\begin{aligned}\mathbf{f}_{p\zeta}^{\boldsymbol{\zeta}}(\boldsymbol{\zeta},\bar{\boldsymbol{\eta}},t) = &\begin{bmatrix}-\sin(\zeta_3)\\ \cos(\zeta_3)\end{bmatrix}\mathbf{h}_3^{\top}U_d(t)\sigma_1\left(|\bar{\boldsymbol{\eta}}-\bar{\boldsymbol{\eta}}_d(\boldsymbol{\zeta},t)|_L^2\right)\\ &-2\begin{bmatrix}\cos(\zeta_3)\\ \sin(\zeta_3)\end{bmatrix}U_d(t)\left(\frac{\partial\sigma_1\left(|\bar{\boldsymbol{\eta}}-\bar{\boldsymbol{\eta}}_d(\boldsymbol{\zeta},t)|_L^2\right)}{\partial\left(|\bar{\boldsymbol{\eta}}-\bar{\boldsymbol{\eta}}_d(\boldsymbol{\zeta},t)|_L^2\right)}\right)\left(\bar{\boldsymbol{\eta}}-\bar{\boldsymbol{\eta}}_d(\boldsymbol{\zeta},t)\right)^{\top}\mathbf{L}\bar{\boldsymbol{\eta}}_d^{\boldsymbol{\zeta}}(\boldsymbol{\zeta},t)\end{aligned} \tag{C.6}$$

$$\begin{aligned}f_{\zeta_3}^{\boldsymbol{\zeta}}(\boldsymbol{\zeta},\bar{\boldsymbol{\eta}},\theta,t) = &\,2k_{\zeta_3}(\zeta_3-\psi_{los}(\mathbf{p}_\zeta,\theta))\left(\frac{\partial\sigma_2\left(|\bar{\boldsymbol{\eta}}-\bar{\boldsymbol{\eta}}_d(\boldsymbol{\zeta},t)|_L^2\right)}{\partial\left(|\bar{\boldsymbol{\eta}}-\bar{\boldsymbol{\eta}}_d(\boldsymbol{\zeta},t)|_L^2\right)}\right)\left(\bar{\boldsymbol{\eta}}-\bar{\boldsymbol{\eta}}_d(\boldsymbol{\zeta},t)\right)^{\top}\mathbf{L}\bar{\boldsymbol{\eta}}_d^{\boldsymbol{\zeta}}(\boldsymbol{\zeta},t)\\ &-k_{\zeta_3}\sigma_2\left(|\bar{\boldsymbol{\eta}}-\bar{\boldsymbol{\eta}}_d(\boldsymbol{\zeta},t)|_L^2\right)(\mathbf{h}_3^{\top}-\psi_{los}^{\mathbf{p}_\zeta}(\mathbf{p}_\zeta,\theta)\mathbf{I}_{2\times3})+\psi_{los}^{\mathbf{p}_\zeta}(\mathbf{p}_\zeta,\theta)\mathbf{f}_{p\zeta}^{\boldsymbol{\zeta}}(\boldsymbol{\zeta},\bar{\boldsymbol{\eta}},t)\\ &+\psi_{los}^{\mathbf{p}_\zeta,x_\zeta}(\mathbf{p}_\zeta,\theta)\mathbf{f}_{p\zeta}(\boldsymbol{\zeta},\bar{\boldsymbol{\eta}},t)\mathbf{h}_1^{\top}+\psi_{los}^{\mathbf{p}_\zeta,y_\zeta}(\mathbf{p}_\zeta,\theta)\mathbf{f}_{p\zeta}(\boldsymbol{\zeta},\bar{\boldsymbol{\eta}},t)\mathbf{h}_2^{\top}\\ &+\psi_{los}^{\theta,\mathbf{p}_\zeta}(\mathbf{p}_\zeta,\theta)\mathbf{I}_{2\times3}f_\theta(\boldsymbol{\zeta},\bar{\boldsymbol{\eta}},\theta,t)+\psi_{los}^{\theta}(\mathbf{p}_\zeta,\theta)f_\theta^{\boldsymbol{\zeta}}(\boldsymbol{\zeta},\bar{\boldsymbol{\eta}},\theta,t)\end{aligned} \tag{C.7}$$

$$\psi_{los}^{\mathbf{p}_\zeta,x_\zeta}(\mathbf{p}_\zeta,\theta) = \frac{2e(\mathbf{p}_\zeta,\theta)\sin(\psi_d(\theta))\Delta}{\left(e(\mathbf{p}_\zeta,\theta)^2+\Delta^2\right)^2}row\left(\sin(\psi_d(\theta)),-\cos(\psi_d(\theta))\right)$$

$$\psi_{los}^{\mathbf{p}_\zeta,y_\zeta}(\mathbf{p}_\zeta,\theta) = \frac{2e(\mathbf{p}_\zeta,\theta)\cos(\psi_d(\theta))\Delta}{\left(e(\mathbf{p}_\zeta,\theta)^2+\Delta^2\right)^2}row\left(-\sin(\psi_d(\theta)),\cos(\psi_d(\theta))\right)$$

$$\psi_{los}^{\theta}(\mathbf{p}_\zeta,\theta) = \psi_d^{\theta}(\theta)-\frac{\Delta}{e(\mathbf{p}_\zeta,\theta)^2+\Delta^2}e^{\theta}(\mathbf{p}_\zeta,\theta)$$

$$\begin{aligned}\psi_{los}^{\theta,\mathbf{p}_\zeta}(\mathbf{p}_\zeta,\theta) = &\frac{2\Delta e(\mathbf{p}_\zeta,\theta)}{\left(e(\mathbf{p}_\zeta,\theta)^2+\Delta^2\right)^2}e^{\theta}(\mathbf{p}_\zeta,\theta)row(-\sin(\psi_d(\theta)),\cos(\psi_d(\theta)))\\ &+\frac{\Delta}{e(\mathbf{p}_\zeta,\theta)^2+\Delta^2}row(\cos(\psi_d(\theta)),\sin(\psi_d(\theta)))\psi_d^{\theta}(\theta)\end{aligned}$$

$$\begin{aligned}f_{\theta}^{\boldsymbol{\zeta}}(\boldsymbol{\zeta},\bar{\boldsymbol{\eta}},\theta,t) = &-\frac{\Delta e(\mathbf{p}_\zeta,\theta)U_d(t)\sigma_1\left(|\bar{\boldsymbol{\eta}}-\bar{\boldsymbol{\eta}}_d(\boldsymbol{\zeta},t)|_L^2\right)}{\left(e(\mathbf{p}_\zeta,\theta)^2+\Delta^2\right)^{\frac{3}{2}}|\mathbf{p}_d^{\theta}(\theta)|}row(-\sin(\psi_d(\theta)),\cos(\psi_d(\theta)),0)\\ &-\frac{2\Delta U_d(t)}{|\mathbf{p}_d^{\theta}(\theta)|\sqrt{\Delta^2+e(\mathbf{p}_\zeta,\theta)^2}}\left(\frac{\partial\sigma_1\left(|\bar{\boldsymbol{\eta}}-\bar{\boldsymbol{\eta}}_d(\boldsymbol{\zeta},t)|_L^2\right)}{\partial\left(|\bar{\boldsymbol{\eta}}-\bar{\boldsymbol{\eta}}_d(\boldsymbol{\zeta},t)|_L^2\right)}\right)\left(\bar{\boldsymbol{\eta}}-\bar{\boldsymbol{\eta}}_d(\boldsymbol{\zeta},t)\right)^{\top}\mathbf{L}\bar{\boldsymbol{\eta}}_d^{\boldsymbol{\zeta}}(\boldsymbol{\zeta},t)\\ &+\mu_\theta\frac{\mathbf{p}_d^{\theta}(\theta)^{\top}}{|\mathbf{p}_d^{\theta}(\theta)|}\mathbf{I}_{2\times3}\end{aligned}$$

Calculation of $\boldsymbol{\alpha}_i^{\theta}(\boldsymbol{\zeta},\bar{\boldsymbol{\eta}},\theta,t)$

$$\boldsymbol{\alpha}_i^{\theta}(\boldsymbol{\zeta},\bar{\boldsymbol{\eta}},\theta,t) = \mathbf{R}(\psi_i)^{\top}\boldsymbol{\eta}_{di}^{\boldsymbol{\zeta}}(\boldsymbol{\zeta},t)\mathbf{f}_{\zeta}^{\theta}(\boldsymbol{\zeta},\bar{\boldsymbol{\eta}},\theta,t), \tag{C.8}$$

where

$$\mathbf{f}_{\zeta}^{\theta}(\boldsymbol{\zeta},\bar{\boldsymbol{\eta}},\theta,t) = \begin{bmatrix}0\\0\\f_{\zeta_3}^{\theta}(\boldsymbol{\zeta},\bar{\boldsymbol{\eta}},\theta,t)\end{bmatrix} \tag{C.9}$$

$$\begin{aligned}f_{\zeta_3}^{\theta}(\boldsymbol{\zeta},\bar{\boldsymbol{\eta}},\theta,t) = &\,k_{\zeta_3}\sigma_2\left(|\bar{\boldsymbol{\eta}}-\bar{\boldsymbol{\eta}}_d(\boldsymbol{\zeta},t)|_L^2\right)\psi_{los}^{\theta}(\mathbf{p}_\zeta,t)+\psi_{los}^{\mathbf{p}_\zeta,\theta}(\mathbf{p}_\zeta,\theta)\mathbf{f}_{p\zeta}(\boldsymbol{\zeta},\bar{\boldsymbol{\eta}},t)\\ &+\psi_{los}^{\theta^2}(\mathbf{p}_\zeta,\theta)f_\theta(\boldsymbol{\zeta},\bar{\boldsymbol{\eta}},\theta,t)+\psi_{los}^{\theta}(\mathbf{p}_\zeta,\theta)f_\theta^{\theta}(\boldsymbol{\zeta},\bar{\boldsymbol{\eta}},\theta,t)\end{aligned} \tag{C.10}$$

$$\psi_{los}^{\mathbf{p}_\zeta,\theta}(\mathbf{p}_\zeta,\theta) = \psi_{los}^{\theta,\mathbf{p}_\zeta}(\mathbf{p}_\zeta,\theta)$$

$$\psi_{los}^{\theta^2}(\mathbf{p}_\zeta,\theta)=\psi_d^{\theta^2}(\theta)+\frac{2\Delta e(\mathbf{p}_\zeta,\theta)}{\left(e(\mathbf{p}_\zeta,\theta)^2+\Delta^2\right)^2}\left(e^\theta(\mathbf{p}_\zeta,\theta)\right)^2-\frac{\Delta}{e(\mathbf{p}_\zeta,\theta)^2+\Delta^2}e^{\theta^2}(\mathbf{p}_\zeta,\theta)$$

$$\begin{aligned}e^{\theta^2}(\mathbf{p}_\zeta,\theta)=row(0,1)\Big(&\psi_d^{\theta^2}(\theta)\mathbf{S}_{2D}^\top\mathbf{R}(\psi_d(\theta))^\top(\mathbf{p}_\zeta-\mathbf{p}_d(\theta))\\&+\psi_d^\theta(\theta)\mathbf{S}_{2D}^\top\left(\mathbf{S}_{2D}^\top\mathbf{R}_{2D}(\psi_d(\theta))^\top(\mathbf{p}_\zeta-\mathbf{p}_d(\theta))\psi_d^\theta(\theta)-\mathbf{R}_{2D}(\psi_d(\theta))^\top\mathbf{p}_d^\theta(\theta)\right)\\&-\mathbf{S}_{2D}^\top\mathbf{R}_{2D}(\psi_d(\theta))^\top\mathbf{p}_d^\theta(\theta)\psi_d^\theta(\theta)-\mathbf{R}_{2D}(\psi_d(\theta))^\top\mathbf{p}_d^{\theta^2}(\theta)\Big)\end{aligned}$$

$$\begin{aligned}f_\theta^\theta(\boldsymbol{\zeta},\bar{\boldsymbol{\eta}},\theta,t)=&-\frac{\Delta e(\mathbf{p}_\zeta,\theta)U_d(t)\sigma_1\left(|\bar{\boldsymbol{\eta}}-\bar{\boldsymbol{\eta}}_d(\boldsymbol{\zeta},t)|_L^2\right)}{\left(e(\mathbf{p}_\zeta,\theta)^2+\Delta^2\right)^{\frac{3}{2}}|\mathbf{p}_d^\theta(\theta)|}e^\theta(\mathbf{p}_\zeta,\theta)\\&-\frac{\Delta U_d(t)\sigma_1\left(|\bar{\boldsymbol{\eta}}-\bar{\boldsymbol{\eta}}_d(\boldsymbol{\zeta},t)|_L^2\right)}{\sqrt{\Delta^2+e(\mathbf{p}_\zeta,\theta)^2}}\frac{\left(x_d^\theta x_d^{\theta^2}+y_d^\theta y_d^{\theta^2}\right)}{\left((x_d^\theta)^2+(y_d^\theta)^2\right)^{\frac{3}{2}}}\\&+\mu_\theta\psi_d^\theta(\theta)row\left(-\sin(\psi_d(\theta)),cos(\psi_d(\theta))\right)(\mathbf{p}_\zeta-\mathbf{p}_d(\theta))-\mu_\theta row\left(\cos(\psi_d(\theta)),sin(\psi_d(\theta))\right)\mathbf{p}_d^\theta(\theta)\end{aligned}$$

Calculation of $\boldsymbol{\alpha}_i^t(\boldsymbol{\zeta},\bar{\boldsymbol{\eta}},\theta,t)$

$$\boldsymbol{\alpha}_i^t(\boldsymbol{\zeta},\bar{\boldsymbol{\eta}},\theta,t)=\mathbf{R}(\psi_i)^\top\left(\boldsymbol{\eta}_{di}^{\zeta,t}(\boldsymbol{\zeta},t)\mathbf{f}_\zeta(\boldsymbol{\zeta},\bar{\boldsymbol{\eta}},\theta,t)+\boldsymbol{\eta}_{di}^\zeta(\boldsymbol{\zeta},t)\mathbf{f}_\zeta^t(\boldsymbol{\zeta},\bar{\boldsymbol{\eta}},\theta,t)+\boldsymbol{\eta}_{di}^{t^2}(\boldsymbol{\zeta},t)-\mathbf{A}_{1i}\boldsymbol{\eta}_{di}^t(\boldsymbol{\zeta},t)\right),\quad\text{(C.11)}$$

where

$$\boldsymbol{\eta}_{di}^{t^2}(\boldsymbol{\zeta},t)=\mathbf{R}(\zeta_3)\mathbf{l}_i^{t^2}(t)\quad\text{(C.12)}$$

$$\boldsymbol{\eta}_{di}^{\zeta,t}(\boldsymbol{\zeta},t)=\boldsymbol{\eta}_{di}^{t,\zeta}(\boldsymbol{\zeta},t)\quad\text{(C.13)}$$

$$\mathbf{f}_\zeta^t(\boldsymbol{\zeta},\bar{\boldsymbol{\eta}},\theta,t)=col\left(\mathbf{f}_{p\zeta}^t(\boldsymbol{\zeta},\bar{\boldsymbol{\eta}},t),f_{\zeta_3}^t(\boldsymbol{\zeta},\bar{\boldsymbol{\eta}},\theta,t)\right)\quad\text{(C.14)}$$

$$\begin{aligned}\mathbf{f}_{p\zeta}^t(\boldsymbol{\zeta},\bar{\boldsymbol{\eta}},t)=&\begin{bmatrix}\cos(\zeta_3)\\\sin(\zeta_3)\end{bmatrix}U_d^t(t)\sigma_1\left(|\bar{\boldsymbol{\eta}}-\bar{\boldsymbol{\eta}}_d(\boldsymbol{\zeta},t)|_L^2\right)\\&-2\begin{bmatrix}\cos(\zeta_3)\\\sin(\zeta_3)\end{bmatrix}U_d(t)\left(\frac{\partial\sigma_1\left(|\bar{\boldsymbol{\eta}}-\bar{\boldsymbol{\eta}}_d(\boldsymbol{\zeta},t)|_L^2\right)}{\partial\left(|\bar{\boldsymbol{\eta}}-\bar{\boldsymbol{\eta}}_d(\boldsymbol{\zeta},t)|_L^2\right)}\right)(\bar{\boldsymbol{\eta}}-\bar{\boldsymbol{\eta}}_d(\boldsymbol{\zeta},t))^\top\mathbf{L}\bar{\boldsymbol{\eta}}_d^t(\boldsymbol{\zeta},t)\end{aligned}\quad\text{(C.15)}$$

$$\begin{aligned}f_{\zeta_3}^t(\boldsymbol{\zeta},\bar{\boldsymbol{\eta}},\theta,t)=&2k_{\zeta_3}(\zeta_3-\psi_{los}(\mathbf{p}_\zeta,\theta))\left(\frac{\partial\sigma_2\left(|\bar{\boldsymbol{\eta}}-\bar{\boldsymbol{\eta}}_d(\boldsymbol{\zeta},t)|_L^2\right)}{\partial\left(|\bar{\boldsymbol{\eta}}-\bar{\boldsymbol{\eta}}_d(\boldsymbol{\zeta},t)|_L^2\right)}\right)(\bar{\boldsymbol{\eta}}-\bar{\boldsymbol{\eta}}_d(\boldsymbol{\zeta},t))^\top\mathbf{L}\bar{\boldsymbol{\eta}}_d^t(\boldsymbol{\zeta},t)\\&+\psi_{los}^{\mathbf{p}_\zeta}(\mathbf{p}_\zeta,\theta)\mathbf{f}_{p\zeta}^t(\boldsymbol{\zeta},\bar{\boldsymbol{\eta}},t)+\psi_{los}^\theta(\mathbf{p}_\zeta,\theta)f_\theta^t(\boldsymbol{\zeta},\bar{\boldsymbol{\eta}},\theta,t)\end{aligned}\quad\text{(C.16)}$$

$$\begin{aligned}f_\theta^t(\boldsymbol{\zeta},\bar{\boldsymbol{\eta}},\theta,t)=\frac{\Delta}{|\mathbf{p}_d^\theta(\theta)|\sqrt{e(\mathbf{p}_\zeta,\theta)^2+\Delta^2)}}\Big(&U_d^t(t)\sigma_1\left(|\bar{\boldsymbol{\eta}}-\bar{\boldsymbol{\eta}}_d(\boldsymbol{\zeta},t)|_L^2\right)\\&-2U_d(t)\left(\frac{\partial\sigma_1\left(|\bar{\boldsymbol{\eta}}-\bar{\boldsymbol{\eta}}_d(\boldsymbol{\zeta},t)|_L^2\right)}{\partial\left(|\bar{\boldsymbol{\eta}}-\bar{\boldsymbol{\eta}}_d(\boldsymbol{\zeta},t)|_L^2\right)}\right)(\bar{\boldsymbol{\eta}}-\bar{\boldsymbol{\eta}}_d(\boldsymbol{\zeta},t))^\top\mathbf{L}\bar{\boldsymbol{\eta}}_d^t(\boldsymbol{\zeta},t)\Big)\end{aligned}$$

Calculation of $\boldsymbol{\alpha}_i^{\bar{\eta}}(\boldsymbol{\zeta},\bar{\boldsymbol{\eta}},\theta,t)$

$$\boldsymbol{\alpha}_i^{\bar{\eta}}(\boldsymbol{\zeta},\bar{\boldsymbol{\eta}},\theta,t)=\mathbf{R}(\psi_i)^\top\boldsymbol{\eta}_{di}^\zeta(\boldsymbol{\zeta},t)\mathbf{f}_\zeta^{\bar{\eta}}(\boldsymbol{\zeta},\bar{\boldsymbol{\eta}},\theta,t)+\left(\mathbf{S}^\top\boldsymbol{\alpha}_i(\boldsymbol{\zeta},\bar{\boldsymbol{\eta}},\theta,t)\mathbf{h}_3^\top+\mathbf{R}(\psi_i)^\top\mathbf{A}_{1i}\right)\mathbf{H}_i,\quad\text{(C.17)}$$

where

$$\mathbf{f}_\zeta^{\bar{\boldsymbol{\eta}}}(\boldsymbol{\zeta},\bar{\boldsymbol{\eta}},\theta,t)=col\left(\mathbf{f}_{p\zeta}^{\bar{\boldsymbol{\eta}}}(\boldsymbol{\zeta},\bar{\boldsymbol{\eta}},t),f_{\zeta_3}^{\bar{\boldsymbol{\eta}}}(\boldsymbol{\zeta},\bar{\boldsymbol{\eta}},\theta,t)\right),\quad\text{(C.18)}$$

$$\mathbf{f}_{p\zeta}^{\bar{\boldsymbol{\eta}}}(\boldsymbol{\zeta},\bar{\boldsymbol{\eta}},t) = 2\begin{bmatrix}\cos(\zeta_3)\\ \sin(\zeta_3)\end{bmatrix} U_d(t)\left(\frac{\partial\sigma_1\left(|\bar{\boldsymbol{\eta}}-\bar{\boldsymbol{\eta}}_d(\boldsymbol{\zeta},t)|_L^2\right)}{\partial\left(|\bar{\boldsymbol{\eta}}-\bar{\boldsymbol{\eta}}_d(\boldsymbol{\zeta},t)|_L^2\right)}\right)(\bar{\boldsymbol{\eta}}-\bar{\boldsymbol{\eta}}_d(\boldsymbol{\zeta},t))^\top \mathbf{LI}_{3r} \tag{C.19}$$

$$\begin{aligned} f_{\zeta_3}^{\bar{\boldsymbol{\eta}}}(\boldsymbol{\zeta},\bar{\boldsymbol{\eta}},\theta,t) = &-2k_{\zeta_3}(\zeta_3-\psi_{los}(\mathbf{p}_\zeta,\theta))\left(\frac{\partial\sigma_2\left(|\bar{\boldsymbol{\eta}}-\bar{\boldsymbol{\eta}}_d(\boldsymbol{\zeta},t)|_L^2\right)}{\partial\left(|\bar{\boldsymbol{\eta}}-\bar{\boldsymbol{\eta}}_d(\boldsymbol{\zeta},t)|_L^2\right)}\right)(\bar{\boldsymbol{\eta}}-\bar{\boldsymbol{\eta}}_d(\boldsymbol{\zeta},t))^\top \mathbf{LI}_{3r}\\ &+\psi_{los}^{\mathbf{p}_\zeta}(\mathbf{p}_\zeta,\theta)\mathbf{f}_{p\zeta}^{\bar{\boldsymbol{\eta}}}(\boldsymbol{\zeta},\bar{\boldsymbol{\eta}},t)+\psi_{los}^{\theta}(\mathbf{p}_\zeta,\theta)f_\theta^{\bar{\boldsymbol{\eta}}}(\boldsymbol{\zeta},\bar{\boldsymbol{\eta}},\theta,t) \end{aligned} \tag{C.20}$$

$$f_\theta^{\bar{\boldsymbol{\eta}}}(\boldsymbol{\zeta},\bar{\boldsymbol{\eta}},\theta,t) = \frac{2\Delta U_d(t)}{|\mathbf{p}_d^\theta(\theta)|\sqrt{e(\mathbf{p}_\zeta,\theta)^2+\Delta^2)}}\left(\frac{\partial\sigma_1\left(|\bar{\boldsymbol{\eta}}-\bar{\boldsymbol{\eta}}_d(\boldsymbol{\zeta},t)|_L^2\right)}{\partial\left(|\bar{\boldsymbol{\eta}}-\bar{\boldsymbol{\eta}}_d(\boldsymbol{\zeta},t)|_L^2\right)}\right)(\bar{\boldsymbol{\eta}}-\bar{\boldsymbol{\eta}}_d(\boldsymbol{\zeta},t))^\top \mathbf{LI}_{3r}$$

Appendix D

Conference paper

The following paper has been submitted to the *50th IEEE Conference on Decision and Control and European Control Conference, 2011.*

Formation control of fully-actuated marine vessels using group agreement protocols

Christoffer Thorvaldsen and Roger Skjetne

Abstract— **This paper addresses the problem of getting fully-actuated marine surface vessels to establish a formation before executing its mission, which here is to traverse a predetermined path. Whereas existing designs typically solve the problem by establishing the formation on the path, the proposed design in this paper allows the vessels to coordinate at an arbitrary location prior to a collective movement to the path. Protocols for group agreement form the basis of the proposed solution, while ideas from maneuvering control theory are incorporated to yield the desired path-following behavior. To demonstrate the design, a simulation is shown, where the formation's capability of handling a severe single vessel failure is illustrated.**

I. Introduction

As an area of research, formation control has attracted increasing effort in recent times. Although the specific applications have been diverse, ranging from survey-missions on the ocean surface to cooperative control of satellites in space, the research efforts share the desire to use formations to enable execution of complex operations that are infeasible or less efficient for single agents. In the marine domain, possible applications of formation control include operations such as underway replenishment, towing of structures, geological surveying, unmanned scouting, and fleet transit. In the future it is also envisioned formations of unmanned ships for efficient transport of cargo.

Many designs for formation control exists in the literature, providing solutions for different classes of dynamical systems and different formation objectives. Examples are the general designs in [2], [9], [10], [11] and [13], the designs for mobile robots in [12] and [14], and the design for spacecraft in [15]. Within the marine control community, a large amount of work has been done within a path-based framework, where one wants the formation to move along a prespecified path with a desired speed. Examples are the formation maneuvering design in [4], the extensions provided in [5], and the guided leader-follower approach in [6].

A common trait in these designs is that the formation is established by controlling the individual vessels to their correct positions relative to a point on the path. When the formation is established, the formation as a whole is already positioned on the path, meaning that the task of coordinating the vessels is entwined with the path-following operation. The idea pursued herein is to provide a design that enables a separation between the tasks of group coordination and the path-following mission. The vessels will then primarily establish a formation in the vicinity of their present location. Secondarily, a collective path-following operation is initiated when the vessels are sufficiently coordinated. By making sure that the vessels are safely coordinated before convergence to the path is attempted, the danger of collisions during the transient motion towards the path is alleviated. Additionally, in regard to an operational philosophy where the formation should be maintained at all costs, robustness to severe vessel failures such as blackouts followed by drift-off of a single vessel, is also achieved.

C. Thorvaldsen and R. Skjetne are with the Department of Marine Technology, Norwegian University of Science and Technology (NTNU), Trondheim, Norway. E-mails: chrith@stud.ntnu.no and skjetne@ieee.org.

The basis of our design is the passivity-based group coordination framework in [2]. Generically, the framework can be used to coordinate output variables of dynamical systems in a decentralized manner while achieving a specified, common velocity in the limit for all the outputs. In [2] the common velocity signal is assumed to be known and available for each system, whereas in [9] this is extended by an adaptive scheme where all but one of the systems estimate the velocity. An application towards formation control is given, where the output variables are coordinated according to a formation constraints function. The presence of local minima in the example design in [2], however, has motivated the use of another approach to achieve coordination.

A. Main contributions

Providing an overall design for marine surface vessels that enables safe formation control by a separation between the coordination tasks and the mission task is the main contribution of this work. By controlling points that are offset from the vessels and using a special case of the framework for group agreement problems, the design circumvents the problem with local minima in a formation constraint function. The paper also shows how the common velocity input can be utilized to ensure path-following for the formation. This is done by a maneuvering design in accordance to [3], with some important modifications to ensure a clear-cut separation between the tasks of establishing the formation and performing path-following.

II. Preliminary background

A. Notations

The euclidean vector norm of $\mathbf{x}$ is denoted $|\mathbf{x}|$, while $||\mathbf{A}||$ denotes the induced euclidean norm of the matrix $\mathbf{A}$. For a collection of vectors $\mathbf{x}_i \in \mathbb{R}^{n_i}$,

$$col(\mathbf{x}_1, \mathbf{x}_2, \ldots, \mathbf{x}_k) = [\mathbf{x}_1^\top, \mathbf{x}_2^\top, \ldots, \mathbf{x}_k^\top]^\top \in \mathbb{R}^{\sum_{i=1}^k n_i}.$$

Whenever convenient, $\big|(\mathbf{x}, \mathbf{y})\big|$ denotes the norm of the vector $col(\mathbf{x}, \mathbf{y})$. For a collection of square matrices $\mathbf{A}_i \in \mathbb{R}^{n \times n}$,

$$diag(\mathbf{A}_1, \mathbf{A}_2, \ldots, \mathbf{A}_k) \quad \in \mathbb{R}^{kn \times kn}$$

denotes a block diagonal matrix. The smallest and largest eigenvalues of the matrix $\mathbf{Q}$ is denoted $\lambda_{min,Q}, \lambda_{max,Q}$. Total time derivatives are denoted by $\dot{\mathbf{f}}, \ddot{\mathbf{f}}$, etc. Partial derivatives of a function $\mathbf{f}(x,y,t)$ is denoted by a superscript $\mathbf{f}^{x^n}(x,y,t) = \frac{\partial^n \mathbf{f}(x,y,t)}{\partial x^n}$, etc. For a scalar multivariable function $f(\mathbf{x})$, we denote $\frac{\partial f(\mathbf{x})}{\partial \mathbf{x}} = col\left(\frac{\partial f(\mathbf{x})}{\partial x_1}, \ldots, \frac{\partial f(\mathbf{x})}{\partial x_n}\right)$. For Kronecker products, see [2] for details, but note the following properties,

$$(\mathbf{A} \otimes \mathbf{B})^\top = \mathbf{A}^\top \otimes \mathbf{B}^\top$$
$$(\mathbf{A} \otimes \mathbf{I}_p)(\mathbf{C} \otimes \mathbf{I}_p) = (\mathbf{AC}) \otimes \mathbf{I}_p,$$

where $\mathbf{I}_p \in \mathbb{R}^{p \times p}$ is the identity matrix, and $\mathbf{C}$ is assumed to be compatible for multiplication with $\mathbf{A}$.

B. Vessel models

The following three degree-of-freedom model for marine surface vessels is assumed (see e.g. [1]):

$$\dot{\boldsymbol{\eta}}_i = \mathbf{R}(\psi_i)\boldsymbol{\nu}_i \tag{1a}$$
$$\mathbf{M}_i\dot{\boldsymbol{\nu}}_i + \mathbf{D}_i(\boldsymbol{\nu}_i)\boldsymbol{\nu}_i + \mathbf{C}_i(\boldsymbol{\nu}_i)\boldsymbol{\nu}_i = \boldsymbol{\tau}_i, \tag{1b}$$

Here, $\boldsymbol{\eta}_i = col(x_i, y_i, \psi_i)$ represents the earth-fixed position and orientation of the i'th vessel, $\boldsymbol{\nu}_i = col(u_i, v_i, r_i)$ contains the body-fixed velocity components in surge, sway, and yaw, and $\boldsymbol{\tau}_i$ is the control input. The mass matrix $\mathbf{M}_i$ is assumed to be constant, positive definite and symmetric (although this is not always the case at forward speed due to added mass effects). The matrices $\mathbf{C}_i(\boldsymbol{\nu}_i) = -\mathbf{C}_i(\boldsymbol{\nu}_i)^\top$, $\mathbf{D}_i(\boldsymbol{\nu}_i) > 0$ are the centripetal/Coriolis and damping matrices, respectively, while $\mathbf{R}(\psi) \in \mathcal{SO}(3)$ is the rotation matrix,

$$\mathbf{R}(\psi) = \begin{bmatrix} \cos(\psi) & -\sin(\psi) & 0 \\ \sin(\psi) & \cos(\psi) & 0 \\ 0 & 0 & 1 \end{bmatrix},$$

An alternative representation of the vessel model is

$$\mathbf{M_2}_i(\psi_i)\ddot{\boldsymbol{\eta}}_i + \mathbf{C_2}_i(\psi_i, \boldsymbol{\nu}_i)\dot{\boldsymbol{\eta}}_i + \mathbf{D_2}(\psi_i, \boldsymbol{\nu}_i)\dot{\boldsymbol{\eta}}_i = \mathbf{R}(\psi_i)\boldsymbol{\tau}_i \tag{2}$$

where

$$\mathbf{M_2}_i(\psi_i) = \mathbf{R}(\psi_i)\mathbf{M}_i\mathbf{R}(\psi_i)^\top, \tag{3}$$
$$\mathbf{D_2}_i(\psi_i, \boldsymbol{\nu}_i) = \mathbf{R}(\psi_i)\mathbf{D}_i(\boldsymbol{\nu}_i)\mathbf{R}(\psi_i)^\top, \tag{4}$$
$$\mathbf{C_2}_i(\psi_i, \boldsymbol{\nu}_i) = \mathbf{R}(\psi_i)\left(\mathbf{C}_i(\boldsymbol{\nu}_i) - \mathbf{M}_i\mathbf{S}r_i\right)\mathbf{R}(\psi_i)^\top, \tag{5}$$

are locally Lipschitz functions, and

$$\mathbf{S} = -\mathbf{S}^\top = \begin{bmatrix} 0 & -1 & 0 \\ 1 & 0 & 0 \\ 0 & 0 & 0 \end{bmatrix}.$$

It can be verified that the following holds:

$$\mathbf{M_2}_i(\psi_i) = \mathbf{M_2}_i(\psi_i)^\top > 0 \tag{6}$$
$$\lambda_{min,M_i}|\mathbf{x}|^2 \leq \mathbf{x}^\top\mathbf{M_2}_i(\psi_i)\mathbf{x} \leq \lambda_{max,M_i}|\mathbf{x}|^2 \tag{7}$$
$$\mathbf{x}^\top\mathbf{D_2}_i(\psi_i, \boldsymbol{\nu}_i)\mathbf{x} > 0 \quad \forall \mathbf{x} \neq \mathbf{0} \tag{8}$$
$$\mathbf{x}^\top\left(\frac{1}{2}\dot{\mathbf{M}}_{\mathbf{2}i}(\psi_i, \boldsymbol{\nu}_i) - \mathbf{C_2}_i(\psi_i, \boldsymbol{\nu}_i)\right)\mathbf{x} = 0 \quad \forall \mathbf{x} \in \mathbb{R}^3 \tag{9}$$

C. Communication topology

A graph is used to describe the lines of communication between the vessels. Each vessel is a node in the graph, and two vessels can exchange state information if an edge (link) exists between them. For convenience, each link is assigned a direction by letting one of the connected nodes be the negative end and the other the positive end. All communication, however, is assumed bidirectional, so that any link can communicate information in both directions. For a group of r vessels with p communication links, the graph is represented by the incidence matrix $\mathbf{B} = \{b_{ij}\} \in \mathbb{R}^{r \times p}$, where

$$b_{ij} = \begin{cases} \pm 1 & \text{if the } i\text{'th node is the positive/negative} \\ & \text{end of the } j\text{'th link} \\ 0 & \text{otherwise} \end{cases} \tag{10}$$

Assumption 1: The communication graph is connected at all times, and it does not contain any cycles.
A necessary condition for this assumption to be satisfied is that the minimum number of links for r vessels is $p = r - 1$. A consequence of the assumption is that the range space of $\mathbf{B}^\top$ spans $\mathbb{R}^p$.

III. Control objective

Consider a group of r vessels to be controlled in formation. To achieve this involves two tasks, a *group coordination* task and a *formation mission* task. The primary task of group coordination is achieved when all the vessels are located at their specified relative position, with a specified relative heading angle, in a local coordinate frame termed the *Formation Reference Frame* $\mathcal{F}$ (see [3]). The secondary objective, the formation mission task, is for the formation as a whole to execute its operational objective. In this paper this is to perform *path-following* along a prespecified smooth path.

A. Setup

Let each vessel in the formation be identified by a unique identifier in the index set $\mathcal{I} = \{1, \ldots, r\}$. The configuration of each vessel i in the formation is given by a possibly time-varying *configuration vector* in $\mathcal{F}$, denoted $\mathbf{l}_i(t) := col(x_{ci}(t), y_{ci}(t), \psi_{ci}(t))$. One can then associate with each vessel an individual Formation Reference Frame $\mathcal{F}_i$, with origin and orientation in the Earth-fixed frame given by

$$\mathbf{x}_{0i} := \boldsymbol{\eta}_i - \mathbf{R}\left(\psi_i - \psi_{ci}(t)\right)\mathbf{l}_i(t), \tag{11}$$

where $\mathbf{x}_{0i} = col(x_{0i}, y_{0i}, \psi_{0i})$ is denoted the *Formation Reference Point* (FRP) for Vessel i. Group coordination is then achieved if all $\mathcal{F}_i$, $i \in \mathcal{I}$, are synchronized into a common $\mathcal{F}$, that is, if $\mathbf{x}_{01} = \mathbf{x}_{02} = \ldots = \mathbf{x}_{0r}$.

Assumption 2: The configuration vectors $\mathbf{l}_i(t) \in \mathcal{C}^2$, and $\exists\ l_{max} < \infty$ so that $\forall i \in \mathcal{I}$ and $\forall t \geq t_0$, then $\max\{|\mathbf{l}_i(t)|, |\dot{\mathbf{l}}_i(t)|\} \leq l_{max}$.

To address the formation mission task, the strategy is that one vessel, which we will denote as the *acting leader* of the formation, will ensure path-following. When all vessels are coordinated, this will indirectly ensure that the formation as

a whole executes its path-following mission. Without loss of generality we let Vessel 1 denote the acting leader, and we target path-following as a *maneuvering problem* [3] involving a geometric task and a dynamic task.

The geometric task is to converge to and follow the desired curve given by the set of points

$$\mathcal{P} = \{\boldsymbol{x} \in \mathbb{R}^3 : \exists \theta \text{ s.t. } \mathbf{x} = \mathbf{p}_d(\theta)\}, \tag{12}$$

where $\mathbf{p}_d(\theta) := col(x_d(\theta), y_d(\theta), \psi_d(\theta))$, with $(x_d(\cdot), y_d(\cdot))$ sufficiently smooth functions parameterized by the scalar variable θ, and

$$\psi_d(\theta) = \arctan\left(\frac{y_d^\theta(\theta)}{x_d^\theta(\theta)}\right) \tag{13}$$

chosen as the direction of the tangential vector to the path in each point $(x_d(\theta), y_d(\theta))$.

The dynamic task is represented by a desired speed assignment $v_s(\theta, t)$ for $\dot{\theta}$, which typically is designed to set up a constant speed in [m/s] for the formation along the path (see [3] for details).

Assumption 3: The path $\mathbf{p_d}(\theta) \in \mathcal{C}^2$, and the speed assignment $v_s(\theta, t) \in \mathcal{C}^1$. There exists $d < \infty$ so that $\forall \theta \in \mathbb{R}$ and $\forall t \geq t_0$, then $\max\{|\mathbf{p_d}^\theta(\theta)|, |v_s(\theta, t)|\} \leq d$.

B. Problem statement

The control problem can now be formally stated by the following two objectives:

Group coordination objective: To develop synchronization control laws to ensure that

$$\lim_{t\to\infty} |\mathbf{x}_{0i}(t) - \mathbf{x}_{0j}(t)| = 0 \quad \forall i, j \in \mathcal{I}. \tag{14}$$

Formation mission objective: To develop a maneuvering control law to ensure that

$$\lim_{t\to\infty} |\mathbf{x}_{01}(t) - \mathbf{p}_d(\theta(t))| = 0, \tag{15}$$

$$\lim_{t\to\infty} |\dot{\theta}(t) - v_s(\theta(t), t)| = 0. \tag{16}$$

The coordination objective is of primary concern and should be achieved before the mission objective is pursued. The reason for this is that having the vessels in formation is a measure for avoiding inter-vessel collision, especially during the transients when converging to the path.

IV. Control design

A. Group coordination task

In order to design control laws to achieve group coordination, the passivity-based group agreement protocols presented in [2] are used. For the vessels with dynamics (2) and outputs (11), the protocols are used to achieve (14) and

$$\lim_{t\to\infty} |\dot{\mathbf{x}}_{0i}(t) - \mathbf{v}_d(t)| = 0 \quad \forall i \in \mathcal{I}, \tag{17}$$

where $\mathbf{v}_d(t)$ is a common velocity input to all vessels that later will be used as a degree-of-freedom to solve the formation mission task.

1) Establishing passivity: Following the outline in [2], the first step is to construct partial control laws that transform the vessel dynamics (2) to strictly state passive dynamic systems from the auxiliary control inputs $\boldsymbol{\alpha}_i$ to the outputs

$$\boldsymbol{\zeta}_i := \dot{\mathbf{x}}_{\mathbf{0}i} - \mathbf{v}_d \quad \forall i \in \mathcal{I}. \tag{18}$$

Using (11), defining $\mathbf{f}_i(\boldsymbol{\eta}_i, t) := \mathbf{R}\left(\psi_i - \psi_{ci}(t)\right) \mathbf{l}_i(t)$, and omitting the argument lists, then (2) are rewritten as

$$\mathbf{M_2}_i\left(\ddot{\mathbf{x}}_{\mathbf{0}i} + \ddot{\mathbf{f}}_i\right) = \mathbf{R}(\psi_i)\boldsymbol{\tau}_i - \mathbf{C_2}_i(\dot{\mathbf{x}}_{\mathbf{0}i} + \dot{\mathbf{f}}_i) - \mathbf{D_2}_i(\dot{\mathbf{x}}_{\mathbf{0}i} + \dot{\mathbf{f}}_i).$$

Choosing the control inputs

$$\boldsymbol{\tau}_i = \mathbf{R}(\psi_i)^\top \Big((\mathbf{C_2}_i + \mathbf{D_2}_i)(\dot{\mathbf{f}}_i + \mathbf{v}_d) + \mathbf{M_2}_i(\dot{\mathbf{v}}_d + \ddot{\mathbf{f}}_i) - \mathbf{K_d}_i(\dot{\mathbf{x}}_{\mathbf{0}i} - \mathbf{v}_d) + \boldsymbol{\alpha}_i \Big), \quad \mathbf{K_d}_i = \mathbf{K_d}_i^\top > 0, \tag{19}$$

yields

$$\mathbf{M_2}_i\dot{\boldsymbol{\zeta}}_i = -\mathbf{C_2}_i\boldsymbol{\zeta}_i - (\mathbf{D_2}_i + \mathbf{K_d}_i)\boldsymbol{\zeta}_i + \boldsymbol{\alpha}_i, \tag{20}$$

which is passive from $\boldsymbol{\alpha}_i$ to $\boldsymbol{\zeta}_i$. To show this, the following positive definite, radially unbounded functions are utilized:

$$S_{\zeta i}(\boldsymbol{\zeta}_i, \psi_i) := \frac{1}{2}\boldsymbol{\zeta_i}^\top \mathbf{M_2}_i(\psi_i)\boldsymbol{\zeta_i}. \tag{21}$$

Taking the time derivatives and using (8) and (9) yields

$$\begin{aligned}\dot{S}_{\zeta i} &= \boldsymbol{\zeta}_i^\top (\frac{1}{2}\dot{\mathbf{M}}_{\mathbf{2}i} - \mathbf{C_2}_i)\boldsymbol{\zeta}_i - \boldsymbol{\zeta}_i^\top(\mathbf{D_2}_i + \mathbf{K_d}_i)\boldsymbol{\zeta}_i + \boldsymbol{\zeta}_i^\top\boldsymbol{\alpha}_i \\ &\leq -\boldsymbol{\zeta}_i^\top \mathbf{K_d}_i\boldsymbol{\zeta}_i + \boldsymbol{\zeta}_i^\top\boldsymbol{\alpha}_i,\end{aligned}$$

which by standard passivity theorems (see [7]) gives the desired result.

2) Synchronization: To complete the first part of the control design, we need to specify the auxiliary control inputs $\boldsymbol{\alpha}_i$. These functions will enable the vessels to synchronize in the limit. Following [2], the functions are chosen as

$$\boldsymbol{\alpha}_i = -\sum_{k=1}^{p} b_{ik}\boldsymbol{\gamma}_k(\mathbf{z}_k) \quad i \in \mathcal{I}, \tag{22}$$

where $\mathbf{B} = \{b_{ij}\} \in \mathbb{R}^{r\times p}$ is the incidence matrix of the communication graph[1]. For the k'th link connecting vessels with indexes i and j, $\mathbf{z}_k$ is the synchronization error between the vessels corresponding to

$$\mathbf{z}_k := \sum_{i=1}^{r} b_{ik}\mathbf{x}_{\mathbf{0}i} = \begin{cases} \mathbf{x}_{\mathbf{0}i} - \mathbf{x}_{\mathbf{0}j} & \text{if } i \text{ is the positive end} \\ \mathbf{x}_{\mathbf{0}j} - \mathbf{x}_{\mathbf{0}j} & \text{if } i \text{ is the negative end} \end{cases} \tag{23}$$

Furthermore, we have that

$$\boldsymbol{\gamma}_k(\mathbf{z}_k) = \frac{\partial P_k(\mathbf{z}_k)}{\partial \mathbf{z}_k}, \tag{24}$$

[1]According to Assumption 1 in Section II-C, the number of columns in $\mathbf{B}$ must be $p = r - 1$.

where according to [2], the functions $P_k(\mathbf{z}_k)$ shall satisfy:

$$P_k \in C^2 \tag{25a}$$

$$P_k(\mathbf{z}_k) > 0 \quad \forall \mathbf{z}_k \neq \mathbf{0} \tag{25b}$$

$$P_k(\mathbf{z}_k) \to \infty \text{ as } |\mathbf{z}_k| \to \infty \tag{25c}$$

$$\mathbf{z}_k^\top \frac{\partial P_k(\mathbf{z}_k)}{\partial \mathbf{z}_k} > 0 \quad \forall \mathbf{z}_k \neq \mathbf{0}. \tag{25d}$$

Examining (22) shows that the synchronizing control input for each vessel consists of feedback from the synchronization errors between the vessel and its "neighbors" in the communication topology. This corresponds to a decentralized design that necessitates only limited inter-vessel communication.

B. Formation mission task

Define $\mathbf{q}$ as the path-following error between the FRP of the acting leader and its desired position $\mathbf{p}_d(\theta)$ on the path:

$$\mathbf{q}(\mathbf{x_{01}}, \theta) := \mathbf{x_{01}} - \mathbf{p}_d(\theta), \quad \mathbf{q} \in \mathbb{R}^3. \tag{26}$$

Since $\mathbf{v}_d = \dot{\mathbf{x}}_{\mathbf{01}} - \boldsymbol{\zeta}_1$, the dynamics of $\mathbf{q}$ becomes

$$\dot{\mathbf{q}} = \mathbf{v}_d - \mathbf{p}_d^\theta(\theta)\dot{\theta} + \boldsymbol{\zeta}_1$$

where $\boldsymbol{\zeta}_1$ is the synchronization velocity error (18) for the acting leader. In the next step we design control laws for $\mathbf{v}_d$ and $\dot{\theta}$ in order to solve (15) and (16) based on the certainty equivalence $\boldsymbol{\zeta}_1 = \mathbf{0}$.

1) Maneuvering control design: To stabilize $\{\mathbf{q} = 0\}$ we select a Hurwitz matrix $\mathbf{A} \in \mathbb{R}^{3\times 3}$ together with $\mathbf{P} = \mathbf{P}^\top > \mathbf{0}$ satisfying $\mathbf{PA} + \mathbf{A}^\top\mathbf{P} = -\mathbf{Q}$ for a given $\mathbf{Q} = \mathbf{Q}^\top > 0$, and consider the CLF

$$V_q(\mathbf{x_{01}}, \theta) = \mathbf{q}(\mathbf{x_{01}}, \theta)^\top \mathbf{P}\mathbf{q}(\mathbf{x_{01}}, \theta). \tag{27}$$

A simple choice for $\mathbf{v}_d$ and $\dot{\theta}$ is

$$\begin{aligned} \mathbf{v}_d &= \mathbf{A}\mathbf{q}(\mathbf{x_{01}}, \theta) + \mathbf{p}_d^\theta(\theta) v_s(\theta, t), \\ \dot{\theta} &= v_s(\theta, t). \end{aligned}$$

This choice stabilizes the path-following error $\{\mathbf{q} = 0\}$ through $\dot{\mathbf{q}} = \mathbf{Aq}$ (also verified by $\dot{V}_q = -\mathbf{q}^\top\mathbf{Qq}$) for $\boldsymbol{\zeta}_1 = \mathbf{0}$. Additionally, it satisfies the speed assignment along the path (16) identically. However, the above control law has some severe flaws. The most notable is that each vessel will continuously receive a commanded velocity that immediately drives them towards the path, irrespective of how well they are coordinated.

To remedy this problem and ensure that coordination is handled with higher priority than path-following, the terms $\mathbf{Aq}$ and $v_s(\theta, t)$ in the maneuvering control law will be weighted by functions that map the synchronization errors into scalar weight signals. These signals should vanish for large synchronization errors and be equal to unity when synchronized. Effectively, this means that the vessels will "forget the path" while synchronizing.

To this end, the functions $\sigma_k : \mathbb{R}_{\geq 0} \mapsto \mathbb{R}_{>0}$ are introduced, which should be $\mathcal{C}^1$, decreasing, and satisfy

$$\sigma_k(0) = 1 \tag{28a}$$

$$\lim_{s\to\infty} \sigma_k(s) = 0. \tag{28b}$$

As input to these functions, we use $|\mathbf{z}|_L^2 := \mathbf{z}^\top\mathbf{L}\mathbf{z}$, where $\mathbf{z} = col(\mathbf{z}_1, \ldots, \mathbf{z}_p)$, $\mathbf{z} \in \mathbb{R}^{3p}$, and $\mathbf{L} = \mathbf{L}^\top \geq 0$ is a weight matrix used to tune the gains for position and orientation errors[2] in $\mathbf{z}$.

With these "forgetting"-functions defined, we assign the dynamic control law

$$\mathbf{v}_d = \sigma_1(|\mathbf{z}|_L^2)\mathbf{A}\mathbf{q}(\mathbf{x_{01}}, \theta) + \sigma_2(|\mathbf{z}|_L^2)\mathbf{p}_d^\theta(\theta) v_s(\theta, t) \tag{29}$$

$$\dot{\theta} = \sigma_2(|\mathbf{z}|_L^2) v_s(\theta, t) - \omega, \tag{30}$$

where ω is a free input used to shape the transient in the path convergence phase. In the path-error $\mathbf{q}$, the closed-loop dynamics becomes

$$\dot{\mathbf{q}} = \sigma_1(|\mathbf{z}|_L^2)\mathbf{A}\mathbf{q} + \mathbf{p}_d^\theta(\theta)\omega + \boldsymbol{\zeta}_1. \tag{31}$$

Motivated by the gradient optimization designs in [3], we assign ω as

$$\omega = \mu(\theta) V_q^\theta(\mathbf{x_{01}}, \theta) = -2\mu(\theta)\mathbf{q}(\mathbf{x_{01}}, \theta)^\top \mathbf{P}\mathbf{p}_d^\theta(\theta), \tag{32}$$

where in contrast to [3], $\mu(\theta) > 0$ is designed as a function of θ to allow normalization with respect to path parameterization. This ensures that the speed of the gradient minimization is independent of how a certain path is parameterized; see Section VI for an example.

Assumption 4: The gain $\mu(\theta) \in \mathcal{C}^1$, and $\exists \mu_{max} < \infty$ so that $\forall \theta \in \mathbb{R}$, then $\mu(\theta) \leq \mu_{max}$.

Differentiating (27) with respect to time yields

$$\begin{aligned} \dot{V}_q &= -\sigma_1(|\mathbf{z}|_L^2)\mathbf{q}^\top\mathbf{Q}\mathbf{q} + 2\mathbf{q}^\top\mathbf{P}\mathbf{p}_d^\theta(\theta)\omega + 2\mathbf{q}^\top\mathbf{P}\boldsymbol{\zeta}_1 \\ &= -\sigma_1(|\mathbf{z}|_L^2)\mathbf{q}^\top\mathbf{Q}\mathbf{q} - \mu(\theta) V_q^\theta(\mathbf{x_{01}}, \theta)^2 + 2\mathbf{q}^\top\mathbf{P}\boldsymbol{\zeta}_1 \end{aligned} \tag{33}$$

For $\mathbf{z}$ confined to compact sets by the control design for group coordination, it follows for $\boldsymbol{\zeta}_1 = \mathbf{0}$ that (15) is satisfied by (26). Furthermore, (16) is satisfied as $\mathbf{z}(t) \to \mathbf{0}$. A detailed analysis of stability for the complete closed-loop system is provided in Section V.

C. Operation phases

The scaling functions $\sigma_k(\cdot)$ and the gradient optimization term in $\dot{\theta}$ were introduced to enable the desired priority levels between the group coordination and the formation mission objectives, resulting in an operation effectively divided into a coordination phase and a path-following phase.

1) Coordination phase: In the beginning of an operation, the synchronization errors are typically large. By proper design, the functions $\sigma_1(|\mathbf{z}|_L^2)$ and $\sigma_2(|\mathbf{z}|_L^2)$ can attain arbitrarily small values for $|\mathbf{z}|_\mathbf{L} \geq c$, where c is a set threshold value. This ensures that the common velocity command signal (29) to each vessel is close to zero when the synchronization errors are large. The result is a low-speed coordination phase where the vessels efficiently positions themselves relatively

[2]The gains should be selected to normalize the position and orientation errors in $|\mathbf{z}|_L^2$. By setting the gains corresponding to $\mathbf{z}_k$'s that are unavailable to the acting leader equal to zero, $\mathbf{v}_d$ can be calculated locally by the acting leader. This can make the design fully decentralized (see Section VII).

to the group without paying any attention to the path-following objective. During this phase, the dynamics of θ is approximately reduced to

$$\dot{\theta} \approx -\mu(\theta) V_q^{\theta}(\mathbf{x_{01}}, \theta),$$

which shows that the point $\mathbf{p}_d(\theta(t))$ will move to a favorable position along the path by minimizing $\theta \mapsto V_q(\mathbf{x_{01}}, \theta)$, and wait there until the formation becomes coordinated.

2) Path-following phase: After the group of vessels is sufficiently coordinated, the path-following phase is initiated by a collective movement towards the path. This is a result of the functions $\sigma_1(|\mathbf{z}|_L^2)$ and $\sigma_2(|\mathbf{z}|_L^2)$ now approaching unity, thereby activating the maneuvering feedback and feed-forward terms in the common velocity command signal. This also activates the speed assignment $v_s(\theta, t)$ in (30), which drives the desired position and heading $\mathbf{p}_d(\theta(t))$ along the path at the desired speed[3].

V. Stability analysis

A. Preliminary definitions and properties

Define

$$\mathbf{x_0} := col(\mathbf{x_{01}}, \ldots, \mathbf{x_{0}}_r) \quad \in \mathbb{R}^{3r} \tag{34}$$

$$\boldsymbol{\alpha}(\mathbf{z}) := col(\boldsymbol{\alpha}_1(\mathbf{z}), \ldots, \boldsymbol{\alpha}_r(\mathbf{z})) \quad \in \mathbb{R}^{3r} \tag{35}$$

$$\boldsymbol{\gamma}(\mathbf{z}) := col(\boldsymbol{\gamma}_1(\mathbf{z}_1), \ldots, \boldsymbol{\gamma}_p(\mathbf{z}_p)) \quad \in \mathbb{R}^{3p} \tag{36}$$

$$\boldsymbol{\zeta} := col(\boldsymbol{\zeta}_1, \ldots, \boldsymbol{\zeta}_r) \quad \in \mathbb{R}^{3r} \tag{37}$$

$$\Upsilon := \mathbf{1}_r \otimes \mathbf{v_d} \quad \in \mathbb{R}^{3r}, \tag{38}$$

where, $\mathbf{1}_r \in \mathbb{R}^r$ is the vector of ones. From the definition of $\boldsymbol{\zeta}_i$ and equations (22), (23), it is verified that the vectors $\mathbf{x_0}$, $\mathbf{z}$, and $\boldsymbol{\alpha}$ satisfy

$$\dot{\mathbf{x}}_\mathbf{0} = \boldsymbol{\zeta} + \Upsilon \tag{39}$$

$$\mathbf{z} = (\mathbf{B}^\top \otimes \mathbf{I}_3)\mathbf{x_0}, \tag{40}$$

$$\boldsymbol{\alpha}(\mathbf{z}) = -(\mathbf{B} \otimes \mathbf{I}_3)\boldsymbol{\gamma}(\mathbf{z}), \tag{41}$$

where $\mathbf{I}_3 \in \mathbb{R}^{3\times 3}$ is the identity matrix. Furthermore, since the sum of entries in any column of $\mathbf{B}$ is equal to zero, the basis for the left nullspace $\mathcal{N}(\mathbf{B}^\top \otimes \mathbf{I}_3)$ is

$$\left\{\mathbf{u} \in \mathbb{R}^{3r} : \mathbf{u} = \mathbf{1}_r \otimes \mathbf{c}, \quad \mathbf{c} \in \mathbb{R}^3\right\}, \tag{42}$$

from which it follows

$$(\mathbf{B}^\top \otimes \mathbf{I}_3)\Upsilon = \mathbf{0}. \tag{43}$$

A consequence of the connectivity assumption on the communication graph is the following lemma:

Lemma 1: For a connected communication graph with r nodes and index set $\mathcal{I}$, then $\forall i, j \in \mathcal{I}$ there exists $\mathbf{K}_{ij} = [a_1\mathbf{I}_3, a_2\mathbf{I}_3, \ldots, a_p\mathbf{I}_3] \in \mathbb{R}^{3\times 3p}$, with $a_i \in \{-1, 0, 1\}$, such that

$$\mathbf{x_{0}}_i - \mathbf{x_{0}}_j = \mathbf{K}_{ij}\mathbf{z}.$$

It follows from this lemma that $\mathbf{z} = \mathbf{0}$ solves the coordination objective (14).

[3]It is also possible to scale $v_s(\theta, t)$ by a third weight function $\sigma_3(|\mathbf{q}|_{L2}^2)$, to ensure that the speed assignment is not activated before the FRP of the acting leader has converged to the path, i.e. $\mathbf{q} \approx 0$.

B. Closed-loop system

The total closed-loop dynamics becomes

$$\mathbf{M_2}_i(\psi_i)\dot{\boldsymbol{\zeta}}_i = -\mathbf{C_2}_i(\psi_i, \boldsymbol{\nu}_i)\boldsymbol{\zeta}_i - \mathbf{D_2}_i(\psi_i, \boldsymbol{\nu}_i)\boldsymbol{\zeta}_i - \mathbf{K_d}_i\boldsymbol{\zeta}_i + \boldsymbol{\alpha}_i(\mathbf{z}), \quad i \in \mathcal{I} \tag{44}$$

$$\dot{\mathbf{z}} = (\mathbf{B}^\top \otimes \mathbf{I}_3)\boldsymbol{\zeta} \tag{45}$$

$$\dot{\mathbf{q}} = \sigma_1(|\mathbf{z}|_L^2)\mathbf{A}\mathbf{q} - 2\mu(\theta)\mathbf{p}_d^{\theta}(\theta)\mathbf{q}^\top\mathbf{P}\mathbf{p}_d^{\theta}(\theta) + \boldsymbol{\zeta}_1 \tag{46}$$

$$\dot{\theta} = \sigma_2(|\mathbf{z}|_L^2)v_s(\theta, t) + 2\mu(\theta)\mathbf{q}^\top\mathbf{P}\mathbf{p}_d^{\theta}(\theta). \tag{47}$$

It can be verified that $\psi_i = \psi_{0i} + \psi_{ci}(t)$, where $\psi_{0i} = \mathbf{e}^\top(\mathbf{K}_{i1}\mathbf{z} + \mathbf{q} + \mathbf{p_d}(\theta))$ and

$$\boldsymbol{\nu}_i = \mathbf{R}(\psi_i)^\top(\mathbf{I}_3 - \mathbf{R}(\psi_{0i})\mathbf{Sl}_i(t)\mathbf{e}^\top)^{-1}\big(\boldsymbol{\zeta}_i + \mathbf{v}_d + \mathbf{R}(\psi_{0i})(\dot{\mathbf{l}}_i(t) - \mathbf{Sl}_i(t)\dot{\psi}_{ci}(t))\big), \tag{48}$$

where $\mathbf{e} = col(0, 0, 1)$, and $(\mathbf{I}_{3\times 3} - \mathbf{R}(\psi_{0i})\mathbf{Sl}_i(t)\mathbf{e}^\top)^{-1}$ is given explicitly by

$$\begin{bmatrix} 1 & 0 & (-y_{ci}(t)\cos\psi_{0i} - x_{ci}(t)\sin\psi_{0i}) \\ 0 & 1 & (-y_{ci}(t)\sin\psi_{0i} + x_{ci}(t)\cos\psi_{0i}) \\ 0 & 0 & 1 \end{bmatrix}.$$

By defining

$$\boldsymbol{\chi} := col(\mathbf{z}, \boldsymbol{\zeta}, \mathbf{q}) \quad \in \mathbb{R}^{3(p+r+1)}, \tag{49}$$

we can write the closed-loop dynamics compactly as

$$\begin{bmatrix} \dot{\boldsymbol{\chi}} \\ \dot{\theta} \end{bmatrix} = \begin{bmatrix} \mathbf{f}_\chi(t, \boldsymbol{\chi}, \theta) \\ f_\theta(t, \boldsymbol{\chi}, \theta) \end{bmatrix} =: \mathbf{F}(t, \boldsymbol{\chi}, \theta). \tag{50}$$

Note that in general, the closed-loop error dynamics are valid for $(\mathbf{z}, \boldsymbol{\zeta}, \mathbf{q}, \theta) \in \{\mathcal{R}\big((\mathbf{B}^\top \otimes \mathbf{I}_3)\big) \times \mathbb{R}^{3r} \times \mathbb{R}^3 \times \mathbb{R}\}$. From Assumption 1, however, we have that $\mathcal{R}(\mathbf{B}^\top) = \mathbb{R}^p$, which implies that $\mathcal{R}\big((\mathbf{B}^\top \otimes \mathbf{I}_3)\big) = \mathbb{R}^{3p}$. This means that the stated closed-loop dynamics is allowed to evolve on the entire state space. The result is summarized in the following theorem:

Theorem 1: Under assumptions 1 – 4, the control laws (19), (29), (30), and (32) render the closed-loop system (50) forward invariant and the set $\{(\boldsymbol{\chi}, \theta, t) : \boldsymbol{\chi} = 0\}$ UGAS. This solves the control objectives (14), (15), and (16).

C. Proof of Theorem 1

1) Forward completeness: Define the function

$$V_{z,\zeta}(t, \boldsymbol{\chi}, \theta) := \sum_{k=1}^{p} P_k(\mathbf{z}_k) + \sum_{i=1}^{r} S_{\zeta,i}\left(\boldsymbol{\zeta}_i, \psi_i(t, \boldsymbol{\chi}, \theta)\right) \tag{51}$$

Using (7), it is seen that $V_{z,\zeta}$ satisfies $\sum_{k=1}^{p} P_k(\mathbf{z}_k) + \lambda_1|\boldsymbol{\zeta}|^2 \leq V_{z,\zeta} \leq \sum_{k=1}^{p} P_k(\mathbf{z}_k) + \lambda_2|\boldsymbol{\zeta}|^2$, where $\lambda_1 = \min_{i\in\mathcal{I}} \lambda_{min,M_i}$ and $\lambda_2 = \max_{i\in\mathcal{I}} \lambda_{max,M_i}$. Since the lower and upper bounds here are positive definite and radially unbounded in $\mathbf{z}$ and $\boldsymbol{\zeta}$, by [7, Lemma 4.3] there exists class-$\mathcal{K}_\infty$ functions ϕ_1, ϕ_2 so that

$$\phi_1(|(\mathbf{z}, \boldsymbol{\zeta})|) \leq V_{z,\zeta} \leq \phi_2(|(\mathbf{z}, \boldsymbol{\zeta})|). \tag{52}$$

Differentiating (51) yields

$$\begin{aligned}\dot{V}_{z,\zeta} &= \left[\frac{\partial}{\partial \mathbf{z}}\left(\sum_{k=1}^{p} P_k(\mathbf{z}_k)\right)\right]^\top \dot{\mathbf{z}} + \sum_{i=1}^{r} \dot{S}_{\zeta,i} \\ &\leq \boldsymbol{\gamma}(\mathbf{z})^\top (\mathbf{B}^\top \otimes \mathbf{I}_3)\boldsymbol{\zeta} + \sum_{i=1}^{r} (-\boldsymbol{\zeta}_i^\top \mathbf{K}_{\mathbf{d}i}\boldsymbol{\zeta}_i + \boldsymbol{\zeta}_i^\top \boldsymbol{\alpha}_i) \\ &= -\boldsymbol{\alpha}^\top \boldsymbol{\zeta} - \sum_{i=1}^{r} (\boldsymbol{\zeta}_i^\top \mathbf{K}_{\mathbf{d}i}\boldsymbol{\zeta}_i) + \boldsymbol{\zeta}^\top \boldsymbol{\alpha} \\ &= -\sum_{i=1}^{r} (\boldsymbol{\zeta}_i^\top \mathbf{K}_{\mathbf{d}i}\boldsymbol{\zeta}_i) \leq 0 \end{aligned} \tag{53}$$

Since $\dot{V}_{z,\zeta} \leq 0$, this implies for all t in the maximum interval of existence $[t_0, T)$, that $V_{z,\zeta}(t) \leq V_{z,\zeta}(t_0)$. Combining this with (52) yields

$$\left|\left(\mathbf{z}(t), \boldsymbol{\zeta}(t)\right)\right| \leq \phi_3\left(\left|\left(\mathbf{z}(t_0), \boldsymbol{\zeta}(t_0)\right)\right|\right) \tag{54}$$

where $\phi_3(\cdot) := \phi_1^{-1} \circ \phi_2(\cdot) \in \mathcal{K}_\infty$.

Next, consider the positive definite, radially unbounded function (27) satisfying

$$\lambda_{min,P}|\mathbf{q}|^2 \leq V_q \leq \lambda_{max,P}|\mathbf{q}|^2. \tag{55}$$

On the time interval $[t_0, T)$, the bounds (54) and the fact that $\sigma_1(\cdot)$ is decreasing give a lower bound on $\sigma_1(|\mathbf{z}(t)|_L^2)$ according to

$$\sigma_1(|\mathbf{z}(t)|_L^2) \geq \sigma_1(||\mathbf{L}||\phi_3\left(\left|\left(\mathbf{z}(t_0), \boldsymbol{\zeta}(t_0)\right)\right|\right)^2) =: \epsilon_1. \tag{56}$$

From (33) we then get the following over $[t_0, T)$:

$$\begin{aligned}\dot{V}_q &\leq -\epsilon_1 \mathbf{q}^\top \mathbf{Q}\mathbf{q} + 2\mathbf{q}^\top \mathbf{P}\boldsymbol{\zeta}_1 \\ &\leq -\epsilon_1 \lambda_{min,Q}|\mathbf{q}|^2 + 2|\mathbf{q}||\mathbf{P}||\boldsymbol{\zeta}_1| \\ &\leq -\frac{1}{2}\epsilon_1 \lambda_{min,Q}|\mathbf{q}|^2 \quad \forall |\mathbf{q}| \geq \frac{4||\mathbf{P}||}{\epsilon_1 \lambda_{min,Q}}|\boldsymbol{\zeta}_1| \end{aligned}$$

For

$$|\mathbf{q}| \geq \frac{4||\mathbf{P}||\phi_3\left(\left|\left(\mathbf{z}(t_0), \boldsymbol{\zeta}(t_0)\right)\right|\right)}{\epsilon_1 \lambda_{min,Q}} =: \epsilon_2,$$

we are thus guaranteed $\dot{V}_q \leq 0$, which yields

$$\begin{aligned}V_q(t) &\leq \max\{V_q(\mathbf{q}(t_0)), \sup_{|\mathbf{q}|=\epsilon_2} V_q(\mathbf{q})\} \\ &\leq V_q(\mathbf{q}(t_0)) + \sup_{|\mathbf{q}|=\epsilon_2} V_q(\mathbf{q}) \\ &\leq \lambda_{max,P}|\mathbf{q}(t_0)|^2 + \lambda_{max,P}\epsilon_2^2 \quad \forall t \in [t_0, T). \end{aligned}$$

From this, we finally get uniform upper bounds for $|\mathbf{q}(t)|$ over the time interval $[t_0, T)$:

$$|\mathbf{q}(t)| \leq \sqrt{\frac{\lambda_{max,P}}{\lambda_{min,P}}}\left(|\mathbf{q}(t_0)| + \epsilon_2\right) \tag{57}$$

Combining this with assumptions 3 and 4, we achieve a uniform upper bound for $|\dot{\theta}|$ over $[t_0, T)$, which shows that there cannot be a finite escape time for the system (50), i.e. $T = +\infty$. By a locally Lipschitz property of the closed-loop system, we conclude that the solutions $\theta(t)$ and $\boldsymbol{\chi}(t)$ exist and are continuous functions over $[t_0, \infty)$.

For the remainder of the analysis, θ will be treated as an external input, continuous in time, that enters the dynamics of $\boldsymbol{\chi}$. Stability of the origin of

$$\dot{\boldsymbol{\chi}} = \mathbf{f}(t, \boldsymbol{\chi}), \tag{58}$$

where $\mathbf{f}(t, \boldsymbol{\chi}) := \mathbf{f}_\chi(t, \boldsymbol{\chi}, \theta(t))$, will be investigated by the means of the Nested Matrosov Theorem for time-varying systems presented in [8].

2) Uniform Global Stability: To apply the Nested Matrosov Theorem, UGS of the origin is first established. By forward completeness of the total closed loop system, the bounds in (54) and (57) hold $\forall t \geq t_0$.

Since $|\boldsymbol{\chi}| \leq |\left(\mathbf{z}, \boldsymbol{\zeta}\right)| + |\mathbf{q}|$, $|\boldsymbol{\chi}| \geq |\left(\mathbf{z}, \boldsymbol{\zeta}\right)|$, and $|\boldsymbol{\chi}| \geq |\mathbf{q}|$, we have that

$$\begin{aligned}&|\boldsymbol{\chi}(t)| \leq \phi_3\left(\left|\left(\mathbf{z}(t_0), \boldsymbol{\zeta}(t_0)\right)\right|\right) + \\ &\sqrt{\frac{\lambda_{max,P}}{\lambda_{min,P}}}\left[|\mathbf{q}(t_0)| + \frac{4||\mathbf{P}||\phi_3\left(\left|\left(\mathbf{z}(t_0), \boldsymbol{\zeta}(t_0)\right)\right|\right)}{\epsilon_1 \lambda_{min,Q}}\right] \\ &\leq \phi_3\left(|\boldsymbol{\chi}(t_0)|\right) + \\ &\sqrt{\frac{\lambda_{max,P}}{\lambda_{min,P}}}\left[|\boldsymbol{\chi}(t_0)| + \frac{4||\mathbf{P}||\phi_3\left(|\boldsymbol{\chi}(t_0)|\right)}{\lambda_{min,Q}\sigma_1\left(||\mathbf{L}||\phi_3\left(|\boldsymbol{\chi}(t_0)|\right)^2\right)}\right] \\ &=: \phi_4(|\boldsymbol{\chi}(t_0)|) \end{aligned}$$

It is verified that $\phi_4(\cdot) \in \mathcal{K}^\infty$, which shows that the origin is UGS.

3) Uniform Global Asymptotic Stability: Defining

$$V_0(t, \boldsymbol{\chi}) := V_{z,\zeta}(t, \boldsymbol{\chi}, \theta(t)), \tag{59}$$

we have from (53) that

$$\dot{V}_0(t, \boldsymbol{\chi}) \leq \sum_{i=1}^{r} (-\boldsymbol{\zeta}_i^\top \mathbf{K}_{\mathbf{d}i}\boldsymbol{\zeta}_i) =: Y_0(\boldsymbol{\chi}) \leq 0 \quad \forall \boldsymbol{\chi}. \tag{60}$$

and where it is noted that $Y_0(\boldsymbol{\chi}) = 0$ implies $\boldsymbol{\zeta} = \mathbf{0}$. Now, define the first auxiliary function

$$V_1(t, \boldsymbol{\chi}) := \mathbf{z}^\top (\mathbf{B} \otimes \mathbf{I}_3)^\ddagger \mathbf{M}_{\mathbf{2}}\boldsymbol{\zeta}, \tag{61}$$

where

$$\mathbf{M}_{\mathbf{2}} := diag(\mathbf{M}_{\mathbf{2}1}, \mathbf{M}_{\mathbf{2}2}, \ldots, \mathbf{M}_{\mathbf{2}r}) \quad \in \mathbb{R}^{3r \times 3r}, \tag{62}$$

and $(\mathbf{B} \otimes \mathbf{I}_3)^\ddagger \in \mathbb{R}^{3p \times 3r}$ is the Moore-Penrose pseudo-inverse of $(\mathbf{B} \otimes \mathbf{I}_3)$ satisfying

$$(\mathbf{B} \otimes \mathbf{I}_3)(\mathbf{B} \otimes \mathbf{I}_3)^\ddagger (\mathbf{B} \otimes \mathbf{I}_3) = (\mathbf{B} \otimes \mathbf{I}_3)$$

Differentiating (61) with respect to time yields

$$\begin{aligned}\dot{V}_1(t, \boldsymbol{\chi}) &= \boldsymbol{\zeta}^\top (\mathbf{B} \otimes \mathbf{I}_3)(\mathbf{B} \otimes \mathbf{I}_3)^\ddagger \mathbf{M}_{\mathbf{2}}\boldsymbol{\zeta} \\ &\quad + \mathbf{z}^\top (\mathbf{B} \otimes \mathbf{I}_3)^\ddagger \left(\dot{\mathbf{M}}_{\mathbf{2}}\boldsymbol{\zeta} + \mathbf{M}_{\mathbf{2}}\dot{\boldsymbol{\zeta}}\right) \\ &=: Y_1(\boldsymbol{\chi}, \boldsymbol{\phi}(t, \boldsymbol{\chi})) \end{aligned}$$

Here, all time dependent terms of $\dot{V}_1(t, \boldsymbol{\chi})$ has been collected in the vector $\boldsymbol{\phi}(t, \boldsymbol{\chi})$, defined as

$$\boldsymbol{\phi}(t, \boldsymbol{\chi}) := col[\mathbf{M}_{\mathbf{2}}\boldsymbol{\zeta}, \dot{\mathbf{M}}_{\mathbf{2}}\boldsymbol{\zeta}, \mathbf{M}_{\mathbf{2}}\dot{\boldsymbol{\zeta}}] \tag{63}$$

Evaluating $Y_1(\boldsymbol{\chi}, \boldsymbol{\phi}(t,\boldsymbol{\chi}))$ at $\boldsymbol{\zeta} = \mathbf{0}$, and using (44) yields:

$$\begin{aligned} Y_1(\boldsymbol{\chi}, \boldsymbol{\phi}(t,\boldsymbol{\chi}))\Big|_{\boldsymbol{\zeta}=0} &= \mathbf{z}^\top (\mathbf{B}\otimes\mathbf{I}_3)^\ddagger \mathbf{M_2}\dot{\boldsymbol{\zeta}}\Big|_{\boldsymbol{\zeta}=0} \\ &= \mathbf{z}^\top (\mathbf{B}\otimes\mathbf{I}_3)^\ddagger \boldsymbol{\alpha}(\mathbf{z}) \\ &= -\mathbf{x_0}^\top (\mathbf{B}\otimes\mathbf{I}_3)(\mathbf{B}\otimes\mathbf{I}_3)^\ddagger (\mathbf{B}\otimes\mathbf{I}_3)\boldsymbol{\gamma}(\mathbf{z}) \\ &= -\mathbf{x_0}^\top (\mathbf{B}\otimes\mathbf{I}_3)\boldsymbol{\gamma}(\mathbf{z}) \\ &= -\mathbf{z}^\top \boldsymbol{\gamma}(\mathbf{z}) < 0 \quad \forall \mathbf{z} \neq \mathbf{0} \end{aligned}$$

The last inequality follows from the definition of $\boldsymbol{\gamma}_k(\mathbf{z}_k)$ in (24) and the properties listed in (25). Now, define the second auxiliary function

$$V_2(\boldsymbol{\chi}) := V_q(\mathbf{q}) \tag{64}$$

which satisfies

$$\dot{V}_2 \leq -\sigma_1(|\mathbf{z}|_L^2)\mathbf{q}^\top \mathbf{Q}\mathbf{q} + 2\mathbf{q}^\top \mathbf{P}\boldsymbol{\zeta}_1 =: Y_2(\boldsymbol{\chi}) \tag{65}$$

Evaluating $Y_2(\boldsymbol{\chi})$ at $\boldsymbol{\zeta}, \mathbf{z} = \mathbf{0}$ yields

$$Y_2(\boldsymbol{\chi})\Big|_{\boldsymbol{\zeta},\mathbf{z}=\mathbf{0}} = -\mathbf{q}^\top \mathbf{Q}\mathbf{q} < 0 \quad \forall \mathbf{q} \neq \mathbf{0}$$

We now have that $Y_0(\boldsymbol{\chi}), Y_1(\boldsymbol{\chi}, \boldsymbol{\phi}(t,\boldsymbol{\chi})), Y_2(\boldsymbol{\chi}) = 0$ together imply $\boldsymbol{\chi} = \mathbf{0}$.

By noting that $V_0(t,\boldsymbol{\chi}), V_1(t,\boldsymbol{\chi}), V_2(\boldsymbol{\chi})$ are locally Lipschitz continuous[4] over $[t_0,\infty)\times\mathbb{R}^{3(r+p+1)}$, and that $Y_0(\boldsymbol{\chi}), Y_1(\boldsymbol{\chi},\boldsymbol{\phi}), Y_2(\boldsymbol{\chi})$ are continuous in their arguments, the only thing left to show is that there exist uniform upper bounds on $|V_i(t,\boldsymbol{\chi})|$ and $|\boldsymbol{\phi}(t,\boldsymbol{\chi})|$ whenever $|\boldsymbol{\chi}|$ is upper bounded. The bounds on $|V_0(t,\boldsymbol{\chi})|, |V_2(\boldsymbol{\chi})|$ follows from (52) and (55), while the bounds on $|V_1(t,\boldsymbol{\chi})|$ is established by using the Cauchy-Schwarz inequality, noting that the norm of the block-diagonal matrix $\mathbf{M_2}$ is uniformly upper bounded by the uniform upper bounds on $||\mathbf{M_{2}}_i||$.

To see that the stated bounds on $|\boldsymbol{\phi}(t,\boldsymbol{\chi})|$ holds, first note that the norms of $\boldsymbol{\nu}_i$, $i\in\mathcal{I}$, are bounded for bounded $|\boldsymbol{\chi}|$ by (48) and assumptions 2 – 3. Uniform upper bounds on $\dot{\mathbf{M}}_{\mathbf{2}i} = \mathbf{R}(\psi_i)\big(\mathbf{S}\mathbf{M}_i\mathbf{e}^\top\boldsymbol{\nu}_i + \mathbf{M}_i\mathbf{S}^\top\mathbf{e}^\top\boldsymbol{\nu}_i\big)\mathbf{R}^\top(\psi_i)$ follows, which in turn shows that $|\dot{\mathbf{M}}_{\mathbf{2}}\boldsymbol{\zeta}|$ is bounded. Since $|\mathbf{M_2}\boldsymbol{\zeta}|$ and $|\mathbf{M_2}\dot{\boldsymbol{\zeta}}|$ also are bounded for bounded $|\boldsymbol{\chi}|$ (the latter follows from (44) and the bounds on $|\boldsymbol{\nu}_i|$), the bounds on $|\boldsymbol{\phi}(t,\boldsymbol{\chi})|$ follows.

All assumptions of [8, Theorem 1] is satisfied, and UGAS for the origin of (58) is established. By lemma (1) and the closed loop dynamics of θ in (47), it follows that the control objectives (14)-(16) are satisfied. □

[4]This follows from [7, Lemma 3.2] by $V_0(t,\boldsymbol{\chi}), V_1(t,\boldsymbol{\chi}), V_2(\boldsymbol{\chi}), \frac{\partial V_0(t,\boldsymbol{\chi})}{\partial \boldsymbol{\chi}}, \frac{\partial V_1(t,\boldsymbol{\chi})}{\partial \boldsymbol{\chi}}, \frac{\partial V_2(\boldsymbol{\chi})}{\partial \boldsymbol{\chi}}$ being continuous on any set $[a,b]\times D$, where $[a,b]\subset[t_0,\infty)$, $D\subset\mathbb{R}^{3(p+r+1)}$.

VI. Simulation

The proposed control-scheme is demonstrated numerically for three ships with dynamics given by (1), where the mass matrices are identical, the damping is given by

$$\mathbf{D}_i(\boldsymbol{\nu}_i) = \mathbf{D}_L + \mathbf{D_u}|u_i| + \mathbf{D_v}|v_i| + \mathbf{D_r}|r_i|, \tag{66}$$

and $\mathbf{C}_i(\boldsymbol{\nu}_i)$ is calculated based on the mass matrix from the procedures in [1]. The numerical values for the involved matrices are

$$\mathbf{M}_i = 10^7 \begin{bmatrix} 0.0275 & 0 & 0 \\ 0 & 0.0763 & -0.0738 \\ 0 & -0.0738 & 6.6910 \end{bmatrix}$$

$$\mathbf{D}_L = 10^6 \begin{bmatrix} 0.0000 & 0 & 0 \\ 0 & 0.0099 & 0.0014 \\ 0 & 0.0007 & 2.8134 \end{bmatrix}$$

$$\mathbf{D}_u = 10^6 \begin{bmatrix} 0.0024 & 0 & 0 \\ 0 & 0.0088 & 0 \\ 0 & 0.1118 & 6.0480 \end{bmatrix}$$

$$\mathbf{D}_v = 10^7 \begin{bmatrix} 0 & 0 & 0 \\ 0 & 0.0003 & 0.0135 \\ 0 & 0 & 1.1887 \end{bmatrix}$$

$$\mathbf{D}_r = 10^8 \times diag(0, 0.0095, 1.5629)$$

The earth-fixed frame gives north-position along its x-axis, and east-position along its y-axis. The parameterized path is chosen as $x_d(\theta) = 100\sin(\frac{\pi}{400}\theta) + 100$, $\mathbf{y}_d(\theta) = \theta + 100$. The desired formation configuration is chosen as $\mathbf{l}_1 = col(0,80,0)$, $\mathbf{l}_2 = col(0,0,0)$, $\mathbf{l}_3 = col(0,-80,0)$, which corresponds to a transversal line formation where a tangential heading angle is common for all the ships. The communication topology is chosen according to two communication links, where Vessel 1 is the positive end of both links. Vessel 3 is set as the acting leader.

The control-specific parameters is chosen according to $\mathbf{K_d}_i = 10^4 \times diag(5,5,1000)$, $\mathbf{A} = diag(-0.02,-0.02,-0.03)$, $\mathbf{P} = \frac{3}{2}\times 10^{-2}\times diag(1,1,10^{-5})$, $\mathbf{L} = diag(\mathbf{L}_0,\mathbf{L}_0)$, $\mathbf{L}_0 = diag(1,1,2500)$. The control-specific functions is chosen according to $P_k(\mathbf{z}_k) = \frac{1}{2}(az_{k1}^2 + az_{k2}^2 + bz_{k3}^2)$, $a = 3000, b = 6\times10^5$, $\sigma_1(s) = \sigma_2(s) = \exp(-0.25s)$, $v_s(\theta,t) = \frac{3}{\sqrt{x_d^\theta(\theta)^2 + y_d^\theta(\theta)^2}}$, $\mu(\theta) = \frac{1}{\sqrt{x_d^\theta(\theta)^2 + y_d^\theta(\theta)^2}}$.

The initial positions of the vessels is chosen as $\boldsymbol{\eta}_{10} = col(-70,185,\frac{\pi}{10})$, $\boldsymbol{\eta}_{20} = col(-50,140,0)$, $\boldsymbol{\eta}_{30} = col(-80,50,-\frac{\pi}{6})$, while $\theta_0 = 50$. To illustrate the strong separation achieved between the group coordination and formation mission objectives, a "blackout" is inflicted to Vessel 1 after $t = 550[s]$ (at this point, the east-position of Vessel 1 is $\approx 1250[m]$). The result is that the vessel slows down and starts drifting south-east at a speed of $\approx 0.6[m/s]$.

The simulation results are shown in Fig.1 and Fig.2. It is seen that the vessels synchronize before they initiate

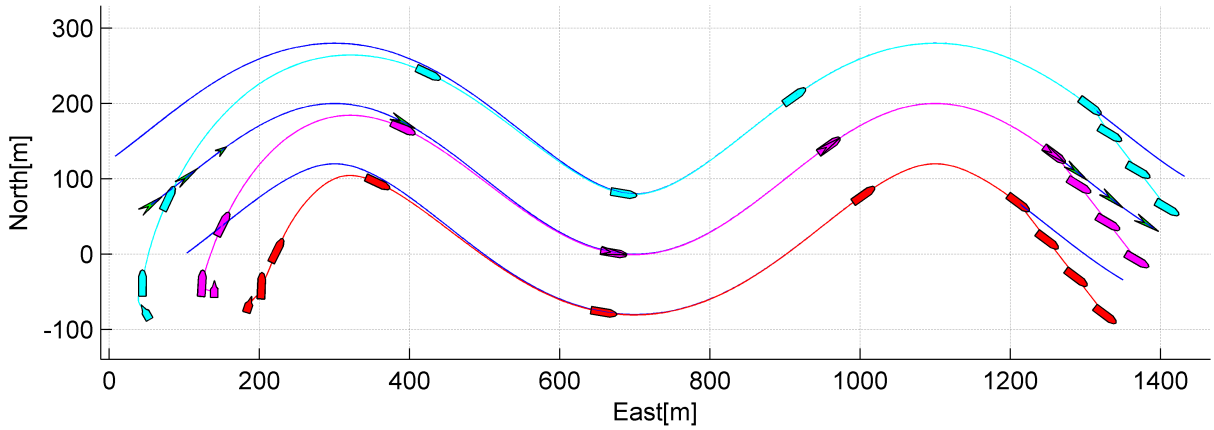

Fig. 1. North-east position plot for the three vessels. The red, purple, and blue ships correspond to vessels 1, 2, and 3, respectively. The green arrow indicates the position of $\mathbf{p}_d(\theta)$ which the FRP of the acting leader should converge to. Initial positions are indicated by smaller-sized ships and arrow.

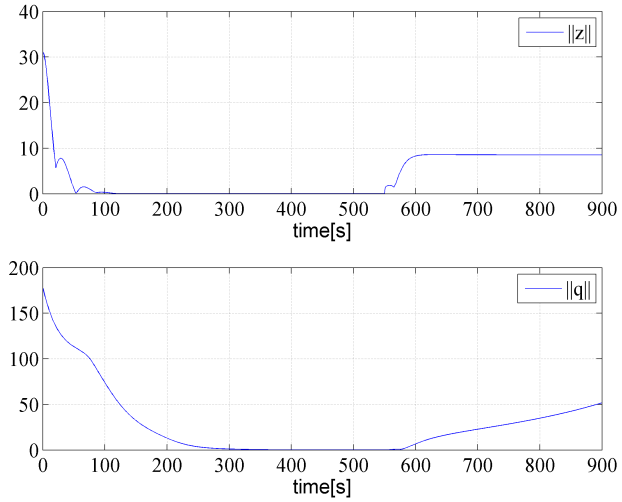

Fig. 2. Time-series of $|\mathbf{z}(t)|_\infty$ and $|\mathbf{q}(t)|_\infty$

movement towards the path. After the blackout, the two vessels that still are operational abandon the formation mission objective, concentrating solely on decreasing the synchronization errors by following the drifting vessel. It is seen that steady state synchronization errors arise after the blackout. This is due to Vessel 1 not partaking in the synchronization work. The steady state errors are, however, kept within reasonable limits.

VII. Conclusion

This paper has addressed the topic of formation control for fully actuated marine surface vessels within a path-following framework. Rooted in an operational philosophy where the formation should be maintained at all costs, the design enables strong separation and prioritization between the task of getting the vessels into formation, and the task of getting the formation to follow a prespecified path. This separation provides inter-vessel anti-collision capabilities during the path-following phase of a mission. However, the design cannot guarantee collision-avoidance during the coordination phase for unfortunate initial conditions.

By following the group agreement protocols in [2], the coordination between the vessels is performed through a decentralized communication topology. However, as path-following requires that each vessel has access to a common velocity signal that is calculated based on the states of the vessels, the proposed solution is in general centralized. It is possible to let the velocity input be calculated locally by the acting leader, and distributed to the other vessels through the communication topology. This would decentralize the design, but at the same time introduce time-delays. Achieving a fully decentralized design has not been the focus in this paper, but is certainly a topic for future work, in addition to the effect of communication delays on the closed loop performance.

References

[1] Fossen, T. I., *Guidance and Control of Marine Craft*. Draft, 2010.

[2] Arcak, M., Passivity as a design tool for group coordination. *IEEE Transactions on Automatic Control,* 52(8):1381-1390, 2007.

[3] Skjetne, R., *The Maneuvering Problem*. PhD thesis, NTNU, 2005.

[4] Skjetne, R., Ihle, I.-A. F., and Fossen, T. I., *Formation control by synchronizing multiple maneuvering systems*. Proc. IFAC Conf. Maneuvering and Contr. Marine Crafts, NTNU, IFAC, Girona, Spain, pp. 280–285., 2003.

[5] Ihle, I.-A. F., Arcak, M., and Fossen, T. I., Passivity-based designs for synchronized path-following. *Automatica,* 43:1508-1518, 2007.

[6] Breivik, M., Hovstein, V. E. and Fossen, T. I., Ship Formation Control: A Guided Leader-Follower Approach. *Proceedings of the 17th World Congress The International Federation of Automatic Control (IFAC'08), pp. 16008-16014,* 2008, 6-11 July - Seoul, Korea.

[7] Khalil, H. K., *NonLinear Systems*. Prentice Hall, 2002.

[8] Loria, A., Panteley, E., Popovic, D., and Teel, A. R., A nested Matrosov Theorem and Persistency of Excitation for Uniform Convergence in Stable Nonautonomous Systems. *IEEE Transactions on Automatic Control,* 50(2):183-198, 2005.

[9] Bai, H., Arcak, M., and Wen, J. T., Adaptive design for reference velocity recovery in motion coordination. *Systems & control letters,* 57:602-610,2008.

[10] Egerstedt, M. and Hu, X., Formation constrained multi-agent control. *IEEE Transactions on Robotics abd Automation,* 17:947-951, 2001.

[11] Leonard, N. E. and Fiorelli, E., Virtual leaders, artificial potentials and coordinated control of groups. *Proceedings of the 40th IEEE conference on Decision and Control,* pages 2968-2973, 2001.

[12] Lewis, M. A. and Tan, K.-H., High precision formation control of mobile robots using virtual structures. *Autonomous Robots,* 4:387-403, 1997.

[13] Olfati-Saber, R. and Murray, R. M., Distributed cooperative control of multiple vehicle formations using structural potential functions. IFAC World Congress, 2002.

[14] Breivik, M., Subbotin, M. V., and Fossen, T. I., Guided formation control for wheeled mobile robots. *Proceedings of the 9th ICARCV*, 2006.

[15] Grøtli, E. I., Chaillet, A., and Gravdahl, J. T., Output Control of Spacecraft in Leader Follower Formation, *Proceedings of the 47th IEEE Conference on Decision and Control,* 2008